Residual Stresses, Cracking and Stress Intensity Factors for Vickers Indentations in Ceramics

Xiaodan Sun

The Queen's College



Supervisor: Prof. Richard Todd

Department of Materials

University of Oxford

Michaelmas Term, 2015

Residual Stresses, Cracking and Stress Intensity Factors for Vickers Indentations in Ceramics

Xiaodan Sun
The Queen's College

Doctor of Philosophy
Michaelmas Term 2015

Abstract

Vickers hardness indentations on Al_2O_3 were studied comprehensively. Beneath indentation, there is a well-defined interface between the plastic zone and the elastic region and the radius of the plastic zone is close to half the indentation diagonal length. The residual stress field around the indentations has been measured by optical fluorescence microscope (FLM) scans. Yoffe's stress model predicted higher stresses than the experimental stress results. The radial crack lengths were measured by FLM scans, and the optical microscope (OM) and SEM methods for crack length measurements were found to significantly underestimate the crack lengths. Post indentation slow crack growth was found on the radial cracks from indentations in alumina and ruby and the threshold stress intensity factor K_{I0} of the radial cracks were determined. The radial-median crack system was found for alumina indentations. Lateral cracks were also found for all the indentations, and their depths were close to the half diagonal lengths. The lateral cracks joined the tips of the radial cracks and had the similar growth rates to the radial cracks.

The indentation parameters of SiC and 3Y-TZP indentations were also measured. Lateral cracking was observed beneath in SiC indentations but not in case of 3Y-TZP. The depth of the lateral crack of the SiC indentation was found to be close to the half diagonal length. The residual stresses and surface profiles around SiC and 3Y-TZP indentations were measured. The lateral crack lengths of the SiC determined from the surface profiles were close to the radial crack lengths. For TZP indentations，the highest volume fraction of the monoclinic zirconia phase was found near the edge of the indentation. Surface uplifts around indentations were found to have the profiles matching with distributions of the volume fraction of the monoclinic phase.

A new Vickers indentation residual stress model has been presented using assumptions based on the experimental findings on alumina indentations. The main novelty of the model is that it predicts the stresses in the presence of cracking, and is therefore testable. The residual stress model has successfully predicted the stress fields around the polycrystalline alumina and SiC indentations but failed on TZP indentations because of the lack of lateral cracking and the tetragonal-to-monoclinic phase transformation. From the residual stress model, a new formula for the indentation stress intensity factor, K, was derived, which provided good results for threshold stress intensity factor, K_{I0}, on alumina, and fracture toughness, K_{IC}, for SiC, and Si_3N_4. Three adjustable parameters can be added to strengthen existing model.

Acknowledgements

I would first of all thank Prof. Richard Todd, who guided me through such a memorable four-year DPhil life. Without his continuous encouragement, patient guidance, and tremendous help both in experiments and writing, this thesis would not have been possible.

Thanks also go to the members in RIT group (Dr. Andrew Norton, Dr. Claire Dancer, Dr Noor Yahya, Dingyue Shi, Emilio Lopez-Lopez, Teresa Rodriguez Suarez, Yuanfei Gao, Tom Scott) for their support and friendship. I am also grateful to all the technicians and materials scientists in this department who have trained me with great patience and responsibility. Special thanks should go to Mi Du, who invited me to the best lunches in Oxford and made my life much easier with the printing work.

I must thank the China Scholarship Council and Oxford University for the CSC-Oxford Scholarship to support me financially for the DPhil. I am also thankful for the grant offered by the Department of Materials to support my last six months in the lab.

Finally, huge thanks to my wife, Wei Wang, and my parents for their unlimited love and infallible support to cheer me up and help me walk through every difficulty in my UK life. More importantly they have enlightened me to let me understand what is most important and what I should pursue in my life for which I am eternally thankful.

Preface

The work presented in this thesis was carried out by the author in the Department of Materials, University of Oxford under the supervision of Prof. Richard I. Todd. The work in this thesis is original and no part of this thesis has previously been submitted for a degree at this or other university.

Part of this work has been presented at the 5th International Congress on Ceramics (ICC5), Beijing, China, August 2015.

Contents

Chapter 1 Introduction 9
1.1 Background 9
1.2 Aims and outline of this project 12
References 13
Chapter 2 Literature review 15
2.1 Ceramics in this study 15
2.2 Indentation fracture theory 19
2.2.1 Introduction to indentation techniques 19
2.2.2 Vickers indentation cracking 21
2.2.3 Yoffe's residual stress model 25
2.2.4 Chiang's residual stress model 29
2.2.5 Vickers indentation fracture toughness 31
2.2.6 Pile-up and sink-in around indentation 42
2.2.7 Subcritical slow crack growth 45
2.3 Residual stress measurement 47
2.3.1 Origin and categories of residual stresses 48
2.3.2 Destructive methods for stress measurement 49
2.3.3 Overview of non-destructive methods 49
2.3.4 Cr^{3+} fluorescence spectroscopy 50
2.3.5 Raman Spectroscopy 59
2.4 Summary 69
References 70
Chapter 3 Materials Preparation and Experimental Procedures 80
3.1 Materials Preparation 80
3.1.1 Single Crystal Alumina 80
3.1.2 Polycrystalline Alumina 80
3.1.3 SiC 82
3.1.4 Zirconia 83
3.2 Beam production 84
3.3 Microstructural Characterization 84
3.3.1 SEM observation 84
3.3.2 Grain Size Measurement 85
3.3.3 Density Measurement 86
3.3.4 Indentation 87
3.4 Cr^{3+} Fluorescence Microscopy and Raman Microscopy 91
3.4.1 Raman microscope 91
3.4.2 Scanning strategy 93
3.4.3 Fitting methods for alumina spectra 94
3.4.4 Fitting methods for SiC and TZP spectra 96
3.4.5 Four-point bending test for PS coefficient measurement 98
References 101

Chapter 4 Vickers indentation study on alumina 102
4.1 Introduction 102
4.2 Experimental results 103
4.2.1 Measurement of indentation parameters 103
4.2.2 Indentation characterisation 105
4.2.3 Residual stress fields around indentations 106
4.2.4 Post-indentation growth measurements from the FLM method 112
4.2.5 Radial crack length measurements from the FLM method 119
4.2.6 Radial crack length measurements from the SEM method 121
4.2.7 FIB milling of the 9.8 N indentations 122
4.2.8 Serial polishing of alumina indentations 123
4.2.9 FLM mapping on the cross-section of a 98 N indentation. 129
4.2.10 Surface profile around the Vickers indentation 130
4.3 Discussion 134
4.3.1 Plastic zone 134
4.3.2 Indentation residual stress 136
4.3.3 Real radial crack length 142
4.3.4 Post-indentation subcritical crack growth 147
4.3.5 Surface profiles and lateral crack lengths of indentations 154
4.3.6 Overview of the cracking system of alumina 160
4.4 Summary 163
References 165
Chapter 5 Vickers indentation studies on SiC and 3Y-TZP indentations 169
5.1 Introduction 169
5.2 Results and discussion 170
5.2.1 Raman spectrum of SiC 170
5.2.2 SiC indentation parameters 172
5.2.3 SiC indentation cracking 174
5.2.4 Surface profiles around SiC indentations 175
5.2.5 Calibration of the PS coefficient of SiC Raman peak 178
5.2.6 Line scans on SiC indentations 183
5.2.7 TZP indentation parameters 186
5.2.8 TZP Indentation cracking 189
5.2.9 Raman spectrum of TZP 190
5.2.10 Raman line scans on TZP indentations 192
5.2.11 TZP indentation surface profiles 196
5.3 Conclusions 200
References 203
Chapter 6 Indentation model 206
6.1 Introduction 206
6.2 Indentation residual stress model 206
6.2.1 Introduction 206
6.2.2 Model assumptions 208

6.2.3 Model for stresses around an indentation in the presence of radial and lateral cracking 211
6.2.4 Relating the model to the experiments 219
6.3 Comparison with experiments and discussion 223
6.3.1 Al_2O_3 223
6.3.2 SiC 229
6.3.3 TZP 234
6.4 Derivation of mechanical energy release rate, *G*, and stress intensity factor, *K*, from the residual stress model 239
6.5 Calculation of the stress intensity factor, *K* for polycrystalline alumina and silicon carbide indentations 244
6.5.1 Al_2O_3 244
6.5.2 SiC 246
6.6 Testing the model with Si_3N_4 indentation results from Quinn and Bradt 249
6.7 Possible adjustable parameters for the model 251
6.7.1 Plastic zone dimension factor, α 252
6.7.2 Weighting factor, β 253
6.7.3 Crack depth dimension factor, γ 254
6.8 The apparent R-curve effect 257
6.9 Advantages and disadvantages of the model 259
6.10 Suggestions for the future use of the Vickers indentation 261
6.11 Summary 264
References 265
Chapter 7 Conclusions and suggestions for the future 267
7.1 Conclusions 267
7.1.1 Vickers indentation study on alumina 267
7.1.2 Vickers indentation study SiC and 3Y-TZP 269
7.1.3 Vickers indentation model 270
7.2 Future work 271
7.2.1 Lateral crack characterization 271
7.2.2 Testing the model on more ceramics 272
7.2.3 The apparent R-curve effect 272
References 274

For Wei and My Son

Chapter 1 Introduction

1.1 Background

The word ‘ceramic’ comes from the Greek word ‘keramos’, which means ‘pottery’ with its old Sanskrit root meaning being ‘to burn’. Although nowadays modern ceramics have much broader scope than pottery, sintering is still necessary in the production of most traditional ceramics. Formed between metallic and non-metallic elements, ceramics are present in crystalline, semi-crystalline or amorphous forms. The father (Richerson et al., 2005) of the modern ceramic engineering Kingery (1960) defined the ceramics as “The art and science of making and using solid articles, which have as their essential component, and are composed in large part of, inorganic nonmetallic materials”. The ionic or covalent bonding normally enables ceramics to have high melting temperature, high hardness, and good corrosion and wear resistance in contrast to metals.

Despite the enviable properties and potential of ceramics, their use in structural components is often inhibited by their low toughness and low fracture strength (Osayande and Okoli, 2008). The past two decades have seen great efforts to improve the fracture toughness of ceramics, such as transformation toughening

(Hannink et al., 2000), crack bridging (Becher et al., 1996) and changing the fracture mode (Yahya and Todd, 2012).

Precise measurement of the fracture toughness of ceramics is important and can often be quite challenging. The fundamental principle of the testing techniques is to introduce cracks and to evaluate the resistance of the material to propagation of the crack. A variety of techniques are based on introducing sharp pre-cracks to beams, of which three standard methods are normally employed: the single edge notched beam (SENB) method (Roberts et al., 1993), chevron notched beam (CNB) method (Munz, 1983) and the surface crack in flexure (SCF) method (Gogotsi, 2003). However, the testing samples for these methods are difficult to prepare (for example, the chevron-notched beam has a complicated shape and very narrow notch gaps (Nose and Fujii, 1988)) and the fracture toughness from notched beams can produce erroneously high values (Munz, 1983, Ritchie et al., 1990, Fett and Munz, 2006).

Alternatively, an indenter, for example, Vickers, Berkovich or Knoop, can be used to introduce cracks and evaluate fracture toughness (Kruzic et al., 2009). The indentation technique is very easy and quick to perform, require only a small amount of material and is able to investigate local microstructural features. Not only limited to fracture toughness (Anstis et al., 1981), the indentation technique is also widely used as an important method to test other mechanical properties of ceramics, such as

elastic and plastic behaviours (Bhattacharya and Nix, 1988), hardness (Sakai, 1993) and Young's modulus (Oliver and Pharr, 1992).

Although the indentation technique has been widely used to study the fracture behaviour of ceramics (Kim et al., 1997, Lawn and Swain, 1975, Anstis et al., 1981, Mullins et al., 2007), it has not been widely accepted by researchers as a standard way of assessing fracture toughness. There is no equation which can be applied universally to ceramics and the fracture toughness results from indentation sometimes do not agree with other techniques or other studies (Li et al., 1989, Ghosh et al., 1995, Kruzic et al., 2003, Quinn and Bradt, 2007). This thesis will assess the validity of the Vickers indentation technique and discuss the factors related to Vickers indentation technique such as lateral cracking, and issues in measuring indentation parameters and subcritical slow crack growth.

The materials targeted in this thesis are widely-used engineering ceramics, alumina (Al_2O_3), silicon carbide (SiC) and Yttria stabilised tetragonal zirconia polycrystals (Y-TZP). These ceramics are normally used in places where good mechanical properties are required. Central to the description of the mechanical properties, the resistance to fracture is a key performance index for many applications such as dental and orthopaedic components (Marx et al., 2004).

Additionally, better knowing the residual stress field created after surface damage, such as those created around an indentation, helps the research of the properties of the material and the assessment of the damage introduced. The residual stress fields around SiC and Y-TZP indentations have been rarely discussed in previous work and therefore will be investigated in this thesis. Measurement of the residual stress field in this thesis was assisted by non-destructive residual stress measurement methods.

1.2 Aims and outline of this project

The project aims to develop a better understanding of the indentation of some widely-used ceramics, namely, Al_2O_3, SiC and Y-TZP and try to build a new model for describing the indentation residual stress field and the indentation fracture toughness. This thesis has 7 Chapters. The indentation theory and the related non-destructive residual stress measurement methods are reviewed in Chapter 2. The Chapter 3 then describes the material and experimental procedure. The cracking behaviour (including the presence and growth of lateral cracking), residual stress field and subcritical crack growth of alumina indentations have been investigated in Chapter 4. Alumina is used here as the model material to fully understand nearly every aspect about the indentation process. In Chapter 5, the residual stress fields around SiC and TZP indentations are primarily investigated. Due to the time limit of this project, more of the details of SiC and TZP indentations have not been fully explored. From the understanding of the alumina indentation in Chapter 4, a new model for the

indentation residual stress field has been proposed originally from Prof. Richard Todd in Chapter 6. This new model is first described with its assumptions and developing route, then the indentation stress fields of alumina, SiC and TZP investigated in Chapter 4 and 5 are used to assess the model. The fracture toughness calculation equation is then derived from the residual stress model and its predictions of the fracture toughness of the ceramics are discussed with respect to the results from other techniques and other fracture toughness equations.

References

ANSTIS, G., CHANTIKUL, P., LAWN, B. R. & MARSHALL, D. 1981. A critical evaluation of indentation techniques for measuring fracture toughness: I, direct crack measurements. *Journal of the American Ceramic Society,* 64**,** 533-538.

BECHER, P. F., HSUEH, C. H., ALEXANDER, K. B. & SUN, E. Y. 1996. Influence of Reinforcement Content and Diameter on the R‐Curve Response in SiC‐Whisker‐Reinforced Alumina. *Journal of the American Ceramic Society,* 79**,** 298-304.

BHATTACHARYA, A. & NIX, W. 1988. Analysis of elastic and plastic deformation associated with indentation testing of thin films on substrates. *International Journal of Solids and Structures,* 24**,** 1287-1298.

FETT, T. & MUNZ, D. 2006. Influence of narrow starter notches on the initial crack growth resistance curve of ceramics. *Archive of Applied Mechanics,* 76**,** 667-679.

GHOSH, A., LI, Z., HENAGER, C., KOBAYASHI, A. & BRADT, R. 1995. Vickers microtoughness of SiC in the median-crack regime. *Fracture Mechanics of Ceramics.,* 11**,** 219-231.

GOGOTSI, G. A. 2003. Fracture toughness of ceramics and ceramic composites. *Ceramics International,* 29**,** 777-784.

HANNINK, R. H., KELLY, P. M. & MUDDLE, B. C. 2000. Transformation toughening in zirconia‐containing ceramics. *Journal of the American Ceramic Society***,** 461-487.

KIM, B.-K., HAHN, J.-W. & HAN, K. R. 1997. Quantitative phase analysis in tetragonal-rich tetragonal/monoclinic two phase zirconia by Raman spectroscopy. *Journal of Materials Science Letters,* 16**,** 669-671.

KINGERY, W. D. 1960. Introduction to ceramics.

KRUZIC, J., KIM, D., KOESTER, K. & RITCHIE, R. 2009. Indentation techniques for evaluating the fracture toughness of biomaterials and hard tissues. *Journal of the mechanical behavior of biomedical materials,* 2**,** 384-395.

KRUZIC, J. J., NALLA, R. K., KINNEY, J. H. & RITCHIE, R. 2003. Crack blunting, crack bridging and resistance-curve fracture mechanics in dentin: effect of hydration. *Biomaterials,* 24**,** 5209-5221.

LAWN, B. & SWAIN, M. 1975. Microfracture beneath point indentations in brittle solids. *Journal of Materials Science,* 10**,** 113-122.

LI, Z., GHOSH, A., KOBAYASHI, A. S. & BRADT, R. C. 1989. Indentation fracture toughness of sintered silicon carbide in the Palmqvist crack regime. *Journal of the American Ceramic Society,* 72**,** 904-911.

MARX, R., JUNGWIRTH, F. & WALTER, P.-O. 2004. Threshold intensity factors as lower boundaries for crack propagation in ceramics. *Biomedical engineering online,* 3**,** 41.

MULLINS, L., BRUZZI, M. & MCHUGH, P. 2007. Measurement of the microstructural fracture toughness of cortical bone using indentation fracture. *Journal of Biomechanics,* 40**,** 3285-3288.

MUNZ, D. 1983. Effect of specimen type on the measured values of fracture toughness of brittle ceramics. *Fracture Mechanics of Ceramics,* 6**,** 1-26.

NOSE, T. & FUJII, T. 1988. Evaluation of Fracture Toughness for Ceramic Materials by a Single‐Edge‐Precracked‐Beam Method. *Journal of the American Ceramic Society,* 71**,** 328-333.

OLIVER, W. C. & PHARR, G. M. 1992. An improved technique for determining hardness and elastic modulus using load and displacement sensing indentation experiments. *Journal of materials research,* 7**,** 1564-1583.

OSAYANDE, L. & OKOLI, O. 2008. Fracture toughness enhancement for alumina system: a review. *Int. J. Appl. Ceram. Technol,* 5**,** 313-323.

QUINN, G. D. & BRADT, R. C. 2007. On the Vickers indentation fracture toughness test. *Journal of the American Ceramic Society,* 90**,** 673-680.

RICHERSON, D., RICHERSON, D. W. & LEE, W. E. 2005. *Modern ceramic engineering: properties, processing, and use in design*, CRC press.

RITCHIE, R. O., DAUSKARDT, R. H., YU, W. & BRENDZEL, A. 1990. Cyclic fatigue‐crack propagation, stress‐corrosion, and fracture‐toughness behavior in pyrolytic carbon‐coated graphite for prosthetic heart valve applications. *Journal of biomedical materials research,* 24**,** 189-206.

ROBERTS, R., ROWE, R. & YORK, P. 1993. The measurement of the critical stress intensity factor (K IC) of pharmaceutical powders using three point single edge notched beam (SENB) testing. *International journal of pharmaceutics,* 91**,** 173-182.

SAKAI, M. 1993. Energy principle of the indentation-induced inelastic surface deformation and hardness of brittle materials. *Acta metallurgica et materialia,* 41**,** 1751-1758.

YAHYA, N. A. & TODD, R. I. 2012. Influence of C doping on the fracture mode and abrasive wear of Al 2 O 3. *Journal of the European Ceramic Society,* 32**,** 4003-4007.

Chapter 2 Literature review

2.1 Ceramics in this study

Aluminium oxide (Al_2O_3) is the most cost effective and most widely used material in the advanced ceramics industry. With high strength and stiffness, excellent dielectric properties, and good wear and corrosion resistance, alumina is extensively used in furnace liners, biomedical implants (Sedel, 2000), catalyst supports (Trueba and Trasatti, 2005), ballistic armour (Martin et al., 2012), wear pads, high temperature applications etc. α-Al_2O_3, with the corundum structure (Hübner and Dorre, 1984) is the most commonly-used polymorph due to its high strength, high refractoriness, and good corrosion and wear resistance, was used in this project. Al_2O_3 is referred as alumina in the polycrystalline form and has two gem-quality single crystalline forms, ruby and sapphire.

SiC is also an important ceramic material. Its high maximum current density and high thermal conductivity make SiC more suitable than the traditional Si for high-temperature and high-voltage semiconductor applications. SiC also has high hardness, low density and good durability, and it is widely used as an abrasive or cutting tool and ballistic armour material (Willardson and Weber, 1998). There are many SiC polytypes (around 200 polytypes have been reported (Liu and Vohra,

1994)) and they differ from each other in the stacking sequence of Si-C double atomic planes along the hexagonal c-axis (Nakashima and Harima, 1997). From the perspective of their crystal structure, SiC polytypes are divided into three groups: Hexagonal (H), Cubic (C) and Rhombohedral (R).

Being the only Ⅳ-Ⅳ semiconductor which has long-range ordered stable polytypes at room temperature (Shaffer, 1969), and with a wide band gap (Nakashima and Harima, 1997), SiC is also an attractive material for electronic and optical applications (Debernardi et al., 1999), such as blue light emitting diodes (LED) (Yoo and Matsunami, 1991). Its physical properties under applied pressure have been investigated experimentally (Olego et al., 1982) and theoretically (Chang and Cohen, 1987).

Although zirconia was discovered early by Hussak (1892), it was not practical until its polymorphism problem was addressed in the 1970s (Gupta et al., 1977). Zirconia has three crystallographic phases at atmospheric pressure: cubic (c), tetragonal (t) and monoclinic (m) (Stevens, 1983). The t>m martensitic, diffusionless phase transformation introduces a 4% volume expansion together with 16% of shear strain (Zhang et al., 2006) and this leads to catastrophic failure of zirconia if the transformation is not accommodated. 2-4 mol% Yttria-stabilised Tetragonal Zirconia Polycrystals (Y-TZP) were regard by some researchers as being first discovered by

Gupta et al. (1977) to be partially stabilized with mainly tetragonal phase at room temperature. A higher amount of stabilizer, such as 10 mol% Yttria (Badwal and Hughes, 1992), leads to the fully stabilized zirconia (FSZ). Normally there is no phase transformation from room temperature to 2500 °C in FSZ. However，the t-m phase transformation in TZP benefits the fracture toughness of TZP by the toughening mechanisms which arrest or slow down crack propagation (Maerten et al., 2013). Since then, the t>m zirconia phase transformation can be well controlled which makes Y-TZP a practical material. 3 mol% Yttria-TZP (3Y-TZP) is in widespread use in biomedical applications especially in prosthetic dentistry due to its excellent biocompatibility and mechanical properties (Denry and Kelly, 2008, Chevalier et al., 2009).

Typical values of the properties of materials used in this study have been summarised in the Table 2.1. These three materials were selected to study the indentation fracture because they are widely used. Alumina and SiC are typical brittle ceramics with relatively high Young's modulus but low fracture toughness. Their fracture toughness values have previously been determined by sharp indenter (Anstis et al., 1981) and the residual stresses around indentations in alumina have been studied (Guo and Todd, 2010a). However, the evolution of the cracking beneath the indentation and the linkage between the residual stress, cracking and fracture toughness has not been carefully explored. This is covered in this study. With a

characteristic phase transformation, the Y-TZP has improved the fracture toughness over traditional, fully stabilised zirconia. Although Vickers indentation has been widely used to measure fracture toughness of Y-TZP, the residual stresses around indentations have rarely been measured. This study includes a residual stress study on Y-TZP indentation and the attempt to understand the indentation cracking and fracture toughness of Y-TZP indentation has also been made.

Table 2.1 Typical values of the properties of materials used in this study

	Young's Modulus (GPa)	Flexural strength (MPa)	Grain Size (μm)	Relative Density (%)	Kc (Mpa · $m^{1/2}$)	Reference
Alumina	375	300-600	1-10	98-99	2.8-4.5	(Teng et al., 2007)
SiC	410	350-450	1-6	98-99	3.0-4.5	(Munro, 1997)
Y-TZP	210	500-700	0.1-0.5	95-98	2.5-4.0	(Eichler et al., 2007)

2.2 Indentation fracture theory

2.2.1 Introduction to indentation techniques

Since the indentation technique was first introduced by Hertz (1882), it has been extensively investigated and developed for more than a century. Indenters, with different geometrical shapes (for example, conical, spherical and pyramidal), are used to form an imprint on the sample surface by their penetration (Chicot and Tricoteaux, 2010). The use of nano-, micro-, or macro-indentation allows us to investigate the mechanical properties of ceramics on different scales by analysing the dimensions of the indentation (Chicot et al., 2007), the load-displacement curve (for load and displacement sensing indentation) (Oliver and Pharr, 1992) and/or the crack patterns (Chicot et al., 2009).

The Hertzian indentation presses a blunt indenter (hard sphere) against the hard surface. The principle of the Hertzian indentation to measure fracture toughness is that a minimum load, *P*, is required to propagate the precursor flaws to form the Hertzian crack. Therefore the fracture toughness is determined from this minimum load which produces Hertzian cracks (Warren, 1995).

Many researchers have tried to use Hertzian indentation to measure fracture toughness. For example, (Frank and Lawn, 1967) on glass, (Powell and Tabor, 1970) on TiC, Warren (1995) on glass and alumina. Compared with the sharp indentation, the Hertzian indentation holds several advantages. First, the only quantity to be measured is a fracture load, whereas the Vickers indentation needs crack length measurement. Second, the contact is purely elastic and the stress condition can be fully characterized (Hamilton and Goodman, 1966, Wilshaw, 1971). In contrast, the Vickers indentation has an elastic-plastic contact stress field which is much more complex and not well characterized.

However, Hertzian indentation is not as popular as Vickers indentation because: (i) the Hertzian indentation fracture toughness result is quite sensitive to the Poisson's ratio of the substrate (Warren, 1995) and Hertzian indentation is limited to a narrow range of highly brittle ceramics, and more heterogeneous and softer ceramics may deform irreversibly beneath the indenter prior to fracture (Marshall et al., 2015). For the Vickers indentation, the Poisson's ratio is not a concern and it is more applicable and widely used; (ii) as plasticity is favored by the small radius of Hertzian sphere (related to the Auerbach's lawn (Auerbach, 1891)), the critical fracture stress condition is incommensurate with the indenter size effect (Marshall et al., 2015). The Vickers indentation has a standard tip and is away from indenter size effect (Kruzic et al., 2009); (iii) the pre-cursor flaw before the indentation is assumed to have a certain

shape, depth, orientation and density depending on how researchers perform their analysis (Warren et al., 1994, Dai et al., 1995). With the Vickers indentation method, there is also some uncertainty with regards to the assumption of the cracking pattern after indentation, but the Vickers indentation results is not sensitive to the pre-cursor flaw. In addition, the Hertzian technique of Warren needs many indentations to be made to identify the minimum load for cracking, whereas the toughness value can be obtained in principle from a single Vickers indentation. The Vickers indentation technique is now predominantly employed as it is more versatile and has less uncertainty.

The use of Vickers indentation for fracture toughness measurement is based upon the understanding of the indentation cracking and the residual stress field, which will be reviewed in the following prior to the Vickers indentation fracture toughness (VIF) technique.

2.2.2 Vickers indentation cracking

Vickers indentation cracking was first studied on some transparent ceramics, such as fused silica and soda-lime glass (Lawn and Swain, 1975), for the cracking can be directly seen from the top surface during or after indentation. Cook and Pharr (1990) studied the indentation cracking on soda-lime glass, and they classified crack morphologies after indentation mainly into four types (Figure 2.1): (A) radial crack,

which is initiated from the indentation corner and propagates parallel to the surface. This crack is referred to more often as the Palmqvist crack (Lankford, 1982, Niihara et al., 1982) in later studies; (B) median crack, which is believed to form below the plastic zone and in the circular or segmented circular form; (C) half-penny crack, which is formed by the median crack propagating upward or Palmqvist crack downward so that the two join up. This “well-developed” crack (Lankford, 1982) was also normally regarded as a radial-median crack (Lawn et al., 1980, Guin et al., 2002); (D) lateral crack, which has a circular shape and propagates parallel to the surface. Although the concept of the cracks mentioned above originated from the observation on glass, it has been widely applied to study Vickers indentation on different ceramics as well.

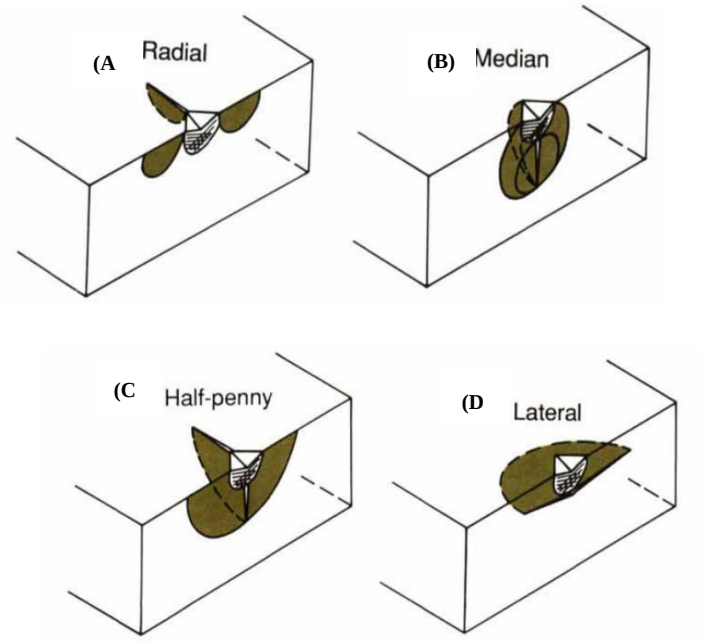


Figure 2.1 Indentation crack types proposed by Cook and Pharr (1990).

For opaque polycrystalline ceramics, the crack pattern can be revealed by decoration (Miyazaki et al., 2010a), in which a dye or lead acetate solution (Jones et al., 1987) is used to decorate the indentation crack, which is view of after breaking the sample with the indentation crack as the failure origin, or serial-polishing through a cross section (Figure 2.2) (Lube, 2001). The examination of the crack pattern enable researchers to choose appropriate cracking mode for fracture toughness calculation (Lankford, 1982)，or to ascertain the shape and the location of the crack (Lube, 2001), or to study the transition of the crack profile at different indentation loads (Miyazaki et al., 2010b).

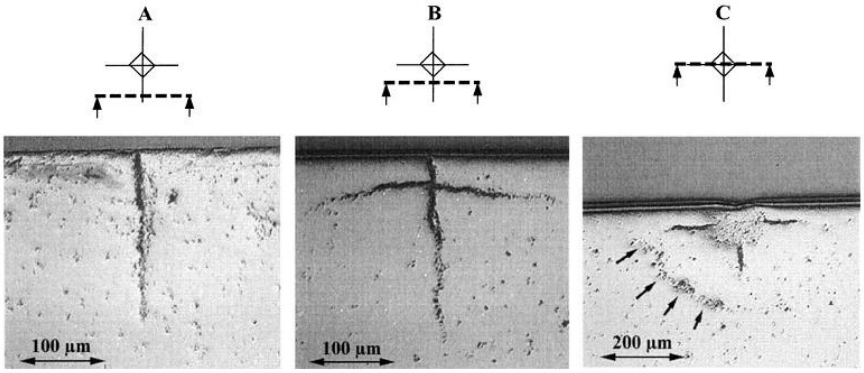


Figure 2.2 Crack pattern of the 196 N Vickers indentation on Si_3N_4 substrate at different stages during serial sectioning (Lube, 2001).

Lawn and Swain (1975) studied the Vickers indentation on soda-lime glass and proposed the hypothesis of sequences of forming a deformation zone and cracking evolution (Figure 2.3):

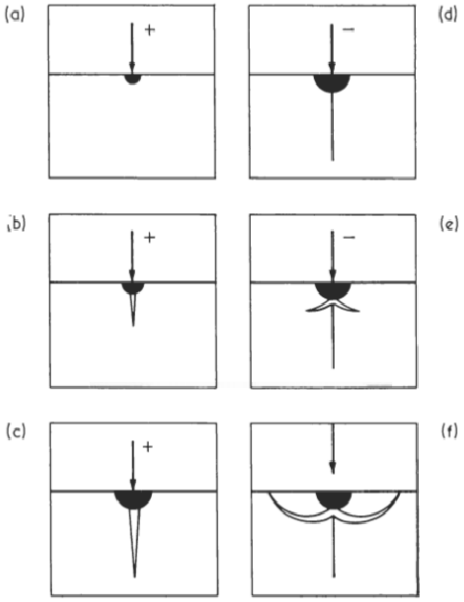


Figure 2.3 Schematic diagram of crack formation process beneath Vickers indentation. Note that a median crack is generated during loading (+) and a lateral crack forms during unloading (-). The dark regions represent the plastic zone (Lawn and Swain, 1975).

At first, irreversible plastic deformation is induced by the sharp point of the indenter, while a tensile stress field is generated on the surface around the indentation and beneath the indentation (Figure 2.3a); further increase of load leads to the formation of a median crack underneath the indentation (Figure 2.3b); the median crack then propagates downward (Figure 2.3c); during unloading, the median crack tries to close up, but total closure is prevented by the fracture steps or debris (Figure 2.3d) (Ostojic and McPherson, 1987); the saucer-shaped lateral crack will then originate from the base of the plastic zone where there is the highest tensile stress and the lateral crack extend to the surface (Figure 2.3e and 2.3f); the median crack during

unloading may intersect the surface to form ‘median-radial’ crack (Lawn et al., 1975). Cook and Pharr (1990) agreed on most of the scenario but pointed out that the lateral crack runs parallel to the surface and indicated that the cracking sequence is material dependent based on their observation on glasses with different compositions. So far, the observation of the indentation crack forming process is limited on the study on glasses, which have mechanical properties which are different to most engineering ceramics. However，for most opaque ceramics, to ascertain the cracking sequence from the end picture on the indentation surface or from the cross section of the indentation is quite difficult. The indentation residual stress models have been proposed trying to explain the formation of the crack. In the following sections, two commonly used stress models will be reviewed. Their applications and limitations are also covered.

2.2.3 Yoffe’s residual stress model

Yoffe (1982) considered that the plastic zone is located in the region confined by the area of contact underneath the Vickers indentation and the material around plastic zone, which is elastic. Yoffe in the beginning used the Boussinesq solution to describe the stress field for a point load *P* on the surface of a semi-infinite half-space.

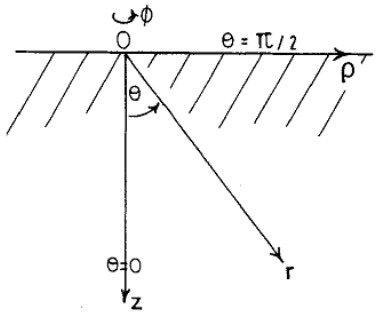


Figure 2.4 Spherical polar coordinate system used by Yoffe (1982).

According to the spherical polar coordinates (*r, θ, Φ*) (Figure 2.4), the stress field can be described as:

$$\sigma_r = \frac{P}{2\pi r^2}[1 - 2v - 2(2 - v)cos\theta]$$

$$\sigma_\theta = \frac{P}{2\pi r^2}\frac{(1 - 2v)\cos^2\theta}{1 + cos\theta}$$

$$\sigma_\emptyset = \frac{P(1 - 2v)}{2\pi r^2}[cos\theta - \frac{1}{1 + cos\theta}]$$

$$\tau_{r\theta} = \frac{P(1 - 2v)}{2\pi r^2}\frac{sin\theta\cos\theta}{1 + cos\theta}$$

Positive tensile stresses occur in the following two forms: σ_r on the surface ($\theta = \pi/2$) and $\sigma_\theta = \sigma_\emptyset$ when $\theta = 0$. These two types of tensile stresses may lead to the ring crack and the median crack, respectively.

However, in terms of indentation, the plastically deformed zone beneath the indentation also permanently changes its volume and shape. This is equal to a stress field caused by a surface inclusion and the stress field can be described by the

Blister field:

$$\sigma_r = \frac{B}{r^3} 4[(5-v)cos^2\theta - (2-v)]$$

$$\sigma_\theta = -\frac{B}{r^3} 2(1-2v)\cos^2\theta$$

$$\sigma_\emptyset = \frac{B}{r^3} 2(1-2v)(2-3\cos^2\theta)$$

$$\tau_{r\theta} = \frac{B}{r^3} 4(1+v)sin\theta cos\theta$$

where *B* is a constant which describes the strength of the field; v is the Poisson ratio.

Yoffe (1982) combined these two sets of equations above and obtained:

$$\sigma_r = \frac{P}{2\pi r^2}[1-2v-2(2-v)cos\theta] + \frac{B}{r^3} 4[(5-v)cos^2\theta - (2-v)]$$

$$\sigma_\theta = \frac{P}{2\pi r^2}\frac{(1-2v)\cos^2\theta}{1+cos\theta} + -\frac{B}{r^3} 2(1-2v)\cos^2\theta$$

$$\sigma_\emptyset = \frac{P(1-2v)}{2\pi r^2}\left[cos\theta - \frac{1}{1+cos\theta}\right] + \frac{B}{r^3} 2(1-2v)(2-3\cos^2\theta)$$

$$\tau_{r\theta} = \frac{P(1-2v)}{2\pi r^2}\frac{sin\theta\cos\theta}{1+cos\theta} + \frac{B}{r^3} 4(1+v)sin\theta cos\theta$$

Similar to Yoffe's model, the Eshelby (1957)'s spherical inclusion model considers the radial compression on the surrounding. However, unlike Yoffe's model, Eshelby's mode is unable to account for the opening of the lateral crack (controlled by σ_r, when θ = 0) and Eshelby's model neglect the free surface (Rouxel, 2015). Yoffe claimed that this combination will represent the external stress field outside the plastic zone and the value of *B* determines the location of the highest tensile stress.

Although Yoffe's model is simple, it helps to explain the formation of lateral, radial and median cracking. For instance, when $P \rightarrow 0$ during unloading, the tensile radial stress develops, at $\theta = 0$, $\sigma_r = 12B/r^3$ (when v=0.25) and this triggers the onset of lateral cracking. Another principal stress $\sigma_\emptyset$ turns positive when $\theta > 36°$ and achieves a maximum at the surface. This can be used to explain why the median crack tends to spread upward towards the surface during unloading, which is observed in indentation experiments (Swain and Hagon, 1976; Lawn and Swain, 1975).

Guo and Todd (2011b) applied confocal Cr^{3+} fluorescence spectroscopy to study the stress variation from the indentation center to the elastic surroundings on an alumina substrate (Figure 2.5). However, there is a significant difference between stresses measured by Guo and Todd and the prediction of Yoffe's model. Guo and Todd believed that this is due to the modification of the residual stresses by the indentation cracking.

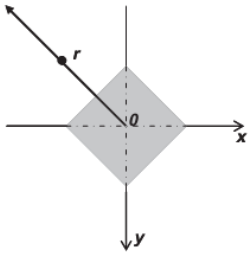


Figure 2.5 Sketch of the line scan, showing the scanning direction (Guo and Todd, 2011a).

2.2.4 Chiang's residual stress model

Chiang et al. (1982) modified the traditional spherical cavity expansion solution by taking consideration of the free surface. For describing the stress field during loading, the pressure *p* should be modified by a radial stress σ_r^s, which is induced by the surface force, to become the indentation pressure (i.e. Hardness, H). Considering the boundary conditions — uniform shear stress within plastic zone and surface with free stress, Chiang et al. (1982) proposed the expressions for the radial σ_r and tangential σ_t stresses during loading:

$$\left(\beta > \frac{r}{\alpha} > 1\right)\begin{cases} \dfrac{\sigma_r^{pl}}{p} = \left[\dfrac{3\ln\left(\dfrac{r}{a}\right)}{1+3ln\beta}\right] - 1 \\ \dfrac{\sigma_t^{pl}}{p} = \left[\dfrac{3\ln\left(\dfrac{r}{a}\right)+1/2}{1+3ln\beta}\right] - 1 \end{cases}$$

$$\left(\frac{r}{\alpha} > \beta\right)\begin{cases} \dfrac{\sigma_r^{el}}{p} = \dfrac{-\beta^3}{\left(\dfrac{r}{a}\right)^3(1+3ln\beta)} \\ \dfrac{\sigma_t^{el}}{p} = \dfrac{\beta^3}{2\left(\dfrac{r}{a}\right)^3(1+3ln\beta)} \end{cases}$$

where superscripts *pl* and *el* represent plastic and elastic regions; *r* is the distance from the cavity center; β is the relative indentation dimension and $\beta = b/a$, where *b* is the radius of the hemispherical plastic zone and *a* is the radius of the hemispherical indentation, *p* is the applied pressure.

Chiang et al. also provided the following expressions for radial σ_r and tangential σ_t stresses after removal of load:

$$\left(\beta > \frac{r}{\alpha} > 1\right)\begin{cases} \dfrac{\sigma_r^{rpl}}{p} = \left[\dfrac{3\ln\left(\frac{r}{a}\right)}{1+3ln\beta}\right] - 1 + \dfrac{1}{(\frac{r}{a})^3} \\ \dfrac{\sigma_t^{rpl}}{p} = \left[\dfrac{3\ln\left(\frac{r}{a}\right)+1/2}{1+3ln\beta}\right] - 1 - \dfrac{1}{2(\frac{r}{a})^3} \end{cases}$$

$$\left(\frac{r}{\alpha} > \beta\right)\begin{cases} \dfrac{\sigma_r^{rel}}{p} = \dfrac{1}{\left(\frac{r}{a}\right)^3}\left[1 - \dfrac{-\beta^3}{1+3ln\beta}\right] \\ \dfrac{\sigma_t^{rel}}{p} = \dfrac{1}{2\left(\frac{r}{a}\right)^3}\left[\dfrac{\beta^3}{1+3ln\beta} - 1\right] \end{cases}$$

where σ^{rpl} and σ^{rel} represents the residual stresses inside and outside the plastic zone.

Chiang et al.'s model is quite useful to describe initiation of indentation cracking and the position of the maximum tensile stress, thus it provides for a theoretical explanation for the consequences of the formation of the cracks. Lube (2001) used decoration and serial sectioning to investigate the crack profile and size of plastic zone of Vickers indentation on silicon nitride; and she found both the size of the plastic zone and the location of lateral cracks match Chiang et al.'s prediction.

Chiang et al.'s model is more robust than Yoffe's and it incorporates a dimension factor, β, to characterize the relative size of the plastic zone, therefore its prediction is more precise than Yoffe's model. The flip side of Chiang et al.'s model is its complexity and it has been less widely applied than Yoffe's model.

Both Yoffe's and Chiang's models for indentation residual stress field actually are only capable of predicting the onset of the cracking. The stress field prediction could not be tested as the cracks are formed and start to propagate in an extremely short time (Lawn and Swain, 1975). After unloading, the stress field predictions of Yoffe's and Chiang et al's models cannot be tested as both models ignore the modification to stresses caused by cracking. In Chapter 6, a new model for the residual stress field is proposed and tested, with the consideration of the relaxation effect of the cracks.

2.2.5 Vickers indentation fracture toughness

2.2.5.1 Introduction

As one of the most important mechanical properties of structural ceramics, fracture toughness, which describes the resistance to fracture, helps in quantifying the 'brittleness' of ceramics. Traditional ways to determine fracture toughness of ceramics include chevron notched beam (CVNB), double cantilever beam (DCB) and single edge notched beam (SENB) and always require complicated preparation

procedures and specific specimens with large dimensions. For instance, a minimum 18mm beam length is required for SENB (Lawn, 1993).

A much simpler choice to measure fracture toughness from measuring the cracks introduced by a sharp Vickers indentation. The Vickers method only needs a small area of well-polished surface and works out K_{IC} by measuring indentation parameters (e.g. applied load, *P*; half diagonal length, *a*; and radial crack length, *c*) (Figure 2.6).

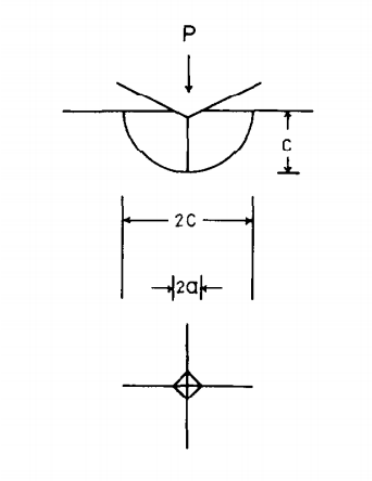


Figure 2.6 Schematic diagram of indentation associated with sharp indenter, showing the median crack system and indentation parameters (Miyata and Jinno, 1980).

The concept of evaluating the fracture toughness of the brittle materials from the indentation imprint was first proposed by Palmqvist (Palmqvist, 1957). Since then, the Vickers indentation fracture (VIF) technique has been quickly developed and VIF measurements were proposed by considering mainly the two classical cracking

modes: radial-median (“half-penny”) mode and Palmqvist mode (Figure 2.7). An indicator of defining the type of the crack system is to use the *c/a* ratio. Ponton and Rawlings (1989) claimed that generally, the crack model will be half-penny type when *c/a*≥2 and Palmqvist type if *c/a*<2. However, this is not always the case, Bhat (1981) suggested that a critical differentiating *c/a* value 3 is more appropriate to his find, while Bamzai et al. (2000) preferred *c/a*=2.5 for their $ErAlO_3$ single crystal and Mott and Roland (2009) proposed *c/a*=2.1. Nevertheless, the general concept behind is that the brittle ceramics with relatively low toughness tend to follow the half-penny model, while ceramics with high toughness are more likely to follow the Palmqvist fashion.

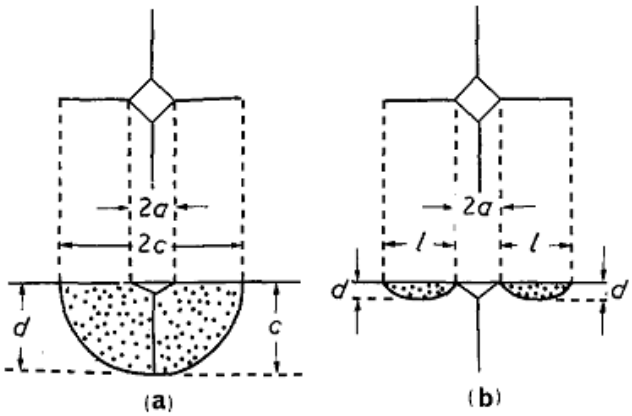


Figure 2.7 Sketch of (a) median crack mode and (b) Palmqvist crack mode for Vickers indentation (Liang et al., 1990).

2.2.5.2 Radial-median crack mode fracture toughness

The Vickers indentation technique was first proposed to measure fracture toughness

of the ceramic materials from the crack lengths by Evans and Charles (1976). They proposed an equation by fitting the fracture toughness results of nine different ceramics with mixture of radial-median cracks and Palmqvist cracks, and demonstrated that this Vickers indentation technique might be a universal test method. Later, many researchers tapped into this field and used similar methods to find the best equations to explain their results (Lawn et al., 1980, Anstis et al., 1981, Niihara, 1983, Laugier, 1985). The investigated ceramics were split into two groups: the ones with a radial-median crack system and those with a Palmqvist crack system.

The investigation of indentations with the radial-median crack system was started from the empirical relationship between crack length *c* and the indentation load *P* in glasses by Lawn and Fuller (1975):

$$c = kP^{2/3}$$

where *k* is an empirical constant. Marshall and Lawn (1979) modified the equation and proposed:

$$K_c = \chi P/c^{3/2}$$

where χ is a constant and K_c is the fracture toughness of the ceramic. This equation has become the fundamental form and the starting point for most of the equations dealing with the radial-median system. It is then considered by Lawn et al.

(1980) that the volume of the plastic zone is constrained by the elastic surroundings. Then the Young's modulus was introduced and the constant χ was found to depend on the ratio of *E/H*:

$$\chi = \beta(\frac{E}{H})^m$$

where β is a constant which depends on the material. Anstis et al. (1981) used this equation and found m=0.5 in their study and calibrated the constant by fitting the equation to the independently measured fracture toughness data. In a later study by Laugier (1985), m = 2/3 and a different constant was found to work better for their investigated ceramics. The issue behind this pursuit of a "perfect" equation is that no equation could satisfactorily work on all ceramics. This leads to the proliferation of VIF equations dealing with both radial-median and Palmqvist crack systems. Some formulae describing indentation fracture toughness in radial-median crack system are summarised in Table 2.1, however most of them are restricted only to specific ceramics and they all ignore the lateral cracking system. Issues with VIF will be discussed in the following Section 2.2.5.4.

Table 2.1 Summary of formulae proposed by researchers for radial-median crack mode.

	Author	Equation	Materials used
1.	Evans and Charles (1976)	$0.15(Ha^{1/2})(c/a)^{-1.5}/\Phi$	WC, Si_3N_4, SiC, B_4C, ZnS, ZnSe
2.	Lawn et al. (1980)	$0.28(Ha^{1/2})(E\Phi/H)^{0.4}(c/a)^{-1.5}$	Si_3N_4, ZnS, ZnSe, ZnO2
3.	Anstis et al. (1981)	$0.016(E/H)^{0.5}(P/c^{3/2})$	WC, Al_2O_3, Glass, Si_3N_4, Si, SiC
4.	Niihara (1983)	$0.129(Ha^{1/2})(E\Phi/H)^{0.4}(c/a)^{-1.5}/\Phi$	Si_3N_4, B4C，Soda-lime silica glass
5.	Niihara et al. (1984)	$0.203(Ha^{1/2})(c/a)^{-1.5}$	B_4C, Si_3N_4, Soda-lime silica glass
6.	Laugier (1985)	$0.010(E/H)^{2/3}P/C^{3/2}$	WC, Al_2O_3, Glass, Si_3N_4, Si, SiC

2.2.5.3 Palmqvist crack mode fracture toughness

A Palmqvist crack (Palmqvist, 1957) is the crack which emanates from corners of the indentation and extends to a depth of the order of the indentation depth (Laugier, 1987). It occurs when the indentation load is relatively small (Liang et al., 1990) or when the material, for instance, TZP, is tough (Reece et al., 1992). Palmqvist cracks have been observed from fractography of the surface through indentation (Hagan and Swain, 1978), or by sectioning (Ogilvy et al., 1977), or from optical microscopy (Evans and Wilshaw, 1976).

Niihara et al. (1982) noticed a transition from Palmqvist to half-penny cracking at a c/a ratio of 2.5 in WC-Co composites. For the Palmqvist mode, they suggested:

$$(\frac{K_c\Phi}{Ha^{1/2}})(\frac{H}{E\Phi})^{2/5} = 0.035(l/a)^{-0.5}$$

Later, Niihara (1983) modified the equation by adding consideration of the semi-elliptical geometry of the Palmqvist crack and he obtained:

$$\left(\frac{K_c\Phi}{Ha^{\frac{1}{2}}}\right)\left(\frac{H}{E\Phi}\right)^{\frac{2}{5}} = 0.048\left(\frac{l}{a}\right)^{-0.5}$$

Niihara et al.'s equations have been applied to most of the calculations of VIF regarding the Palmqvist crack system (Casolco et al., 2008, Gotman et al., 1998, Tang et al., 2008). Another popular equation is proposed by Laugier (1987) from the modification of the half-penny equation to describe the Palmqvist crack

$$K_c = 0.015\left(\frac{l}{a}\right)^{-0.5}\left(\frac{E}{H}\right)^{2/3}P/c^{3/2}$$

The Palmqvist cracking mode equations are much less used compared with the radial-median equations. The main reason is most ceramics are relatively brittle and tend to have radial-median cracks beneath indentations within the normal indentation load range (normally 10 N - 500 N). One premise of using any VIF equation is ascertaining the cracking system. This is advised to be done by viewing the cracks beneath the indentation. However, some researchers used the c/a ratio as the criterion (Gotman et al., 1998), which is not ideal. More issues of the VIF technique are discussed in the following section.

2.2.5.4 Issues with the Vickers indentation toughness technique

Although VIF is a simple and economical method to measure fracture toughness and has been widely used in industry and academia, for instance the ISO 26602

international standard and ASTM F 2094 American standard have accepted IF method as way of grading silicon nitride bearing balls (Miyazaki and Yoshizawa, 2014), the reproducibility is poor compared with other conventional methods and there is no compelling formula which could be used for calculating fracture toughness for most ceramics. Up till now, many issues with the VIF technique have been discovered and they are listed below:

(1) Empirically calibrated constant in VIF equations

It is notable that all of the equations proposed in the past (either applied to the radial-median crack mode or Palmqvist modes) employed adjustable parameters made by forcibly fitting the equation with results from other methods or reference materials. For instance, the 0.016 ± 0.004 parameter in Anstis et al. (1981)'s equation is by empirical calibrations. This was not predicted by a physical model and there was a 25% standard deviation on fitting of this constant. Quinn and Bradt (2007) used three VIF equations to compare with reference materials and found that VIF equations gave 10-30% errors. This has shown the inconsistency of the VIF equations and the forcibly calibrated parameters lying in the equation can be a key factor which leads to their inconsistency problem.

(2) Variation of indentation cracking behavior and disruption of the lateral crack to the residual stress field.

Traditional indentation models assume a well-defined cracking pattern, such as the two radial-median cracks perpendicular to each other. However, the cracking behavior depends strongly on the material (Cook and Pharr, 1990) and the transition of the cracking mode from radial-median to Palmqvist has also been found in some cases (Liang et al., 1990). As most ceramics are non-transparent, ideally the cracking pattern has to be examined, by sectioning for example, before applying any VIF equations and this is contrary to the ease of testing, which is one of the core advantages of the VIF technique. Lateral cracking has commonly been seen under the indentation (Cook and Pharr, 1990, Kruzic et al., 2003, Lube, 2001), however, previous researchers always tended to ignore its presence and impact.

(3) Influence of microstructure

The scale of the radial crack for the indentation is typically around 30-200 μm, therefore the influence of microstructure (with inhomogeneity larger than 1 μm) on crack propagation and crack pattern is more significant than for the long crack fracture toughness measurement method (Anstis et al., 1981). One example would be the bridging effect in whisker-reinforced alumina (Fett et al., 1994) which significantly affected the stress intensity factor and therefore the validity of the VIF equations.

(4) ‘Fast’ crack length measurement and subcritical slow crack growth

The traditional indentation model has the assumption that the crack length is measured immediately after unloading of the indenter, at which time the crack reaches equilibrium with the stress field and the crack tip is just at the stress intensity which allows the crack extension (Kruzic et al., 2009). Only at this time does the stress intensity factor, K, ahead of the crack tip represent the fast fracture toughness, K_{IC}. The crack growth speed at this critical point will be as large as 10^{-2} ms^{-1} (De Aza et al., 2002), therefore it will be extremely difficult for the measurement to be done at this fastest growth regime. Researchers tend to either use very short intervals (normally a few seconds) between the completion of the indentation and the measurement of crack length or indent the sample in an inert environment (Anstis et al., 1981, Cook and Pharr, 1990, Chantikul et al., 2006). However, it is hard to know whether the moment the crack length is measured is within a sufficiently fast growth regime to make VIF valid; and an absolutely water free environment is difficult to achieve and a tiny amount of water could have an impact on the results (Kruzic et al., 2009). The slow crack growth mechanism starts to play a role after the fastest growth regime, the stress intensity factor will be lower than K_{IC} and the fracture toughness will not be correctly measured. The slow crack growth will be further reviewed in Section 2.2.7. Additionally, for the fast measurement of the crack length, the optical microscope is normally employed, and its relatively low resolution may lead to an underestimation of the crack length and therefore an overestimation of fracture toughness.

(5) Indentation size effect and the R-curve effect

The Vickers hardness of the material, *H*, is normally incorporated in the VIF equations. For some ceramics, this parameter may increase when the load decreases (indentation size effect) and the indentation size effect will normally diminish above a certain load but this critical load varies with the material, such as 3-5 N for α-SiC (Li et al., 1989) or 120 N for Si_3N_4 (Quinn and D QUINN, 1997). The phenomenon of increase in toughness as the crack grows in ceramics is called R-curve behavior (Vekinis et al., 1990). The toughness measured by VIF will vary with load unless reaching the R-curve plateau (Kruzic et al., 2009). However, the R-curve measurement on the Vickers indentation normally disagrees with the R-curve behavior measured by other methods. For instance, the R-curve effect could be seen from indentation on some materials, such as α-SiC and Si_3N_4 inherently with no rising R-curve (Li et al., 1989, Ghosh et al., 1995, Quinn and Bradt, 2007). Based on this fact, Kruzic et al. (2009) claimed that the VIF technique should not be considered to measure R-curves. The unpredictability of the Vickers indentation fracture toughness depending on the load comes from the factors listed in this section and this has certainly increased the difficulties for accurate VIF measurements and interpreting the VIF results.

The issues mentioned above have become hurdles for universally applying the VIF technique. Quinn and Bradt (2007) have criticized harshly the VIF method and stated

that the VIF method should not be accepted. Their statement may appear extreme. The author of this project believes that part of the inaccuracy of the present VIF equations come from the fact that the Vickers indentation technique itself has not been fully understood and validated and the measurement of the indentation parameters have not been taken carefully. Further work is still required on the assessment of the validity of the Vickers indentation technique as a tool for fracture toughness measurement and this is the main theme of this thesis.

The surface profiles and the slow crack growth behaviors of the Vickers indentations were also investigated in this project and the issues relating to them are also reviewed in the following sections.

2.2.6 Pile-up and sink-in around indentation

For Vickers indentation, the contact surface is considered to be a square based pyramid so that the boundary of the imprint is supposed also to be square. However, for most metals, pile-ups and sink-ins may form near the indentation imprint, which represents an upward or inward flow of material respectively. This becomes an important issue when it comes to micro-/nano-indentation tests in which case the indentation size effect is inevitably considered. For instance, Iost and Bigot (1996) have found that the indentation size effect in Ti-6Al-4V and 2024-T3 material is just

an artefact and they developed an equation to add the consideration of the pile-up and to calculate the real contact area. The study of the topography of the indentation imprint therefore enables us to better understand the materials' mechanical behaviour.

Conversely, pile-up is rare in ceramics as the plasticity is low and therefore the materials flow is limited (Iost and Bigot, 1998). Typically, plasticity dominates in metallic materials and the material which is displaced forms pile-ups around the indentation (Figure 2.8a); on the contrary, "pin-cushion" (Peralta et al., 2004) indentations may form on ceramics caused by the sinking in of the material (Figure 2.8b). Fischer‐Cripps and Lawn (1996) found there is no pile-up for their Si_3N_4+4% Yttria material, while Gubicza et al. (1997) used AFM (Atomic Force Microscopy) to measure the surface profile of the line scan on Vickers indentations for the 90 wt% Si_3N_4 - 4 wt% Al_2O_3 – 6wt% Y_2O_3 and they found that pile-up around indentations was present and the amount of pile-up at the edges of the indentation is nearly the same as that at the indentation corners. Iost and Bigot (1998) claimed that the pile-ups found by Gubicza do not have the same origin as the bulge around the indentation in metals and cracking is likely to exist under the plastic zone, which is more likely to be the explanation. Marshall et al. (1982) have also regarded the uplift of the surface around indentation as the result of the lateral cracking and used simply beam theory to model the uplift. Their approach will be used and further discussed in Section

4.3.5.

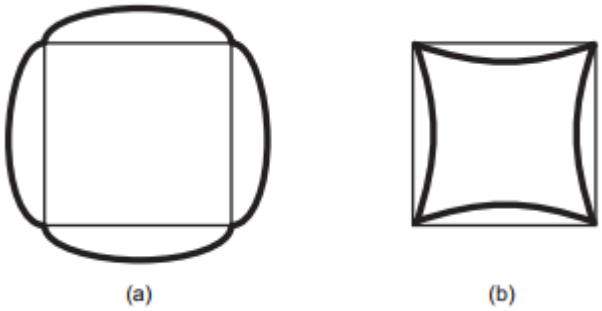


Figure 2.8 Indentation on materials with (a) high plasticity and (b) low plasticity (Iost and Bigot, 1998).

Six techniques are mainly used for examining the surface profile of the indentation (Marteau et al., 2014): AFM, confocal microscopy, interferometry, SEM, optical microscopy and tactile profilometry. SEM and optical microscopy are only used for surface observation and are not suitable for three-dimensional examination. Confocal and interferometric microscopies are rapid procedures with good resolution and contact with the sample surface is not needed. AFM normally has the best resolution, but it is more time-consuming and the mapping scale is small and it is unsuitable when the surface cannot be touched because it is either too stiff or too soft (danger of scratching). For micro- and nano-indentations, AFM is usually used due to its good resolution. The indentations used in this project are relatively large indentations and has beyond the maximum imaging area of AFM. Therefore an

interferometric profilometer (MicroXAM) was used to measure the surface profile around the indentation.

2.2.7 Subcritical slow crack growth

One problem with measuring VIF is the issue of subcritical slow crack growth. In principle, only at the time immediately after the indentation cycle is complete, will the stress intensity factor at the radial crack tip be equal to the fracture toughness, K_c (Anstis et al., 1981). The high state of stress near the crack tip enhances (Salomonson and Rowcliffe, 1995) the chemical interaction between the crack tip bounds and the environmental species (normally water). This mechanism drives the crack growing at a rate determined by the reaction kinetics (Wiederhorn, 1967, Michalske and Freiman, 1983, Wan et al., 1990, Wiederhorn, 1969).

An empirical power relationship is often used to analyse the slow crack growth behavior and has the following expression:

$$V = AK_{\mathrm{I}}^{n}$$

where the A and n and constants, which depend on the crack region and material/environment interaction (Ebrahimi et al., 2000). The complete slow crack growth behaviour is most suitably described in the logarithmic crack velocity, *V,* vs. applied stress intensity factor, K_I, diagram (Figure 2.9). K_{IC} is the fast fracture stress

intensity and K_{I0} is the threshold below which no crack growth happens (Lawn, 1993).

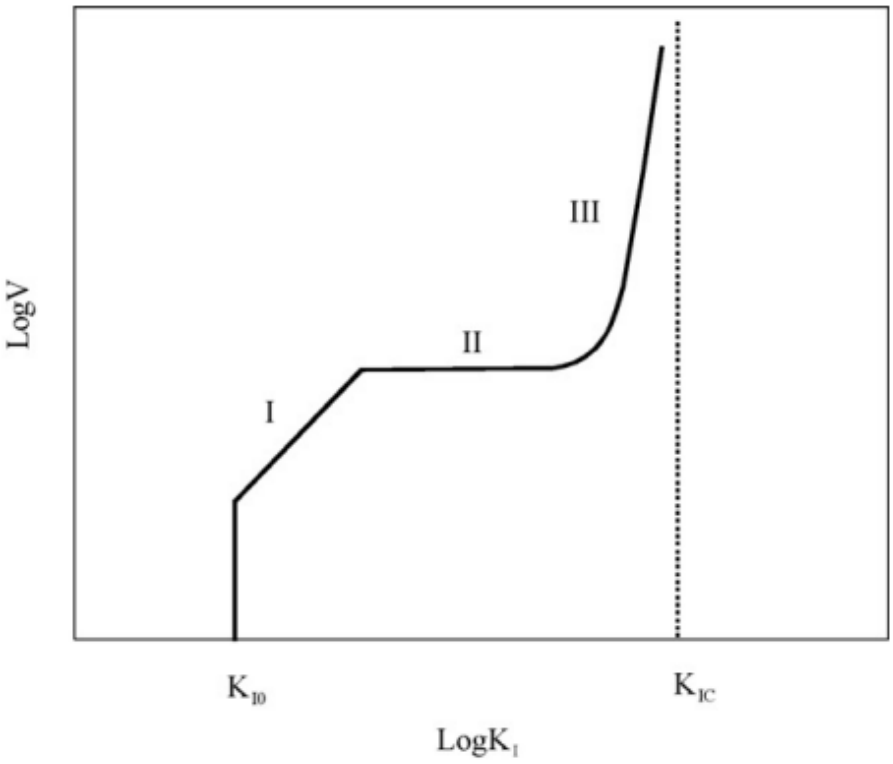


Figure 2.9 Crack velocity as a function of applied stress intensity factor (Bouras et al., 2008).

Both static and dynamic fatigue methods have been widely used to study the subcritical crack growth and determine the related parameters (Ritterk Jr and Sherburne, 1970, Marshall and Lawn, 1980, Chantikul et al., 1981, Cook et al., 1982). There have been however, only few studies on the *K-v* curves using indentation cracks and observing the crack growth behavior directly (Yoda, 1987, Muraoka et al., 1993, Gupta and Jubb, 1981) and most of these studies are confined to research on soda-lime glass.

Researchers who have worked on VIF testing of ceramics have always minimised the transfer time after indentation to view samples under the microscope (Anstis et al., 1981, Cook and Lawn, 1983, Liang et al., 1990, Quinn and Bradt, 2007). However, it is indeed extremely hard to know whether the stress intensity factor, K, they were measuring truly reflects the fracture toughness, K_c, of the material, which is associated with catastrophic crack extension. According to the K-v curve, the speed of crack growth is expected to be very high (Ebrahimi et al. (2000) suggested a velocity above 10^{-4} m/s for alumina) when K is close to K_c and the indentation radial crack may therefore have propagated very significantly in only one second (Cook and Liniger, 1993). Non-reactive substances (such as oil) slow down the crack growth, however as noticed by Anstis et al. (1981) the crack growth was still fast even when the specimen was indented in oil as it is difficult to be absolutely isolated from water. Li et al. (1989) suggested measuring the stress intensity, K_0, for crack arrest is more useful for long term design than K_c. The slow crack growth phenomenon of indentation cracks was found and discussed in this thesis, and its implications on the VIF measurements are also included in the discussion.

2.3 Residual stress measurement

In this section, the definition and the origin of residual stresses are firstly reviewed, followed by a detailed introduction to stress measurement techniques with the emphasis on the fluorescence and Raman microscopy methods.

2.3.1 Origin and categories of residual stresses

Withers and Bhadeshia (2001) pointed out that ‘’residual stress is that which remains in a body that is stationary and at equilibrium with its surroundings’’. The misfit between different phases or regions thermally or mechanically introduced or caused by phase transformation is the origin of residual stresses (as illustrated in Figure 2.10).

In terms of the Vickers indentation technique, the residual stresses are introduced by the mismatch between the plastic and elastic zones (Chiang et al., 1982). The direct measurement of the indentation residual stresses is very helpful for research of the Vickers indentation technique.

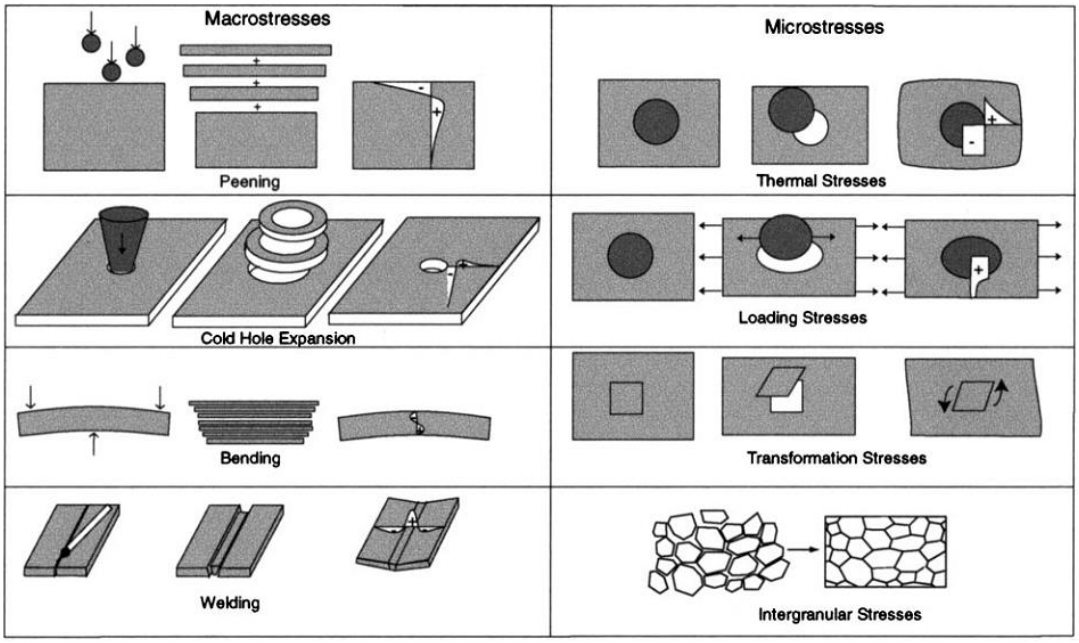


Figure 2.10 Types of residual stresses caused by misfit between different phases or different regions (Withers and Bhadeshia, 2001).

2.3.2 Destructive methods for stress measurement

Generally, stress measurement techniques can be classified into destructive and non-destructive types. Curvature measurement (Clyne and Gill, 1996), hole drilling (Steinzig and Takahashi, 2003) and crack compliance methods (Cheng and Finnie, 1993) are commonly used destructive methods. When residual stress has been or is being generated, one can use destructive methods to deliberately remove some material from the component after which stresses are relaxed and the shape change of the component can be recorded (Withers and Bhadeshia, 2001). However, destructive methods are not always practical for brittle thin ceramics, or for thin coatings and their usages are often limited due to their destructive nature.

2.3.3 Overview of non-destructive methods

With no or minimal damage introduced to components, non-destructive residual stress measurement methods have been widely used and researched in-depth. Traditional non-destructive method includes neutron diffraction (Todd et al., 1997), ultrasonics (Degtyar et al., 1997), X-ray diffraction (Levin et al., 1994), magnetic methods (Withers et al., 2008), eddy current method (Withers and Bhadeshia, 2001) and piezospectroscopic methods (including Raman (Pezzotti, 1999), fluorescence (Ma and Clarke, 1994) and cathodoluminescence (Pezzotti et al., 2003)). For alumina and SiC based materials, some of these non-destructive stress measurement techniques have been successfully applied. For example, thermal

residual stresses were successfully measured by Levin et al. (1994) using X-ray diffraction and by Todd et al. (1997) using neutron diffraction on alumina. In terms of the spatial resolution, piezospectroscopic methods excel as the sampling volume in piezospectroscopic methods is normally smaller than in other non-destructive techniques (Withers and Bhadeshia, 2001). Cr^{3+} fluorescence spectroscopy is a good example of a piezospectroscopic method and is introduced in the following sections.

2.3.4 Cr^{3+} fluorescence spectroscopy

2.3.4.1 Principle

Piezospectroscopic methods rely on the fact that the transition energy between different electronic or vibration states will be changed when applying stress to strain the lattice. By this means, the frequency of luminescence lines, such as Raman and fluorescence lines, shift systematically with changes in stress condition (Ma and Clarke, 1993b).

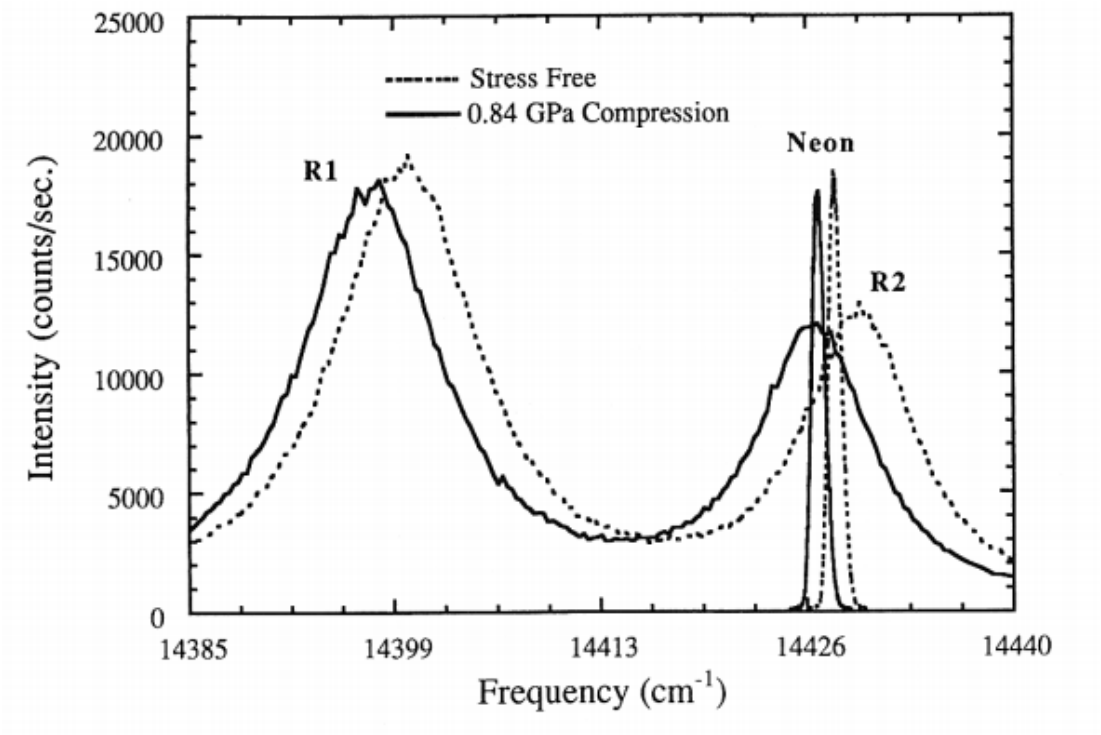


Figure 2.11 The R1 and R2 fluorescent peaks from the Cr^{3+} ions in the alumina lattice and their shifts due to stress.

As a persistent impurity in alumina, Cr^{3+} has strong R-line fluorescence peaks (Figure 2.11) and is easy to detect even in alumina containing only a trace of Cr^{3+} (Grabner, 1978). Cr^{3+} substitutes for Al^{3+} in alumina and coordinates oxygen ions octahedrally. However, the coordinating octahedron is distorted with a degraded point symmetry of $D_{3d}(\bar{3}m)$ and is elongated along the *c* axis; and this leads to the asymmetry of the electrostatic crystal field and splitting of the ^2E energy level (Figure 2.12). The resultant fluorescent radiations with energies of 1.790 and 1.794 eV give rise to the doublet R1 and R2 lines which have the wavenumbers around 14402 and 14432 cm^{-1}, respectively (Ma and Clarke, 1993b). Although the splitting of the R1 and

R2 lines induced by stress was reported at liquid helium temperature (Kaplyans.Aa and Przhevus.Ak, 1967), owing to the thermal broadening effect this is masked at room temperature so that there is no stress-induced splitting of the R1 and R2 lines at room temperature (Ma and Clarke, 1994).

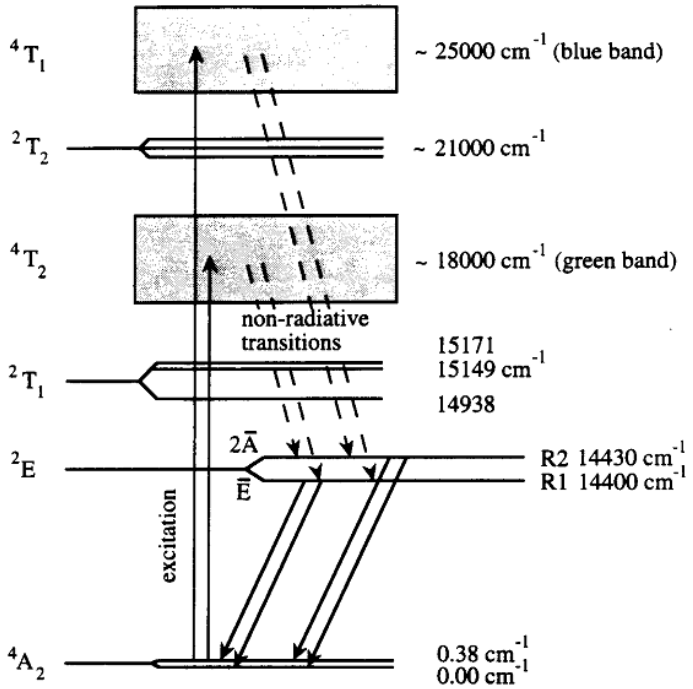


Figure 2.12 Graph of low-lying electronic levels for Cr^{3+} in sapphire, showing the splitting of the ^2E energy level and the nonphonon radiative transitions (He and Clarke, 1997).

When stress is applied, the distortion of the crystal field around Cr^{3+} alters the chromium-oxygen bond length which in turn changes the energy of the radiative transition between the ^2E and $^4A_2$ energy levels, thus leading to the variation of the frequency of the fluorescent radiation. The relation of the change in frequency and

the applied stress is expressed by the tensorial relationship (Grabner, 1978):

$$\Delta\nu = \Pi_{ij}\sigma_{ij}^{*}$$

where $\Delta\nu$ is the frequency shift of R line; Π_{ij} are the piezospectroscopic coefficients; σ_{ij}^{*} are the applied stresses.

For single crystal sapphire, the $D_{3d}(\bar{3}m)$ point symmetry of alumina (Grabner, 1978) results in the fact that the off-diagonal components in the Π_{ij} tensor are zero and the diagonal components are symmetrical about the *c* axis. Then the PS (piezospectroscopic) coefficient tensor is expressed as:

$$\begin{bmatrix} \Pi_{11} & 0 & 0 \\ 0 & \Pi_{11} & 0 \\ 0 & 0 & \Pi_{33} \end{bmatrix}$$

However, the Ma and Clarke (1993a) found that in reality, $\Pi_{11} \neq \Pi_{22}$, because of the slight deviation from the ideal point symmetry. If the stress is purely hydrostatic pressure, in which case $\sigma_{11} = \sigma_{22} = \sigma_{33} = -P$, then,

$$\Delta\nu = (\Pi_{11} + \Pi_{22} + \Pi_{33})P = \Pi_m P \qquad \text{Equation 2.1}$$

For the R1 peak, the PS coefficient for the matrix Π_m was determined by He and Clarke (1995) to be 7.59 $cm^{-1}GPa^{-1}$ in sapphire, which is nearly the same as experimental results (7.59-7.98 $cm^{-1}GPa^{-1}$) in polycrystalline alumina (Pezzotti et al., 2006). Thus, the hydrostatic stress can be determined from the R1 peak shift. Molis and Clarke (1990) also reported in their four point bending test that this equation is equally suitable for tension.

For polycrystalline alumina, signals from multiple grains are sampled when grains are significantly smaller than the sample volume (Guo and Todd, 2010a). Although the PS coefficients are anisotropic, when the texture is random and grains on various directions are sampled, then the R1 peak shift, $\Delta\nu_{R1}$, can be linked with the hydrostatic stress component, σ_{hydro}, averaged over the sampled grains, which is an isotropic stress and acts equally in all directions (Equation 2.2).

$$\Delta\nu_{R1} = \Pi_{ave}\sigma_{hydro} \qquad \text{Equation 2.2 (He and Clarke, 1995)}$$

where Π_{ave} is the PS coefficient for hydrostatic stress σ_{hydro}.

To calibrate Π_{ave} in polycrystalline ceramics, the ceramic bar is put in a four-point bending jig and mounted under the fluorescence microscope. The sample bar is typically a slender parallelepiped (e.g. 3×4×20 mm，B×W×L) (Pezzotti, 1999) so that simple beam theory can be applied. When the load (well below the fracture stress) is added through the jig, the stress along the length of the sample can be regarded as uniaxial and this stress changes linearly from tension to compression through the thickness of the beam. Based upon the standard four-point-bending elastic beam equation, the uniaxial stress, and hence the hydrostatic component of stress as a function of distance from the neutral axis for a given bending moment can be calculated (Pezzotti, 1999). Therefore, when the R1 peak shift is recorded accordingly under the microscope when loading the jig, the PS coefficient for polycrystalline ceramics can be determined from Equation 2.2. This principle was

also applied to the calibration of the PS coefficients of SiC and TZP in Chapter 5.

It was found by McCumber and Sturge (1963) that the R lines shift to smaller wavenumbers when temperature is increased. This was also proved in He and Clarke's (1995) experiments where they found a linear function to describe the frequency dependence:

$$\nu\,(T) = \nu\,(T_0) + \alpha\,(T - T_0)$$

The coefficient α are -0.144 and -0.134 $cm^{-1}/℃$ for R1 and R2, respectively (Figure 2.13). Change of temperature due to heating of the probed volume is neglectable under typical conditions, as was pointed out by He and Clarke (1995).

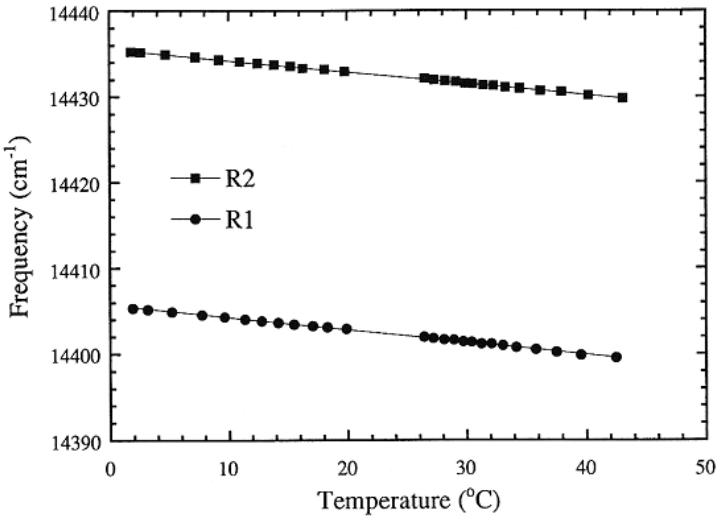


Figure 2.13 Frequencies for R1 and R2 lines as the function of temperature in 0.05-wt%Cr-doped sapphire (He and Clarke, 1995).

2.3.4.2 Applications of fluorescence spectroscopy in alumina based ceramics

Compared with the conventional methods for measuring residual stress in ceramics, such as X ray diffraction (Levin et al., 1994) and neutron diffraction (Todd et al., 1997). Cr^{3+} fluorescence microscopy has a high spatial resolution and consumes less time and cost than other techniques (Guo and Todd, 2010a).

The application of fluorescence microscopy in alumina was initially promoted by Clarke's group. Ma and Clarke (1993b) established the PS equations for polycrystalline alumina and also found that the thermally induced residual stress in the *a* and *c* crystallographic directions of polycrystalline alumina can be known from the peak shift. In their following paper (Ma and Clarke, 1994) the average compressional stresses along the c-axis in alumina were found to be in the range of 140-230 MPa with grain sizes of 2-16 micron due to different length of annealing time. However their results are smaller than (~10%) the prediction from Evans (1978) in the smaller grain size material, and this was thought to be the result of the effectiveness of residual stress relaxation by diffusion flow.

Molis and Clarke (1990) implemented the technique in a study of a 10 N Vickers indentation on sapphire. They measured the compressive stresses within the indentation and the largest compressive stress (-370MPa) was at the indentation corner; while a tensile stress (93 MPa) was detected around the crack tip.

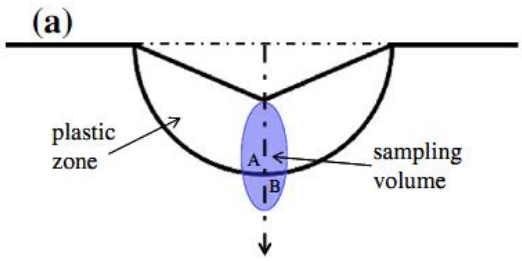
Compressive stresses decrease away from indentation; however these stresses in the region where lateral cracking can be observed are significantly smaller than those in area with no lateral cracking around. This is believed to be caused by the relaxation of elastic constraint by lateral cracking.

Wu et al. (2008) found that the peak shift and broadening near indentations in alumina/SiC nanocomposites are much higher than in polycrystalline alumina and they claimed that the larger extent of broadening around scratches or indentations is due to a higher dislocation density within the sampling volume, therefore the plastically deformed layer in alumina/SiC nanocomposites is deeper. Following their investigation, Guo and Todd (2010a) improved the resolution of Cr^{3+} fluorescence microscopy by using a confocal microscope and pointed out that the fact that the sampling volume in Al_2O_3 is much larger than that in alumina/SiC nanocomposites when using a non-confocal microscope, is not considered by Wu et al. Guo and Todd (2010a) also proposed a probe response function (PRF) and they calculated maximum that the probeable depth (in confocal settings) for polycrystalline alumina and for 10 vol% SiC nanocomposites are ~15 μm and ~4 μm，respectively. This work shows that the stresses and peak broadening in and around the indentations in alumina and alumina/SiC nanocomposites are in fact very similar.

Furthermore, Guo and Todd (2010a) analysed the broadened peaks of spectra

collected within the indentation of polycrystalline Al_2O_3 and found that the spectra can be well-fitted by a four-peak fitting method (Figure 2.14b). In four-peak fitting, two doublets were used to fit the R1 and R2 peaks individually and a fixed peak area ratio was used as the constraint for each doublet. The broad peaks in their analysis were related to the plastic zone, while the sharp peaks were related to the sampling volume beneath the plastic zone, where the dislocation density is less (Guo and Todd, 2011a) (Figure 2.14a,b).

Guo and Todd (2010b) also used confocal Cr^{3+} fluorescence microscopy to examine the residual stresses caused by grinding and polishing. Using their PRF, they were able to obtain the magnitude and spatial distribution of the residual stresses below the surface of the coarsely ground specimens. The depth of the plastic deformation (~1.3 μm), in their results, was about three times larger than that for polishing (~0.4 μm) with 3 μm diamond paste.



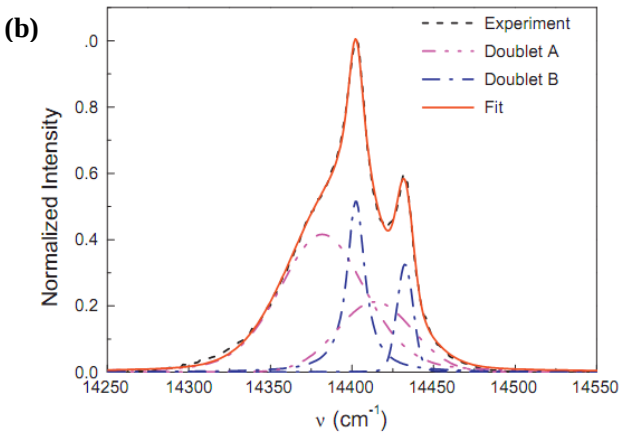


Figure 2.14 (a) Sketch of sampling volume at center of indentation on alumina; (b) four-peak fitting method for analysing the broadened peak within the sunken area of the indentation.

2.3.5 Raman Spectroscopy

2.3.5.1 Raman effect

Discovered by Indian physicist C.V. Raman in 1928, Raman is one of the most commonly used spectroscopies for ascertaining fingerprints of species and molecular motion (Schwartz, 2010). The Raman effect is based on the inelastic scattering of a monochromatic excitation source and every substance has its own characteristic spectrum. Therefore the method has been used for identifying chemical compounds, the structure of materials and the amount and distribution of species (Gogotsi, 1997). Raman spectroscopy has been applied widely to the study of inorganic (Nakamoto, 1986) and organic (Lin-Vien et al., 1991) compounds.

2.3.5.2 Raman spectroscopy for studying mechanical behaviour of SiC and TZP

As the atomic distance changes with the applied stress, the phonon Raman bands also shift with stress enabling stress measurement at high resolution. Raman spectroscopy is the only method which is able to measure local stresses with a resolution of 1 μm in a wide range of the materials (Colomban, 2002) . For example, Raman spectroscopy has been successfully applied to study local stresses in silicon integrated circuits (De Wolf, 1996) and diamond CVD films (Windischmann and Gray, 1995). However, this technique is not suitable for all materials as the peak can be insufficiently sensitive to stress or the peak intensity can be too low which makes for difficulties in detection (Belnap et al., 1994). Some materials can avoid this problem when alternative luminescent sources are available, for example Cr^{3+} fluorescence spectroscopy for alumina (Molis and Clarke, 1990).

2.3.5.3 Raman spectroscopy on SiC

Since there are no fluorescent ions in SiC, researchers generally use the Raman effect to measure residual stresses in this ceramic (Liu and Vohra, 1994, Grodecki et al., 2009). In crystals, the atomic distance, and therefore the bonding forces, change with the stress, and this leads to the shift of the Raman bands. However previous research on SiC has only unfolded its piezospectroscopic effect at a relatively high

residual stress, and it has been less discussed for situations involving a relatively low level of residual stress situation, e.g. indentation residual stress. This work aims to establish a method of measuring residual stress in SiC from Raman microscopy and hence to understand the residual stresses around SiC indentations.

In contrast to the use of Cr^{3+} spectroscopy with alumina, Raman spectroscopy as a tool for measuring residual stress in SiC materials has been less discussed in the literature. This comes from the complexity of phonon modes for each SiC polytype and the requirement for high quality SiC crystals capable of sustaining high pressure.

2.3.5.4 Behaviour of the SiC Raman modes under high pressure

The behavior of the Raman modes in 3C-SiC has been investigated under pressures of up to 80 GPa (Mitraet al, 1969; Olego et al, 1982; Goncharovet al, 1990; Aleksandrovet al, 1992). Olego et al. (1982) studied the frequency shift of Raman bands of single crystal 3C-SiC under pressures up to 22.5 GPa, and they obtained the relationship between frequencies of the TO (transverse optical) and LO (longitudinal optical) modes and the relative lattice compression by least-squares fitting:

$$\omega_{\mathrm{TO}} = (796.5 \pm 0.3) + (3734 \pm 30)\left(-\frac{\Delta a}{a_0}\right)$$

$$\omega_{\mathrm{LO}} = (973 \pm 0.3) + (4532 \pm 30)(-\frac{\Delta a}{a_0})$$

where ω_{TO} and ω_{LO} are the TO and LO phonon frequencies (cm^{-1}), respectively, and a_0 is the stress free lattice constant. Replacing $\frac{\Delta a}{a_0}$ by hydrostatic pressure *p* (in GPa), the following expressions for the pressure dependence were obtained:

$$\omega_{\mathrm{TO}} = (796.2 \pm 0.3) + (3.88 \pm 0.08)\mathrm{p} - (2.2 \pm 0.4) \times 10^{-2}\mathrm{p}^2$$

$$\omega_{\mathrm{LO}} = (972.7 \pm 0.3) + (4.75 \pm 0.09)\mathrm{p} - (2.5 \pm 0.4) \times 10^{-2}\mathrm{p}^2$$

A similar experiment was conducted by Liu and Vohra (1994) for 6H-SiC with pressure up to 95 GPa (Figure 2.15). And they obtained the

$$\omega_{\mathrm{TO}} = 789.2 + 3.11\mathrm{p} - 0.009\mathrm{p}^2$$

$$\omega_{\mathrm{LO}} = 970.1 + 3.83\mathrm{p} - 0.013\mathrm{p}^2$$

They also found that below a pressure of 40 GPa, 6H-SiC is more ionic, but is more covalent if higher pressure is applied. This leads to an increase of the LO-TO splitting. Considering that the around the Vickers indentation the residual stress level is normally a few GPa or less (Guo and Todd, 2011b), the work regarding the behavior of SiC Raman modes under low pressure will be more relevant to the work in the thesis.

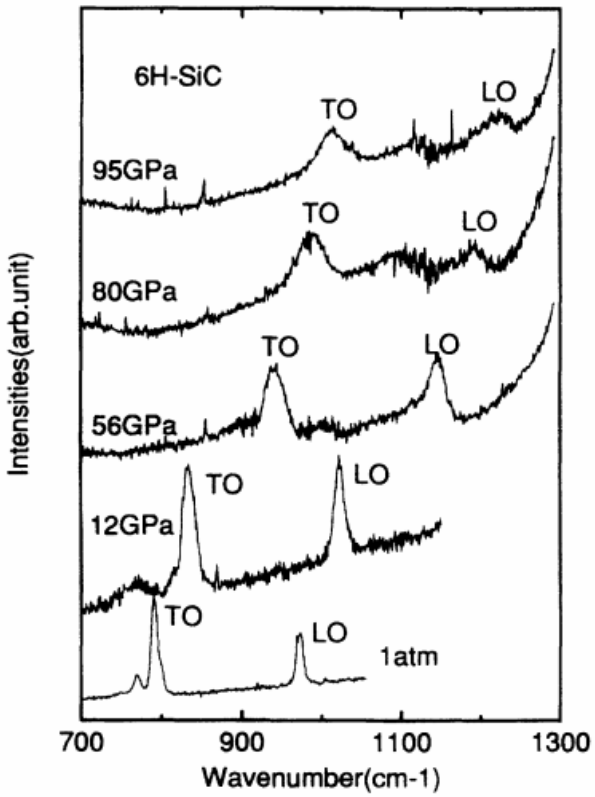


Figure 2.15 Raman spectra of the 6H-SiC sample in the diamond anvil cell in response to different pressures. The strong background near 1300 cm^{-1} is due to the tail of the Raman mode of the diamond anvil (Liu and Vohra, 1994).

2.3.5.5 Raman Spectroscopy for low pressure measurements on SiC

The behaviors of SiC Raman modes under low pressure conditions were researched in composite materials containing SiC to understand the mechanical properties and strengthening mechanisms. Residual stresses in 3C-SiC whiskers in an alumina matrix were analysed by DiGregorio et al. (1992) using Raman microscopy. The whiskers grow along the [111] direction and hydrostatic pressure was applied by a diamond anvil cell. A linear least-square fit of the frequency shift—pressure curve

gave the following equation:

$$\omega^{\mathrm{TO}} - \omega_0^{\mathrm{TO}} = \mathrm{X}(5.03 \pm 0.50)\mathrm{cm}^{-1}\mathrm{GPa}^{-1}$$

where ω^{TO} and ω_0^{TO} are the frequencies of the TO mode with and without stress; *X* is the applied pressure. It can be seen that the hydrostatic stress coefficient they obtained is appreciably larger than the first order in the applied pressure in Olego et al.'s result (where the coefficient is 3.88 ± 0.08 $cm^{-1}GPa^{-1}$). This discrepancy is due to the increased anharmonicity induced by the high degree of disorder in SiC whiskers (DiGregorio et al., 1992). Therefore, directly using the PS coefficient from the results originating from single-crystals (such as (Olego et al., 1982)) to calculate stress may lead to dubious results.

DiGregorio and Furtak (1992) then analysed the residual stresses of 6H-SiC particles in Al_2O_3/SiC composites using a similar method. The following equations were obtained from calibration and used for calculating residual stresses:

$$\omega^{\mathrm{TO}} - \omega_0^{\mathrm{TO}} = \mathrm{X}(3.53 \pm 0.21)\mathrm{cm}^{-1}\mathrm{GPa}^{-1}$$

$$\omega^{\mathrm{LO}} - \omega_0^{\mathrm{LO}} = \mathrm{X}(4.28 \pm 0.22)\mathrm{cm}^{-1}\mathrm{GPa}^{-1}$$

The residual stresses they measured in 30% SiC samples are of order -1600 MPa, and they found the residual stress in composites reinforced by 6H-SiC particles is higher than that in composites reinforced with 3C-SiC whiskers. Ferroni and Pezzotti (2002) assessed the residual stress in Al_2O_3/SiC Nanocomposites using

fluorescence and Raman microscopy. However, they directly used the piezospectroscopic coefficients proposed by DiGregorio et al. (1992) for their 3C-SiC whiskers in an alumina matrix. This means Ferroni and Pezzotti's results are likely unreliable because as described previously, the PS coefficients from one form of SiC may not work properly for another form of polycrystalline SiC.

So far, no work has been done on the residual stress around SiC indentations. In this thesis, the PS coefficient of commercial SiC (SiC type D from Morgan Advanced Materials plc) will be analysed and the residual stress field around the SiC indentations will be measured (Chapter 5).

2.3.5.6 Raman spectroscopy on TZP

Although, the monoclinic and tetragonal peaks from the Raman spectrum of zirconia have been studied at the early age of the application of zirconia (Keramidas and White, 1973, Phillippi and Mazdiyasni, 1971), there have been only a few studies on the response of the zirconia, especially the monoclinic and tetragonal peaks of partially stabilised zirconia, to the applied stress.

The change of the Raman lines in pure zirconia with stresses up to 16 GPa was studied by Kourouklis and Liarokapis (1991). The isomorphic zirconia (monoclinic)

was found to transform to the tetragonal phase at the hydrostatic stress of 3.5 GPa and remain stable up to 12 GPa. However, this was done on pure zirconia with no stabilizer and tetragonal phase. To the author's knowledge, only two papers have dealt with the quantitative calibration of the PS coefficient of the tetragonal or the monoclinic peaks in the partially stabilised zirconia spectrum. Sergo et al. (1995) calibrated the monoclinic line at a Raman shift of 614cm^{-1} with respect to the applied uniaxial stress and the tetragonal line at 634 cm^{-1} on the Ce-TZP and the PS coefficients were 2.1 cm^{-1}/GPa and 2.4 cm^{-1}/GPa, respectively. Sergo et al. (1995) also indicated from the experiments that these two lines are most sensitive to the applied stress. Belnap et al. (1994) also calibrated the tetragonal peak at a frequency of 635 cm^{-1} with respect to the applied uniaxial stress and found the PS coefficient of 1.83 cm^{-1}/GPa. This was used in the stress measurement on TZP indentation conducted in Chapter 5 because the data fitting method used by Belnap et al. (1994) is more rigorous than that of Sergo et at. (1995).

Vickers indentation has been used as a tool for the study of t → m phase transformation on zirconia. The volume percentage of the monoclinic phase V_m could be calculated from the intensities of the monoclinic I_m and tetragonal I_t Raman peaks by (Muñoz Tabares and Anglada, 2010):

$$V_m = \frac{I_m}{K_{mt} I_t + I_m}$$

where K_{mt} is a factor for correcting the difference of the scattering cross section between the selected monoclinic and tetragonal phases. K_{mt} is obtained by fitting the experimental data to this equation. Different authors have found different K_{mt} values, and hence different equations (Clarke and Adar, 1982, Katagiri et al., 1986, Lim et al., 1992, Kim et al., 1997, Casellas et al., 2001). Muñoz Tabares and Anglada (2010) compared their equations and found the equation proposed by Katagiri et al. (1986) has the least error compared with other proposed equations regarding monoclinic concentration and this equation will be used in Chapter 5:

$$V_m = \frac{0.5(I_m^{181} + I_m^{190})}{2.2I_t^{147} + 0.5(I_m^{181} + I_m^{190})}$$

where the intensities of the monoclinic peaks at around 181 and 190 cm^{-1}, I_m^{181} and I_m^{190} and the tetragonal peak at 147 cm^{-1}, I_t^{147} were used.

Behrens et al. (1993) found the stresses induced by a 500 N indentation on 3Y-TZP introduced significant t→m transformation around and below the indent. The largest amount of transformation (Figure 2.16) was found around the edge of the indentation and this agrees with the results from Reece et al. (1992) with 300 N indentation on Ce-TZP, Nemli et al. (2012) with 294 N indentation on Y-TZP and Gogotsi (1997) with a 200 N indentation on Y-TZP. It has also been reported that the tensile and shear stresses are more likely to induce transformation from the tetragonal to the monoclinic phase than by compressive stresses because of the transformational

dilatation of 4% (Behrens et al., 1993). The edge of the indentation has the highest level of tensile and shear stresses (Pittayachawan et al., 2009). This explains why the highest transformation occurs around the impression. Although a peak shift in the Raman spectrum around indentations has been found (Gogotsi, 1997), the residual stress field around the indentation has not been measured quantitatively. In Chapter 5, the indentation stress field in 3Y-TZP will be measured and discussed in relation to the phase transformation.

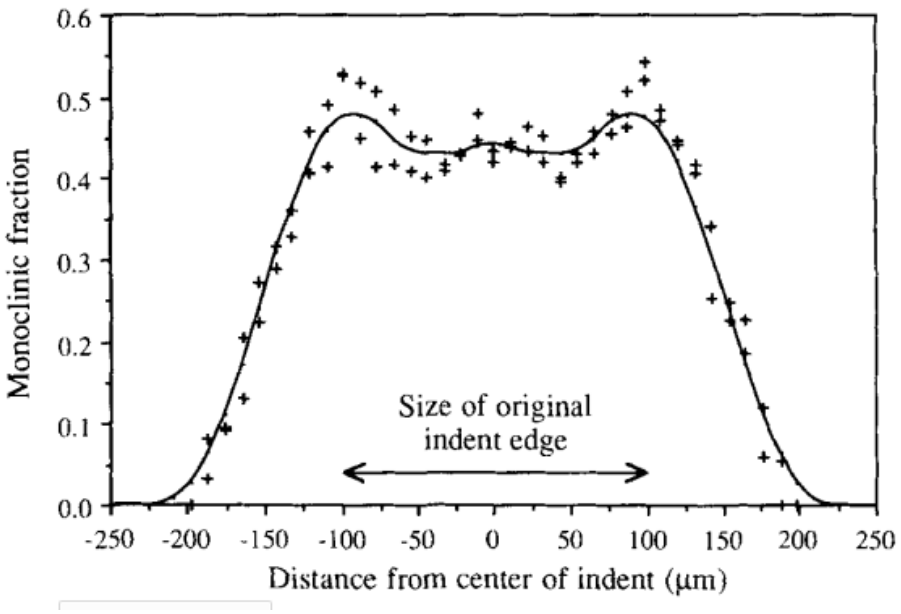


Figure 2.16 Monoclinic intensity fraction of a polished-away indent. The crosses (+) are real data and the line is the fitting curve of the data points (Behrens et al., 1993).

2.4 Summary

Although the Vickers indentation technique has been widely used to study the fracture behaviour of ceramics, it has not been widely accepted by researchers as a standard way of assessing fracture toughness. There is no equation which can be applied universally to ceramics and there are many issues with VIF technique. Most of the understanding on VIF technique is obtained from transparent ceramics, such as glass, and less than non-transparent ceramics. This thesis aims to develop a better understanding of the indentations of some widely-used ceramics, namely, Al_2O_3, SiC and Y-TZP, and discuss the aspects related to VIF technique which were normally ignored in the previous research, such as lateral cracking, issues in measuring indentation parameters and subcritical slow crack growth.

Better knowing the residual stress field created after surface damage, such as that created around an indentation, helps the research of the properties of the material and the assessment of the damage introduced. Measurement of the residual stress field can be assisted by non-destructive residual stress measurement methods. The FLM technique has been used to investigate the residual stress on Al_2O_3 and will be used to analyse the residual stress field around Al_2O_3 indentations. Raman spectroscopy has been employed to investigate residual stress on SiC and Y-TZP and will be to study SiC and Y-TZP indentations.

Based on the experimental results obtained (Chapter 4 and 5), this thesis builds a new model (Chapter 6) for better describing the indentation residual stress field and indentation fracture toughness.

References

ALEKSANDROV, I., GONCHAROV, A., YAKOVENKO, E. & STISHOV, S. 1992. High pressure study of diamond, graphite and related materials. *High-pressure research: application to earth and planetary sciences*, 409-416.

ANSTIS, G., CHANTIKUL, P., LAWN, B. R. & MARSHALL, D. 1981. A critical evaluation of indentation techniques for measuring fracture toughness: I, direct crack measurements. *Journal of the American Ceramic Society,* 64, 533-538.

AUERBACH, F. 1891. Measurement of hardness. *Ann. Phys. Chem,* 43, 61.

BADWAL, S. & HUGHES, A. 1992. The effects of sintering atmosphere on impurity phase formation and grain boundary resistivity in Y 2 O 3-fully stabilized ZrO 2. *Journal of the European Ceramic Society,* 10, 115-122.

BAMZAI, K., KOTRU, P. & WANKLYN, B. 2000. Fracture mechanics, crack propagation and microhardness studies on flux grown ErAlO3 single crystals. *Journal of Materials Science & Technology,* 16.

BEHRENS, G., DRANSMANN, G. W. & HEUER, A. H. 1993. On the Isothermal Martensitic Transformation in 3Y‐TZP. *Journal of the American Ceramic Society,* 76, 1025-1030.

BELNAP, D. J., TSAI, J.-F. & SHETTY, D. K. 1994. Direct measurement of crack shielding in ceramics by the application of Raman microprobe spectroscopy. *Journal of materials research,* 9, 3183-3193.

BHAT, D. G. 1981. Comment on "Elastic/plastic indentation damage in ceramics: The median/radial crack system". *Journal of the American Ceramic Society,* 64, C‐165-C‐166.

BOURAS, S., ZERIZER, I., GHELDANE, F., BOUAZZA, M. & BOUZABATA, B. 2008. Study of the resistance to crack propagation in alumina by acoustic emission. *Ceramics International,* 34, 1857-1865.

CASELLAS, D., CUMBRERA, F., S NCHEZ-BAJO, F., FORSLING, W., LLANES, L. & ANGLADA, M. 2001. On the transformation toughening of Y–ZrO 2 ceramics with mixed Y–TZP/PSZ microstructures. *Journal of the European Ceramic Society,* 21, 765-777.

CASOLCO, S., XU, J. & GARAY, J. 2008. Transparent/translucent polycrystalline nanostructured yttria stabilized zirconia with varying colors. *Scripta Materialia,* 58, 516-519.

CHANG, K. J. & COHEN, M. L. 1987. Ab initio pseudopotential study of structural and high-pressure properties of SiC. *Physical Review B,* 35, 8196.

CHANTIKUL, P., ANSTIS, G., LAWN, B. R. & MARSHALL, D. 2006. A critical evaluation of indentation

techniques for measuring fracture toughness: II, strength method. *Journal of the American Ceramic Society,* 64**,** 539-543.

CHANTIKUL, P., LAWN, B. R. & MARSHALL, D. 1981. Micromechanics of flaw growth in static fatigue: influence of residual contact stresses. *Journal of the American Ceramic Society,* 64**,** 322-325.

CHENG, W. & FINNIE, I. 1993. Measurement of residual stress distributions near the toe of an attachment welded on a plate using the crack compliance method. *Engineering Fracture Mechanics,* 46**,** 79-91.

CHEVALIER, J. M., GREMILLARD, L., VIRKAR, A. V. & CLARKE, D. R. 2009. The tetragonal‐monoclinic transformation in zirconia: lessons learned and future trends. *Journal of the American Ceramic Society,* 92**,** 1901-1920.

CHIANG, S., MARSHALL, D. & EVANS, A. 1982. The response of solids to elastic/plastic indentation. I. Stresses and residual stresses. *Journal of Applied Physics,* 53**,** 298-311.

CHICOT, D., DUARTE, G., TRICOTEAUX, A., JORGOWSKI, B., LERICHE, A. & LESAGE, J. 2009. Vickers Indentation Fracture (VIF) modeling to analyze multi-cracking toughness of titania, alumina and zirconia plasma sprayed coatings. *Materials Science and Engineering: A,* 527**,** 65-76.

CHICOT, D., MERCIER, D., ROUDET, F., SILVA, K., STAIA, M. & LESAGE, J. 2007. Comparison of instrumented Knoop and Vickers hardness measurements on various soft materials and hard ceramics. *Journal of the European Ceramic Society,* 27**,** 1905-1911.

CHICOT, D. & TRICOTEAUX, A. Mechanical Properties of Ceramics by Indentation: Principle and Applications.

CLARKE, D. & ADAR, F. 1982. Measurement of the crystallographically transformed zone produced by fracture in ceramics containing tetragonal zirconia. *Journal of the American Ceramic Society,* 65**,** 284-288.

CLYNE, T. & GILL, S. 1996. Residual stresses in thermal spray coatings and their effect on interfacial adhesion: a review of recent work. *Journal of Thermal Spray Technology,* 5**,** 401-418.

COLOMBAN, P. 2002. Analysis of strain and stress in ceramic, polymer and metal matrix composites by Raman spectroscopy. *Advanced Engineering Materials,* 4**,** 535-542.

COOK, R., LAWN, B. R. & ANSTIS, G. 1982. Fatigue analysis of brittle materials using indentation flaws. *Journal of materials science,* 17**,** 1108-1116.

COOK, R. F. & LAWN, B. R. 1983. A modified indentation toughness technique. *Journal of the American Ceramic Society,* 66**,** c200-c201.

COOK, R. F. & LINIGER, E. G. 1993. Kinetics of indentation cracking in glass. *Journal of the American Ceramic Society,* 76**,** 1096-1105.

COOK, R. F. & PHARR, G. M. 1990. Direct observation and analysis of indentation cracking in glasses and ceramics. *Journal of the American Ceramic Society,* 73**,** 787-817.

DAI, D., HILLS, D., WARREN, P. & NOWELL, D. 1995. The propulsion of surface flaws by elastic indentation testing. *Acta metallurgica et materialia,* 43**,** 985-991.

DE AZA, A., CHEVALIER, J., FANTOZZI, G., SCHEHL, M. & TORRECILLAS, R. 2002. Crack growth resistance of alumina, zirconia and zirconia toughened alumina ceramics for joint prostheses. *Biomaterials,* 23**,** 937-945.

DE WOLF, I. 1996. Micro-Raman spectroscopy to study local mechanical stress in silicon integrated circuits. *Semiconductor Science and Technology,* 11**,** 139.

DEBERNARDI, A., ULRICH, C., SYASSEN, K. & CARDONA, M. 1999. Raman linewidths of optical

phonons in 3C-SiC under pressure: First-principles calculations and experimental results. *Physical Review B,* 59**,** 6774.

DEGTYAR, A., LAVRENTYEV, A. & ROKHLIN, S. 1997. New method for determination of applied and residual stresses in anisotropic materials from ultrasonic velocity measurement. *Materials evaluation,* 55**,** 1162-1168.

DENRY, I. & KELLY, J. R. 2008. State of the art of zirconia for dental applications. *Dental materials,* 24**,** 299-307.

DIGREGORIO, J., FURTAK, T. & PETROVIC, J. 1992. A technique for measuring residual stress in SiC whiskers within an alumina matrix through Raman spectroscopy. *Journal of Applied Physics,* 71**,** 3524-3531.

DIGREGORIO, J. F. & FURTAK, T. E. 1992. Analysis of Residual Stress in 6H‐SiC Particles within Al2O3/SiC Composites through Raman Spectroscopy. *Journal of the American Ceramic Society,* 75**,** 1854-1857.

EBRAHIMI, M., CHEVALIER, J. & FANTOZZI, G. 2000. Slow crack-growth behavior of alumina ceramics. *Journal of materials research,* 15**,** 142-147.

EICHLER, J., R DEL, J., EISELE, U. & HOFFMAN, M. 2007. Effect of Grain Size on Mechanical Properties of Submicrometer 3Y‐TZP: Fracture Strength and Hydrothermal Degradation. *Journal of the American Ceramic Society,* 90**,** 2830-2836.

ESHELBY, J. D. The determination of the elastic field of an ellipsoidal inclusion, and related problems. Proceedings of the Royal Society of London A: Mathematical, Physical and Engineering Sciences, 1957. The Royal Society, 376-396.

EVANS, A. 1978. Microfracture from thermal expansion anisotropy--I. Single phase systems. *Acta Metallurgica,* 26**,** 1845-1853.

EVANS, A. G. & CHARLES, E. A. 1976. Fracture toughness determinations by indentation. *Journal of the American Ceramic Society,* 59**,** 371-372.

EVANS, A. G. & WILSHAW, T. R. 1976. Quasi-static solid particle damage in brittle solids—I. Observations analysis and implications. *Acta Metallurgica,* 24**,** 939-956.

FERRONI, L. P. & PEZZOTTI, G. 2002. Evidence for bulk residual stress strengthening in Al2O3/SiC nanocomposites. *Journal of the American Ceramic Society,* 85**,** 2033-2038.

FETT, T., MUNZ, D., YU, C. T. & KOBAYASHI, A. S. 1994. Determination of bridging stresses in reinforced Al2O3. *Journal of the American Ceramic Society,* 77**,** 3267-3269.

FISCHER‐CRIPPS, A. C. & LAWN, B. R. 1996. Stress Analysis of Contact Deformation in Quasi‐Plastic Ceramics. *Journal of the American Ceramic Society,* 79**,** 2609-2618.

FRANK, F. & LAWN, B. R. On the theory of Hertzian fracture. Proceedings of the Royal Society of London A: Mathematical, Physical and Engineering Sciences, 1967. The Royal Society, 291-306.

GHOSH, A., LI, Z., HENAGER, C., KOBAYASHI, A. & BRADT, R. 1995. Vickers microtoughness of SiC in the median-crack regime. *Fracture Mechanics of Ceramics.,* 11**,** 219-231.

GOGOTSI, G. 1997. Raman spectroscopy and mechanical behavior of zirconia materials. *Refractories and industrial ceramics,* 38**,** 224-230.

GONCHAROV, A., IAKOVENKO, E. & STISHOV, S. 1990. Silicon carbide stability at high pressures(Ustoichivost' karbida kremniia pri vysokikh davleniiakh). *Pis'ma v Zhurnal Eksperimental'noi i Teoreticheskoi Fiziki,* 52**,** 1092-1095.

GOTMAN, I., TRAVITZKY, N. & GUTMANAS, E. 1998. Dense in situ TiB 2/TiN and TiB 2/TiC ceramic matrix composites: reactive synthesis and properties. *Materials Science and Engineering: A,* 244**,** 127-137.

GRABNER, L. 1978. Spectroscopic technique for the measurement of residual stress in sintered Al2O3. *Journal of Applied Physics,* 49**,** 580-583.

GRODECKI, K., WYSMOŁEK, A., STĘPNIEWSKI, R., BARANOWSKI, J., HOFMAN, W., TYMICKI, E. & GRASZA, K. 2009. Raman Piezospectroscopy of Phonons in Bulk 6H-SiC. *Acta Physica Polonica A,* 116**,** 6-9.

GUBICZA, J., ROZLOSNIK, N. & JUH SZ, A. 1997. Comment on "Indentation size effect: reality or artefact?". *Journal of materials science letters,* 16**,** 1904-1905.

GUIN, J. P., ROUXEL, T., SANGLEBŒUF, J. C., MELSCO T, I. & LUCAS, J. 2002. Hardness, toughness, and scratchability of germanium–selenium chalcogenide glasses. *Journal of the American Ceramic Society,* 85**,** 1545-1552.

GUO, S. & TODD, R. 2011a. Quantitative optical fluorescence microprobe measurements of stresses around indentations in Al2O3 and Al2O3/SiC nanocomposites: The influence of depth resolution and specimen translucency. *Acta materialia,* 59**,** 2637-2647.

GUO, S. & TODD, R. I. 2010a. Confocal fluorescence microscopy in alumina-based ceramics: Where does the signal come from? *Journal of the European Ceramic Society,* 30**,** 641-648.

GUO, S. & TODD, R. I. 2010b. Cr3+ microspectroscopy measurements and modelling of local variations in surface grinding stresses in polycrystalline alumina. *Journal of the European Ceramic Society,* 30**,** 2533-2545.

GUO, S. & TODD, R. I. 2011b. Quantitative optical fluorescence microprobe measurements of stresses around indentations in Al2O3 and Al2O3/SiC nanocomposites: The influence of depth resolution and specimen translucency. *Acta materialia,* 59**,** 2637-2647.

GUPTA, P. K. & JUBB, N. J. 1981. Post‐Indentation Slow Growth of Radial Cracks in Glasses. *Journal of the American Ceramic Society,* 64**,** C‐112-C‐114.

GUPTA, T., BECHTOLD, J., KUZNICKI, R., CADOFF, L. & ROSSING, B. 1977. Stabilization of tetragonal phase in polycrystalline zirconia. *Journal of materials science,* 12**,** 2421-2426.

H BNER, H. & DORRE, E. 1984. Alumina: processing, properties and applications. Springer-Verlag, Berlin.

HAGAN, J. & SWAIN, M. V. 1978. The origin of median and lateral cracks around plastic indents in brittle materials. *Journal of Physics D: Applied Physics,* 11**,** 2091.

HAMILTON, G. & GOODMAN, L. 1966. The stress field created by a circular sliding contact. *Journal of Applied Mechanics,* 33**,** 371-376.

HE, J. & CLARKE, D. R. 1995. Determination of the Piezospectroscopic Coefficients for Chromium‐Doped Sapphire. *Journal of the American Ceramic Society,* 78**,** 1347-1353.

HE, J. & CLARKE, D. R. 1997. Polarization Dependence of the Cr3+ R‐Line Fluorescence from Sapphire and Its Application to Crystal Orientation and Piezospectroscopic Measurement. *Journal of the American Ceramic Society,* 80**,** 69-78.

HERTZ, H. Verhandlungen des Vereins zur Beforderung des Gewerbe Fleisses, 61 (1882) 449. *Translated and reprinted in English in "Hertz's Miscellaneous Papers"(Macmilla & Co., New York, 1896) Ch,* 6.

HUSSAK, E. 1892. Über Brazilit, ein neues Tantal (Niob) Mineral von der Eisenmine Jacupiranga.

Neues Jahrb. Mineral. Geol. Paläontol., 2**,** 141-159.

IOST, A. & BIGOT, R. 1996. Indentation size effect: reality or artefact? *Journal of materials science,* 31**,** 3573-3577.

IOST, A. & BIGOT, R. 1998. Reply to "Comment on Indentation Size Effect: Reality or Artifact?". *Journal of Materials Science Letters,* 17**,** 1889-1891.

JONES, S., NORMAN, C. & SHAHANI, R. 1987. Crack-profile shapes formed under a Vickers indent pyramid. *Journal of Materials Science Letters,* 6**,** 721-723.

KAPLYANS.AA & PRZHEVUS.AK 1967. DEFORMATIONAL SPLITTING OF LUMINESCENCE SPECTRUM LINES AND STRUCTURES OF EXCHANGE-LINKED PAIS OF CHROMIUM IONS IN RUBY. *Soviet Physics Solid State,Ussr,* 9**,** 190-&.

KATAGIRI, G., ISHIDA, H., ISHITANI, A. & MASAKI, T. 1986. Direct determination by a Raman microprobe of the transformation zone size in Y 2 O 3 containing tetragonal ZrO 2 polycrystals. *Advances in ceramics,* 24**,** 537-544.

KERAMIDAS, V. G. & WHITE, W. B. 1973. Raman scattering from CaxZr1−xO2−x 阳 x, a system with massive point defects. *Journal of Physics and Chemistry of Solids,* 34**,** 1873-1878.

KIM, B.-K., HAHN, J.-W. & HAN, K. R. 1997. Quantitative phase analysis in tetragonal-rich tetragonal/monoclinic two phase zirconia by Raman spectroscopy. *Journal of Materials Science Letters,* 16**,** 669-671.

KOUROUKLIS, G. A. & LIAROKAPIS, E. 1991. Pressure and temperature dependence of the Raman spectra of zirconia and hafnia. *Journal of the American Ceramic Society,* 74**,** 520-523.

KRUZIC, J., KIM, D., KOESTER, K. & RITCHIE, R. 2009. Indentation techniques for evaluating the fracture toughness of biomaterials and hard tissues. *Journal of the mechanical behavior of biomedical materials,* 2**,** 384-395.

KRUZIC, J. J., NALLA, R. K., KINNEY, J. H. & RITCHIE, R. 2003. Crack blunting, crack bridging and resistance-curve fracture mechanics in dentin: effect of hydration. *Biomaterials,* 24**,** 5209-5221.

LANKFORD, J. 1982. Indentation microfracture in the Palmqvist crack regime: implications for fracture toughness evaluation by the indentation method. *Journal of Materials Science Letters,* 1**,** 493-495.

LAUGIER, M. 1987. New formula for indentation toughness in ceramics. *Journal of Materials Science Letters,* 6**,** 355-356.

LAUGIER, M. T. 1985. The elastic/plastic indentation of ceramics. *Journal of Materials Science Letters,* 4**,** 1539-1541.

LAWN, B. & SWAIN, M. 1975. Microfracture beneath point indentations in brittle solids. *Journal of Materials Science,* 10**,** 113-122.

LAWN, B., SWAIN, M. & PHILLIPS, K. 1975. On the mode of chipping fracture in brittle solids. *Journal of Materials Science,* 10**,** 1236-1239.

LAWN, B. R. 1993. *Fracture of brittle solids*, Cambridge university press.

LAWN, B. R., EVANS, A. & MARSHALL, D. 1980. Elastic/plastic indentation damage in ceramics: the median/radial crack system. *Journal of the American Ceramic Society,* 63**,** 574-581.

LAWN, B. R. & FULLER, E. 1975. Equilibrium penny-like cracks in indentation fracture. *Journal of Materials Science,* 10**,** 2016-2024.

LEVIN, I., KAPLAN, W. D., BRANDON, D. & WIEDER, T. 1994. Residual stresses in alumina-SiC

nanocomposites. *Acta metallurgica et materialia,* 42**,** 1147-1154.

LI, Z., GHOSH, A., KOBAYASHI, A. S. & BRADT, R. C. 1989. Indentation fracture toughness of sintered silicon carbide in the Palmqvist crack regime. *Journal of the American Ceramic Society,* 72**,** 904-911.

LIANG, K., ORANGE, G. & FANTOZZI, G. 1990. Evaluation by indentation of fracture toughness of ceramic materials. *Journal of Materials Science,* 25**,** 207-214.

LIM, C. S., FINLAYSON, T. R., NINIO, F. & GRIFFITHS, J. R. 1992. In‐Situ Measurement of the Stress‐Induced Phase Transformations in Magnesia‐Partially‐Stabilized Zirconia Using Raman Spectroscopy. *Journal of the American Ceramic Society,* 75**,** 1570-1573.

LIN-VIEN, D., COLTHUP, N. B., FATELEY, W. G. & GRASSELLI, J. G. 1991. *The handbook of infrared and Raman characteristic frequencies of organic molecules*, Elsevier.

LIU, J. & VOHRA, Y. K. 1994. Raman modes of 6H polytype of silicon carbide to ultrahigh pressures: A comparison with silicon and diamond. *Physical review letters,* 72**,** 4105.

LUBE, T. 2001. Indentation crack profiles in silicon nitride. *Journal of the European Ceramic Society,* 21**,** 211-218.

MA, Q. & CLARKE, D. R. 1993a. Measurement of residual stresses in sapphire fiber composites using optical fluorescence. *Acta metallurgica et materialia,* 41**,** 1817-1823.

MA, Q. & CLARKE, D. R. 1993b. Stress Measurement in Single‐Crystal and Polycrystalline Ceramics Using Their Optical Fluorescence. *Journal of the American Ceramic Society,* 76**,** 1433-1440.

MA, Q. & CLARKE, D. R. 1994. Piezospectroscopic determination of residual stresses in polycrystalline alumina. *Journal of the American Ceramic Society,* 77**,** 298-302.

MAERTEN, A., ZASLANSKY, P., MOCHALES, C., TRAYKOVA, T., MUELLER, W., FRATZL, P. & FLECK, C. 2013. Characterizing the transformation near indents and cracks in clinically used dental yttria-stabilized zirconium oxide constructs. *Dental materials,* 29**,** 241-251.

MARSHALL, D. & LAWN, B. 1980. FLAW CHARACTERISTICS IN DYNAMIC FATIGUE. THE INFLUENCE OF RESIDUAL CONTACT STRESSES. *J. AM. CERAM. SOC. J. Am. Ceram. Soc.,* 63**,** 532.

MARSHALL, D., LAWN, B. & EVANS, A. 1982. Elastic/plastic indentation damage in ceramics: the lateral crack system. *Journal of the American Ceramic Society,* 65**,** 561-566.

MARSHALL, D. B., COOK, R. F., PADTURE, N. P., OYEN, M. L., PAJARES, A., BRADBY, J. E., REIMANIS, I. E., TANDON, R., PAGE, T. F. & PHARR, G. M. 2015. The Compelling Case for Indentation as a Functional Exploratory and Characterization Tool. *Journal of the American Ceramic Society,* 98**,** 2671-2680.

MARTEAU, J., BIGERELLE, M., BOUVIER, S. & IOST, A. 2014. Reflection on the measurement and use of the topography of the indentation imprint. *Scanning,* 36**,** 115-126.

MARTIN, C. A., JOHNSON, D. E., OWEN, D. P., PETERSON, R. O. & DUDT, P. J. 2012. Method for making ballistic armor using low-density ceramic material. US Patent 8,105,510.

MCCUMBER, D. E. & STURGE, M. D. 1963. Linewidth and Temperature Shift of the R Lines in Ruby. *Journal of Applied Physics,* 34**,** 1682-1684.

MICHALSKE, T. A. & FREIMAN, S. W. 1983. A molecular mechanism for stress corrosion in vitreous silica. *J. Amer. Ceram. Soc,* 66**,** 4.

MITRA, S., BRAFMAN, O., DANIELS, W. & CRAWFORD, R. 1969. Pressure-induced phonon frequency shifts measured by Raman scattering. *Physical review,* 186**,** 942-944.

MIYATA, N. & JINNO, H. 1980. Use of Vickers indentation method for evaluation of fracture toughness

of phase-separated glasses. *Journal of Non-Crystalline Solids,* 38**,** 391-396.

MIYAZAKI, H., HYUGA, H., YOSHIZAWA, Y.-I., HIRAO, K. & OHJI, T. 2010a. Crack profiles under a Vickers indent in silicon nitride ceramics with various microstructures. *Ceramics International,* 36**,** 173-179.

MIYAZAKI, H., HYUGA, H., YOSHIZAWA, Y., HIRAO, K. & OHJI, T. 2010b. Crack profiles under a Vickers indent in silicon nitride ceramics with various microstructures. *Ceramics International,* 36**,** 173-179.

MIYAZAKI, H. & YOSHIZAWA, Y.-I. 2014. Refined measurements of indentation fracture resistance of alumina using powerful optical microscopy. *Ceramics International,* 40**,** 2777-2783.

MOLIS, S. E. & CLARKE, D. R. 1990. Measurement of Stresses Using Fluorescence in an Optical Microprobe: Stresses around Indentations in a Chromium‐Doped Sapphire. *Journal of the American Ceramic Society,* 73**,** 3189-3194.

MOTT, P. & ROLAND, C. 2009. Limits to Poisson's ratio in isotropic materials. *Physical Review B,* 80**,** 132104.

MU OZ TABARES, J. A. & ANGLADA, M. J. 2010. Quantitative Analysis of Monoclinic Phase in 3Y‐TZP by Raman Spectroscopy. *Journal of the American Ceramic Society,* 93**,** 1790-1795.

MUNRO, R. 1997. Material properties of a sintered α-SiC. *Journal of Physical and Chemical Reference Data,* 26**,** 1195-1203.

MURAOKA, M., EBATA, K. & AB , H. 1993. Effect of Humidity on Small‐Crack Growth in Silica Optical Fibers. *Journal of the American Ceramic Society,* 76**,** 1545-1550.

NAKAMOTO, K. 1986. *Infrared and Raman spectra of inorganic and coordination compounds*, Wiley Online Library.

NAKASHIMA, S. & HARIMA, H. 1997. Raman investigation of SiC polytypes. *physica status solidi (a),* 162**,** 39-64.

NEMLI, S. K., YILMAZ, H., AYDIN, C., BAL, B. T. & TIRAŞ, T. 2012. Effect of fatigue on fracture toughness and phase transformation of Y‐TZP ceramics by X‐ray diffraction and Raman spectroscopy. *Journal of Biomedical Materials Research Part B: Applied Biomaterials,* 100**,** 416-424.

NIIHARA, K. 1983. A fracture mechanics analysis of indentation-induced Palmqvist crack in ceramics. *Journal of Materials Science Letters,* 2**,** 221-223.

NIIHARA, K., MORENA, R. & HASSELMAN, D. 1982. Evaluation ofK Ic of brittle solids by the indentation method with low crack-to-indent ratios. *Journal of Materials Science Letters,* 1**,** 13-16.

OGILVY, I., PERROTT, C. & SUITER, J. 1977. On the indentation fracture of cemented carbide part 1--Survey of operative fracture modes. *Wear,* 43**,** 239-252.

OLEGO, D., CARDONA, M. & VOGL, P. 1982. Pressure dependence of the optical phonons and transverse effective charge in 3C-SiC. *Physical Review B,* 25**,** 3878.

OLIVER, W. C. & PHARR, G. M. 1992. Improved technique for determining hardness and elastic modulus using load and displacement sensing indentation experiments. *Journal of materials research,* 7**,** 1564-1583.

OSTOJIC, P. & MCPHERSON, R. 1987. A review of indentation fracture theory: its development, principles and limitations. *International journal of fracture,* 33**,** 297-312.

PALMQVIST, S. 1957. Indentation hardness and fracture toughness in single crystal. *Jernkontorets Ann,* 141**,** 300-306.

PERALTA, P., LEDOUX, R., HAKIK, M., DICKERSON, R. & DICKERSON, P. 2004. Characterization of surface deformation around vickers indents in monocrystalline materials. *Metallurgical and Materials Transactions A,* 35**,** 2247-2255.

PEZZOTTI, G. 1999. In situ study of fracture mechanisms in advanced ceramics using fluorescence and Raman microprobe spectroscopy. *Journal of raman spectroscopy,* 30**,** 867-875.

PEZZOTTI, G., LETO, A., TANAKA, K. & SBAIZERO, O. 2003. Piezo-spectroscopic assessment of nanoscopic residual stresses in Er3+-doped optical fibres. *Journal of Physics: Condensed Matter,* 15**,** 7687.

PEZZOTTI, G., TATEIWA, T., ZHU, W., KUMAKURA, T., YAMADA, K. & YAMAMOTO, K. 2006. Fluorescence spectroscopic analysis of surface and subsurface residual stress fields in alumina hip joints. *Journal of biomedical optics,* 11**,** 024009-024009-10.

PHILLIPPI, C. & MAZDIYASNI, K. 1971. Infrared and Raman spectra of zirconia polymorphs. *Journal of the American Ceramic Society,* 54**,** 254-258.

PITTAYACHAWAN, P., MCDONALD, A., YOUNG, A. & KNOWLES, J. C. 2009. Flexural strength, fatigue life, and stress‐induced phase transformation study of Y‐TZP dental ceramic. *Journal of Biomedical Materials Research Part B: Applied Biomaterials,* 88**,** 366-377.

PONTON, C. B. & RAWLINGS, R. D. 1989. Vickers indentation fracture toughness test Part 1 Review of literature and formulation of standardised indentation toughness equations. *Materials Science and Technology,* 5**,** 865-872.

POWELL, B. & TABOR, D. 1970. The fracture of titanium carbide under static and sliding contact. *Journal of Physics D: Applied Physics,* 3**,** 783.

QUINN, G. D. & BRADT, R. C. 2007. On the Vickers indentation fracture toughness test. *Journal of the American Ceramic Society,* 90**,** 673-680.

QUINN, J. & D QUINN, G. 1997. Indentation brittleness of ceramics: a fresh approach. *Journal of materials science,* 32**,** 4331-4346.

REECE, M., TETLOW, P. & GALIOTIS, C. 1992. Phase transformation around indentations in zirconia. *Journal of Materials Science Letters,* 11**,** 575-577.

RITTERK JR, J. E. & SHERBURNE, C. L. 1970. Dynamic and static fatigue of silicate glasses. DTIC Document.

ROUXEL, T. 2015. Driving force for indentation cracking in glass: composition, pressure and temperature dependence. *Philosophical Transactions of the Royal Society of London A: Mathematical, Physical and Engineering Sciences,* 373**,** 20140140.

SALOMONSON, J. & ROWCLIFFE, D. 1995. Measurement of indentation residual stresses in materials susceptible to slow crack growth. *Journal of the American Ceramic Society,* 78**,** 173-177.

SCHWARTZ, D. T. 2010. Raman Spectroscopy: Introductory Tutorial. *Renishaw Raman Microscope*.

SEDEL, L. 2000. Evolution of alumina-on-alumina implants: a review. *Clinical orthopaedics and related research,* 379**,** 48.

SERGO, V., CLARKE, D. R. & POMPE, W. 1995. Deformation Bands in Ceria‐Stabilized Tetragonal Zirconia/Alumina: I, Measurement of Internal Stresses. *Journal of the American Ceramic Society,* 78**,** 633-640.

SHAFFER, P. T. B. 1969. A review of the structure of silicon carbide. *Acta Crystallographica Section B: Structural Crystallography and Crystal Chemistry,* 25**,** 477-488.

STEINZIG, M. & TAKAHASHI, T. 2003. Residual stress measurement using the hole drilling method and

laser speckle interferometry part IV: measurement accuracy. *Experimental Techniques,* 27**,** 59-63.

STEVENS, R. 1983. *An introduction to zirconia*, Magnesium Elektron Limited.

SWAIN, M. & HAGAN, J. 1976. Indentation plasticity and the ensuing fracture of glass. *Journal of Physics D: Applied Physics,* 9**,** 2201.

TANG, Y., YONEZU, A., OGASAWARA, N., CHIBA, N. & CHEN, X. 2008. On radial crack and half-penny crack induced by Vickers indentation. *Proceedings of the Royal Society A: Mathematical, Physical and Engineering Science,* 464**,** 2967-2984.

TENG, X., LIU, H. & HUANG, C. 2007. Effect of Al2O3 particle size on the mechanical properties of alumina-based ceramics. *Materials Science and Engineering: A,* 452–453**,** 545-551.

TODD, R., BOURKE, M., BORSA, C. & BROOK, R. 1997. Neutron diffraction measurements of residual stresses in alumina/SiC nanocomposites. *Acta materialia,* 45**,** 1791-1800.

TORO, R. G., MALANDRINO, G., FRAGAL , I. L., KESHU, W., LETO, A. & PEZZOTTI, G. 2006. Cathodoluminescence Investigation of Residual Stress in Er3+:YAlO3 Thin Films Grown on (110) SrTiO3 Substrate by Metal-Organic Chemical Vapor Deposition. *The Journal of Physical Chemistry B,* 110**,** 23977-23981.

TRUEBA, M. & TRASATTI, S. P. 2005. γ - Alumina as a Support for Catalysts: A Review of Fundamental Aspects. *European journal of inorganic chemistry,* 2005**,** 3393-3403.

VEKINIS, G., ASHBY, M. F. & BEAUMONT, P. 1990. R-Curve behaviour of Al 2 O 3 ceramics. *Acta metallurgica et materialia,* 38**,** 1151-1162.

WAN, K.-T., LATHABAI, S. & LAWN, B. R. 1990. Crack velocity functions and thresholds in brittle solids. *Journal of the European Ceramic Society,* 6**,** 259-268.

WARREN, P. 1995. Determining the fracture toughness of brittle materials by Hertzian indentation. *Journal of the European Ceramic Society,* 15**,** 201-207.

WARREN, P., HILLS, D. & ROBERTS, S. 1994. Surface flaw distributions in brittle materials and Hertzian fracture. *Journal of materials research,* 9**,** 3194-3202.

WIEDERHORN, S. 1967. Influence of Water Vapor on Crack Propagation in Soda - Lime Glass. *Journal of the American Ceramic Society,* 50**,** 407-414.

WIEDERHORN, S. 1969. Fracture of ceramics. *Mechanical and thermal properties of ceramics.* NBS Spec. Publ.

WILLARDSON, R. K. & WEBER, E. R. 1998. *SiC materials and devices*, Academic Press.

WILSHAW, T. 1971. The Hertzian fracture test. *Journal of Physics D: Applied Physics,* 4**,** 1567.

WINDISCHMANN, H. & GRAY, K. 1995. Stress measurement of CVD diamond films. *Diamond and related materials,* 4**,** 837-842.

WITHERS, P. & BHADESHIA, H. 2001. Residual stress. Part 1 &# 8211; Measurement techniques. *Materials Science and Technology,* 17**,** 355-365.

WITHERS, P., TURSKI, M., EDWARDS, L., BOUCHARD, P. & BUTTLE, D. 2008. Recent advances in residual stress measurement. *International Journal of Pressure Vessels and Piping,* 85**,** 118-127.

WU, H. Z., ROBERTS, S. G. & DERBY, B. 2008. Residual stress distributions around indentations and scratches in polycrystalline Al2O3 and Al2O3/SiC nanocomposites measured using fluorescence probes. *Acta materialia,* 56**,** 140-149.

YODA, M. 1987. Subcritical crack growth of glass. *Engineering Fracture Mechanics,* 28**,** 77-84.

YOFFE, E. 1982. Elastic stress fields caused by indenting brittle materials. *Philosophical Magazine A,* 46**,** 617-628.

YOO, W. S. & MATSUNAMI, H. 1991. Solid-state phase transformation in cubic silicon carbide. *Japanese journal of applied physics,* 30**,** 545-553.

ZHANG, Y., JIN, X., RONG, Y., HSU, T., JIANG, D. & SHI, J. 2006. On the t→ m martensitic transformation in Ce－Y-TZP ceramics. *Acta materialia,* 54**,** 1289-1295.

Chapter 3 Materials Preparation and Experimental Procedures

3.1 Materials Preparation

3.1.1 Single Crystal Alumina

In this work, single crystal sapphire and ruby were used to provide a comparison with polycrystalline alumina in order to understand the indentation residual stress and cracking behaviour. The c-plane single crystal sapphire and ruby for indentation work were from Fluoroware Inc. Sapphire and ruby pieces had the thickness typically around 300~400 μm with one side of each piece pre-polished by the supplier.

3.1.2 Polycrystalline Alumina

Starting with TM-DAR alumina powder (Tai-Mei, 100nm particle size, 99.99% purity), the main steps of alumina preparation are listed in Table 3.1. Samples after sintering were lapped and polished (Buehler Automet-300) from 15 micron to 1 micron to minimise surface plasticity (Table 3.2). The grain size of the sample was measured to be 2.0 μm (Figure 3.1) and the density was measured to be 3.92 g/cm^{-3} (99.0% relative to the theoretical maximum).

Table 3.1 Summary of ceramic preparation procedure

	Step	Equipment	Description
1	Slurry making		mix alumina powder with distilled water at volume ratio of 4:1; add 0.25 wt% MgO, 2.1wt% dispersant (A40) and 2 wt% binder
2	Ball milling	Bottle rolling machine	milling for at least 12 hrs
3	Sieving	300 mesh sieve	remove the balls and dilute slurry
4	Freeze drying	Edwards Shell freezer and Micro Modulyo freeze dryer, UK	freeze slurry in rotating flask for 3 hrs and dry out slurry for 24 hrs
5	Sieving	106 mesh sieve	
6	Pressing	uniaxial compression machine	uniaxial compression at 54 MPa + cold isostatic pressing (CIPing) at 160 MPa
7	Sintering	tube furnace (R.H.F. 1600 Carbolite, UK)	1550℃ in air for 2 hrs
8*	Thermal etching	tube furnace	1550℃ in air for 15 min (for grain size measurement)

Table 3.2 Summary of polishing procedure

Plate	Diamond paste	Time on each stage
diamond embedded pad (55 μm and 15 μm)	N/A	until flat
cloth	9 μm	1 hr
cloth	6 μm	2 hr
cloth	3 μm	1 hr
cloth	1 μm	1 hr

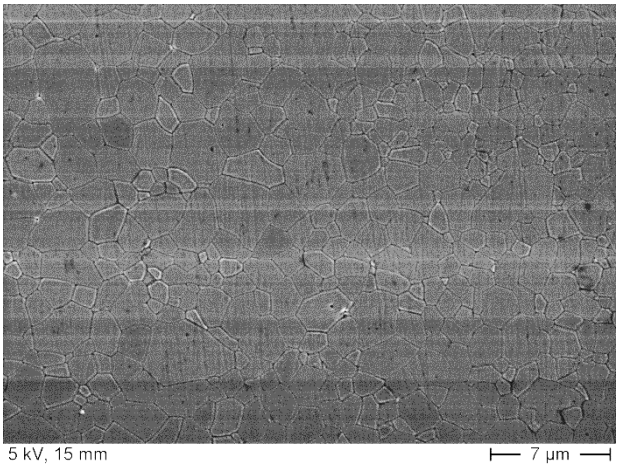


Figure 3.1 SEM micrograph of polycrystalline alumina.

3.1.3 SiC

The SiC material used in this project is a commercial pressurelessly sintered SiC comes from the Morgan Technical Ceramics. It has two types: SiC-D and SiC-E. SiC-D has randomly shaped grains (Figure 3.2a) with the grain size of 6 micron and a density of 98.2%, while the SiC-E has needle-like grains (Figure 3.2b) with a grain size of 29 micron and the density of 97.9%. SiC-D has a more uniform microstructure than SiC-E, therefore SiC-D was selected and used in the all the following research activities.

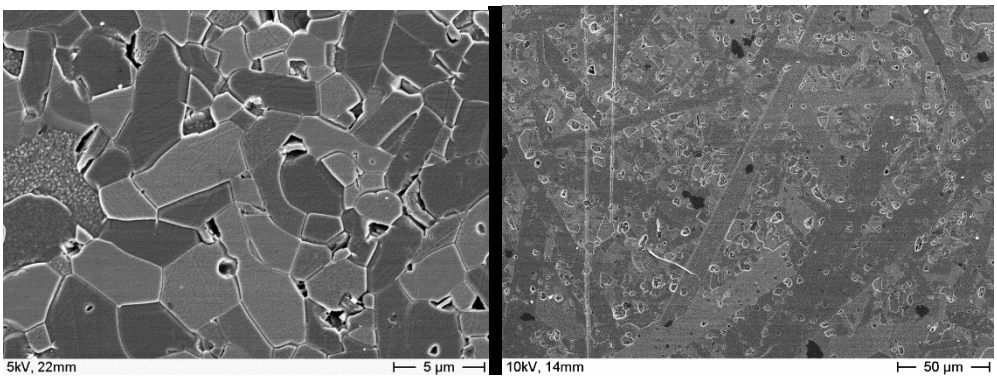


Figure 3.2 SEM micrographs of SiC-D (a) and SiC-E (b).

3.1.4 Zirconia

The 3Y-TZP samples were prepared in the following process. Starting with the TZ-3Y-E (Tosoh CO., Japan) powder which already contains 3 mol% Y_2O_3 addition, a CIPed (Stansted Fluid Powder Ltd., UK) green body was calcined to a peak temperature of 1550 ℃ for 1 hour with the heating and cooling rates both at 5 ℃ /min. Annealing at 1100 ℃ for 1 hr after sintering helped to transform any monoclinic phase generated by the polishing process back to tetragonal. The samples had an average grain size of 0.4 µm (Figure 3.3) and a relative density of 99.2%. The properties of the materials used in this study were shown in Table 3.3.

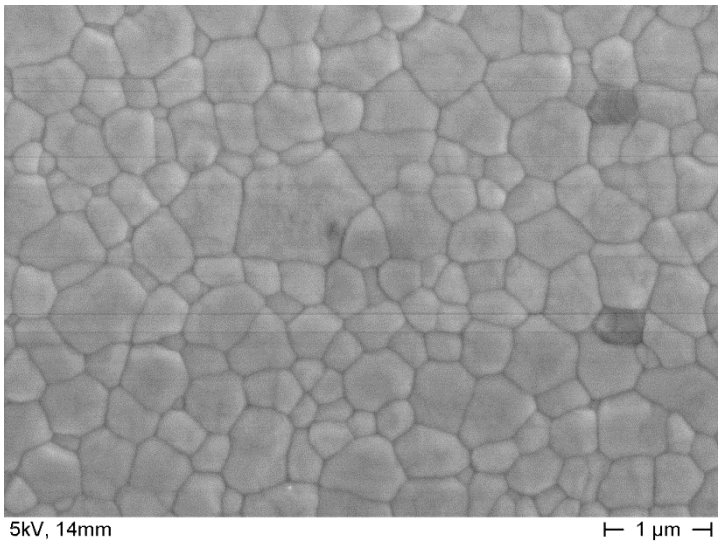


Figure 3.3 SEM micrograph of 3Y-TZP (courtesy of Tom Scott).

3.2 Beam production

Three SiC beams for piezospectroscopic coefficient calibration were manufactured from the as-sintered disc samples. The beams with the dimension of ~25 mm×3.6 mm×1.8 mm were cut from the discs using a precision saw (IsoMet 5000, Buehler, USA). The faces subjected to the tensile loading in the four-point bending jig and used for line scans on the Raman microscope were polished to a 1 µm mirror finish.

3.3 Microstructural Characterization

3.3.1 SEM observation

The ceramic samples were firstly attached to a stub using carbon tabs and coated with a thin layer of Platinum (~2.5 nm thick) using a 208HR Pt coater to become

surface conductive. Silver paint was then applied on sides of the sample to ensure a good conductivity from the sample surface to the stub. Samples were then viewed in SEMs (JEOL 840A, 840F, 5510).

3.3.2 Grain Size Measurement

Polycrystalline alumina samples were thermally etched at a temperature of 1500 ℃ (50 ℃ below the sintering temperature) for 15 min in air. The SiC samples were chemically etched by the Murakami's reagent to reveal the grains, whereas the 3Y-TZP samples received thermal etching during the annealing process. .

The ceramic samples were coated with a 2.5 nm thick Pt layer to become surface conductive and silver was also applied to the sides of the sample to improve the conductivity. The grain size of the specimen was measured from the SEM (JSM 840A and JSM 840F, JEOL, Japan) pictures of the surface using the line intercept method (Mendelson, 1969).

$$G = 1.56\frac{L}{MN}$$

where G is the average grain size; M is the magnification of the SEM pictures; L is the total length of the intercepting lines; N is the counted number of grain boundary

intersections. To convert the two dimensional linear intercepts to the three dimensional, the number 1.56 is a geometrical factor to convert 2D linear intercepts to 3D conditions.

3.3.3 Density Measurement

The Archimedes method was used to measure the density of the specimens. The samples were first put into a drying oven at 100 ℃ for 1 hour to be completely dried out, and their dry weight W_{dry} was measured by an accurate scale. Next they were placed in a beaker filled with boiling distilled water for 1 hour to fill any possible open pores in the samples with water. Then, samples were weighed whilst in water to obtain the wet weight W_{wet}. Later, the samples were weighed after the removal of the surface water by damp paper (W_{damp}). The relative density ρ_R was then calculated by:

$$\rho_R = \frac{100}{\rho_T}\left(\frac{W_{dry}\rho_{H_2O}}{W_{damp} - W_{wet}}\right)$$

where ρ_{H_2O} is the density of water (1.0) and ρ_T is the theoretical density of the material (3.986 for alumina). For each specimen its W_{dry} and W_{damp} were measured three times while the W_{wet} was measured nine times. All measurements were repeated at least three times to give an averaged value.

3.3.4 Indentation

A Vickers indenter was used for making indentations with load of or larger than 9.8 N. A microindenter (MH2, Matsuzawa Co., Japan) was employed for making indentations with load smaller than 9.8 N. For all the indentations, a contact time of 10 s was used as a standard.

The morphologies of the indentation sometimes differed from the standard geometry. Badly split or asymmetrical cracks, spalling or gross chipping could be found. These unusual indentations were generally rejected and only the indentations with primary cracks emanating straightforwardly from each corner were accepted according to Miyazaki and Yoshizawa's (2014) suggestion.

3.3.4.1 Indentation parameters by optical microscope

The indentation diagonal and crack lengths were measured under the optical microscope. At each indentation load, at least 5 indentations were made and both diagonals and all four surface radial crack lengths were measured for each indentation. The indentations were firstly located with a 5× lens, and then measured with 100× lens for better accuracy. For the indentation with crack dimension beyond the viewing scope of the single snap shot, multiple snaps along the crack path were adhered together in order to measure the full crack length (from crack tip to the indentation

center). The dimensions of the indentations with loads below 9.8 N were measured by SEM images.

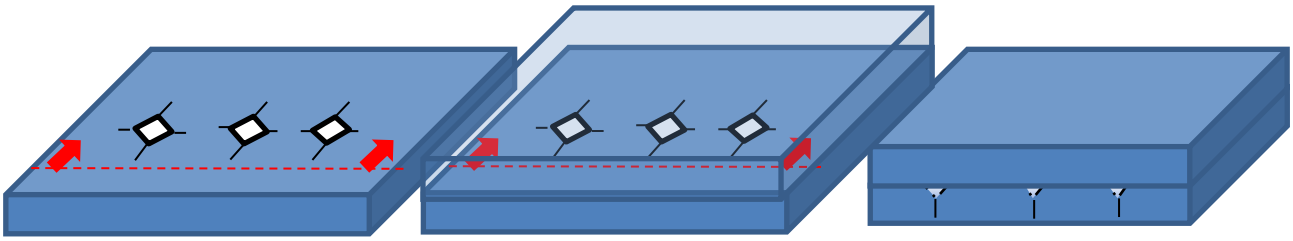
3.3.4.2 Indentation surface profile examination

Surface profiles of indentations at various loads were examined by MicroXAM-5000-pxy 3D surface profiler to investigate the relations between surface profiles and lateral cracking of indentations. The 50× objective lens was used to give the best resolution (with the spatial resolution of 0.22×0.26 μm, and the z resolution up to 2 nm).

3.3.4.3 Serial polishing

To reveal the crack pattern beneath indentations, indentations were first made on polished surfaces of investigated specimen (Figure 3.4a) and another sample was tightly attached to it by wax to reduce the edge rounding effect during polishing (Figure 3.4b) prior to polishing from the edge of the sample to the center of the indentations (Figure 3.4c). The indentations were oriented in a way that the diagonals were parallel to the edges of samples, and the distance between the indentation centers and the starting edge has been preliminarily measured before polishing. For alumina, a 305 mm Φ cloth and 3 micron paste were used for polishing to ensure the polishing rate was low enough to see the developing of crack profile

and gentle enough not to cause damage and to get a better surface finish. Polishing was monitored by micrometer and direct observation of polished cross-section under optical microscope. For SiC, due to the scarcity of time, the samples were polished more aggressively by using the diamond lapping films. The diamond films have the 5 grades (1, 3, 6, 9 and 15 μm) in 203 mm Φ.



(a) (b) (c)

Figure 3.4 Schematic diagrams of serial polishing, with red arrows showing polishing direction. (a) Indentations on surface with radial cracks either parallel or normal to the edge; (b) A protective sample was attached on the indented surface to reduce edge rounding effect; (c) Cracking patterns were revealed when specimens were polished to the center of indentations.

3.3.4.4 FIB milling of the cross-section of the indentation

For 9.8 N indentations, the presence of the lateral cracks was very hard to ascertain from the serial polishing method because the size of the 9.8 N indentations are

relatively small and the indentations can be easily polished away during polishing. The focused ion beam was used to examine the cross-sectional image of the cracks underneath the 9.8 N indentations. The FIB machine (FEI FIB 200) used Ga^+ ions (ion energy: 30 keV) and the milling was performed at 1000 pA beam current. The material around the indentation was milling away slice by slice like serial polishing and the whole sample was tilted at 30 degrees for viewing the crack pattern (Figure 3.5).

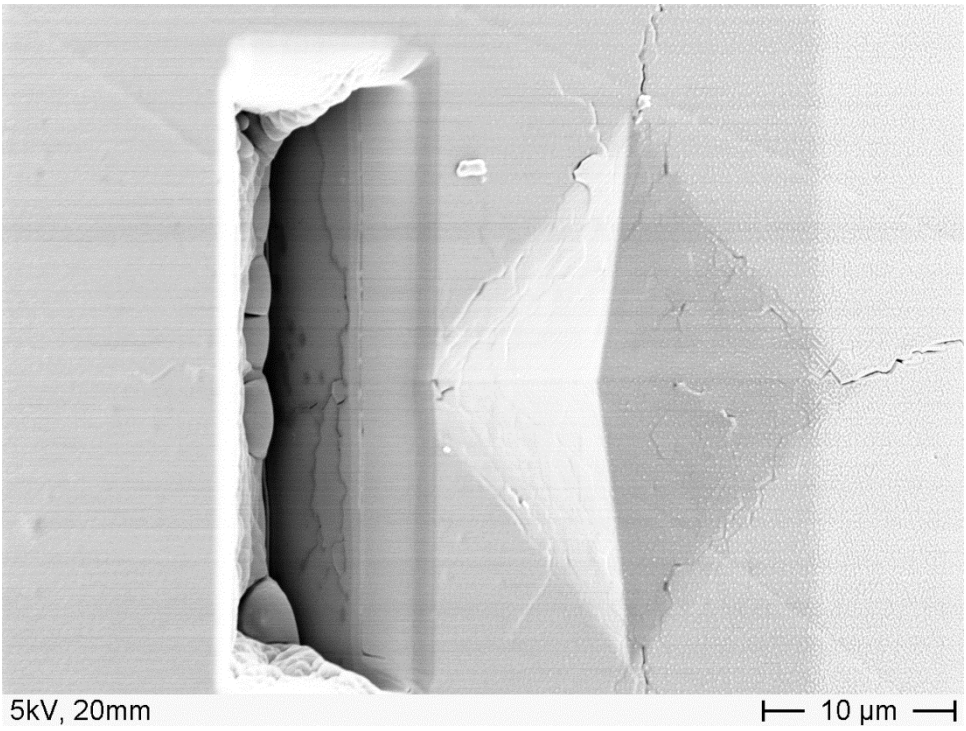


Figure 3.5 SEM image of the lateral crack beneath a 9.8 N indentation, with sample tilted at 30 degrees for viewing.

3.4 Cr^{3+} Fluorescence Microscopy and Raman Microscopy

3.4.1 Raman microscope

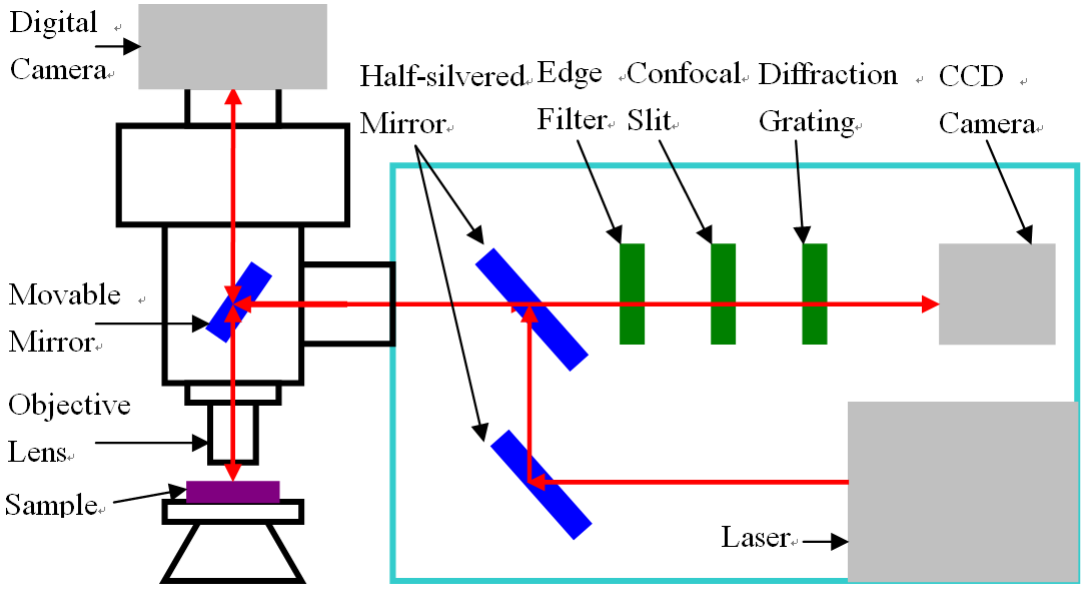


Figure 3.6 Sketch of the construction of the Renishaw Raman Microscope

A Raman microscope (Renishaw, 1000 sieries, UK) integrated with an automated stage (Prior, UK) was used for the fluorescence and Raman test on ceramics (Figure 3.6). The laser source is a 632.8 nm red line He-Ne laser with a power of 50 mW, and a set of Neutral Density Filters (NDF) were used for cutting down the power of the laser to 1%, 10%, 25%, and 50% of the maximum intensity if necessary. The laser was illuminated on the sample surface through an objective lens (5×, 20×, 50× or 100×) and the signal from the sample surface was collected in a back scattered

configuration. The laser light was filtered out and the remaining luminescence was analysed by a diffraction grating and was received by the CCD detector at the very end of the light path.

The control of the noise level of the signal is undoubtedly important. Increasing the time per acquisition and the number of accumulations increases the signal to noise ratio, however, a compromise has to be made between scanning time and the signal intensity as the dropping down of the stage under gravity can become an important issue when the scanning time is longer than 12 hours.

The confocal capability of this Raman microscope further helps to improve the resolution. It was achieved by setting two confocal slits to ensure that the only the signal from the focused region can be collected and most of the out-of-focus signal will be filtered out. One slit is a 10μm wide real slit which sits just before the diffraction grating. The other slit is a virtual slit which is formed by reducing the height of the imaging area on the CCD from 20 pixels to 2 pixels which corresponds to 10 μm in real space. These two slits are normal to each other to form an effective pinhole. Fluorescence and Raman measurements in this study used confocal setting unless otherwise declared. For fluorescence scan on alumina, a 2 s exposure time for each spectrum was used. The signal intensity from the Raman effect was noticeably lower than the Cr^{3+} fluorescence of alumina, therefore a much longer

acquisition time (typically 30s) was normally used on the SiC and TZP to perform Raman line scan.

3.4.2 Scanning strategy

With the aid of the motorised stage, the Raman microscope has line scan, depth scan and in-plane mapping functions.

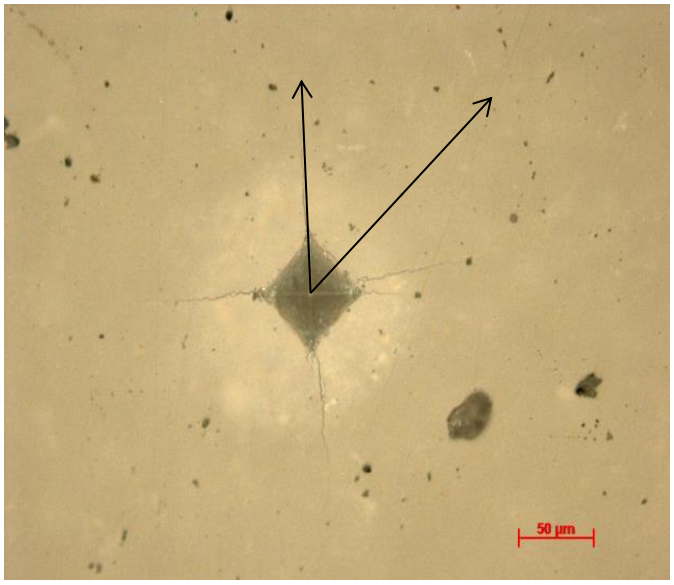


Figure 3.7 Directions of line scans on surfaces of a 49 N alumina indentation

(a) Line scan: with the scanning route drawn on the live image or the still image from single or multiple snaps, the laser was scanned along the designed route and the signal was collected at the same time (Figure 3.7). A 1µm step size was used for all the line scan experiments. A 100× objective lens was used in all the FLM and Raman line tests to ensure a good resolution, unless otherwise declared.

(b) Depth scan (in the z direction): this is also a one-dimensional scanning strategy mainly used for measuring the axial resolution of the laser beam on the specimen. z is defined to be 0 when the laser is on the surface; $z > 0$ when the laser is focused above surface; and $z < 0$ when focused inside the specimen. The step size for the depth scan was 0.5 μm.

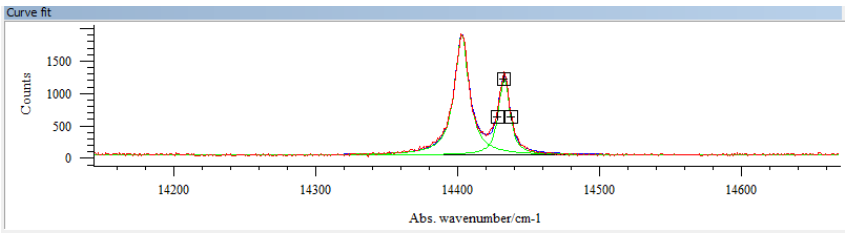
(c) Area mapping scan: for collecting the fluorescence signal from a large area of surface, the area mapping scan was employed. For the sake of good accuracy, a 1 μm step size both in the x and y directions and a snake style scanning pattern were always used. However, compromises have to be made when dealing with large scanning areas as they can be time-consuming to finish.

3.4.3 Fitting methods for alumina spectra

To determine the peak shift and peak width of the characteristic peaks of alumina, it is important to achieve statistical accuracy by fitting appropriate mathematical peak function to the data.

The fluorescence spectrum of alumina outside the indentation plastic zone was well fitted by two mixed Lorentzian and Gaussian functions in the Wire 3.2 software supplied with the Raman microscope (Figure 3.8), and the peak shift of R1 was used

for calculating residual stress. The form of the Lorentzian and Gaussian function is shown in Equation 3.1. The spectrum within the indentation plastic zone was broadened (Figure 3.9a) and the signal was collected from both plastic zone and the elastic surrounding beneath the plastic zone. In this case the four-peak fitting described in the work of Guo and Todd (2011) was used to fit the spectrum with the fitting performed in the Auto2Fit software (7-D Software), and to determine the peak shift introduced by the residual stresses within the plastic zone. According to their findings, two-peak fitting was only performed when the apparent R1/R2 peak area ratio was close to 2.



Curve Name	Centre	Width	Height	% Gaussian	Type	Area
Curve 1	14403.1	11.9436	1865.04	0	Mixed	34990.1
Curve 2	14433.1	9.45473	1190.44	23.8328	Mixed	16321.5

Figure 3.8 Two-peak fitting method in Wire 3.2 software for spectrum of alumina outside the indentation plastic zone。

$$f = a\left[m\frac{2}{\pi}\frac{w}{4(x-c)^2+w^2} + (1-m)\frac{\sqrt{4\ln 2}}{w\sqrt{\pi}}\exp\left(\frac{-4\ln 2(x-c)^2}{w^2}\right)\right] \qquad \text{Equation 3.1}$$

where *a* is the peak area, *m* is the weight of Lorentzian function; *c* is the position of the peak center and *w* is the peak width.

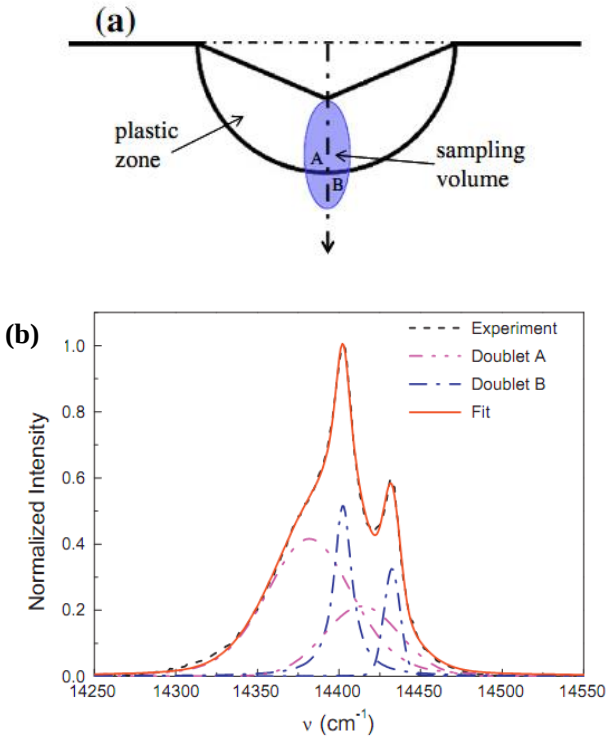


Figure 3.9 (a) Sketch of sampling volume at center of indentation on alumina; (b) four peak fitting method for analysing the broadened peak within sunken area of indentation (Guo and Todd, 2011).

3.4.4 Fitting methods for SiC and TZP spectra

The spectrum of SiC was truncated into the frequency range of 750-830 cm^{-1} to calibrate the PS coefficient of the 789 cm^{-1} peak as the background in this range was relatively flat which favours accurate fitting. Similar to the two-peak fitting in alumina, three Gaussian-Lorentzian curves were used to fit the peaks in the Wire 3.2 software at the frequencies of 767 cm^{-1}, 789 cm^{-1} and 797 cm^{-1} when there was no peak shift (Figure 3.10).

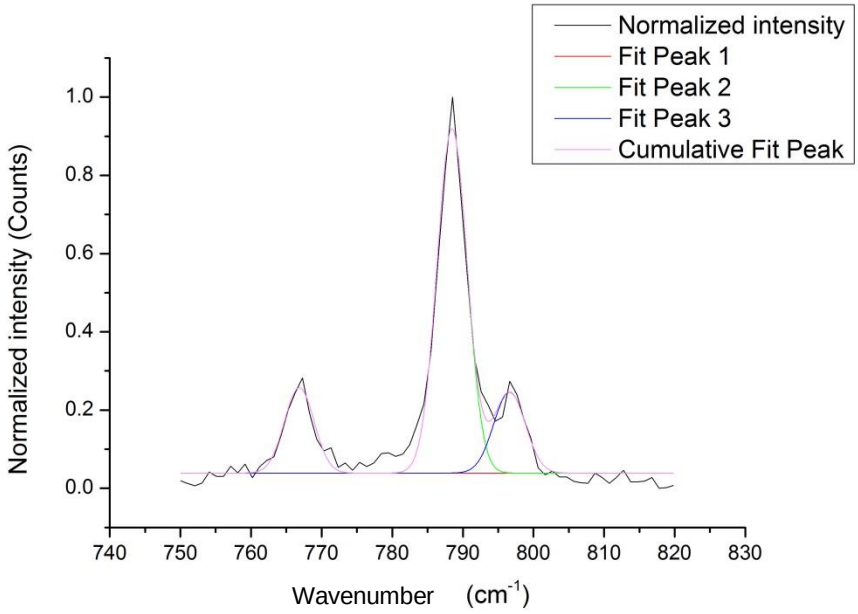


Figure 3.10 Three peaks fitting method for SiC-D spectrum.

Similarly, the TZP spectrum was also fitted with multiple Gaussian-Lorentzian curves (6 curves) in the Wire 3.2 software (Figure 3.11).

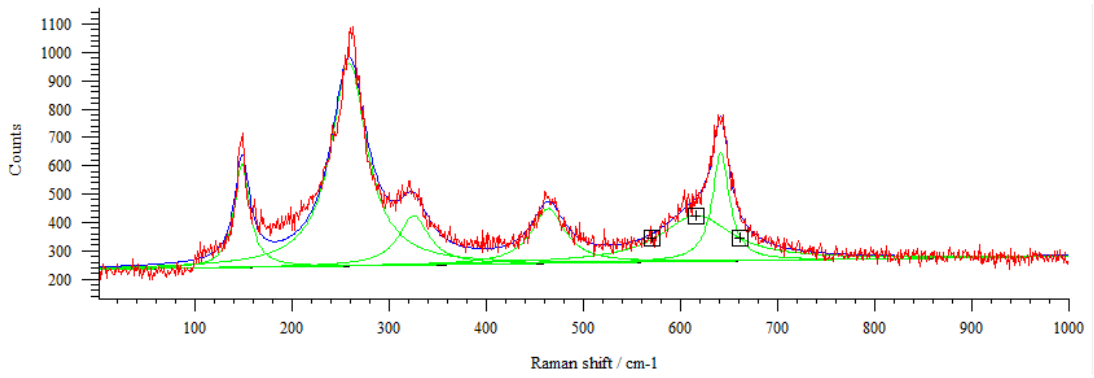


Figure 3.11 Fitting of the 3Y-TZP spectrum with multiple curves.

3.4.5 Four-point bending test for PS coefficient measurement

To measure the PS coefficient of the 6H-SiC A_{1t} peak, a four-point bending jig was designed (Figure 3.12) according to the British Standard BS EN 843-1:2006. The principle of this method has been elucidated by Pezzotti (1999). As the parallelepipedal specimen (with the dimension of ~25 mm×3.6 mm×1.8 mm in this study) was loaded in the standard four-point bending condition, an uniform stress gradient was formed at the central part of the beam with maximum tensile/compressive stress located at the edge of the beam (Figure 3.13 and Equation 3.2). By recording the stresses by the load cell and peak shift by a FLM microscope, the PS coefficient can be directly calculated. The load in the four point bending jig was applied by screwing in the micrometer and a load cell (Omega Engineering, Inc.) was employed to record the load applied. Calibration of the load cell on a mechanical testing machine (Instron, Inc.) showed (Figure 3.14) the perfectly linear relationship between applied load and the gauge reading. This indicates the load cell is ideal for the calibration of the PS coefficient of the SiC Raman peak.

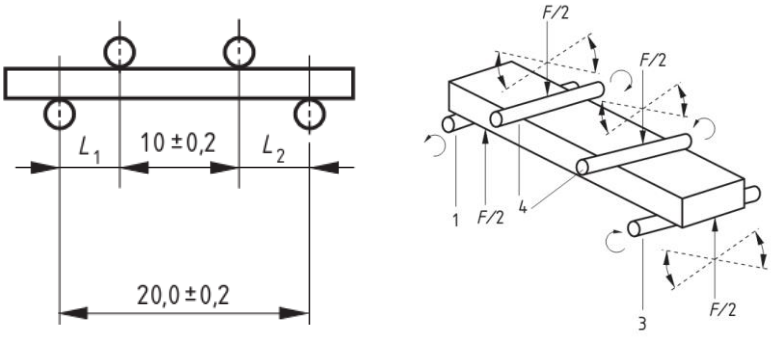


Figure 3.12 Sketch of the point bending loading flexure (British Standard BS EN 843-1:2006).

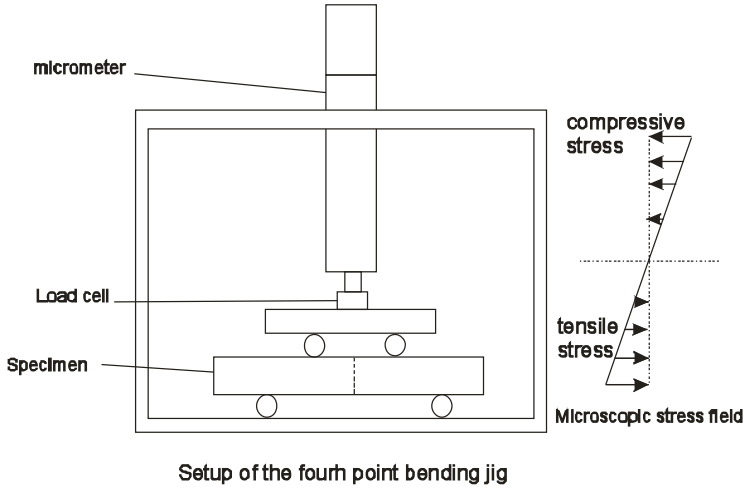


Figure 3.13 Setup of the four-point bending jig and the stress distribution along line scan on the central part of the beam perpendicular to the edge of the beam.

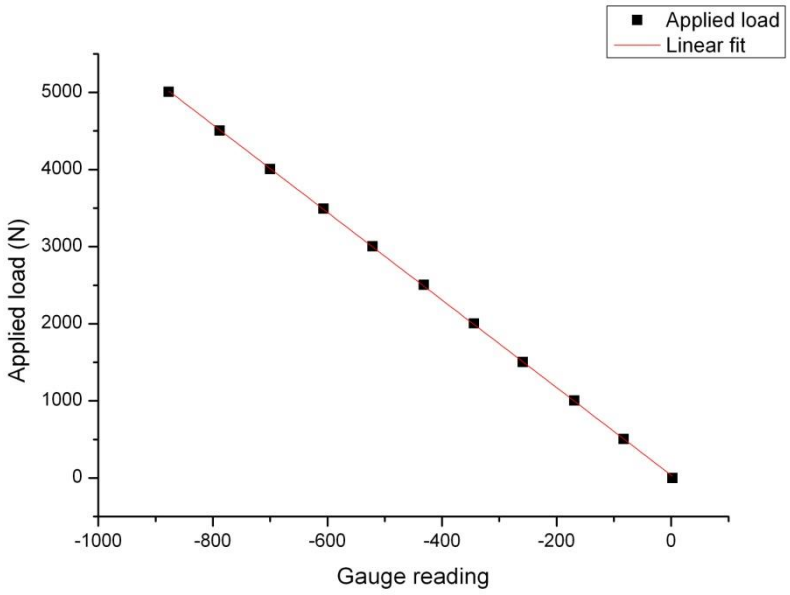


Figure 3.14 Calibration of the load cell.

For four-point bending on a rectangular beam, the maximum tensile stress/compressive would be:

$$\sigma = \frac{3\mathrm{Fa}}{\mathrm{bh}^2} \qquad \text{Equation 3.2}$$

where σ is the maximum tensile/compressive stress; F is the force applied by micrometer; a is the span of the distance between centre of the inner and outer support rollers; b is the width of test piece; h is the thickness of test piece.

References

GUO, S. & TODD, R. I. 2011. Quantitative optical fluorescence microprobe measurements of stresses around indentations in Al2O3 and Al2O3/SiC nanocomposites: The influence of depth resolution and specimen translucency. Acta materialia, 59, 2637-2647.

MENDELSON, M. I. 1969. Average grain size in polycrystalline ceramics. Journal of the American Ceramic Society, 52, 443-446.

PEZZOTTI, G. 1999. In situ study of fracture mechanisms in advanced ceramics using fluorescence and Raman microprobe spectroscopy. Journal of Raman spectroscopy, 30, 867-875.

Chapter 4 Vickers indentation study on alumina

4.1 Introduction

Vickers indentation is widely used in ceramics as a method of measuring fracture toughness of ceramic materials, which is normally calculated by putting the Vickers indentation parameters into a certain equation. Ideally, a universal equation which applies to most ceramics is desired. However, depending on the ceramics, the appropriate equation for fracture toughness measurement varies a lot (Anstis et al., 1981). There has also been consistent discussion of the geometry of the associated cracking and its relationship with the model which is considered as the theoretical background for the calculation for fracture toughness (Lawn et al., 1980). The VIF (Vickers Indentation Fracture toughness) equations proposed by previous researchers in the 1970s and 1980s are still extensively used today, although they contain many uncertainties and potential issues (Section 2.2.5.4). Therefore, a better understanding of the Vickers indentation technique is urgently needed. Alumina was used in this chapter as a model material to understand nearly every aspect relating to Vickers indentations.

For understanding indentations on alumina, this Chapter has set up several key objectives: (1) determine the indentation parameters; (2) understand the residual stress fields in the vicinities of the indentations; (3) understand the cracking pattern beneath indentations; (4) understand the plastic zone of the indentations; (5) investigate the slow crack growth for the indentation cracks; (6) understand the surface profiles around indentations

Finally, with these observations and conclusions, a new Vickers indentation model for the indentation stress field is proposed in Chapter 6 where its validity is also examined on alumina, SiC and TZP.

4.2 Experimental results

4.2.1 Measurement of indentation parameters

The grain size of the sample was measured to be 2.0 μm and the density was measured to be 3.92 g/cm^{-3} (99.0% relative to the theoretical maximum). The Poisson's ratio is assumed to be 0.23 (determined by the ultrasonic methods (Munro, 1997, Astm, 2003)) and this value is used in all calculations.

The indentation parameters of the macro-indentations were measured by optical microscope and are shown below (Table 4.1). For each indentation load, at least 5 indentations were considered. Both diagonals and all four surface radial crack lengths were measured for each indentation. The hardness of alumina was constant (~22 GPa) when the load was above 9.8 N (Figure 4.1).

Table 4.1 Indentation parameters for indentations measured by optical microscope at different loads.

	Half diagonal length (μm)	Radial crack length (μm)
9.8 N	13.8 ± 1.1	38.6 ± 2.2
24.5 N	22.7 ± 0.9	76.4 ± 3.7
49 N	30.3 ± 0.9	120.9 ± 3.9
98 N	48.1 ± 0.6	212.2 ± 10.6

The indentation size effect is a phenomenon in which the hardness measured from the indentation method increases quickly as the load decreases. This effect was only observed in alumina when the load was near or below 9.8 N (Figure 4.1).

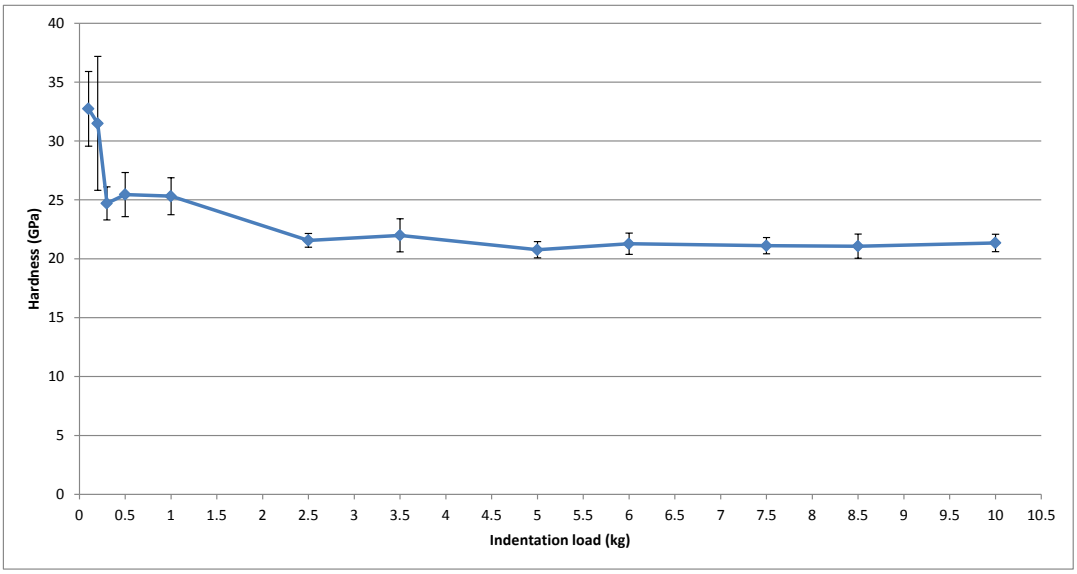


Figure 4.1 Hardness vs. indentation load graph for indentations on Al_2O_3 specimens.

4.2.2 Indentation characterisation

The surface of a 9.8 N indentation was viewed by SEM and the image (Figure 4.2a). The radial cracks emanating from the corners were found to propagate in an intergranular mode (Figure 4.2b).

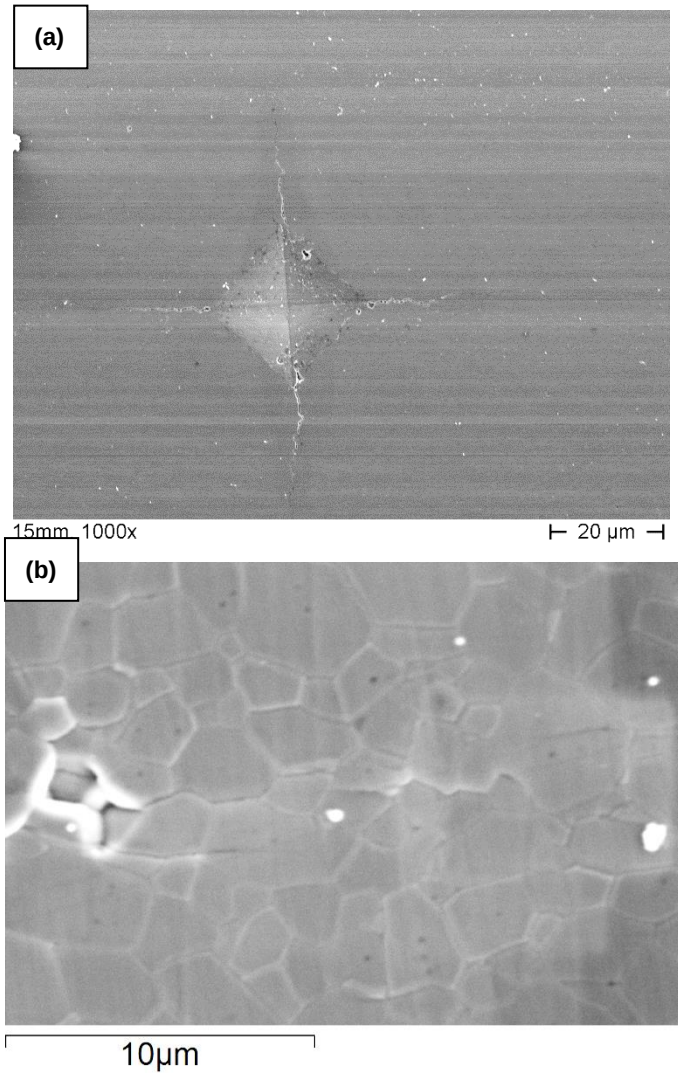


Figure 4.2 SEM micrographs of (a) imprint of 9.8 N indentation, (b) radial crack of 9.8 N indentation.

4.2.3 Residual stress fields around indentations

To characterise the residual stress fields, optical fluorescence line scans and mappings were made around the indentations.

.

4.2.3.1 Line scans

Line scans with the direction shown in Figure 4.3 were carried out on the surface of specimen indented with loads of 9.8 N, 24.5 N and 49 N.

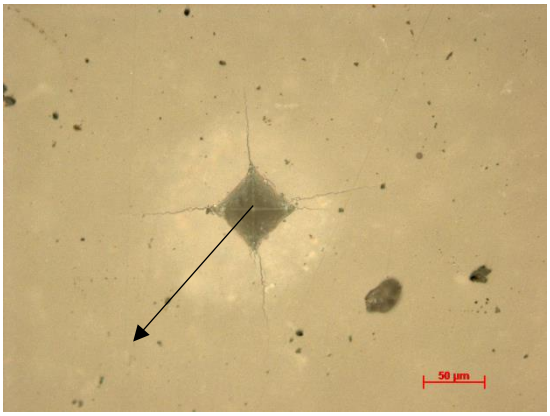


Figure 4.3 Direction of line scan on surfaces of a 49 N indentation.

The spectra collected within the plastic zone were fitted by the four-peak fitting method described in Section 3.4.3 while those outside the plastic zone were fitted by the two-peak fitting method. When to use four-peak fitting or two-peak fitting was determined by the R1/R2 ratio (Guo, 2008). The R1 peak shift was determined after fitting and the peak shift was then converted to the residual hydrostatic stress σ via the PS relationship of the R1 peak (Equation 4.1) in polycrystalline alumina:

$$\Delta\nu = \Pi_m \, \sigma \qquad \text{Equation 4.1}$$

where Π_m = 7.59 $cm^{-1}GPa^{-1}$ (He and Clarke, 1995).

The distribution of the residual stresses along the scanning line was seen by plotting $\Delta\nu$ as a function of the distance from the indentation center. The results (Figure 4.4) show that the residual stress decreases within the distance from the indentation center and is much larger within the radius of the plastic zone which is approximately equal to half of the indentation diagonal length.

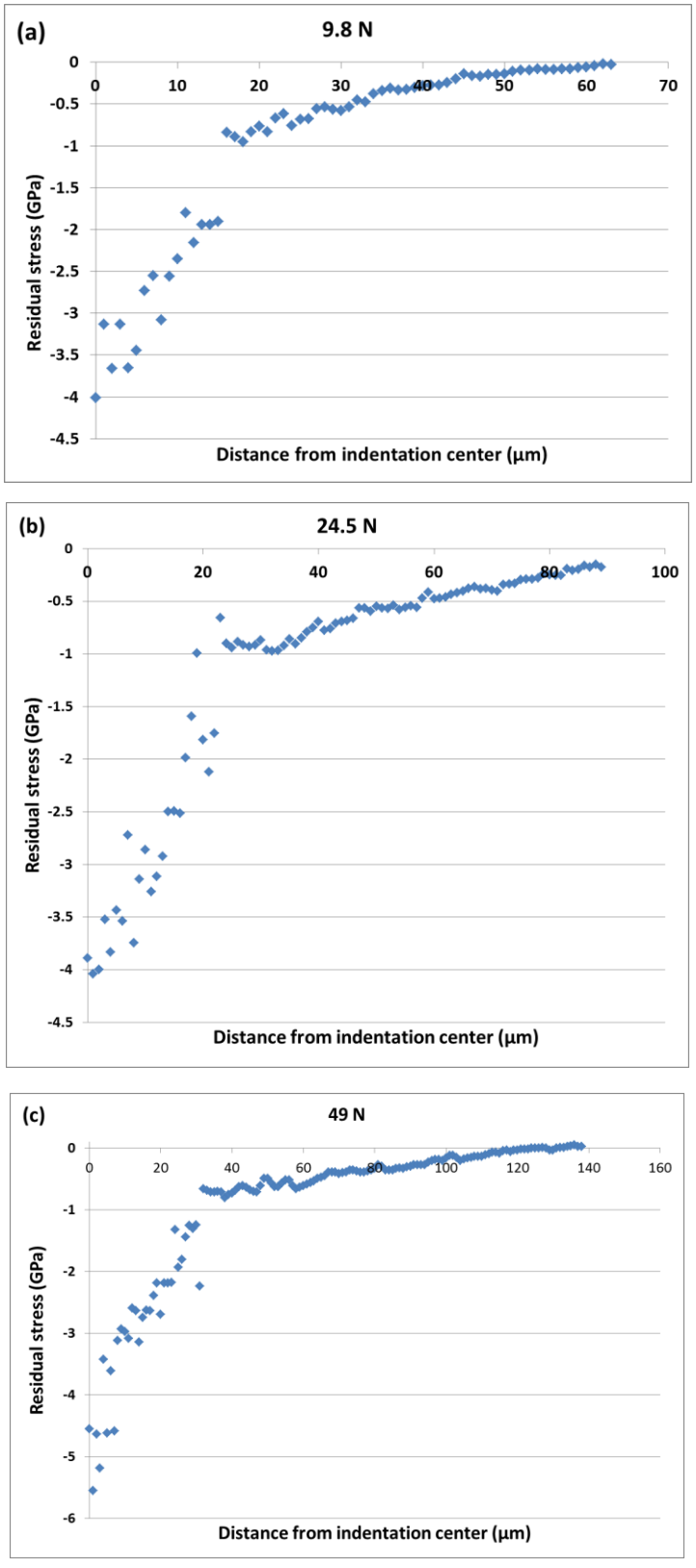
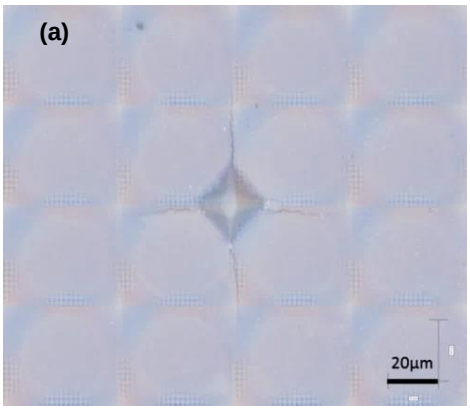
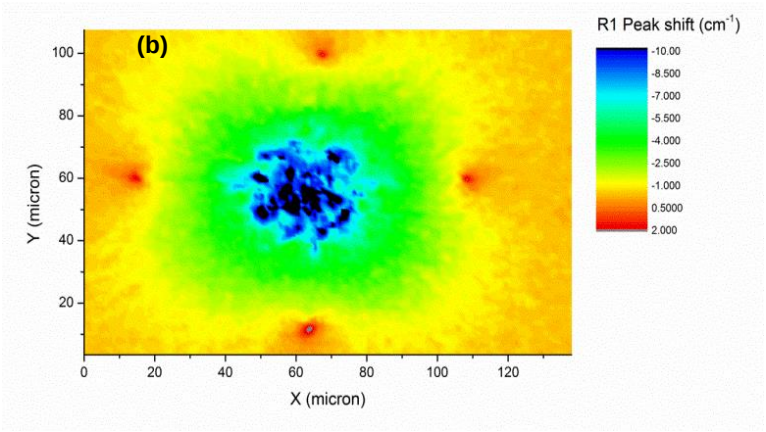


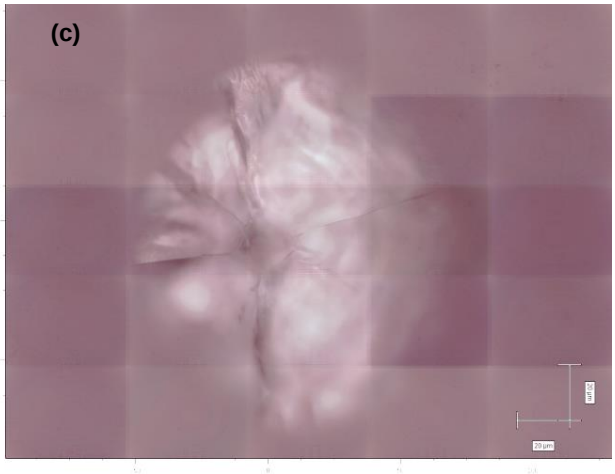
Figure 4.4 Distribution of the residual stresses along the scanning lines on (a) 9.8 N, (b) 24.5 N and (c) 49 N indentations.

4.2.3.2 Fluorescence mapping for 9.8 N indentations

Peak position fluorescence maps of the 9.8 N indentations (Figure 4.5) on alumina and single crystal sapphire indicate the stress distribution around the indentation. All the spectra collected are fitted with two peaks which means the peak position is not accurate within the indents where four peak fitting was found to be necessary for accurate measurements. However, information outside the indentation imprint can be accurately obtained and the stresses in the vicinity of the indentation are in a compressive stress state. From the mapping result on alumina, the tensile stress field around the radial crack tips can be seen clearly. There is also a zone encircling the indentation on the sapphire mapping, which indicates a residual tensile stress and is very likely the front of the subsurface lateral crack (Limpichaipanit, 2008). Figure 4.5d also indicates that the lateral crack connected the radial crack tip and the contour of the lateral crack was approximately circular. However, distance along radial crack direction (A) on the lateral crack loop (~130.8 µm) was found to be slightly longer than that (~124.7 µm) from the direction at the 45 degrees to the radial crack direction (B). This indicated that the lateral crack connects the radial crack tips and its shape is close to circular but has slightly larger radius along the direction of the radial crack.


(a)
20µm


(b)
R1 Peak shift (cm-1)
-10.00
-8.500
-7.000
-5.500
-4.000
-2.500
-1.000
0.5000
2.000
Y (micron)
X (micron)
0
20
40
60
80
100
120


(c)

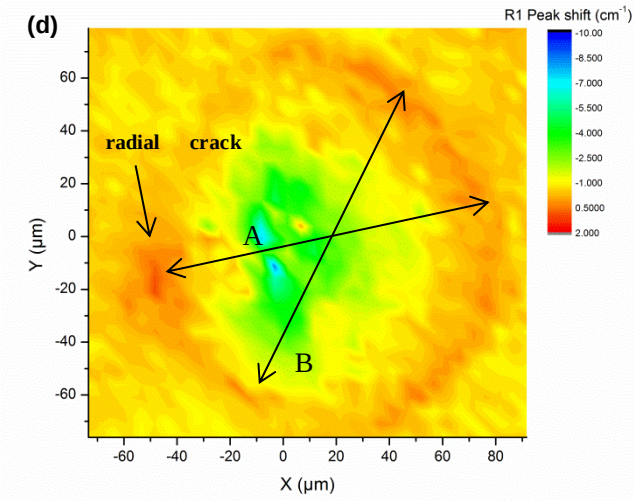


Figure 4.5 Optical image of 9.8 N indentations on (a) polycrystalline alumina and (c) sapphire; and the corresponding peak position shift (in unit of cm^{-1}) maps for (b) alumina and (d) sapphire indentations.

4.2.4 Post-indentation growth measurements from the FLM method

As mentioned in the literature review (Section 2.2.5.4), it is very important to define the position of the radial crack tip and thus the radial crack length. The FLM method offers a way to identify the radial crack tip and the slow crack growth behaviour of the radial crack.

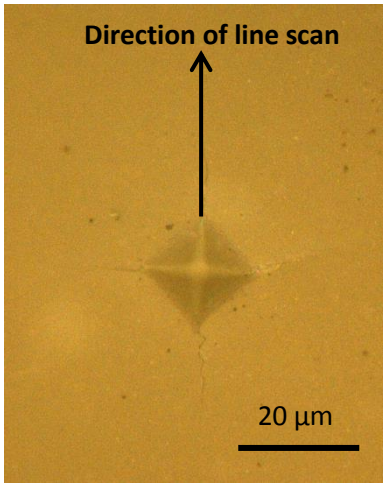


Figure 4.6 Line scan direction along a radial crack of a 9.8 N indentation on polycrystalline alumina.

FLM line scans were made along the radial crack of a 9.8 N indentation (Figure 4.6) and the line scans were repeated after the indentation was made to monitor the change in the residual stress field. Because there are 6-15 minutes set-up time and at least 2-5 minutes scanning time for the FLM line scan, the indentation crack length could not be measured by FLM immediately after the indentation. It was found that the radial cracks experienced post-indentation crack growth. Figure 4.7 shows the position of the maximum positive peak shift moved further from the indentation center as time went on.

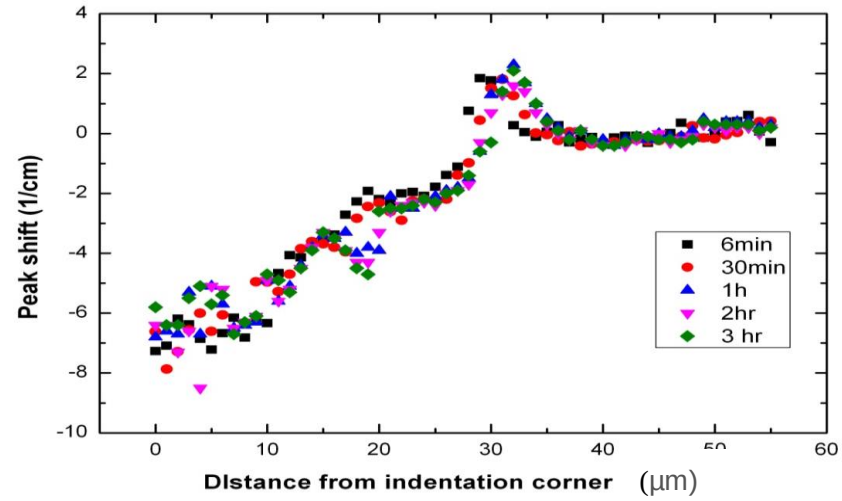


Figure 4.7 Peak shift along line scan at different times after 9.8 N indentation on polycrystalline alumina.

The mode I crack tip stress field has been described as (Irwin, 1957):

$$\sigma_{rr} = \frac{K_I}{\sqrt{2\pi r}} cos\frac{\theta}{2}\left[1 + sin^2\frac{\theta}{2}\right]$$

$$\sigma_{\theta\theta} = \frac{K_I}{\sqrt{2\pi r}} cos^3\frac{\theta}{2}$$

$$\tau_{r\theta} = \frac{K_I}{\sqrt{2\pi r}} sin\frac{\theta}{2} cos^2\frac{\theta}{2}$$

where r and θ are polar co-ordinates, with $\theta = 0°$ representing the direction of crack propagation; K_I is the stress intensity factor; σ and τ are normal and shear stresses, respectively. The major part of the residual stress sampled along the direction of the crack propagation $(\theta = 0°)$ and when $\theta = 0°$, the distribution of the residual stress sampled by laser, σ, $(= \sigma_{rr} + \sigma_{\theta\theta})$, as a function of the distance from the indentation tip, *r,* is plotted in Figure 4.8. This figure shows that the mean

stress ahead of the crack increases to infinity as r tends to 0. The crack tip position is therefore located at the position of maximum tensile stress.

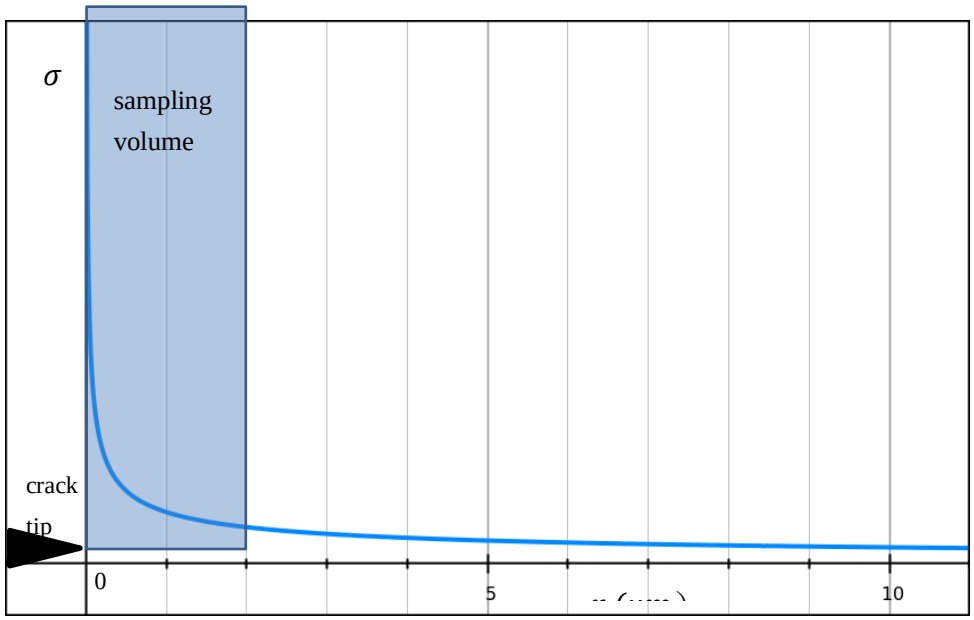


Figure 4.8 Distribution of the total residual stress as a function of the distance from the indentation tip (blue curve) and the sampling volume of the laser beam (area filled with blue colour.

The diameter of the laser beam is around 2 micron and the signal collected therefore comes roughly from within 1 micron from the laser beam center. As seen from Figure 4.8, the total residual stress sampled will reach its maximum when the laser beam position is 1 micron behind of the crack tip on the line scan direction. Therefore, we

assume the crack tip is 1 micron behind the maximum positive R1 peak shift, and the distance from the indentation center to the radial crack tip, *c*, was then measured.

The radial crack length on a 49 N alumina indentation (Figure 4.9) was measured by the method described above and it also shows radial crack length increased with time from 135 µm at the shortest possible measuring time after indentation to 145 µm long after indenting.

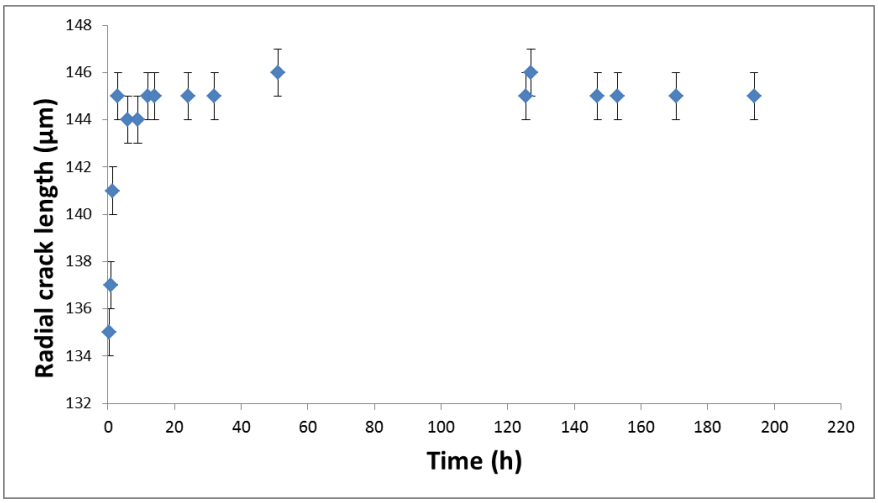


Figure 4.9 Length of a radial crack at different time after 49 N indentation on polycrystalline alumina.

It can be seen from the results that, for polycrystalline alumina, the radial crack grew quickly in its first 3 hours after indentation and then stopped growing. Another similar test was run on a 49 N indentation on single crystal ruby. As ruby is more transparent,

the growth of the lateral crack can be monitored at the same time. Ruby was selected over sapphire as its richer Cr^{3+} content can significantly reduce sampling time in FLM scans.

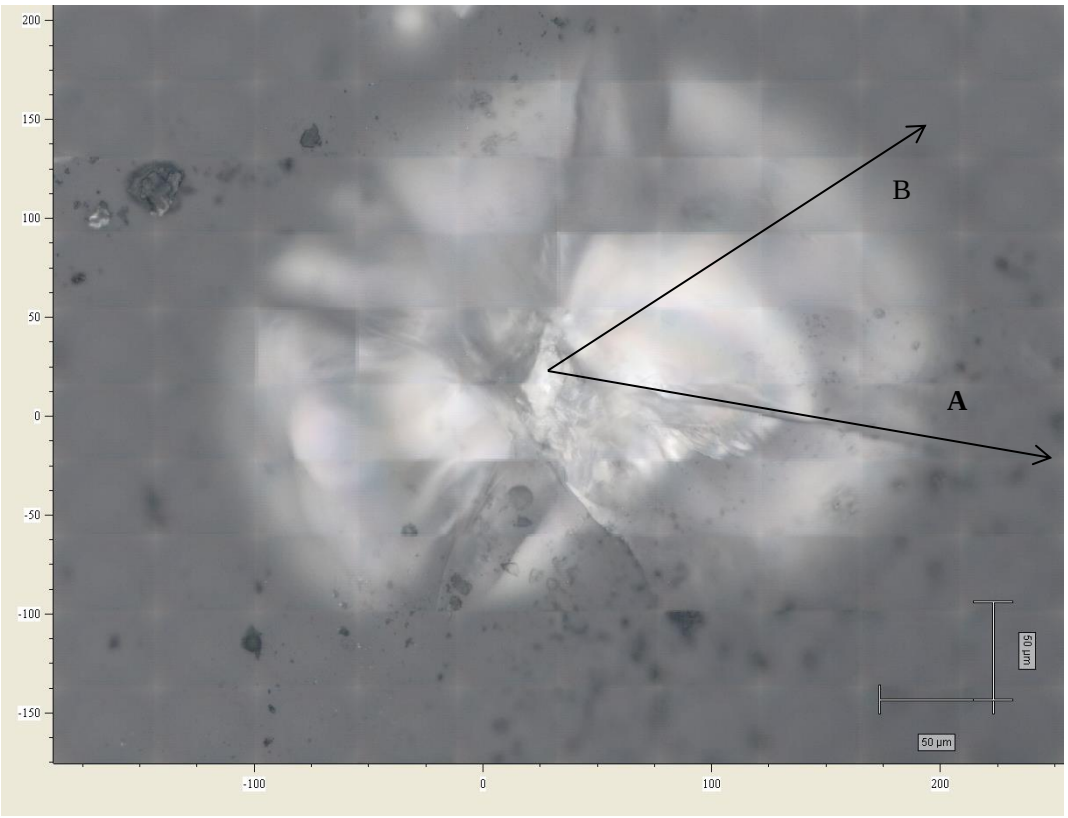


Figure 4.10 Scan directions (A and B) on the surface of a 49 N indentation on ruby.

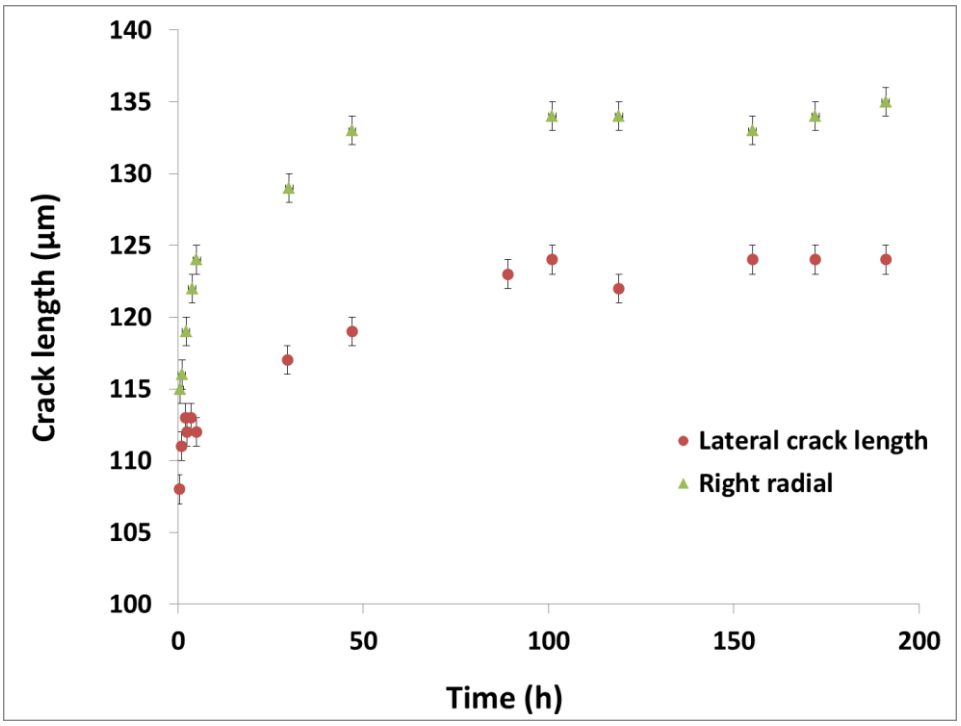


Figure 4.11 Lateral (B) and radial crack (A) lengths as a function of time.

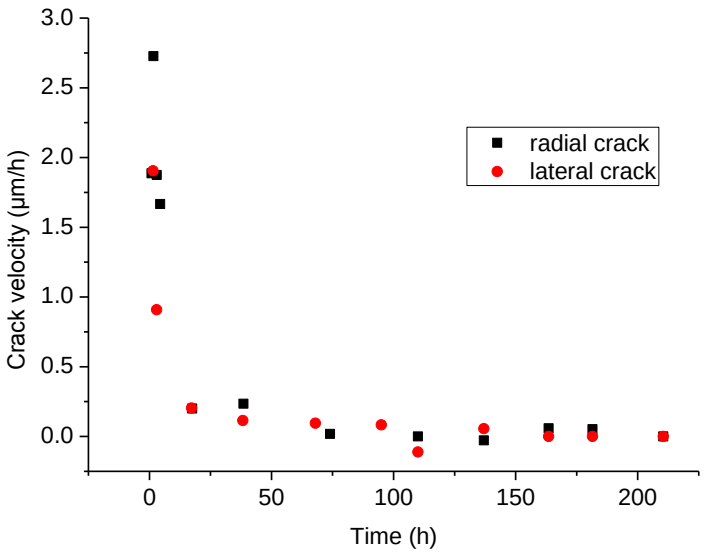


Figure 4.12 Plot of crack velocity vs time for radial and lateral crack.

The crack length measurements from the two scanning directions (A and B on Figure 4.10) have been shown in Figure 4.11 and the results indicate that both lateral and radial cracks grew initially rapidly after making the indentation and then the growth plateaued. The crack velocity - time plot of the results is shown in Figure 4.12 to better compare the velocities of the two cracks. The crack velocity is estimated by finding the velocity between two consecutive data points in the Figure 4.11. The lateral crack was observed to have a similar growth rate to the radial crack (Figure 4.2) and both terminated nearly at the same time which agrees with the finding of Cook and Liniger (1993) on glass. This observation will be used in Chapter 6 to be an important assumption of the model.

4.2.5 Radial crack length measurements from the FLM method

It has been demonstrated above that the radial crack length can be measured by the line scan along the radial crack. Here the similar lines scans were made on the radial cracks of 9.8-98 N indentations on alumina using the FLM method. For each indentation load, the same indentations as were measured in Section 4.2.1 were used. The slow crack growth of the radial crack has been identified previously. Therefore, to minimise uncertainties in the crack length measurement from this source, all the cracks were measured 7 days after indentation.

The results are summarized in Table 4.2 in comparison with the results from Table 4.1. The radial crack lengths from the FLM method were found to be significantly longer than the values measured from optical microscopy (OM). The measurements from FLM and OM were actually performed on exactly the same indentations; therefore this difference must come from the resolution limit of FLM and OM methods and the FLM appears to have better resolution than OM. The crack length difference as a percentage of the result (in the range of 11% - 26%) from OM also increased as the indentation load decreased. This indicates the resolution limit of the OM method affected the small crack results more than from long cracks. The fact that the results measured by FLM method were longer than those measured by the OM method will be further discussed in Section 4.3.3.

Table 4.2 Indentation radial crack lengths measured by FLM line scan and OM at different loads on polycrystalline alumina measured at 7 days after indentation.

Indentation load	Radial crack length measured by FLM (μm)	Radial crack length measured by OM (μm)	crack length difference in % of the OM results
9.8 N	48.5 ± 2.7	38.6 ± 2.2	26%
24.5 N	91.5 ± 3.1	76.4 ± 3.7	20%
49 N	137.0 ± 4.4	120.9 ± 3.9	13%
98 N	235.7 ± 5.8	212.2 ± 10.6	11%

4.2.6 Radial crack length measurements from the SEM method

The radial cracks of a 9.8 N alumina indentation were measured by both SEM and OM methods. Figure 4.13 is an SEM image taken in the vicinity of a radial crack tip of a 9.8 N indentation on alumina. A discontinuity of the crack path had been found near the radial crack tip, and this is possibly because the Pt coating has been deposited into the fine opening near the crack tip, which makes the radial crack length measurement difficult. For the same indentation (Table 4.3), the radial crack length by SEM methods on average is 1.8 μm longer than by OM, but still much less than the average radial crack length from FLM at 9.8 N. This will be discussed in Section 4.3.3.

Table 4.3 Comparison of the lengths of the radial cracks of a 9.8 N indentation measured by SEM and OM

	Measured from SEM (μm)	Measured from OM (μm)
Top radial	41.7	35.7
Bottom radial	33.8	33.6
Left radial	35.9	34.9
Right radial	36.8	40.6
Mean radial crack length	38.0	36.2

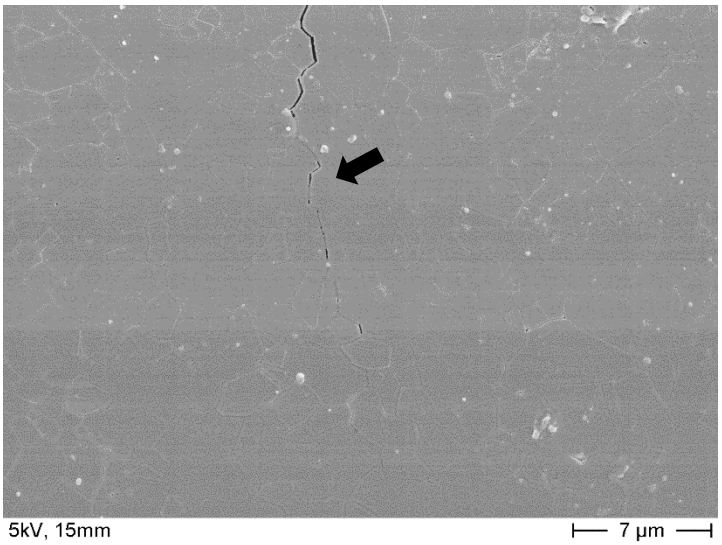


Figure 4.13 Radial crack tip of a radial crack of a 9.8 N indentation, showing the apprent discontinuity of the crack path near the radial crack tip.

4.2.7 FIB milling of the 9.8 N indentations

For 9.8 N indentations, the presence of the lateral cracks was very hard to ascertain from the serial polishing method. The focused ion beam was used to examine the cross-sectional image of the cracks underneath the 9.8 N indentations (Figure 4.14). Two 9.8 N indentations were investigated. Lateral cracks were found beneath 9.8 N indentations and the average depth of the lateral cracks was 12.4 ± 1.3 µm.

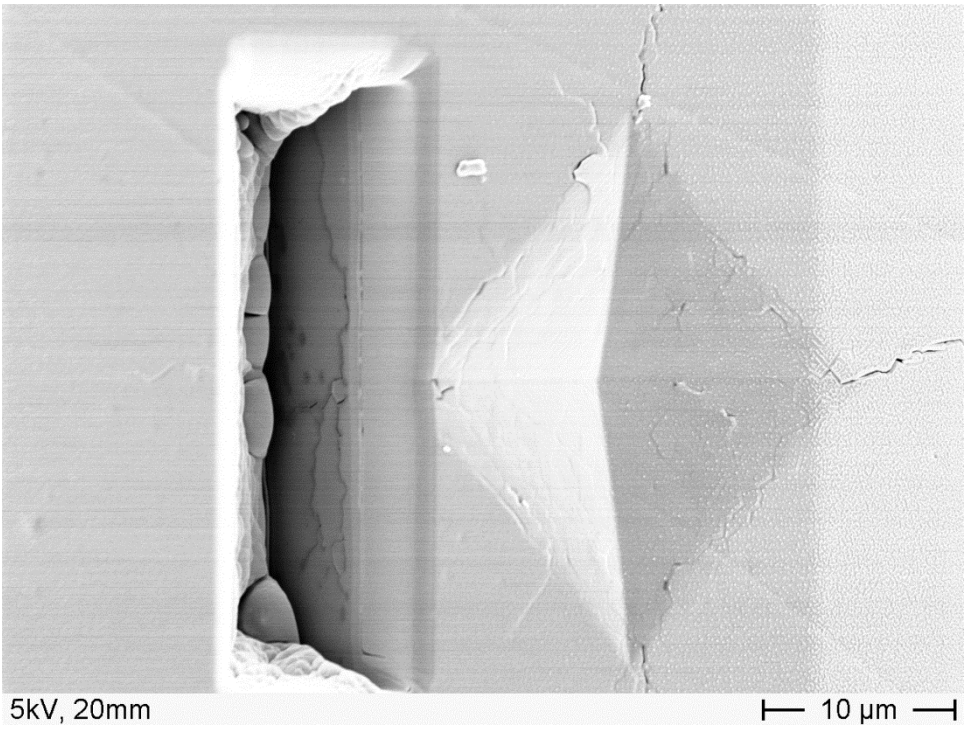


Figure 4.14 SEM image of the lateral crack beneath 9.8 N indentation, with sample tilted at 30 degrees for viewing.

4.2.8 Serial polishing of alumina indentations

In this section, serial polishing was used to verify the subsurface cracking of 9.8-98 N alumina indentations. Ideally, it would be desirable to record every different stage of the serial polishing to get a 3-D picture of the lateral cracking. However, for 9.8 N, 24.5 N, 34.3 N and 98 N indentations, only pictures of some intermediate positions were finally obtained (Figure 4.15), while a full series of cross-section pictures of 49 N indentation has been obtained (Figure 4.16) and shows the half-penny crack system.

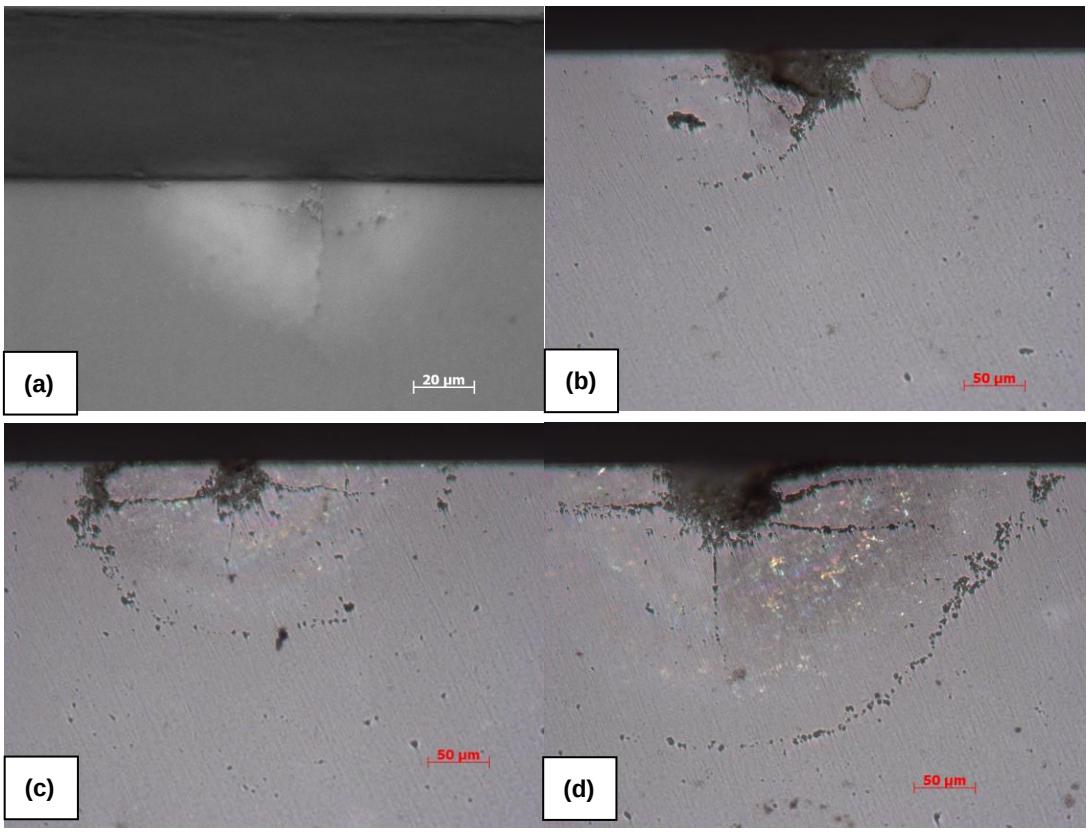
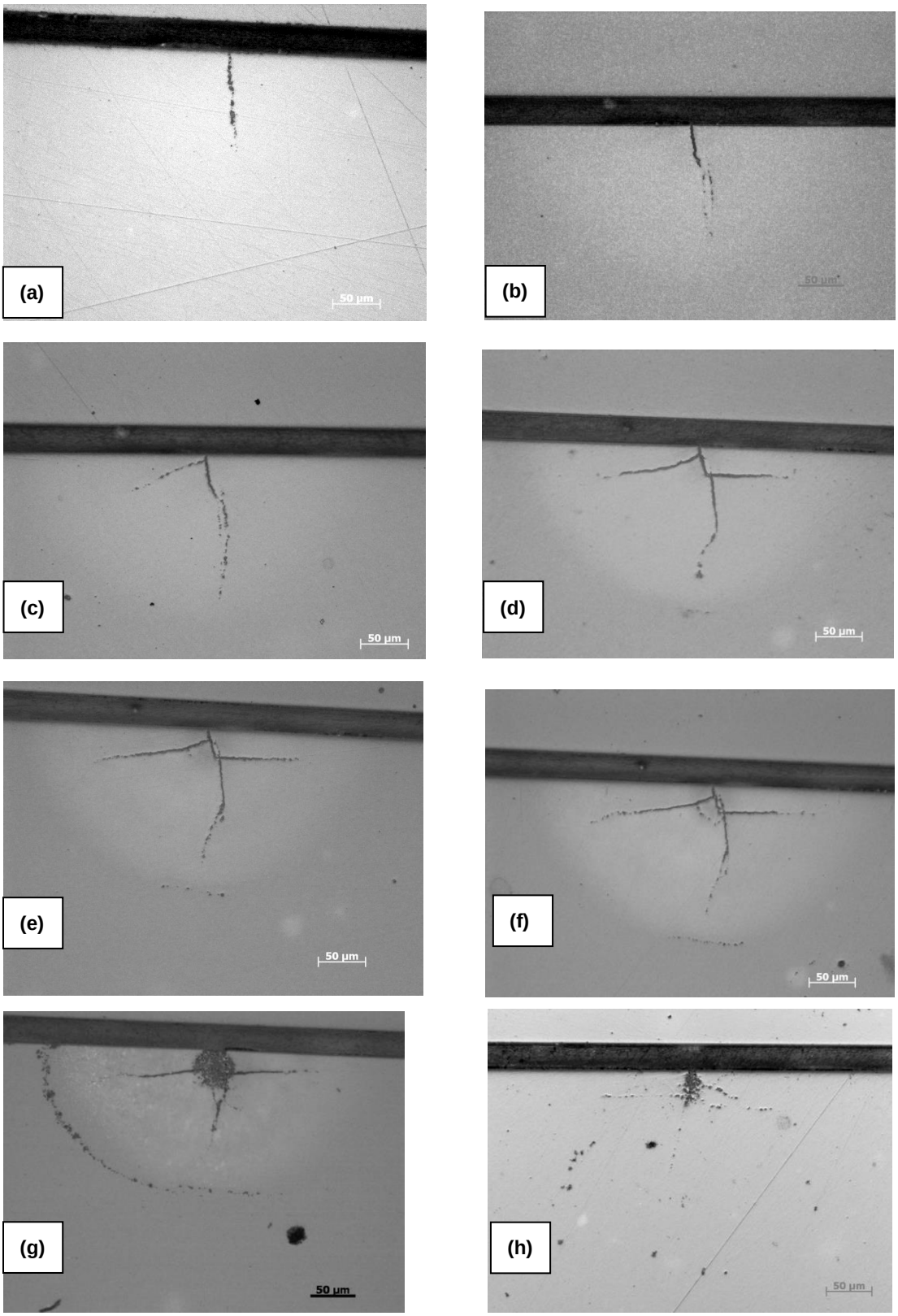


Figure 4.15 Optical micrographs of crack patterns beneath (a) 9.8 N, (b) 24.5 N, (c) 34.3N (d) 98 N indentations.


(a)
50 µm
(b)
50 µm
(c)
50 µm
(d)
50 µm
(e)
50 µm
(f)
50 µm
(g)
50 µm
(h)
50 µm

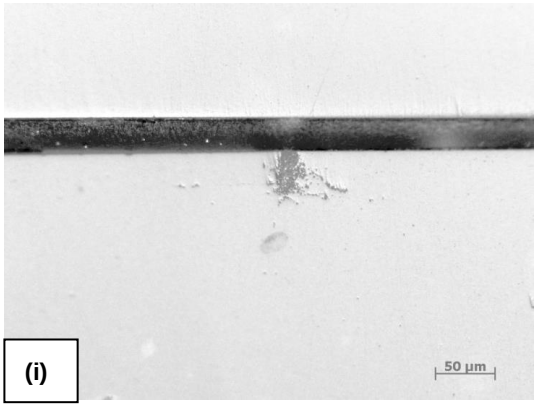


Figure 4.16 Sequential micrographs of the cross section of the 49 N indentation at different stages of the serial polishing.

Although the images do not make complete 3D representations of the subsurface cracking of 9.8 N, 24.5 N and 98 N indentations, the appearance of the hazy zone (Figure 4.15a) and the annular trace of the radial crack front (Figure 4.15d, Figure 4.16g) suggest that the half-penny crack system applies to 9.8 N, 24.5 N and 98 N indentations on alumina, in which case no transformation from the Palmqvist crack system to the half-penny crack system in the load range of 9.8 N - 98 N is evident. A SEM image of the cross-section of another 49 N indentation also clearly shows the radial crack has a shape close to a semicircle (Figure 4.17). However, it can be seen from the images (Figure 4.15, 4.16 and 4.17) that the serial polishing has significantly increased the radial crack length compared with the radial crack length measured on the unsectioned specimen. For instance, the average radial crack length of

unsectioned 49 N indentations was 120.9 ± 3.9 µm, however, measured on the Figure 4.16g the radial crack length at the surface was 185.1 µm.

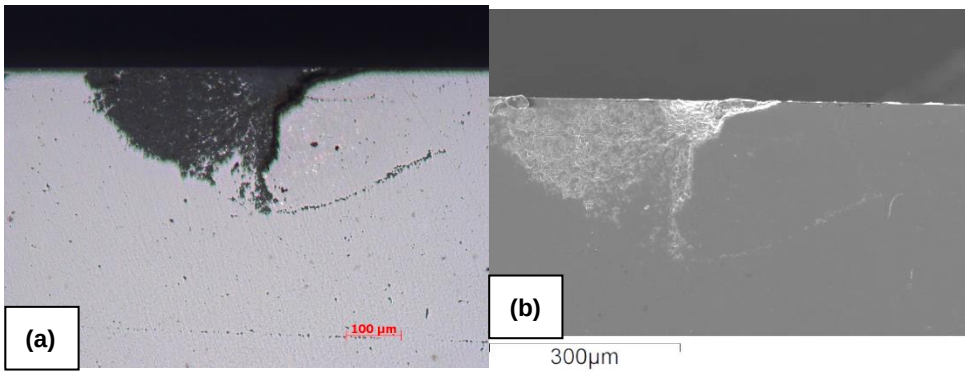


Figure 4.17 (a) Optical image of cross-section appearance of 49 N indentation (b) corresponding SEM picture of cross-section, showing evidence of elongated half-penny cracks.

The depths of the lateral cracks can be directly estimated from the images during serial polishing. For 49 N and 98 N indentations, the average depths of the lateral cracks were measured from several indentations for each load. For 24.5 N, only one indentation shown in Figure 4.15b was considered. The left branch of the lateral crack shown in Figure 4.15b was measured, although the falling out of the material has been found on the right hand side of the indentation. For the 9.8 N indentations, the depths of the lateral cracks were measured from the FIB polishing described in Section 4.2.7. Table 4.4 summarises the lateral crack depths measured from the

cross-section images and they are close to but slightly shorter than the half diagonal lengths for different indentation loads.

Table 4.4 Lateral crack depth for different indentation loads measured from serial polishing or FIB trench milling on alumina.

	Average Lateral Crack Depth (μm)	Half diagonal length (μm)
9.8 N	12.4 ± 1.3 (measured by FIB)	13.8 ± 1.1
24.5 N	21.6 ± 1.0 (measured by serial polishing)	22.7 ± 0.9
49 N	26.1 ± 3.3 (measured by serial polishing)	30.3 ± 0.9
98 N	43.1 ± 7.2 (measured by serial polishing)	48.1 ± 0.6

In conclusion, (1) the radial-median crack system was found in the 9.8-98 N alumina indentations; (2) lateral cracks were also found for all the indentations, and the their depths were measured from the cross-sectional images and were found close to the half diagonal lengths.

4.2.9 FLM mapping on the cross-section of a 98 N indentation.

The breadths of R1 fluorescence peaks have been shown to be sensitive to the extent of the plastic deformation because dislocations and twinning introduce large stress variations thereby broadening the peak width in the spectrum (Wu et al., 2008). An R1 peak width map derived from the FLM mapping therefore can be used to interpret the location and the extent of the plastic deformation. The FLM mapping was performed on the cross-section of a 98 N indentation (Figure 4.18). The plastic zone (Figure 4.18) is found to be tightly confined to a region which is approximately semi-circular and with no evidence of the plastic deformation zone outside this region. The peak width map also shows the shows the size of the plastic zone (~92µm, measured directly from the peak width map) approximates to the size of the 98 N indentation diagonal length (96 µm). This will be discussed in Section 4.3.1.

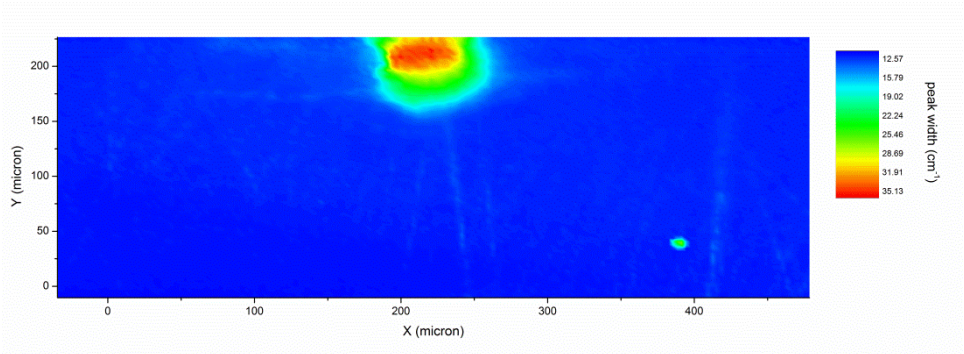
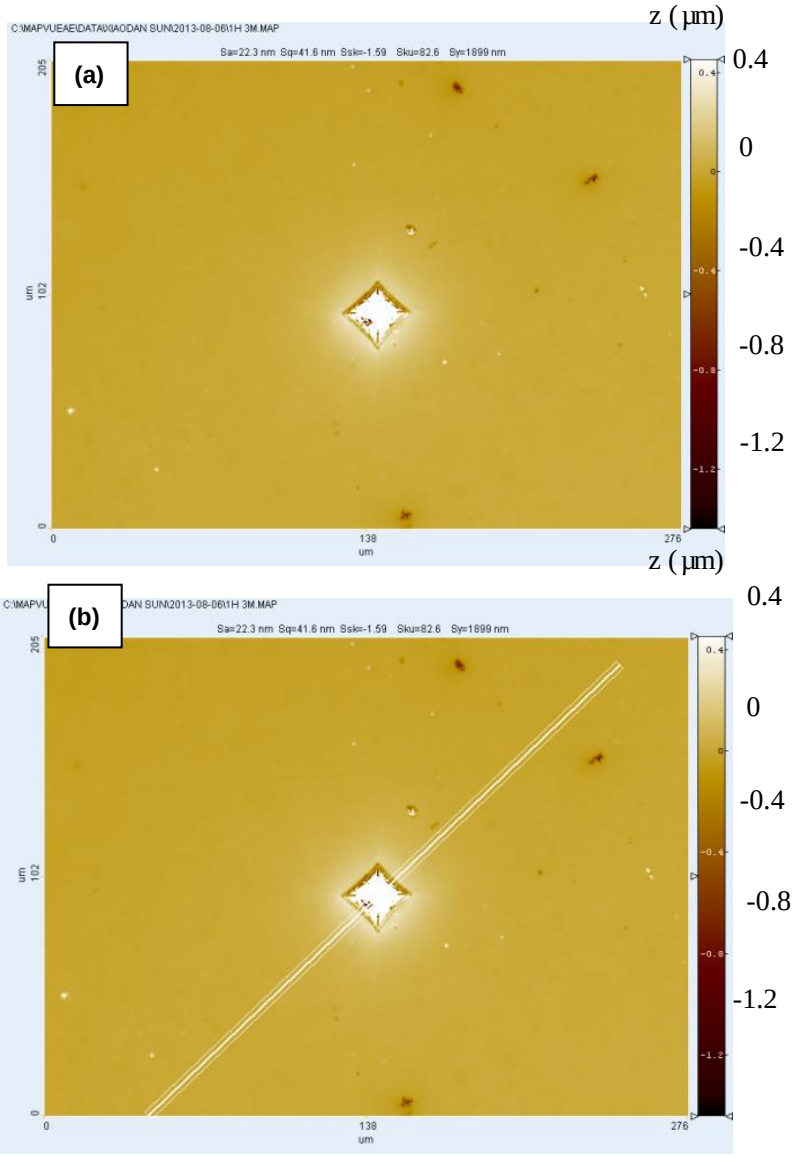
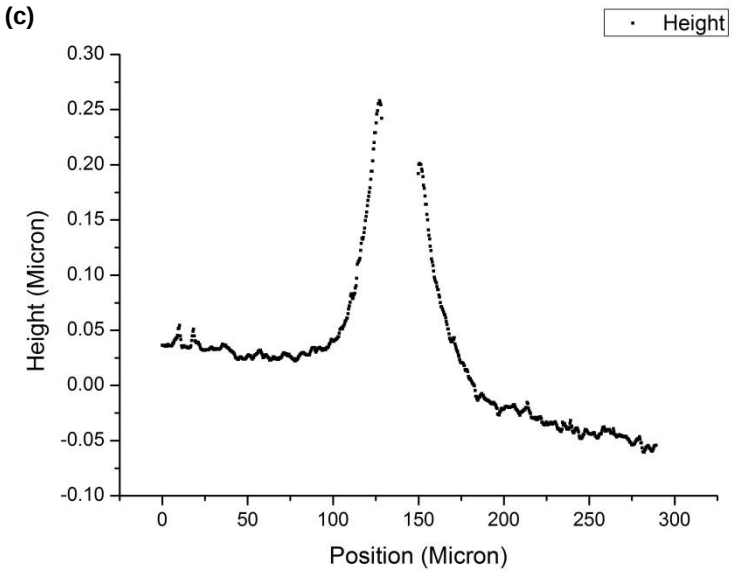


Figure 4.18 Peak width map of a FLM mapping on the cross-section of a 98N indentation.

4.2.10 Surface profile around the Vickers indentation

In this study, MicroXAM-100, an interferometric microscope, is used as this technique is accurate enough to measure the surface profiles of indentations and is rapid. The surface profilometer, MicroXAM-100, has a spatial resolution of 0.22×0.26 μm, and z resolution of 2 nm. Indentations were made on the alumina surface with different loads and the surface profile was measured by the surface profilometer. A surface profile of the line across the midpoints of and normal to the indentation edges (Figure 4.19b) can be easily obtained from the mapping result (Figure 4.19a). The line scan profile (Figure 4.19c) was also imported into Origin to subtract the baseline (Figure 4.19d) if there was a tilt on the surface.


z (µm)
0.4
0
-0.4
-0.8
-1.2
(a)
Sa=22.3 nm Sq=41.6 nm Ssk=-1.59 Sku=82.6 Sy=1899 nm
205
102
0
um
0
138
276
um
z (µm)
0.4
0
-0.4
-0.8
-1.2
(b)
Sa=22.3 nm Sq=41.6 nm Ssk=-1.59 Sku=82.6 Sy=1899 nm
205
102
0
um
0
138
276
um


(c)
Height
0.30
0.25
0.20
0.15
0.10
0.05
0.00
-0.05
-0.10
Height (Micron)
0
50
100
150
200
250
300
Position (Micron)

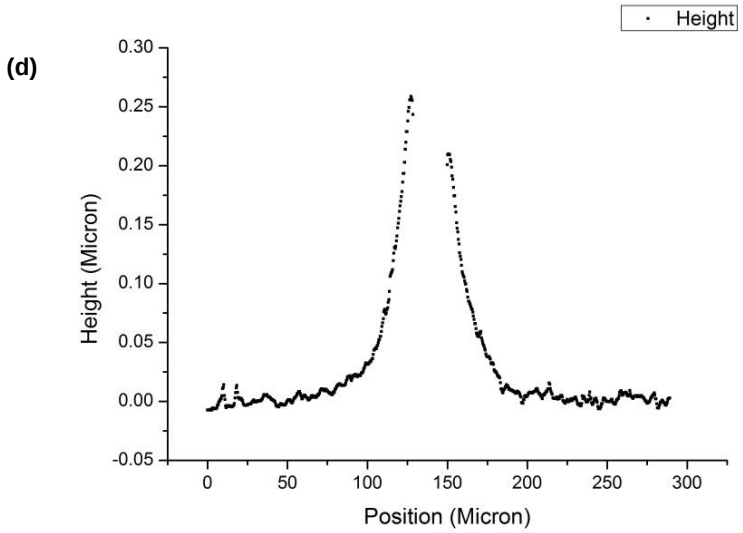


Figure 4.19 (a) Mapping of the surface profile of 9.8 N indentation and (b) direction of the line scan on the mapping result. Surface profiles of the line scan on 9.8 N indentation (c) without and (d) with baseline subtracted by origin.

Around the indentation, an uplift zone can be seen; however the surfaces inside the indentation cannot be measured due to the lack of reflection of the light. A platinum coating was applied to enhance the reflectivity of the surface, but the mapping result stayed nearly the same as without the coating and the surface profile within the imprint still could not be obtained.

The line scan along the diagonal of the indentation (line 3 in Figure 4.20) normally has the surface profile similar to the line scan normal to the indentation edge (line 1

and 2 in Figure 4.20). The opening of the profile of line 3 is larger than line 1 and 2 and as the opening of the indenter imprint is larger on the diagonal direction.

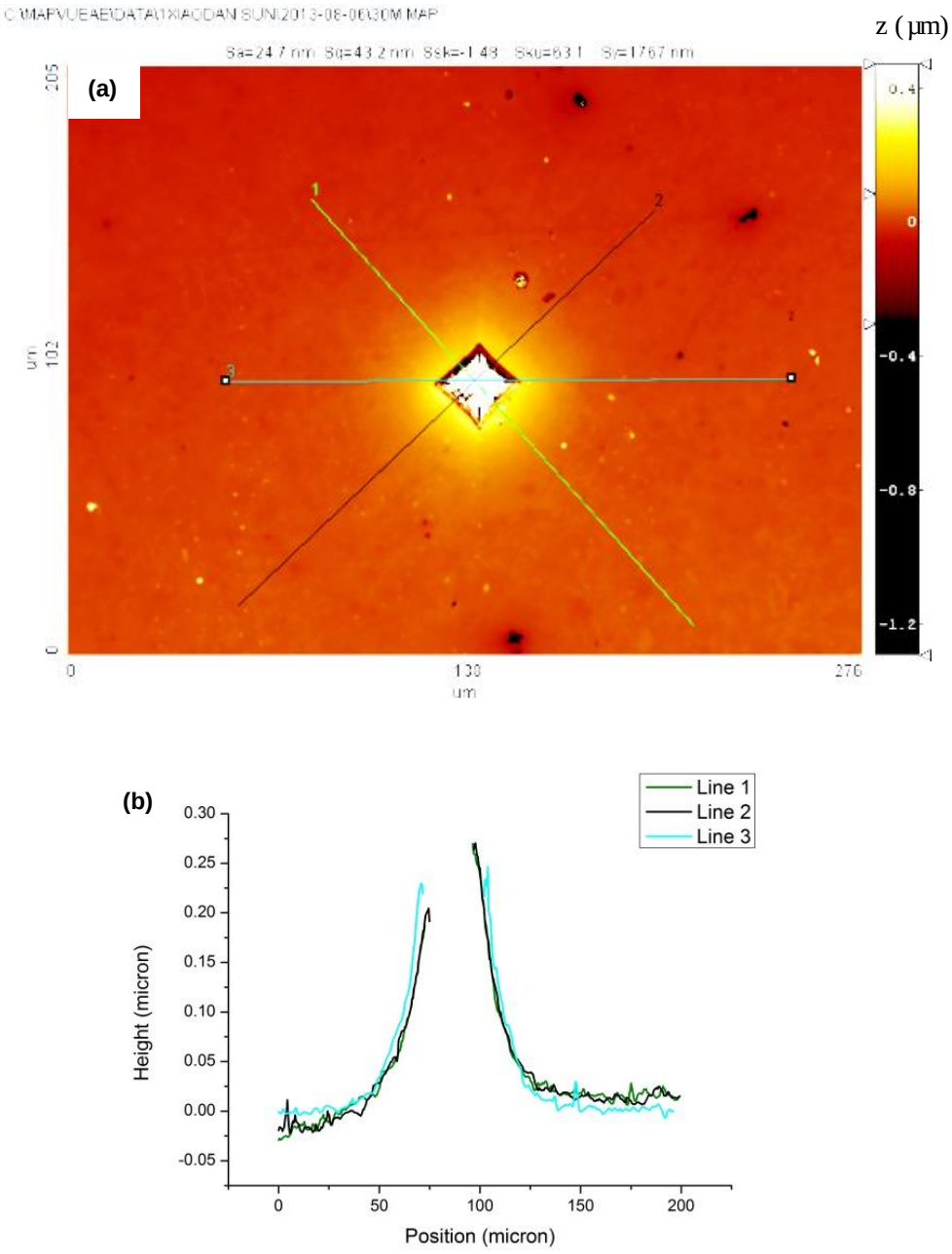


Figure 4.20 (a) directions of the line scans and (b) the corresponding surface profile of three line scans on a 49 N indentation.

The lateral crack forms during the unloading of the indenter, and this has been proved in glass (Lawn and Swain, 1975) and some ceramics (Evans and Wilshaw, 1976). The uplift around the indentation in soda-lime glass was treated by Lawn and Swain (1975) as being induced by the lateral crack under the surface and they also found that no uplift can be observed when indentation cracks are absent. The uplift found in this section was therefore most likely introduced by the lateral crack beneath the surface. Marshall et al. (1982) also regarded the uplift of the surface around indentations as being the result of the lateral cracking and they used simple beam theory to model the uplift. Their approach will be used and further discussed in Section 4.3.5.

4.3 Discussion

4.3.1 Plastic zone

In Section 4.2.9, the plastic zone of the 98 N indentation was characterised and has a semi-spherical shape with a diameter close to the half-diagonal length of the indentation. The direct evidence of the location of the plastic zone can be supported by the images of the polished cross-section, in which an intense zone of micro-fracture and grain pullout can be seen beneath the indentation. This is due to the deformation bands (dislocation pileups, twins) introduced by the plasticity, which occur during indentation and cause stress concentrations which nucleate

microcracks, leading to the pullout of the surface material during polishing. For instance, the polished section of Si_3N_4 of Lube (2001)'s results has shown the radius of the microcracking zone correspond closely to the indentation half diagonal.

In Chiang et al. (1982)'s model, the relative dimension β, defined as the ratio of the hemispherical plastic zone radius to the radius of the hemisphere with the same volume of the indentation, was used to characterise the relative dimension of the plastic zone. In the present finding, β=2.2, which is close to most of the results of ceramics investigated by Chiang et al. (1982), and close to the materials with low E/H predicted in their model, such as pure alumina and SiC used in this project. The ceramics with higher E/H value needs more justification for use in the model describe in Chapter 6, where the Chiang et al. (1982) model predicted a higher value of β. CVD ZnS is a notable example with β= 4.0 predicted by Chiang et al. (1982) and β= 4.1 observed by Van der Zwaag et al. (1980) from the roughened area outside the indentation induced by grain boundary sliding. However, they also found a distinct region of much more intense plasticity directly beneath the indenter with radius equal to the indentation half diagonal from the investigation of the cross sections, which is in line with the present finding. The experimental evidence indicates the present finding may be reasonable for the more brittle ceramics. The apparent departure from the classical indentation theory in the materials with high E/H is due to two main reasons. Firstly, the extent of the plastic zone on its own does not indicate the extent

of the plastic deformation at any point within it. The concentration of the most intense plasticity beneath the plastic zone, with little amount, if any, outside the region, has been seen from the experimental evidence mentioned above. Second is because the classical indentation models ignore the effect of the radial of the median cracking on the plasticity, and the cracking during indentation limits the extent of the yield outside the indentation. The implication from it is that the cracking distinguished during indentation (Cook and Pharr, 1990) partially replaces plasticity as a way of the accommodating the volume expansion of the indentation, therefore contracting the growth of the plastic zone to less than the effective plastic zone radius predicted by the classical models like the one from Chiang et al. (1982).

The fact that there is a well-defined interface between the plastic zone and the elastic region and the radius of the plastic zone is close to half the indentation diagonal length will be used as an assumption in Chapter 6.

4.3.2 Indentation residual stress

The indentation process creates the plastic zone in which permanent deformation occurs. This was verified by Hockey (1971) as the dislocation networking and twinning deformation were found in the plastic zone. During unloading, the plastic zone is constrained by the elastic region outside the plastic zone, which creates the

residual stress field in the elastic region. Here, the residual stress results are compared with the prediction from Yoffe (1982)'s model. In Yoffe's model (Figure 4.21), a blister field is used to evaluate local stress around an indentation:

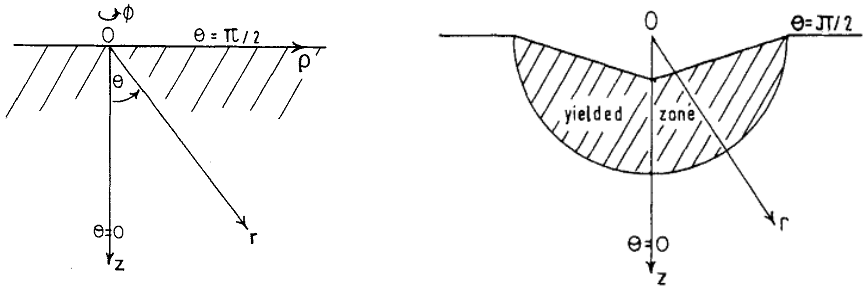


Figure 4.21 (a) Coordinate system used by Yoffe (1982); (b) sketch of plastic zone surrounded by elastic field.

$$\sigma_r = \frac{B}{r^3} 4[(5-v)cos^2\theta - (2-v)]$$

$$\sigma_\theta = -\frac{B}{r^3} 2(1-2v)\cos^2\theta$$

$$\sigma_\emptyset = \frac{B}{r^3} 2(1-2v)(2-3\cos^2\theta)$$

where *B* is a constant; v is the Poisson's ratio θ and *r* are the polar coordinates defined in Figure 4.21; σ_r

The use of a surface line scan (θ =π/2) on alumina (Poisson's ratio, v=0.23) simplifies these equations:

$$\sigma_r = -\frac{7.04B}{r^3}$$

$$\sigma_\theta = 0$$

$$\sigma_\emptyset = \frac{2.08B}{r^3}$$

The value of *B* can be calculated from the geometry of the indenter (Cook and Pharr, 1990):

$$B = \frac{6E\Delta V}{5\pi}$$

where ΔV is the volume change after indentation; *E* is the Young's modulus of the material. For a Vickers indentation: $B = 9.192 \times 10^{-3} E(2\mathrm{a})^3$, where *a* is half of the diagonal length (Limpichaipanit, 2008), for a 9.8 N indentation, *a* is 13.8 μm，*E* ≈ 400 GPa, then from the equation above, *B* = 7.73×10^4 GPa·μm^3

The hydrostatic residual stress predicted by Yoffe's model on the surface is:

$$\sigma = \frac{\sigma_r + \sigma_\theta + \sigma_\emptyset}{3} = -\frac{1.65B}{r^3} = -\frac{1.28 \times 10^5}{r^3}$$

When comparing the experimental results of line scans in alumina with Yoffe's prediction (Figure 4.22a, b and c), it is found that Yoffe's model deviates significantly from the experimental results as the predicted stress is more compressive then the experimental results. When close to the indentation center the magnitude of the predicted stress is larger by the factor of 6-30. The log-log plots of the residual stress results are shown in Figure 4.23, and the curve form of Yoffe's model (in a gradient of

-3) does not follow the results. For analysis of the present results, more discussions will be made in Chapter 6.

Yoffe's model did not consider relaxation of the stress by the radial and lateral cracking around the indentation on unloading; therefore her prediction was higher than the experimental results. In Chapter 6, a new model is described in detail to better explain the residual stress field around indentations in the presence of cracking.

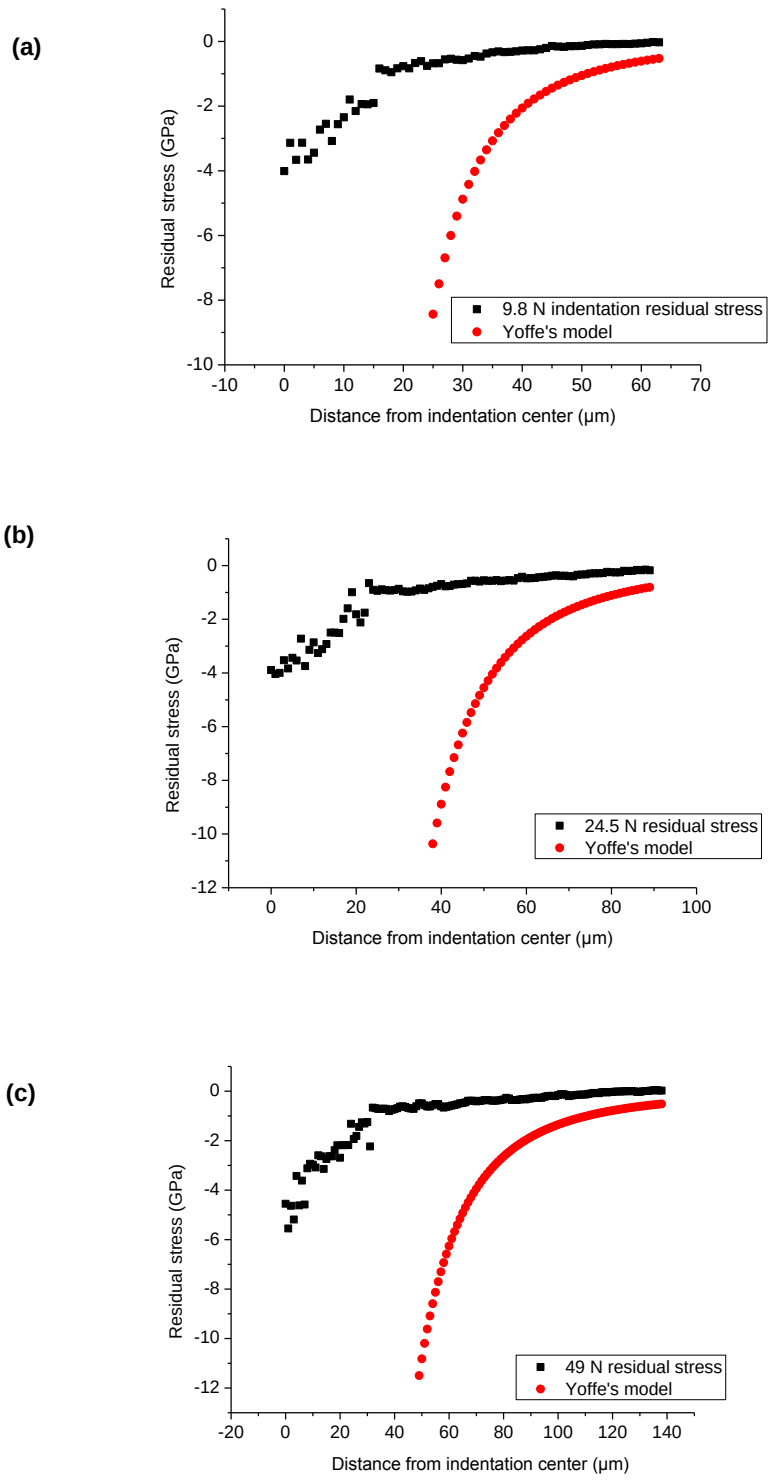


Figure 4.22 Line scan results on (a) 9.8 N, (b) 24.5 N and (c) 49 N indentations in comparison with the predictions of the Yoffe's model.

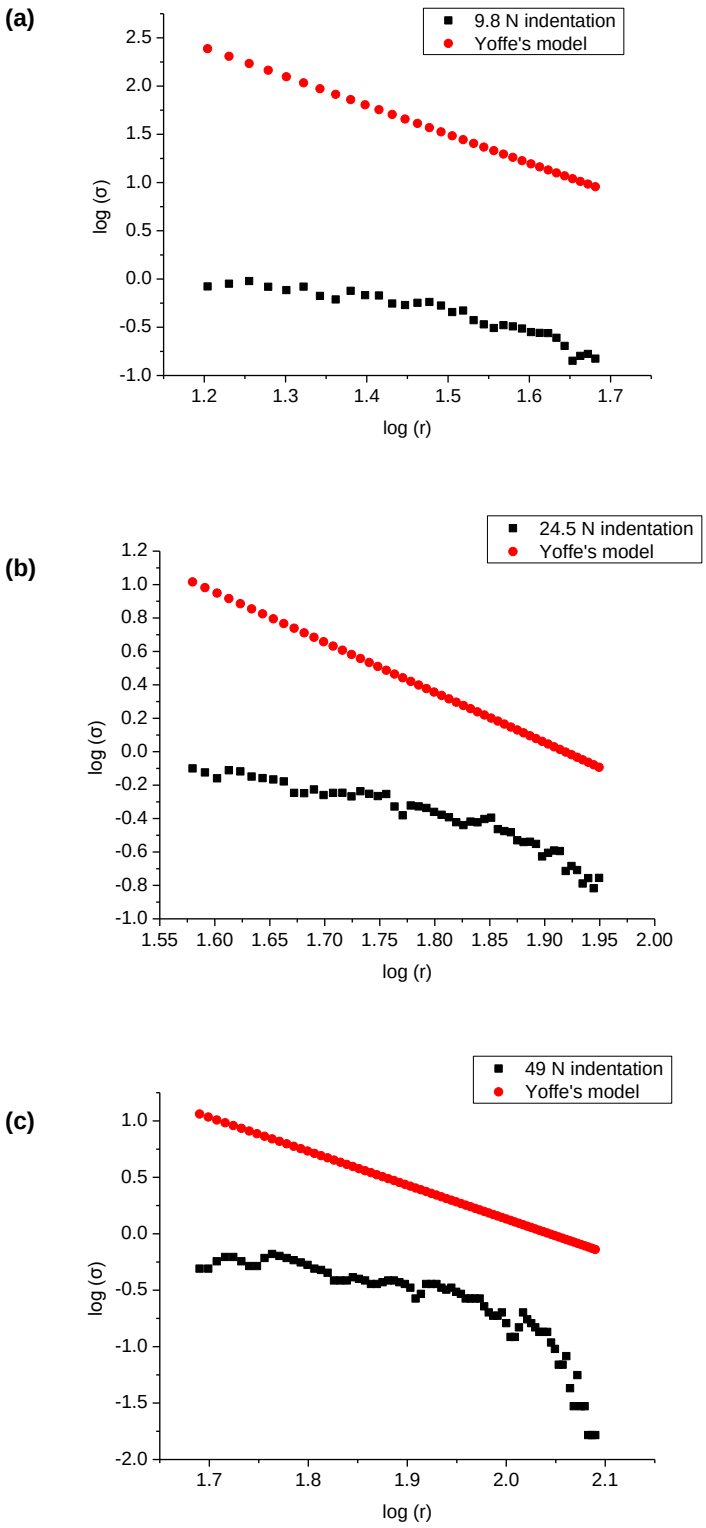


Figure 4.23 log-log plot of the results shown in Figure 4.22 in comparison with the prediction of the Yoffe's model.

4.3.3 Real radial crack length

For the calculation of Vickers indentation fracture toughness, the accuracy of the measurement of indentation parameters, especially the radial crack length, is very important. Normally, the crack length is measured by the optical microscope. Miyazaki and Yoshizawa (2014) carefully reviewed the measurements of radial crack length of standard alumina specimens from different laboratories, and suggested that optical microscopes with high resolution should be employed to avoid errors. The measurement under an objective with lower magnification leads to the underestimation of the radial crack length. Miyazaki et al. (2013) found that the radial crack length measured by a 20× objective lens is 15 μm shorter than by 50× for a 196 N indentation on SiC. In this project, all the radial crack lengths from OM were measured under the 100× objective lens for the best accuracy. The results in Section 4.2.6 show that even the use of an objective lens with a high magnification can seriously underestimate the crack length.

Some researchers chose SEM for measuring radial crack length, for example, Fünfschilling et al. (2011) have used SEM for determining the position of the radial crack tip. The SEM method, although with very good resolution, typically around 5-10 nm (Fünfschilling et al., 2011), however, has its drawbacks. The ceramic SEM samples need coating to become conductive and the coating material may be

deposited into the crack tip which further affects the crack length measurement. This has been also seen in Section 4.2.6. Marx et al. (2004) encountered a similar issue as sputtering a gold or carbon coating onto the surface partly hid the crack. For the sake of precise crack length measurement, they instead used an Environmental Scanning Electron Microscope which made the conductive coating unnecessary. This however requires sophisticated equipment and is time consuming. However, the FLM method provide the radial crack length most close to the actual length and the radial crack tip from the FLM line scan is clearly defined.

The discrepancies in the radial crack length results from OM (c_{OM}) and FLM (c_{FLM}) discovered previously in Section 4.2.5 are largely due to the resolution limit of the optical microscope as the OM cannot resolve the very fine crack opening near the tip of the radial crack. The discrepancy found here is quite significant for small indentation loads; for example, the mean radial crack length measured from OM on 9.8 N indentations is 9.9 µm shorter than FLM (around 20% of the FLM result). This has shown that measuring crack length by OM may not give us the true value for the crack length, which may lead to further inaccuracy of the Vickers indentation fracture toughness.

The crack opening displacement of Vickers indentation radial cracks has been studied by Fett et al. (2005) on materials with no strong R-curve effect. The R-curve effect is normally found in course-grained specimens, for example, Steinbrech et al. (1990) found a strong R-curve effect in the alumina with mean grain size larger than 15 μm. The alumina used here has a grain size (2 μm) much less than this. Bleise and Steinbrech (1994) also found the R-curve effect in alumina is less obvious in indentation cracks than the long cracks in single edge notched beams. Therefore, the alumina we used is considered to be without strong R-curve behaviours. The near-tip displacement proposed by Fett et al. (2005) gives:

$$\delta = \frac{4KE\sqrt{c}}{\pi(1-\nu^2)}(Ax^{\frac{1}{2}} + Bx^{\frac{3}{2}} + Cx^{\frac{5}{2}}) \qquad \text{Equation 4.2}$$

where $A = \sqrt{\pi/2}\sqrt{c/a}$; $B = 0.011 + 1.8197\ln(c/a), C = -0.6513 + 2.121\ln(c/a)$, where *c* is the radial crack length, a is the size of the plastic zone, which is approximate to the half indentation diagonal length , ν is the Poisson's raito, *E* is the Young's modulus and *K* is the crack tip toughness.

Here, *c* is measured by FLM on the assumption that radial crack lengths measured using FLM give the most accurate values. The average *K*=2.39 MPa$\sqrt{m}$ was calculated from the model in Chapter 6 by the Equation 6.39. Then the near-tip crack opening displacement (COD) profiles for different indentation loads were calculated and are shown in Figure 4.24.

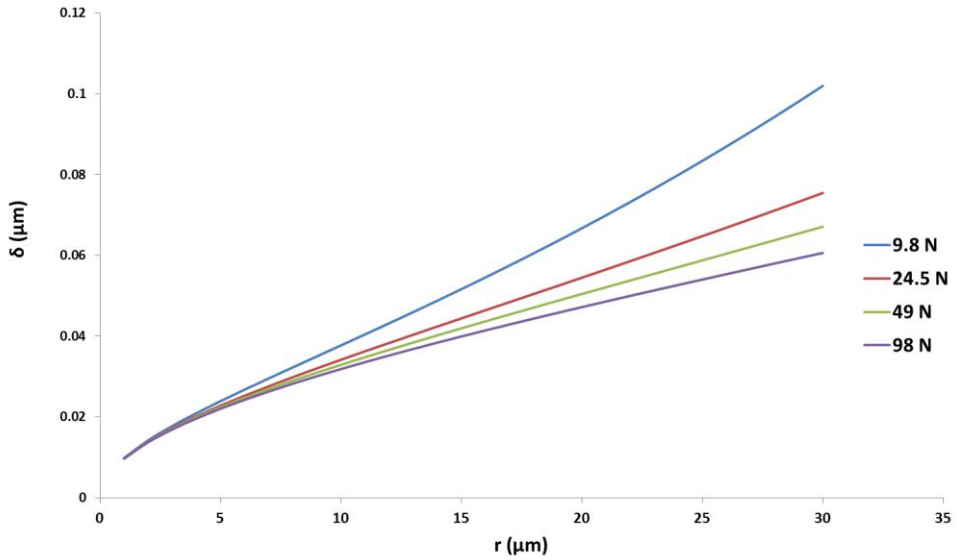


Figure 4.24 Calculated COD for different indentation loads, where *r* is the distance from indentation radial crack tip and δ is the COD.

Table 4.5 Underestimation of the OM at different indention loads.

	Measured $c_{FLM} - c_{OM}$ (μm)	Calculated COD (nm)
9.8 N	9.9	37.7
24.5 N	15.1	44.4
49 N	16.1	43.7
98 N	23.5	52.0
Average	16.2	44.5

For different loads, the underestimation $(c_{FLM} - c_{OM})$ between radial crack length measured by FLM (c_{FLM}) and that by OM (c_{OM}) were used to calculate the COD at which the crack becomes invisible to OM method accordingly (Table 4.5). An

averaged COD value of 44.5 nm was suggesting that OM using the 100× lens cannot distinguish the crack with a width below 44.5×2 = 89 nm. This was taken as the resolution of the OM using a 100× lens.

The theoretical resolving power of the optical microscope is determined by:

$$\delta_0 = 0.61\,\lambda\,/\mathrm{NA}$$

where δ_0 is the two point resolving power (Miyazaki et al., 2013), λ is the wavelength, *NA* is the numerical aperture of objective lens. The 100× objective lens used in this thesis has a *NA* of 0.9. The microscope used the white light centred at a wavelength of 550 nm. Then δ_0 for the objective lens was 0.37 μm. The resolution of the OM using 100× lens calculated from COD method, 89 nm, was better than the theoretical resolution of the objective lens 370 nm. This is because the δ_0 is the shortest distance between two objects which can be separated by the optical image, but the individual object with the size smaller than the resolution limit can still be distinguished (Jönsson and Beech, 2013). Therefore, it is no surprise that crack tips with openings smaller than δ_0 can be identified by optical microscope.

For Vickers indentation toughness measurements on ceramics, there is no doubt that precise radial crack length measurement is critical. Here, we have shown that the

FLM provides a more reliable method than OM so the results from FLM are used in the later calculations related to alumina indentations. The disadvantages are that a FLM scan takes few minutes to complete so that the crack length couldn't be determined immediately after indentation; and that the ceramic material needs to be fluorescence active.

The OM and SEM methods for crack length measurements were found to significantly underestimate the crack lengths. The FLM line scan has shown much better accuracy therefore is recommended for measuring the indentation radial crack length of the alumina based ceramics. For ceramics without fluorescence effect, the COD method described above can be used to correct the radial crack lengths measured by OM method.

4.3.4 Post-indentation subcritical crack growth

Post indentation subcritical crack growth has been found in Section 4.2.4 on polycrystalline alumina and single crystal ruby. As reviewed previously in Chapter 2, the K_I-v curve is the most suitable way of characterising the slow crack growth behaviour. For the radial crack of 49 N indentations on polycrystalline alumina and single crystalline ruby investigated in Section 4.2.4 (Figure 4.9 and 4.11), the K_I-v curve was plotted (Figure 4.25 and 4.26). Here, the stress intensity factor, K_I, was

calculated using the method described in Chapter 6 by Equation 6.39; the crack velocity was estimated by finding the velocity between two adjacent data points on the Figure 4.9 and 4.11; namely, $V_2=(C_3-C_1)/(t_3-t_1)$, where c is the radial crack length, t is the time. Towards the end of the propagation the radial crack growth is flat so there are a limited number of data points on the K_I-v curve.

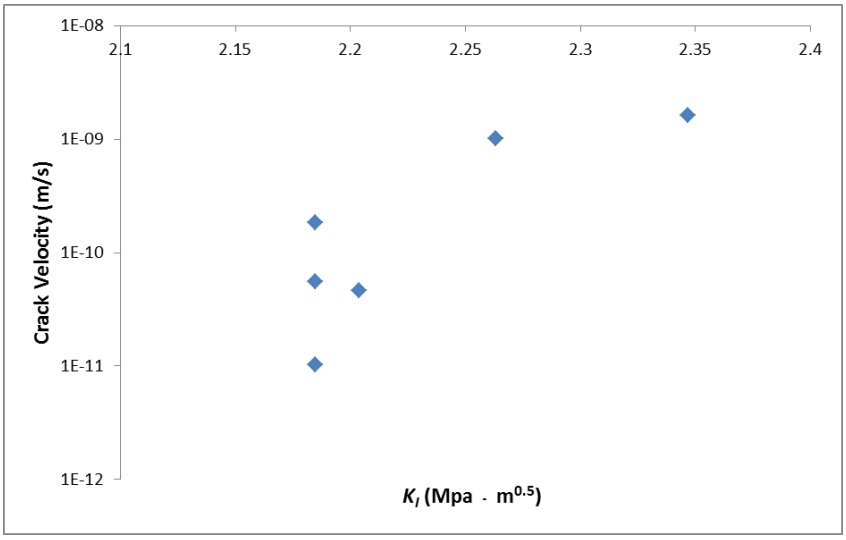


Figure 4.25 K_I-v plot for the subcritical growth of the 49 N indentation radial crack on polycrystalline alumina.

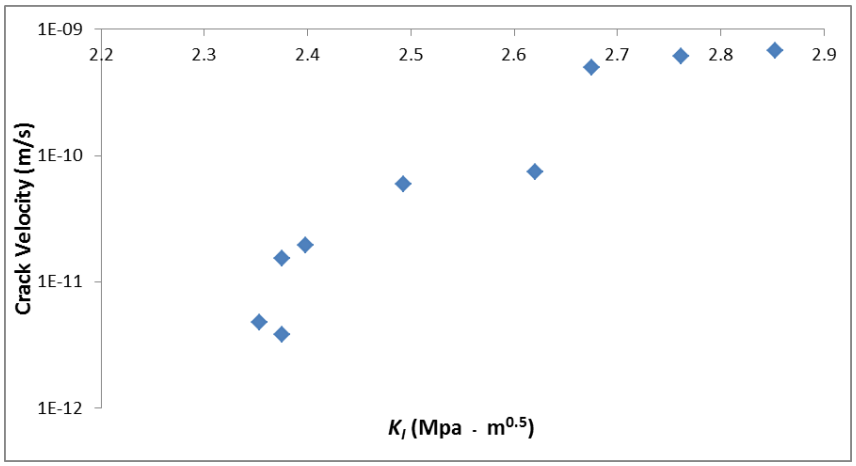


Figure 4.26 K_I-v plot for the subcritical growth of the 49 N indentation radial crack on ruby.

Table 4.6 Summary of the previous results of K_{I0} derived from the measurements of the K_I-v curve of polycrystalline alumina in air. *The K_{I0} of the Ebrahimi et al. (2000)'s was obtained by author by extrapolating their result to the crack velocity of 10^{-11} m/s.

Author	K_{I0}	grain size (μm)	measured threshold crack velocity
Ebrahimi et al. (2000)	2.8 MPa$\sqrt{m}$*	1.9*	
De Aza et al. (2002)	2.5 ± 0.2 MPa$\sqrt{m}$	1.7	10^{-11} m/s
Krell et al. (2003)	2.6 MPa$\sqrt{m}$	0.6	10^{-13} m/s
	2.8 MPa$\sqrt{m}$	0.8	10^{-13} m/s

The precise measurement of the K_I-v curve for ceramics is always difficult (Krell et al., 2003) and very hard to reproduce (Salem, 2006). To better compare with the other results, Table 4.6 listed the previous results K_{I0} derived from the measurements of the K_I-v curve of polycrystalline alumina in air. The crack lengths of these studies (shown in Table 4.6) were obtained from optical microscopy. The crack growth velocity in the low crack growth regime (region Ⅰ) of the K_I-v curve in the previous research on single or polycrystalline alumina were typically $\leqslant 10^{-8}$…10^{-6} m/s (Krell et al., 2003, Ebrahimi et al., 2000, De Aza et al., 2002) and the data points on the current results all fell into region Ⅰ by this measure. This suggests that the post-indentation crack growth observed in this study is actually close to the end of the crack propagation and the final stress intensity factor K is the threshold K_{I0}, below

which the crack will not propagate. In principle the crack growth rate at the threshold stress intensity factor K_{I0} should be infinitely close to zero. Often a critical crack growth rate is used as an approximation to define K_{I0}. This critical rate is, however, hard to define. The observation of the previous research on different aluminas (grain size 1.7-25 μm) (Evans, 1972, De Aza et al., 2002), suggested the critical rates of 10^{-11}…10^{-10} m/s, which agrees with the conventional K_I-v curves (Krell et al., 2003). However, the number of data points approaching these critical rates are always limited (De Aza et al., 2002) and the measurement is sometimes hindered by the difficulty of measuring very low crack growth velocities. For instance, Ebrahimi et al. (2000) were only able to measure the crack velocity down to the range of 10^{-6}…10^{-7} m/s, and their K_{I0} results were obtained by extrapolating their result in region Ⅰ down to the crack velocity of 10^{-11} m/s in order to compare them with other results. The author of this thesis has also noticed that Krell et al. (2003) managed to measure the crack propagation rates as low as 10^{-13} m/s in the alumina with submicron grain size in a long time study with measuring time up to 6 months. This indicates that further research is required for ascertaining the crack growth rate at K_{I0}. Considering their work was based on alumina with very fine grain size and that the microstructure will affect the slow crack growth behaviour (Krell et al., 2003), a threshold velocity of about 10^{-11}…10^{-10} m/s conventionally accepted by the researchers was used in this thesis.

Seen from Figure 4.25，when the crack velocity went down to around 10^{-11} m/s, the threshold K_{I0}, for the 49 N indentation radial crack on polycrystalline alumina is 2.2 MPa$\sqrt{m}$ and this is very close to the K_{I0} obtained by (De Aza et al., 2002).

As discussed above, the radial crack lengths measured by FLM on alumina indentations are finally accepted as the actual radial crack length. As the FLM cannot measure crack length immediately after indentation and there is unfortunately no equipment available which enabled immediate crack length measurement, FLM measurements were performed after the end of the radial crack propagation. The stress intensity factors calculated and discussed in model in Chapter 6 will therefore all refer to the threshold stress intensity factor K_{I0}.

The mechanisms of slow crack growth have been described by Chevalier et al. (1999). In region I of the K_I-v curve, the crack growth is due to the reaction between the ceramics and corrosion molecules (water, in most cases) and is controlled by the thermally activated reaction kinetics. For Al_2O_3, the reactions steps are (De Aza et al., 2002) : (1) H_2O is absorbed to the Al-O bond. (2) reaction activated based on the simultaneous transfer of proton and electron and (3) hydroxyls form on the crack surface. In ambient temperature and humidity, ceramics which are metal oxides will follow this mechanism of slow crack growth. Therefore, the 3Y-TZP indentation

investigated in this project is also expected to experience slow crack growth (Chevalier et al., 1999). For SiC indentation, significant slow crack growth was not found at the room temperature in air. Its slow crack growth behaviour can only be activated either by increasing the concentration of the corrosive molecule, such as testing in water (Evans and Lange, 1975), or increase the testing temperature, such as 900 to 1100℃ by McHenry and Tressler (1980).

The slow crack growth of single crystalline Al_2O_3 in also promoted by water (Wiederhorn, 1969). Shiono et al. (1983) found that the promotional effect of water on slow crack growth has the ranking of: fine grained alumina (grain size of 5 μm) > course grained alumina (grain size of 15 μm) > sapphire. This is because the lattice disorder or segregated impurities along grain boundaries promote the reaction with water molecules (Krell et al., 2003). Krell et al. (2003) also found that the impurity level plays a more important role for extremely fine grained (sub-μm) polycrystalline alumina. The threshold K_{I0} for ruby indentation in this study was 2.4 MPa$\sqrt{m}$ and was larger than that for polycrystalline alumina (2.2 MPa$\sqrt{m}$). This is because slow crack growth proceeds preferentially along grain boundraies (Krell et al., 2003).

It is also useful to perform a statistical analysis to test the sensitivity of K_{I0} to different the different alumina materials (i.e. polycrystalline alumina and ruby). Here, a

one-way ANOVA (analysis of variance) analysis (Tabachnick et al., 2001) was employed. Non-significance of the test statistic (F-statistic) associated with this technique would imply that the material type has no effect on K_{I0}. The level of significance, α =0.05 was used to test the assumption. From the result, p=0.30 was obtained. As p>0.05 (Tabachnick et al., 2001), this indicates that the material type has a significant impact on the K_{I0} results and this agrees with the scientific analysis above.

So far, no research has been done to compare the slow crack growth behaviour of ruby and polycrystalline alumina, and more future work needs to be done to fully understand the slow crack growth behaviour of ruby.

In conclusion, the threshold K_{I0} of the radial cracks of the 49 N indentations on polycrystalline alumina and the ruby were determined to be 2.2 MPa$\sqrt{m}$ and 2.4 MPa$\sqrt{m}$, respectively. The K_{I0} of alumina was found close to De Aza et al. (2002)'s results on the polycrystalline alumina with similar grain size.

4.3.5 Surface profiles and lateral crack lengths of indentations

As discussed previously in Section 2.2.6, the upward or inward flow of materials during the indentation process forms pile-up or sink-in near the indentation imprint. Indentations on ceramics mostly do not have pile-up around the indentation as the plasticity for ceramics is normally low. A piece of evidence is from the direct observation of the indentation imprint (Figure 4.2), where only a tiny amount of the sink-in can be noticed.

There are three possible conditions for the configuration of the radial-median-lateral crack system: (1) lateral crack longer than the radial crack (Figure 4.27A); in this case the radial crack will have a minor interaction with the propagation of the lateral crack, (2) lateral equal to radial; (3) lateral shorter than the radial (Figure 4.27B). From the results in Section 4.2.3.2, the case (2) seems to be more appropriate for alumina. In this case, the lateral crack system can be modelled by the simple plate theory (Roark, 1965) and was treated by Marshall et al. (1982) as the combination of four triangular quarter plates, each with a force of $P_r/4$ acting at the apex. With the neutral surface defined as 0XZ (Figure 4.27B), the bending moment at position x is :

$$M = {}^{P_r x}/_{4}$$

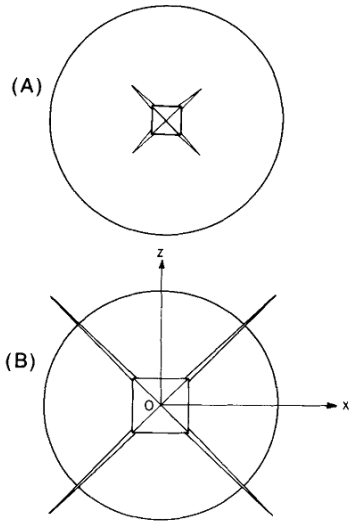


Figure 4.27 Two typical crack configurations (A) lateral crack longer than radial crack; (B) lateral crack shorter than the radial crack (Marshall et al., 1982).

The second moment of area can be written as (rectangular cross-section):

$$I = {\omega h^3}/{6}$$

where *h* is the thickness of the plate and ω is the half width and for a quarter-plate $\omega = x$. Then the radius of curvature *R* at position *x* is

$$R = {EI_x}/{M_x} = {2Eh^3}/{3P_r}$$

R does not depend on *x*, the beam therefore has a circular profile and the for samll displacement following equation can be derived from straightforward geometry:

$$(2Ru_{rx})^{1/2} = c - x$$

where *c* is the lateral crack length and u_{rx} is the surface uplift at distance x from the indentation center

Marshall et al. (1982) measured the lateral crack length *c* from direct observation from the top views of several translucent ceramics and set it to be the intercept on the abscissa of the $(u_{rx})^{1/2}\ vs.x$ plot. Actually, it is hard to define the span of the lateral crack from the optical image because the poor subsurface resolution and the small crack opening displacement will give significant underestimation of the crack length; however, their method can be used to find the lateral crack length as the materials they have investigated obey the relationship of $(2Ru_{rx})^{1/2} = c - x$ very well.

The plot of the square root of the uplift $(u_{rx})^{1/2}$ as a function of the distance from center of the indentation x (Figure 4.29) was derived from the left arm surface profile of a 9.8 N indentation (Figure 4.28). In Figure 4.29, a region with good linear dependence can be found (highlighted by the blue ellipse). This region was fitted with a straight line (Figure 4.30) and the fitting line was extrapolated to x = 0 to find the lateral crack length c^*. There are several points at the very left hand end of the curve which did not follow the linear relationship possibly due to the impact of the sink-in of the indentation. The distance between the c^* and the cut-off point, d, was found to be

close to the depth of the lateral crack, *h*. This is because this simple plate model assumes that the thickness of the plate is close to zero and in reality the depth of the lateral crack is not neglectable. Therefore, the curvature of the plate will be affected by the end effect at the built-in end when the data point was close to the lateral crack tip and was within the distance of the thickness of the plate (lateral crack depth).

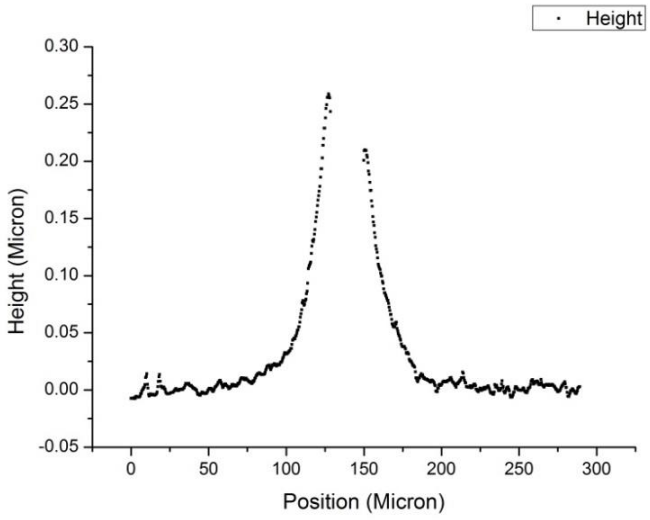


Figure 4.28 Surface profile of the line scan on a 9.8 N indentation.

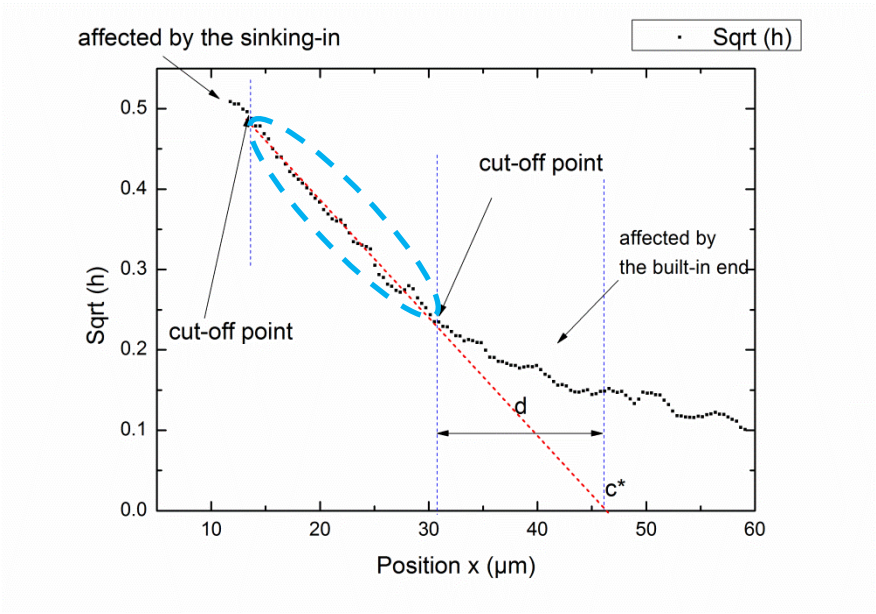


Figure 4.29 Sqrt *(u)* vs. *x* map of the left arm of line scan, showing the linear region (blue circle), the fitting line (red line) and cut-off point.

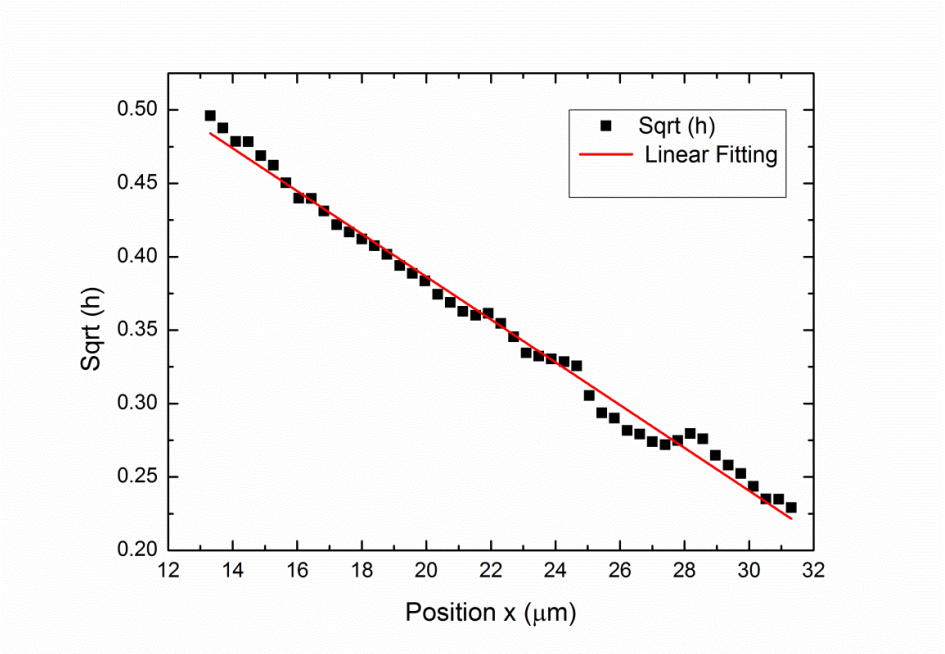


Figure 4.30 Linear fitting for the selected data to calculate lateral crack length.

The lateral crack lengths c^* of 9.8 N, 24.5 N, 49 N and 98 N indentations obtained by this method are listed in Table 4.7. At least 10 measurements were taken into account for each load. For these measurements, the coefficients of determination (R^2) for the linear fitting shown in Figure 4.30 were in the range 0.96-0.99 (for instance, R^2=0.98 for the fitting in Figure 4.30). For most cases, R^2> 0.95 is considered to be a strong fitting level and this implies the fitting was acceptable (Montgomery et al., 2015).

Compared with the radial crack length, c, measured by FLM method, the lateral crack lengths, c^* is close to c although c^* is slightly smaller with loads above 9.8 N.

Table 4.7 Lateral crack lengths c^* of 9.8 N, 24.5 N, 49 N and 98 N indentations obtained from simple plate model in comparison with radial crack length, c, measured by FLM method..

	Half diagonal length (μm)	Lateral crack length c* measured by surface profilometer (μm)	c measured by FLM (μm)
9.8 N	13.8 ± 1.1	49.4 ± 2.3	48.5 ± 2.7
24.5 N	22.7 ± 0.9	88.0 ± 4.7	91.5 ± 3.1
49 N	30.3 ± 0.9	128.5 ± 5.9	137.0 ± 4.4
98 N	48.1 ± 0.56	219.2 ± 9.1	235.7 ± 5.8

The indirect lateral crack length measurement here suggests that the lateral crack extends to a length similar to the radial cracks. This finding will further discussed in the following Section 4.3.6.

4.3.6 Overview of the cracking system of alumina

For cracking system in alumina, several key findings of the experiments are summarised here:

(1) The radial-median crack system was found in the 9.8-98 N alumina indentations;

(2) Lateral cracks were also found for all the indentations, the their depths were found close to the half diagonal lengths;

(3) Lateral crack joins the tips of the radial cracks and lateral crack is close to but not perfectly circular (extend further along the radial crack directions than between them). This is found from the FLM mapping on the sapphire surface.

(4) The lateral crack has the similar length as the radial crack. This is obtained from the understanding in Section 4.3.5.

(5) The lateral crack was observed to have a similar growth rate as the radial crack (Figure 4.13) and both terminated nearly at the same time (from the results in Section 4.2.4).

The radial-median system under alumina indentations has also been previously reported (Sullivan and Lauzon, 1986) and the lateral crack was found to be present at a load of 200 N (Reece and Guiu, 1991) even at very low loads (50-200g) (Elfallagh and Inkson, 2009, Arsecularatne et al., 2011).

The length of the lateral crack is very difficult to measure. Previous research (Cook and Pharr, 1990, Marshall et al., 1982) on transparent ceramics suggest that the lateral crack length is larger than radial crack length, however, the very small opening at the crack tip is expected to cause a systematic underestimation of the lateral crack length from direct measurement due to the increased scattering of light. For opaque materials the lateral crack is not directly visible. Sectioning (Lube, 2001), as sometimes used, however, is also not reliable as the crack may extend during this process (Marshall et al., 1982). The surface profilometer although not ideal, does provide an indirect way of measuring lateral crack length. The lateral crack lengths were found normally slightly (less than 10%) shorter than the radial crack lengths and this has also been seen in the FLM line scans on the 49 ruby (Section 4.2.4). The reason is that the lateral crack has a shape that is close to but not perfectly circular (extend further along the radial cracks than between them), which was observed in Section 4.2.3.2. This agrees well with the finding on 98 N indentation on soda-lime glass (Whittle and Hand, 2013) where the shape of the lateral crack were measured by confocal microscopes.

The finding (3) and (4) also matches with the Whittle and Hand (2013)'s observation that the lateral and the radial-median crack share the same terminus during the crack growth and the tips of the radial-median crack and the lateral crack are exactly coincident.

These findings on alumina indentations will be employed as the fundamental assumptions to build the indentation model in Chapter 6

4.4 Summary

(1) Plastic zone

- There is a well-defined interface between the plastic zone and the elastic region and the radius of the plastic zone is close to half the indentation diagonal length.

(2) Residual stress field.

- The residual stress field around the indentations has been measured by FLM scans.
- Yoffe's model predicted higher stresses than the residual stress results because Yoffe's model did not consider relaxation of the stress by the radial and lateral cracking.

(3) Indentation cracking system.

- The indentation parameters for 9.8-98 N alumina indentations were measured. The half indentation diagonal lengths were measured by OM. The radial crack lengths were measured by FLM, OM and SEM. The OM and SEM methods were found to significantly underestimate the crack lengths. The FLM line scan has shown much better accuracy and is therefore recommended for measuring the indentation radial crack length of alumina based ceramics.

- Post indentation slow crack growth was found on the radial cracks of the 49 N alumina and ruby indentations. The threshold K_{I0} of the radial cracks of the indentations on polycrystalline alumina and the ruby were determined to be 2.2 MPa$\sqrt{m}$ and 2.4 MPa$\sqrt{m}$, respectively.

- The radial-median crack system was found in the 9.8-98 N alumina indentations.

- Lateral cracks were also found for all the indentations, and their depths were found to be close to the half diagonal lengths. Lateral cracks join the tips of the radial cracks and are close to, but not perfectly circular (they extend further along the radial cracks than between them). The lateral crack has a similar length to the radial crack.

- The lateral crack was observed to have a similar growth rate to the radial crack in ruby and growth of both terminated at nearly the same time.

References

ANSTIS, G., CHANTIKUL, P., LAWN, B. R. & MARSHALL, D. 2006. A critical evaluation of indentation techniques for measuring fracture toughness: I, direct crack measurements. *Journal of the American Ceramic Society*, 64, 533-538.

ANUNMANA, C., ANUSAVICE, K. J. & MECHOLSKY JR, J. J. 2009. Residual stress in glass: Indentation crack and fractography approaches. *Dental Materials*, 25, 1453-1458.

CHAUDHURI, P., WINTER, M., WIEGHARDT, K., GEHRING, S., HAASE, W., NUBER, B. & WEISS, J. 1988. Syntheses and magnetic properties of a heteropolyoxotungsten (VI) iron (III) cation and [LFeIII (. mu.-MO4) 3FeIIIL] complexes (M= chromium (VI), molybdenum (VI)). Crystal structures of L2Fe2 (CrO4) 3. cntdot. H2O and [L3Fe3W4O14 (OCH3) 3](ClO4) 2. cntdot. 0.5 H2O (L= 1, 4, 7-trimethyl-1, 4, 7-triazacyclononane). *Inorganic Chemistry*, 27, 1564-1569.

COOK, R. F. & PHARR, G. M. 1990. Direct observation and analysis of indentation cracking in glasses and ceramics. *Journal of the American Ceramic Society*, 73, 787-817.

EVANS, A. & WILSHAW, T. R. 1976. Quasi-static solid particle damage in brittle solids—I. Observations analysis and implications. *Acta Metallurgica*, 24, 939-956.

FISCHER‐CRIPPS, A. C. & LAWN, B. R. 1996. Stress Analysis of Contact Deformation in Quasi‐Plastic Ceramics. *Journal of the American Ceramic Society*, 79, 2609-2618.

GUBICZA, J., ROZLOSNIK, N. & JUH SZ, A. 1997. Comment on "Indentation size effect: reality or artefact?". *Journal of materials science letters*, 16, 1904-1905.

GUO, S. 2008. Fluorescence microscopy investigation on residual stresses in alumina-based ceramics. *University of Oxford*.

GUO, S. 2009. Fluorescence microscopy investigation on residual stresses in alumina-based ceramics. D.Phil D.Phil. thesis, *University of Oxford*.

HE, J. & CLARKE, D. R. 1995. Determination of the Piezospectroscopic Coefficients for Chromium‐Doped Sapphire. *Journal of the American Ceramic Society*, 78, 1347-1353.

IOST, A. & BIGOT, R. 1996. Indentation size effect: reality or artefact? *Journal of materials science*, 31, 3573-3577.

LAWN, B. & SWAIN, M. 1975. Microfracture beneath point indentations in brittle solids. *Journal of Materials Science*, 10, 113-122.

LAWN, B. R., EVANS, A. & MARSHALL, D. 1980. Elastic/plastic indentation damage in ceramics: the median/radial crack system. *Journal of the American Ceramic Society*, 63, 574-581.

MARSHALL, D., LAWN, B. & EVANS, A. 1982. Elastic/plastic indentation damage in ceramics: The lateral crack system. *Journal of the American Ceramic Society*, 65, 561-566.

ROARK, R. J. 1965. Formulas for stress and strain. *New York: McGraw-Hill*, 1965, 4th ed., 1.

YOFFE, E. 1982. Elastic stress fields caused by indenting brittle materials. *Philosophical Magazine A*, 46, 617-628.

ANSTIS, G., CHANTIKUL, P., LAWN, B. R. & MARSHALL, D. 1981. A critical evaluation of indentation techniques for measuring fracture toughness: I, direct crack measurements. *Journal of the American Ceramic Society,* 64, 533-538.

ARSECULARATNE, J., HOFFMAN, M., O'KELLY, K. & PAYRAUDEAU, N. 2011. FIB tomographic analysis of subsurface indentation crack interactions with pores in alumina. *Journal of the American*

Ceramic Society, 94, 4017-4024.

ASTM, S. 2003. Standard Test Method for Dynamic Young's Modulus, Shear Modulus, and Poisson's Ratio by Impulse Excitation of Vibration. *West Conshohocken: ASTM International*, 1876-1878.

BLEISE, D. & STEINBRECH, R. W. 1994. Flat R‐Curve from Stable Propagation of Indentation Cracks in Coarse‐Grained Alumina. *Journal of the American Ceramic Society*, 77, 315-322.

CHEVALIER, J., OLAGNON, C. & FANTOZZI, G. 1999. Subcritical Crack Propagation in 3Y‐TZP Ceramics: Static and Cyclic Fatigue. *Journal of the American Ceramic Society*, 82, 3129-3138.

CHIANG, S., MARSHALL, D. & EVANS, A. 1982. The response of solids to elastic/plastic indentation. I. Stresses and residual stresses. *Journal of Applied Physics*, 53, 298-311.

COOK, R. F. & LINIGER, E. G. 1993. Kinetics of indentation cracking in glass. *Journal of the American Ceramic Society*, 76, 1096-1105.

COOK, R. F. & PHARR, G. M. 1990. Direct observation and analysis of indentation cracking in glasses and ceramics. *Journal of the American Ceramic Society*, 73, 787-817.

DE AZA, A., CHEVALIER, J., FANTOZZI, G., SCHEHL, M. & TORRECILLAS, R. 2002. Crack growth resistance of alumina, zirconia and zirconia toughened alumina ceramics for joint prostheses. *Biomaterials*, 23, 937-945.

EBRAHIMI, M., CHEVALIER, J. & FANTOZZI, G. 2000. Slow crack-growth behavior of alumina ceramics. *Journal of materials research*, 15, 142-147.

ELFALLAGH, F. & INKSON, B. 2009. 3D analysis of crack morphologies in silicate glass using FIB tomography. *Journal of the European Ceramic Society*, 29, 47-52.

EVANS, A. 1972. A method for evaluating the time-dependent failure characteristics of brittle materials—and its application to polycrystalline alumina. *Journal of materials science*, 7, 1137-1146.

EVANS, A. & LANGE, F. 1975. Crack propagation and fracture in silicon carbide. *Journal of materials science*, 10, 1659-1664.

EVANS, A. & WILSHAW, T. R. 1976. Quasi-static solid particle damage in brittle solids—I. Observations analysis and implications. *Acta Metallurgica*, 24, 939-956.

F NFSCHILLING, S., FETT, T., OBERACKER, R., HOFFMANN, M. J., SCHNEIDER, G. A., BECHER, P. F. & KRUZIC, J. J. 2011. Crack‐Tip Toughness from Vickers Crack‐Tip Opening Displacements for Materials with Strongly Rising R‐Curves. *Journal of the American Ceramic Society*, 94, 1884-1892.

FETT, T., NJIWA, A. K. & R DEL, J. 2005. Crack opening displacements of Vickers indentation cracks. *Engineering Fracture Mechanics*, 72, 647-659.

GUO, S. 2008. Fluorescence microscopy investigation on residual stresses in alumina-based ceramics. *University of Oxford*.

HE, J. & CLARKE, D. R. 1995. Determination of the Piezospectroscopic Coefficients for Chromium‐Doped Sapphire. *Journal of the American Ceramic Society*, 78, 1347-1353.

HOCKEY, B. J. 1971. Plastic deformation of aluminum oxide by indentation and abrasion. *Journal of the American Ceramic Society*, 54, 223-231.

IRWIN, G. 1957. Analysis of Stresses and Strains Near the End of a Crack Traversing a Plate. *J. Appl. Mech*.

J NSSON, P. & BEECH, J. 2013. *Introduction to Optical Microscopy*.

KRELL, A., PIPPEL, E., WOLTERSDORF, J. & BURGER, W. 2003. Subcritical crack growth in Al 2 O 3 with submicron grain size. *Journal of the European Ceramic Society,* 23, 81-89.

LAWN, B. & SWAIN, M. 1975. Microfracture beneath point indentations in brittle solids. *Journal of Materials Science*, 10, 113-122.

LAWN, B. R., EVANS, A. & MARSHALL, D. 1980. Elastic/plastic indentation damage in ceramics: the median/radial crack system. *Journal of the American Ceramic Society*, 63, 574-581.

LIMPICHAIPANIT, A. 2008. Wear and indentation of Al2O3/SiC nanocomposites. University of Oxford.

LUBE, T. 2001. Indentation crack profiles in silicon nitride. *Journal of the European Ceramic Society*, 21, 211-218.

MARSHALL, D., LAWN, B. & EVANS, A. 1982. Elastic/plastic indentation damage in ceramics: the lateral crack system. *Journal of the American Ceramic Society*, 65, 561-566.

MARX, R., JUNGWIRTH, F. & WALTER, P.-O. 2004. Threshold intensity factors as lower boundaries for crack propagation in ceramics. *Biomedical engineering online*, 3, 41.

MCHENRY, K. & TRESSLER, R. E. 1980. Fracture Toughness and High‐Temperature Slow Crack Growth inSiC. *Journal of the American Ceramic Society*, 63, 152-156.

MIYAZAKI, H. & YOSHIZAWA, Y.-I. 2014. Refined measurements of indentation fracture resistance of alumina using powerful optical microscopy. *Ceramics International*, 40, 2777-2783.

MIYAZAKI, H., YOSHIZAWA, Y.-I. & YASUDA, K. 2013. Round robin on indentation fracture resistance of silicon carbide ceramics by using a powerful optical microscope. *Ceramics International,* 39, 611-617.

MONTGOMERY, D. C., PECK, E. A. & VINING, G. G. 2015. *Introduction to linear regression analysis, John Wiley & Sons.*

MUNRO, R. 1997. Evaluated material properties for a sintered {alpha}-alumina. *Journal of the American Ceramic Society*, 80.

REECE, M. & GUIU, F. 1991. Indentation Fatigue of High‐Purity Alumina in Fluid Environments. *Journal of the American Ceramic Society*, 74, 148-154.

ROARK, R. J. 1965. Formulas for stress and strain. *New York: McGraw-Hill*, 1965, 4th ed., 1.

SALEM, J. A. 2006. Slow crack growth and fracture toughness of sapphire for the international space station fluids and combustion facility, *National Aeronautics and Space Administration, Glenn Research Center.*

SHIONO, T., OTA, R. & SOGA, N. 1983. KI-v diagram for single-and polycrystalline α-Al2O3. *J. Soc. Mater. Sci. Jpn*, 32, 1254-1259.

STEINBRECH, R. W., REICHL, A. & SCHAARW CHTER, W. 1990. R‐Curve Behavior of Long Cracks in Alumina. *Journal of the American Ceramic Society*, 73, 2009-2015.

SULLIVAN, J. & LAUZON, P. 1986. Shape profiles of cracks formed under a Vickers pyramid indenter. *Journal of Materials Science Letters*, 5, 247-248.

TABACHNICK, B. G., FIDELL, L. S. & OSTERLIND, S. J. 2001. *Using multivariate statistics.*

VAN DER ZWAAG, S., HAGAN, J. & FIELD, J. 1980. Studies of contact damage in polycrystalline zinc sulphide. *Journal of materials science*, 15, 2965-2972.

WHITTLE, B. & HAND, R. The relationship between the median/radial and lateral cracks of vickers indents in soda-lime-silica-glass. *ICF10, Honolulu (USA)* 2001, 2013.

WIEDERHORN, S. 1969. Fracture of ceramics. Mechanical and thermal properties of ceramics. *NBS Spec. Publ.*

WU, H. Z., ROBERTS, S. G. & DERBY, B. 2008. Residual stress distributions around indentations and scratches in polycrystalline Al2O3 and Al2O3/SiC nanocomposites measured using fluorescence probes. *Acta materialia*, 56, 140-149.

YOFFE, E. 1982. Elastic stress fields caused by indenting brittle materials. *Philosophical Magazine A*, 46, 617-628.

Chapter 5 Vickers indentation studies on SiC and 3Y-TZP indentations

5.1 Introduction

In Chapter 4, the Al_2O_3 indentations were studied and from the results on alumina the new residual stress model was proposed in Chapter 6. For testing the new model, SiC and 3Y-TZP were considered as the candidates in addition to Al_2O_3. SiC was chosen as it has high hardness, high strength, excellent wear resistance, low weight and good net shape manufacturing capabilities (Willardson and Weber, 1998), and SiC was used as a good candidate for a wide range of abrasives, refractories, structural and other high-performance applications (Chang and Cohen, 1987). 3Y-TZP is also an important ceramic material with unique transformation toughening behaviour. There has been growing interest in Tetragonal Zirconia Polycrystals with 3 mol% Y_2O_3 as the stabiliser (3Y-TZP) for orthopaedic and dental practices because of their good biocompatibility and mechanical properties (Nawa et al., 2013).

Although Vickers indentation has been commonly used for measure fracture toughness of SiC and TZP (Harada et al., 2013, Laugier, 1985) and the phase transformation around the TZP indentation (Reece et al., 1992). The residual stresses in the vicinity of the indentations for both ceramics have not been measured

before. In this Chapter, the indentation parameters of both ceramics were first measured and their cracking systems were ascertained by their cross-sectional images. Then the PS effects of their Raman peaks were used to measure stress fields around indentations. The surface profiles around the indentations were also determined.

5.2 Results and discussion

5.2.1 Raman spectrum of SiC

Figure 5.1 is a typical Raman spectrum of SiC with no residual stress (on the surface which was annealed to remove residual stress introduced during sintering) in the spectrum range of 130-1000 cm^{-1}, and the Raman peaks were identified and attributed to different SiC polytypes, according to the characteristic Raman mode position of the SiC polytypes (Table 5.1). Due to the proximity and hence the overlap between some of the 3C, 4H and 6H Raman peaks, there were few peaks which could not be easily resolved (Figure 5.1). The 6H-SiC was found prevalent in the sample, while at least one of the 4H- and 3C-SiC polytypes was also co-existed in the SiC sample.

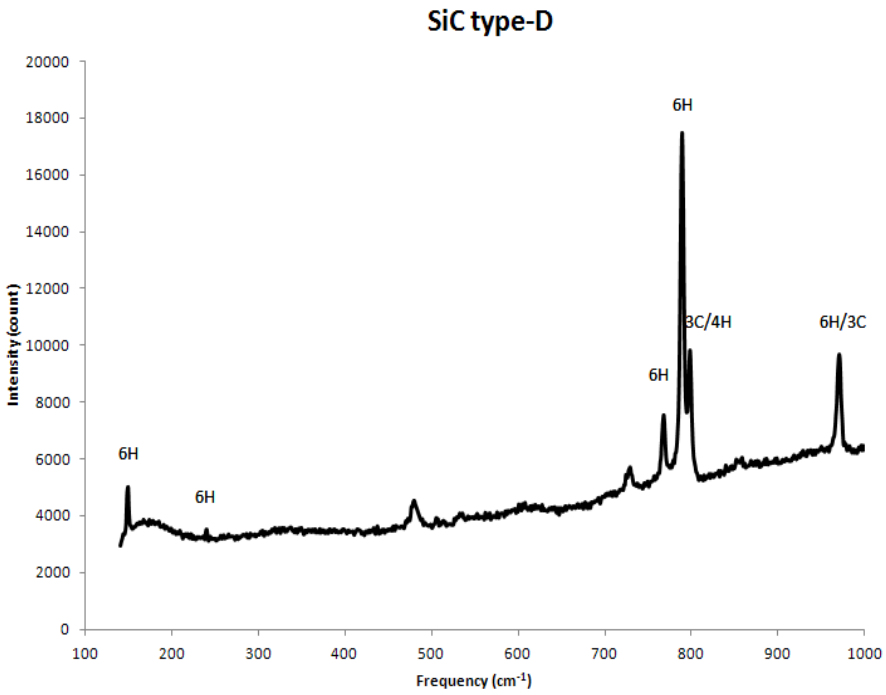


Figure 5.1 Raman spectrum on the free surface of SiC.

The SiC used in this project was from the Morgan Advanced Materials plc. and was produced by sintering SiC powder with sintering aids in the inert temperature up to 2000 ºC or higher. However, the detailed composition and the processing route of the SiC are confidential. For a sintering temperature over 1700 ºC, the 6H-SiC is generally expected to largely present in the specimen (Willardson and Weber, 1998) and this agrees with the findings here.

Table 5.1 Raman modes for different SiC polytypes. LO: longitudinal optical mode. TO：transverse optical mode.

SiC Polytype	Raman Modes Position (cm^{-1})		Reference
6H (active modes in frequency range of 700-1300cm-1)	TO	789 (strong)	(Feldman et al., 1968)
		767 (weak)	
		798(weak)	
		888 (weak)	
	LO	969	
	TA	148	
		240	
4H	TO	757	(Feldman et al., 1968)
		797	
	LO	966	
	TA	202	
		264	
3C	TO	798	(Debernardi et al., 1999)
	LO	972	(Feldman et al., 1968)
	LO-TO splitting	176	(Debernardi et al., 1999)

5.2.2 SiC indentation parameters

Figure 5.2 shows an example of a 24.5 N SiC indentation on the surface. The half indentation diagonal length, *a*, was measured from the OM (Table 5.2). The Raman peaks of the SiC indentation are not as strong as the FLM and the peak shift with respect to the applied stress was small. The crack tip was not able to be distinguished from Raman scan along the crack path, which leads to the difficulties in direct measurement of crack lengths by Raman line scan. The radial crack length*, c,* for SiC was measured from OM first then the underestimation of the crack length in OM was corrected by the method described in Section 4.3.3 with the assumption that

the resolution of OM is ~89 nm. The SiC materials in use is mainly consisted of 6H-SiC which normally has a flat R-curve behaviour (Li et al., 1989); and the grain size of the SiC is fine (6 μm), so the method in Section 4.3.3 can be used here.

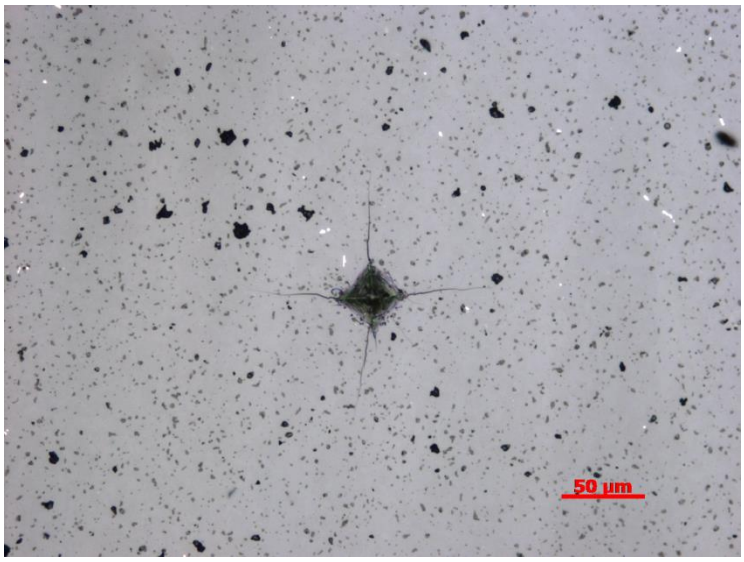


Figure 5.2 Optical micrograph of a 24.5 N indentation on SiC surface.

In the Equation 4.2, the COD of 44.5 nm was used as the input for δ, and the 'real' radial crack length was represented by (c' +Δc) where c' is the radial crack length measured by OM, and Δc is the correction for the measurement from OM.

$$\delta = \frac{4KE\sqrt{c}}{\pi(1-v^2)}\left(Ax^{\frac{1}{2}} + Bx^{\frac{3}{2}} + Cx^{\frac{5}{2}}\right)$$

where $A = \sqrt{\pi/2}\sqrt{(c' + \Delta c)/a}$; $B = 0.011 + 1.8197\ln((c' + \Delta c)/a), C = -0.6513 + 2.121\ln((c' + \Delta c)/a)$

The radial crack tip fracture toughness of SiC has not been independently measured and here we use K_{SiC} measured previously in our group by single edge notched beam method (2.5 MPa$\sqrt{\mathrm{m}}$). Young's modulus E_{SiC} = 430 GPa, Poisson's ratio ν = 0.18. For each indentation load, *Δc* was calculated by the iteration and the corrected *c* was shown in Table 5.2. The corrected radial crack lengths were then used for all the calculations relating to SiC indentation parameters.

Table 5.2 Indentation parameters of SiC under different loads. *a* is the half indentation diagonal length. *c'* is the crack length measured directly by optical microscope. *c* is the corrected value by considering the underestimation of OM.

load (N)	a (μm)	stdev of a	c' (μm)	Δc	c (μm)	stdev of c
9.8	12.2	0.7	40.1	14.0	54.1	2.5
24.5	20.7	0.6	76.9	16.7	93.6	3.8
49	27.1	1.5	123.9	18.5	142.4	6.0
98	44.1	1.3	213.7	20.5	234.2	8.3

5.2.3 SiC indentation cracking

The cross sections of the 49 N SiC indentations were investigated by serial polishing. Figure 5.3 shows cross-sectional image of a 49 N indentation with indentation edge parallel to the polishing surface and lateral cracking was found underneath the surface. The depth of the lateral crack (~31 μm) is close to the average half-diagonal length of the 49 N indentations (27.1±1.5 μm).

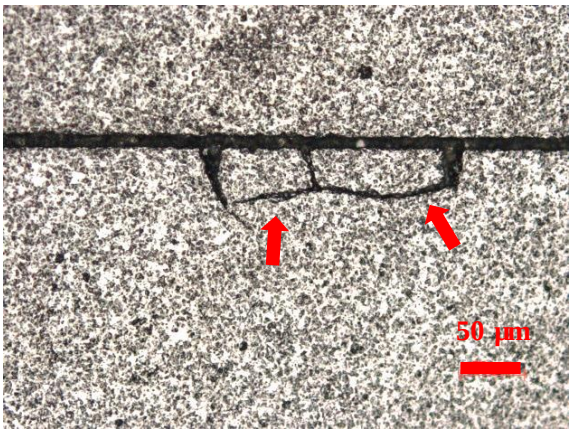


Figure 5.3 Cross-sections of 49 N SiC indentations with indentation edge parallel to the polishing surface, showing the presence of the lateral crack (red arrow).

Previous researchers have found the indentation loads used (9.8 N – 98 N) in this work generate radial-median cracks on SiC (Lankford and Davidson, 1979, Magnani et al., 2000, Laugier, 1987), whereas the Palmqvist crack system work for the loads below 10 N (Li et al., 1989). Therefore, the *c* measured here for SiC indentations refers to the radial-median crack length.

5.2.4 Surface profiles around SiC indentations

For SiC, the uplift zone around the indentation was also found by microXAM mapping (Figure 5.4). From the line scan surface profiles, lateral crack lengths for different loads were the calculated (Table 5.3) using the method described in Section 4.3.5. The lateral crack lengths of the SiC determined by simple plate method are found

close to the radial crack length, and this is similar to the findings for alumina indentation.

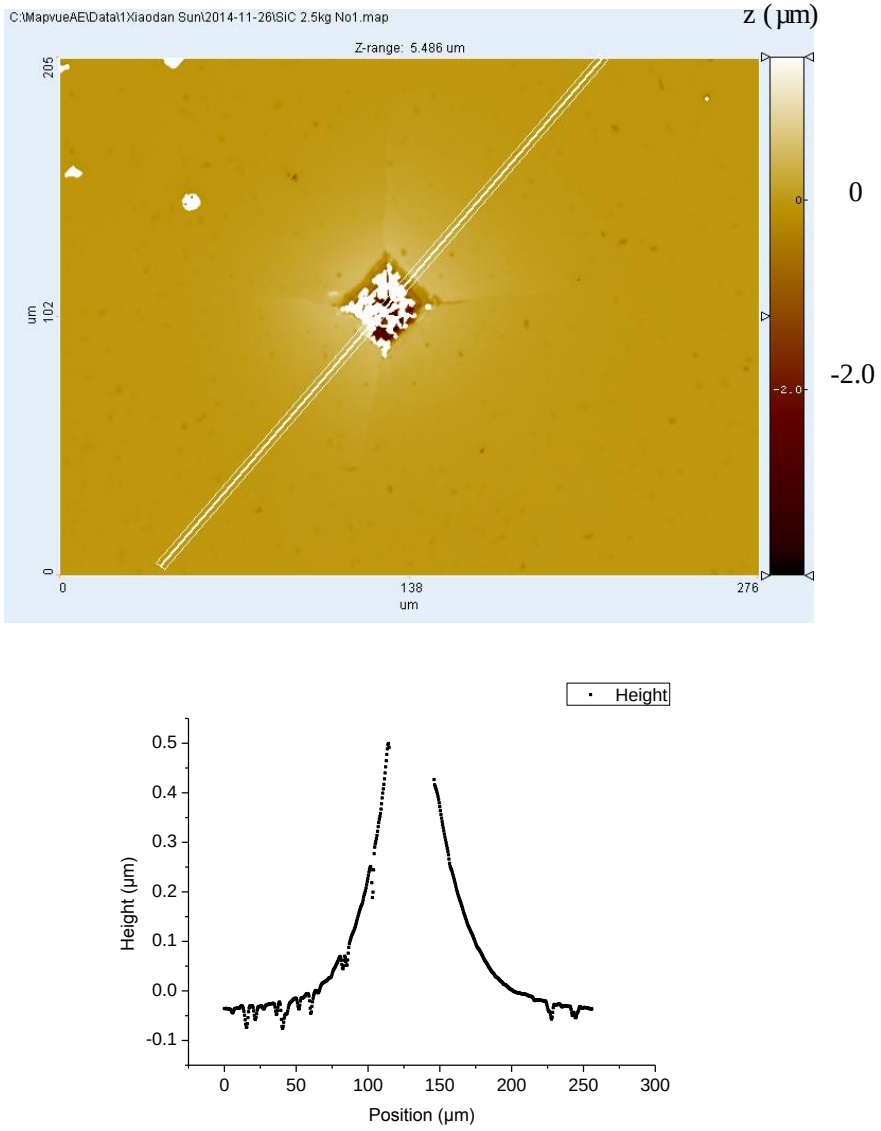


Figure 5.4 (a) Direction of the line scan on the mapping of the surface profile of the 24.5 N SiC indentation and the (b) line scan profile.

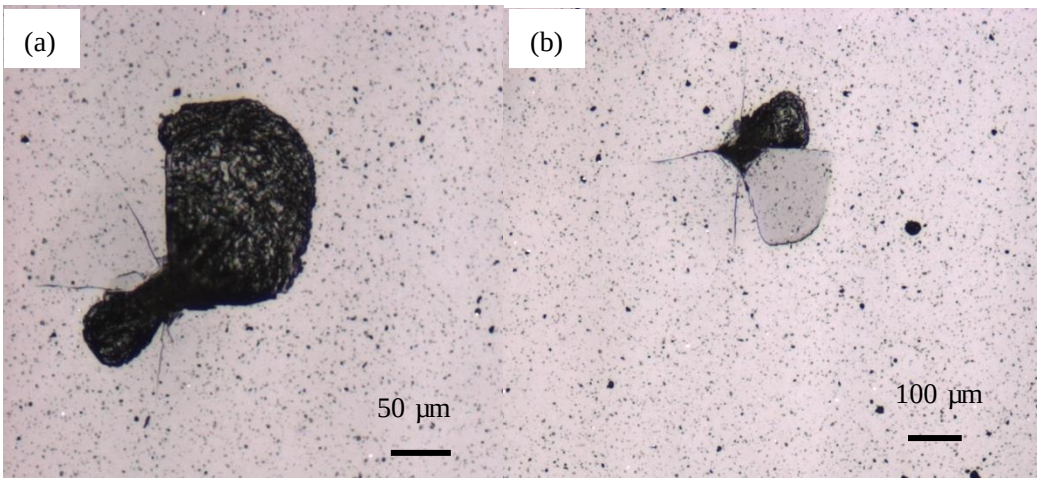
Sometimes the SiC materials above the lateral crack were chipped (Figure 5.5b) or completely delaminated (Figure 5.5a), and Figure 5.5a and 5.5b show the lateral cracks seem to join the tip of the radial crack and this also indicates that the length of

the lateral crack is similar to the radial crack length. Similar chipping phenomenon was also found (Figure 5.5c) by Yonezu et al. (2009) in indentations on TiB2 and was regarded as the delamination of the material above the lateral crack.

Table 5.3 Lateral crack lengths c^* of 9.8 N, 24.5 N, 49 N and 98 N indentations obtained from simple plate model in comparison with radial crack length, c.

	Lateral crack length c* measured by surface profilometer (μm)	stdev of c*	Radial crack length c (μm)	stdev of c
9.8 N	47.8	3.1	54.1	2.5
24.5 N	81.8	4.7	93.6	3.8
49 N	132.8	7.7	142.4	6
98 N	210	20.3	234.2	8.3

.



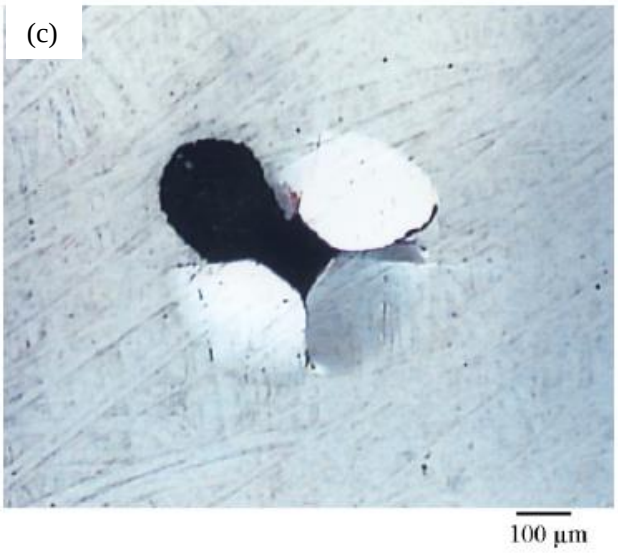


Figure 5.5 Optical images of (a) 49 N indentation and (b) 98 N indentation on SiC surface and (c) of a 294.3 N indentation on the surface of the TiB_2 (Yonezu et al., 2009).

In conclusion, the lateral cracks of the SiC indentations have the similar length as the radial cracks and the lateral cracks seem to join the radial crack tips of the indentations.

5.2.5 Calibration of the PS coefficient of SiC Raman peak

The 789 cm^{-1} peak of 6H (α)-SiC, which represents the A_{1t} TO mode (DiGregorio et al., 1992), had the strongest intensity, was not overlapped with other peaks and was found more sensitive to stress than other 6H peaks in the spectrum, therefore was chosen as the peak to calibrate the PS coefficient. This peak has been proved to

work well in measuring residual stress in SiC whiskers (DiGregorio et al., 1992) and SiC particles (DiGregorio and Furtak, 1992). The peak fitting method has been described in Chapter 3.

5.2.5.1 Axial resolution of the laser beam on SiC

The method for calibrating PS coefficient of the 789 cm^{-1} peak of 6H (α)-SiC has been previously described in the Section 3.4.5. On an opaque material such as silicon and SiC, the axial resolution can be obtained by measuring the FWHM (full width at half maximum) of the intensity-defocus distance curve (Lipkin and Clarke, 1995). The FWHM of the curve can be measured manually or from the fitting results by using Gaussian-Lorentzian function (Figure 5.6a and b). The error, R^2 of the fitting was found to in the range of 0.96-0.99, which is acceptable. The axial resolutions of the laser beam on single crystal Si (as a reference material) and SiC materials have been summarised in Table 5.4.

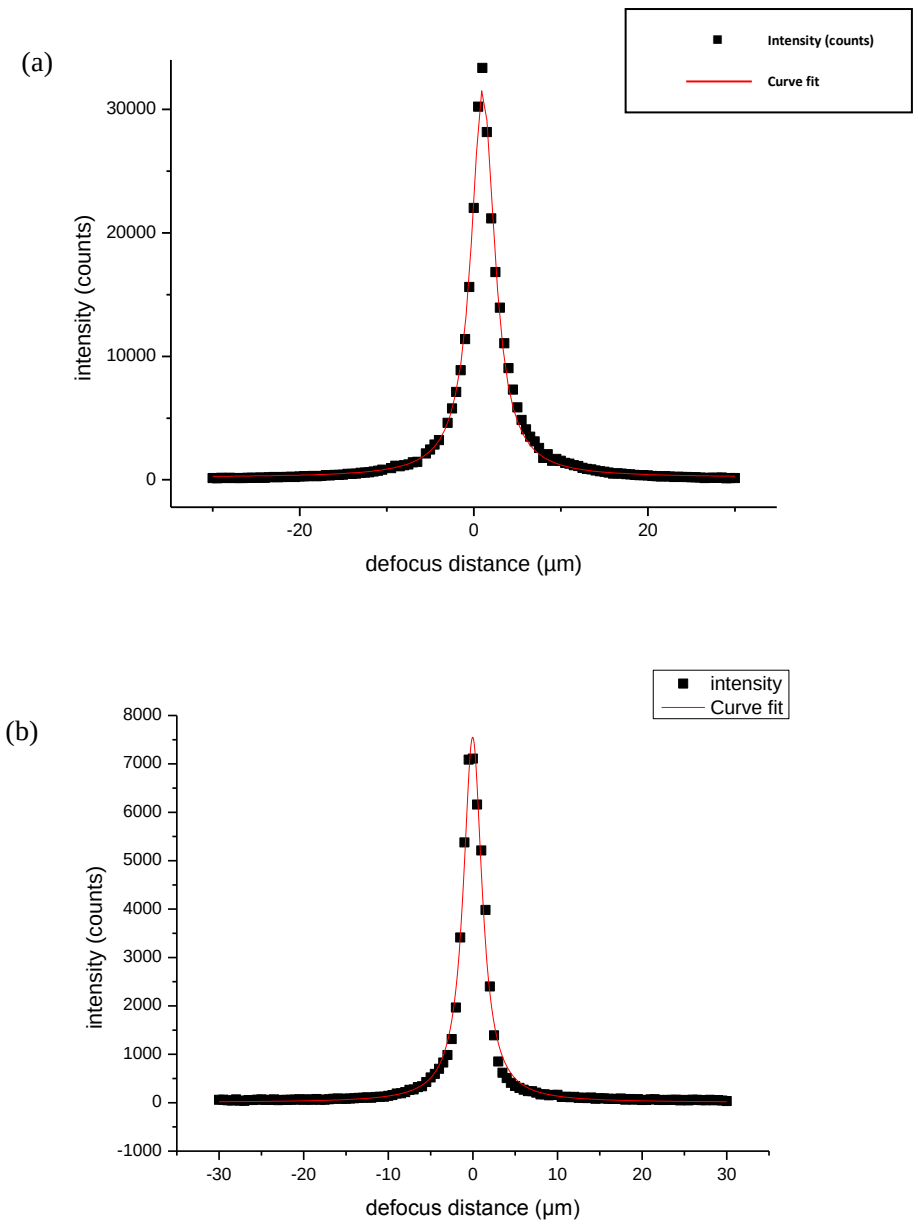


Figure 5.6 Gaussian-Lorentzian fitting for the intensity-defocus distance plots of (a) Si, using 50× objective lens and the step size = 0.5 µm, (b) SiC, using 100×objective lens and the step size = 0.5 µm.

Table 5.4 Measured axial resolutions for SiC and Si under different magnification.

Materials	Lens magnification	FWHM (μm)
SiC	100	3.5
	50	7.4
	20	14.2
Si	100	1.4
	50	3.3
	20	14.4

It is claimed by the manufacturer that the best axial and lateral resolutions are 1μm and 2 μm, respectively. The best lateral resolution of this equipment has been measured by Guo and Todd (2011) on Si and was 1.5 μm. For alumina, the axial resolution has been determined by Guo (2008) in his DPhil thesis and is 3.2 μm under the 100× lens. Here, a slit size of 10 micron was used for all the tests and the axial resolution was found to increase as magnification of the lens increases. The best resolution (1.4 μm) was achieved using Si and is close to that claimed by manufacturer of the equipment.

For measuring the PS coefficient in a polycrystalline sample, the laser beam should sample enough grains to give an accurate average stress value, in which case an objective lens with relatively low magnification and therefore large sampling volume would favour this measurement. However, the lens with low magnification will

degrade the resolution of each acquisition. The grain size of the SiC is around 6 μm, therefore, the 50× objective lens was chosen for the calibration of the PS coefficient and the following residual stress measurements on the surface around the SiC indentation.

5.2.5.2 Line scan on SiC beam for calibration of PS coefficient of 6H-SiC 789 cm^{-1} peak

The SiC beam was loaded on the four point bending jig described in the Section 3.4.5, the laser scanned from the compressive side to the tensile side of the beam and the spectra were collected by the 50× objective lens. In the results (Figure 5.7) the 789 cm^{-1} peak shift decreases consistently with a linear increase of the tensile stress. The PS coefficient (Π) between 789 cm^{-1} peak frequency shift ($\Delta\nu$) and the uniaxial stress was found by linear fitting to be -1.625 ± 0.035 $GPa^{-1}cm^{-1}$ (averaged value for three tests). Considering the stress on the beam was uniaxial, the PS coefficient, Π_m, for the hydrostatic stress, P, was $\Pi_m = 3\Pi$ = -4.88 ± 0.11 $GPa^{-1}cm^{-1}$ ($\Delta\nu = \Pi_m P$). The PS coefficient obtained in this section was then used for the following residual stress measurement in the vicinity of the indentations on SiC,

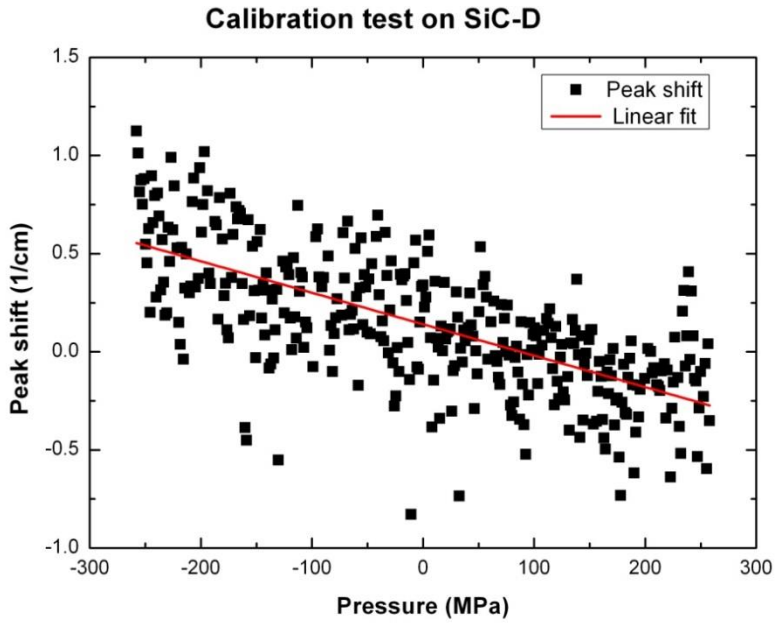


Figure 5.7 A_{1t} peak shift as a function of the applied pressure on the SiC beam.

5.2.6 Line scans on SiC indentations

Line scans were performed (Figure 5.8) on the 9.8 N, 24.5 N, and 49 N indentations on SiC to examine the residual stress around the indentation. There was a great difficulty in fitting the spectra from inside the indentation as the peaks get much broader when the plastic zone was sampled (Figure 5.9) (the implication of broadening effect has been explained in the Section 2.3.4.2). Because the peaks are so close to each other, the broadened peaks cannot be resolved and only the spectra outside the plastic zone were well fitted with the three-peak fitting method. Therefore the peak shifts within in the indentation were not measured here. Residual

hydrostatic stresses on the line scan outside the indentation were then calculated by PS relationship $\Delta\nu = \Pi_m P$ found for the 789 cm^{-1} peak.

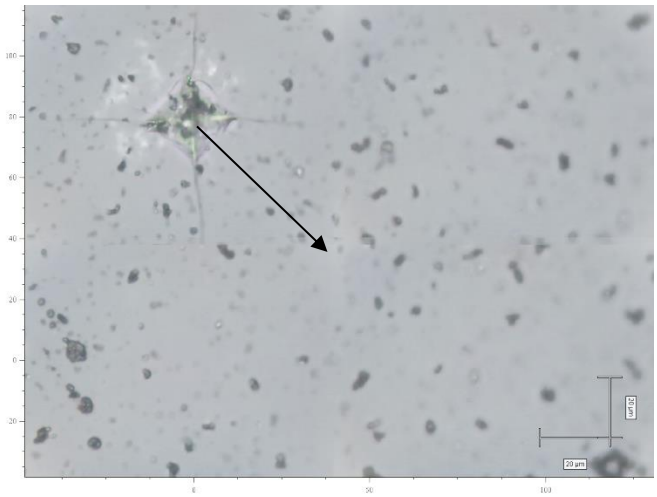


Figure 5.8 Line scan direction on 9.8 N indentation on SiC.

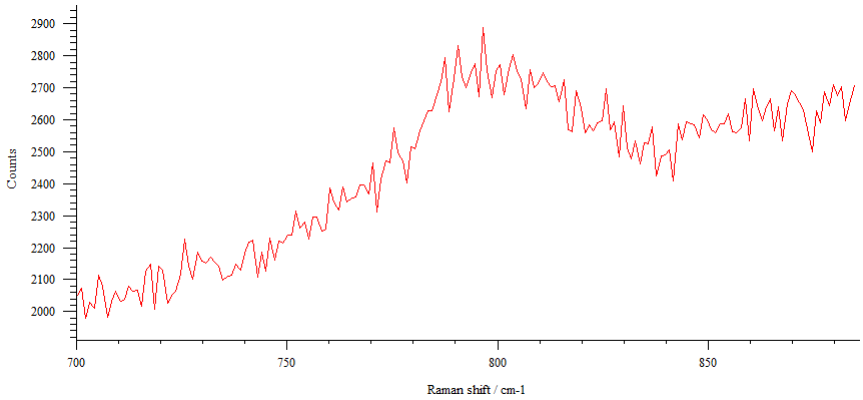
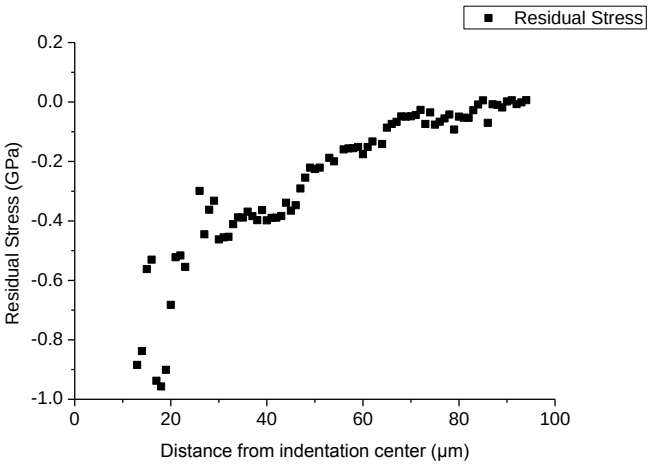
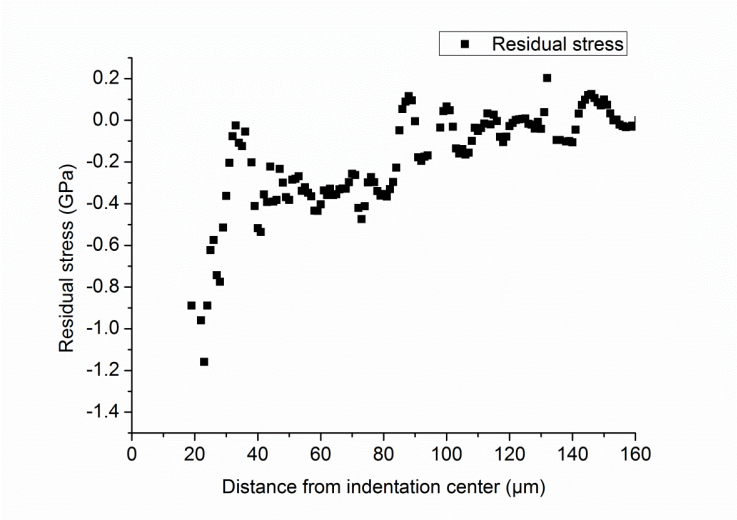


Figure 5.9 Raman spectrum from the point inside the 9.8 N SiC indentation.

(a)



(b)



(c)

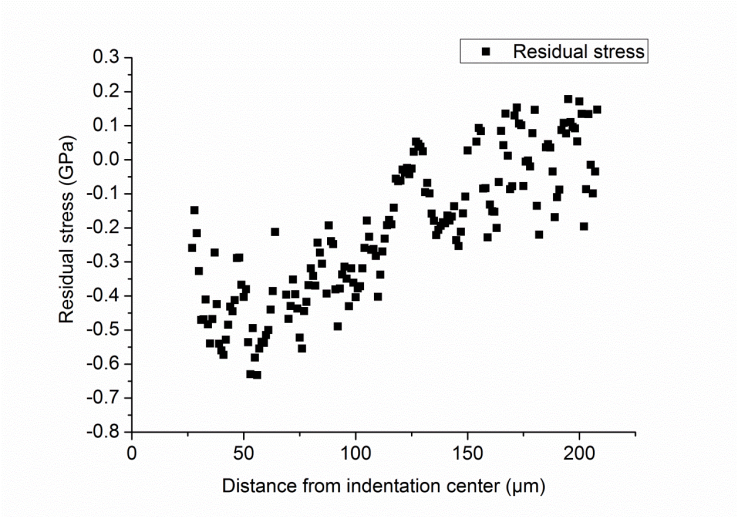


Figure 5.10 Hydrostatic residual stresses on the line scan near (a) 9.8, (b) 24.5 and (c) 49 N SiC indentations as a function of the distance from indentation center.

According to author's knowledge, this is the first time the residual stress near the SiC indentations has been measured. Similar to line scans on alumina, the residual stress becomes less compressive when away from the indentation (Figure 5.10). However, the residual stress profiles have wavelike fluctuations and this is probably because of nonuniformity of the composition or the polytypes of the SiC from one to another grains and because the cavities on the surface scattered the laser and relaxed the residual stresses on the surface locally. The residual stresses near the 49 N indentation were found less compressive near the indentation edge and this will be further discussed in Chapter 6.

In this section, the residual stress field near the SiC indentations have been successfully measured. In Chapter 6, a residual stress model was proposed based on the understanding of alumina indentations. The residual stress profiles on the SiC indentations were used in Chapter 6 to further test the validity of the model.

5.2.7 TZP indentation parameters

Figure 5.11a shows an example of the 98 N TZP indentations. Previous works (Jones et al., 1987, Liang et al., 1990, Reece et al., 1992, Nawa et al., 2013) on TZP have all shown that under the load of 500 N, the Vickers indentations on TZP form Palmqvist shape cracks and lateral cracks were not found. The TZP indentations

were therefore assumed to follow the Palmqvist crack system and the parameters, *a* and *l* (Palmqvist crack length), were measured from the OM and were corrected by the same method as SiC (Table 5.5). K_{TZP} measured by single edge notched beam method was 4.6 MPa$\sqrt{\mathrm{m}}$, Young's modulus, Young's modulus E_{TZP} = 213 GPa, Poisson's ratio v = 0.31. For the 9.8 N TZP indentation, the crack was often not seen near the indent (Figure 5.11b).

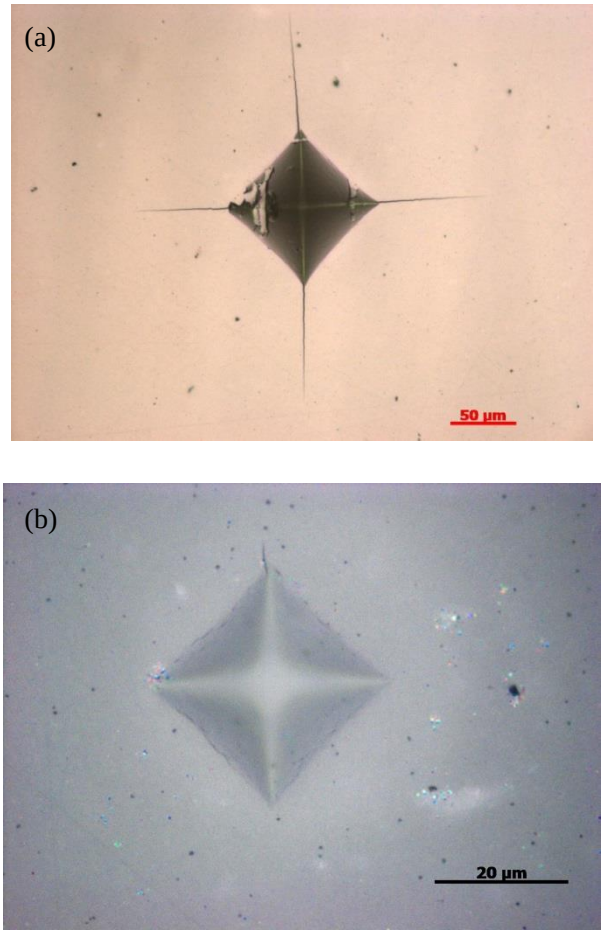


Figure 5.11 Optical images of the (a) 98 N and (b) 9.8 N TZP indentations.

Table 5.5 Indentation parameters of TZP under different loads. *a* is the half indentation diagonal length. *l** is the Palmqvist crack length measured directly by optical microscope. *l* is the corrected value by considering the underestimation of OM.

	load (N)	*a*	stdev of *a*	*l**	*Δl*	*l*
TZP	9.8	17.9	0.1	N/A	N/A	N/A
	24.5	27.6	0.9	24.7	1.2	25.9
	49	39.4	1.9	48.6	1.3	49.9
	98	58.5	1.0	81.3	1.9	83.1

Y-TZP is a material with a strong R curve (Anderson and Braun, 1990). For TZP with a very fine grain size, the R-curve effect is mostly attributed to the well-known tetragonal-monoclinic phase transformation around the crack tip (Casellas et al., 2001). The crack opening displacement will deviate from one without the R curve effect and was difficult to model (Fünfschilling et al., 2011). So far, there has been no published work to characterise the crack opening displacement of the Y-TZP. However, it can be noticed from the work done by Fünfschilling et al. (2011) on materials with strong R-curve behaviours that within the distance below 5 μm from the crack tip, the crack opening displacement profile was pretty close to the profile with no R-curve (the difference was less than 10%). Table 5.5 shows results following the methods described in Section 4.3.3, the calculated underestimation of Palmqvist crack length was normally less than 2 μm. Therefore in this distance to the crack tip, the error introduced by the method in Section 4.3.3 is expected to be small.

Therefore, the Palmqvist crack lengths corrected in the Table 5.5 were accepted as the indentation parameters for the TZP indentations.

5.2.8 TZP Indentation cracking

To obtain the cross-sectional image of the TZP indentation, a 49 N TZP indentation was made on a polished beam and then the beam was broken from the indentation site in the bending manner. Figure 5.12a shows the half of the indentation imprint on the surface. Figure 5.12b shows the cross-section of the indentation on the fracture surface and no lateral cracking was found underneath the TZP indentation.

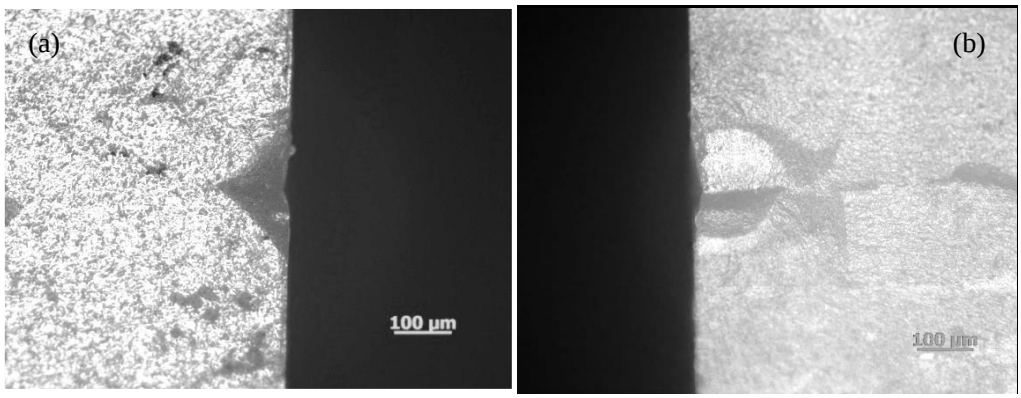


Figure 5.12 Optical images of the (a) indentation imprint on the indented surface (b) cross-section of the indentation on the fracture surface.

5.2.9 Raman spectrum of TZP

The Raman spectra of 3Y-TZP were collected in a spectrum range of 0~1000 cm^{-1} on the free surface with no residual stress (Figure 5.13) and near the indentation (Figure 5.14). When there was no stress, only the peaks corresponding to the tetragonal zirconia phase could be distinguished; and the peaks corresponding to the monoclinic phase were seen when sampled near the indentation. This indicates that the tetragonal zirconia phase largely existed in the sample and phase transformation may have taken place on the surface due to residual stress.

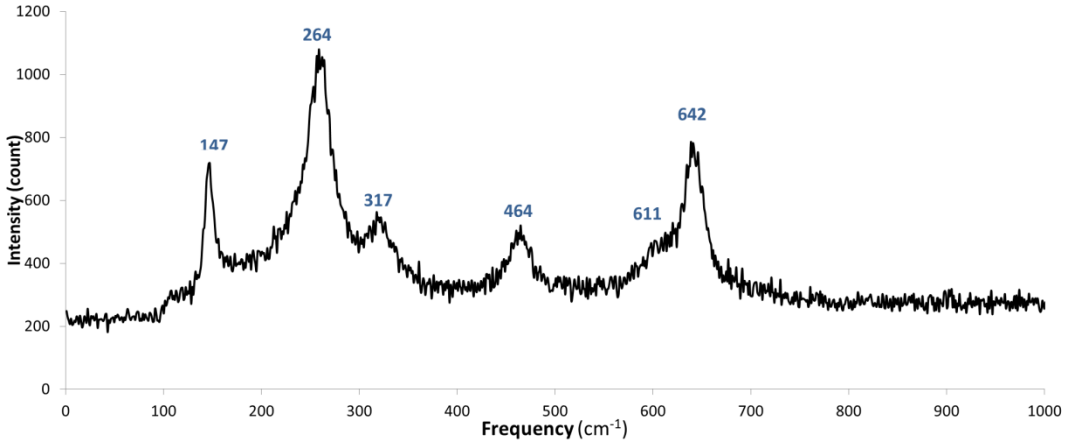


Figure 5.13 Raman spectrum collected from the free surface of the TZP specimen, showing the peaks corresponding to tetragonal zirconia phase.

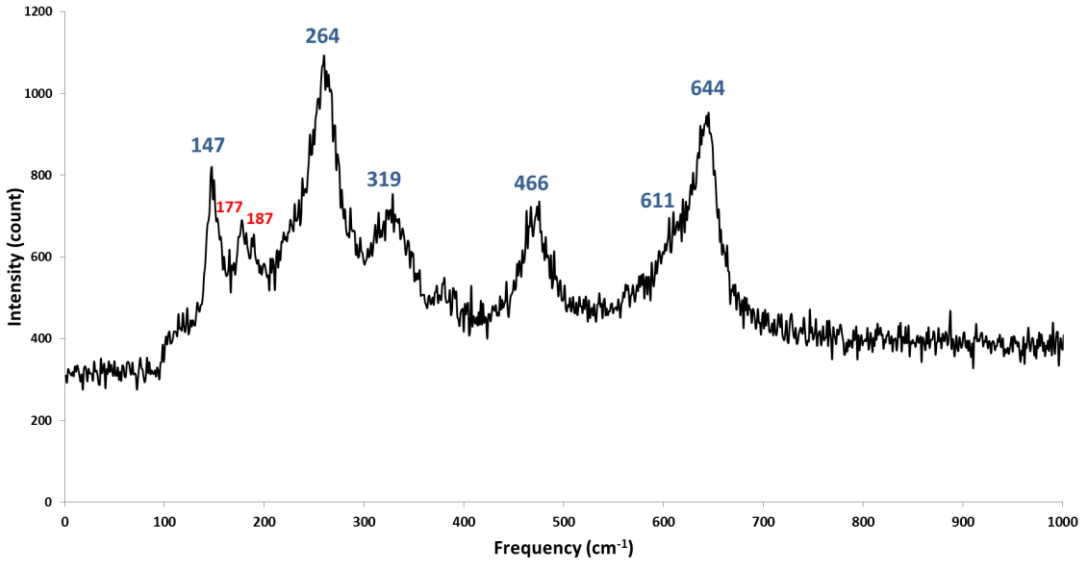


Figure 5.14 Raman spectrum collected from the point close to an indentation on TZP specimen, showing the peaks corresponding to tetragonal (blue labels) and the monoclinic (red labels) zirconia phase.

The Raman peak of the tetragonal zirconia phase at a frequency of 642 cm^{-1} was selected for the measurement of stress, as Kourouklis and Liarokapis (1991) have found that this peak showed the highest peak shift in response to the applied stress among the Raman peaks of tetragonal zirconia phase. The piezospectroscopic coefficient of this peak with response to the uniaxial stress was determined to be –1.83 $GPa^{-1}cm^{-1}$ from the calibration work from Belnap et al. (1994) and has been used in the following stress measurement. The peak fitting method has been described in Chapter 3. The axial resolution of the laser beam on the TZP surface under the 100× lens was determined by the method described in Section 5.2.5.1.

The FWHM of the intensity-defocus distance curve is 9.8 μm and tens of TZP grains (grain size: 0.41 μm) will be sampled under the lens (100×) with best resolution. Therefore, the 100× lens was used for all the following line scans on the TZP indentations.

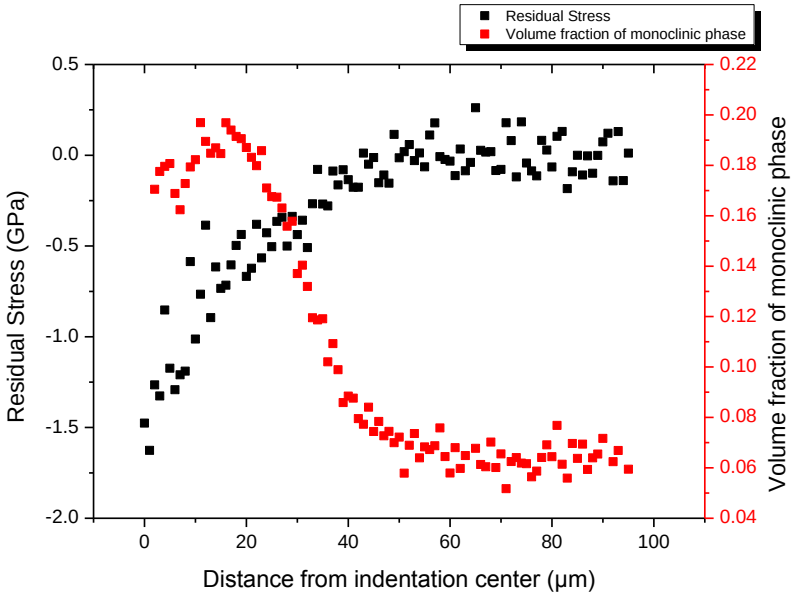
5.2.10 Raman line scans on TZP indentations

The line scans similar to that on SiC have been done on 9.8, 24.5, 49 N indentations on TZP. The shift of the 642 cm^{-1} peak was recorded and then converted to the stress as a function of the distance from the indentation center (Figure 5.15).

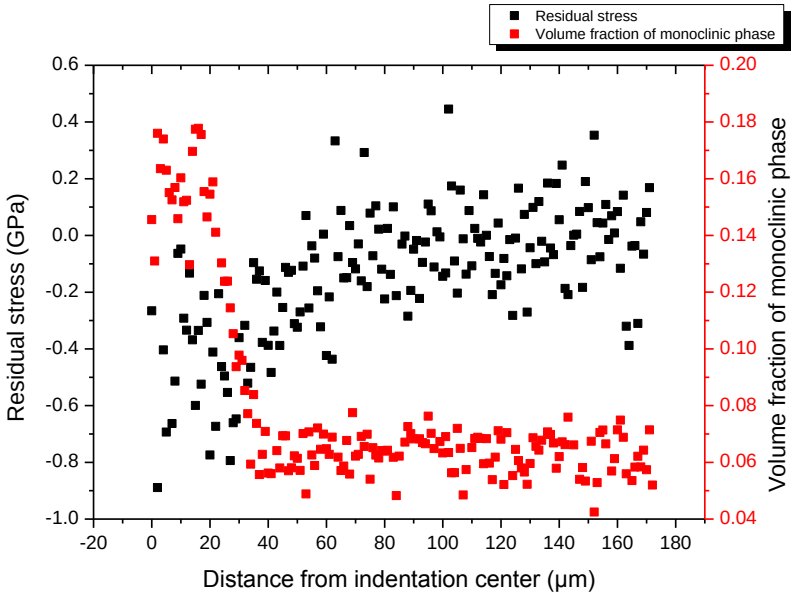
The content of the monoclinic phase, V_m, was calculated by the equation proposed by Katagiri et al. (1986) in the following, which was reported by Muñoz Tabares and Anglada (2010) to have the least error compared with other proposed equations regarding monoclinic concentration. The intensities of Raman peaks at around 177 and 187 cm^{-1}, I_m^{177} and I_m^{187}, corresponding to monoclinic phase and their adjacent peak at around 147 cm^{-1}, I_t^{147}, corresponding to the tetragonal phase were used in these equations. The peaks were fitted using multiple curves (described in Section 3.4.4).

$$V_m = \frac{0.5(I_m^{177} + I_m^{187})}{2.2I_t^{147} + 0.5(I_m^{177} + I_m^{187})}$$

(a)


Residual Stress
Volume fraction of monoclinic phase
Residual Stress (GPa)
Volume fraction of monoclinic phase
Distance from indentation center (μm)

(b)


Residual stress
Volume fraction of monoclinic phase
Residual stress (GPa)
Volume fraction of monoclinic phase
Distance from indentation center (μm)

(c)

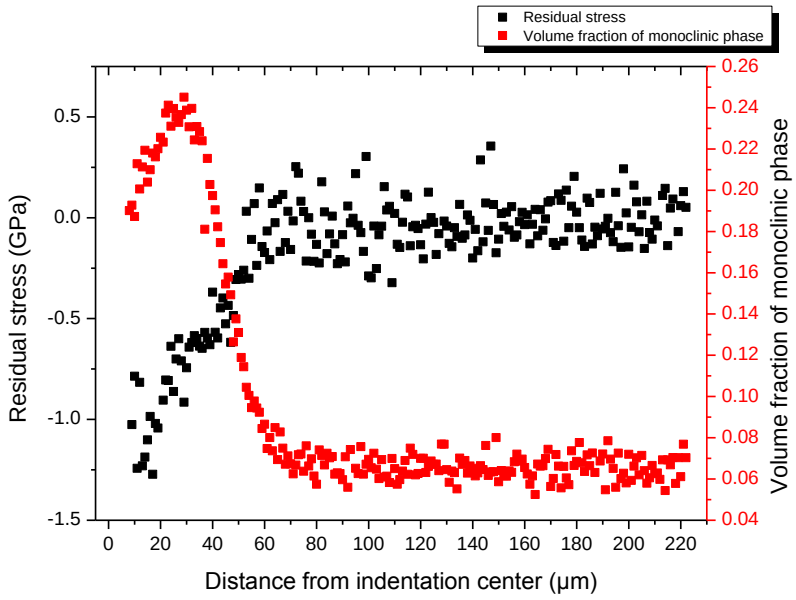


Figure 5.15 Shift of 642 cm^{-1} peak of the tetragonal zirconia phase and the volume fraction of monoclinic phase as a function of the distance from the indentation center on (a) 9.8, (b) 24.5 and (c) 49 N indentations.

The profiles of the volume fraction of the monoclinic zirconia phase vs distance curves generally follow the trend of residual stress profiles (Figure 5.15). The volume fraction of the monoclinic zirconia phase increases from indentation center to near the indentation edge then decreases to where there is no residual stress (Figure 5.15). On the free surface of the TZP sample, ~6.5% monoclinic zirconia was found which was introduced during processing of TZP, which is similar to the finding from Reece et al. (1992) on Y-TZP indentation line scans. The residual stress profiles were further discussed in Chapter 6.

The highest concentration of the monoclinic zirconia phase was found around the edge of the indentations. Reece et al. (1992), Behrens et al. (1993), Gogotsi and Lomonova (2000) and Nemli et al. (2012) have reported similar findings on TZP indentation studies. It has been reported that the tensile and shear stresses are more likely to induce phase transformation from tetragonal to monoclinic phase than by compressive stresses because of the transformation dilatation of 4% (Behrens et al., 1993). For ceramics more brittle than TZP (Lawn et al., 1980), the tensile stress around the indentation can be relaxed by radial-median and lateral cracking. The TZP indentations have the Palmqvist cracks which have much shallower depth than the radial-median crack (Kaliszewski et al., 1994, Sullivan and Lauzon, 1986), and have no lateral crack. Therefore, the residual tensile stresses around the plastic zone are expected to be less relaxed by cracking and will be enhanced by dilatation due to transformation upon unloading of the indenter (Reece et al., 1992). The edge of the indentation has the highest level of tensile and shear stresses (Pittayachawan et al., 2009). This explains why the highest transformation occurs around the edge of the impression. The center of the indentation has higher compressive stresses, however, the phase transformation is more easily induced by tensile and shear stresses than compressive stress (Behrens et al., 1993). Therefore the amount of transformation found in the indentation center was less than the edge of the indentation.

In this section, the residual stress fields and the phase transformation around the TZP indentations were characterised. The phase transformation was introduced by the stresses. The highest amount of phase transformation was found near edge of the indentation and a large amount of transformation was also found in the indentation center.

5.2.11 TZP indentation surface profiles

For TZP indentations, an uplift zone was also found on the surface (Figure 5.16) of the indentation. The line scan profiles for different indentation loads were shown in Figure 5.17.

As there is no lateral cracking underneath the surface, this is mainly due to the phase transformation around the indentation (Reece et al., 1992). Compared with the distribution profiles of the volume fraction of the monoclinic phase, the surface uplift around the indention measured from the line scan perpendicular to the indentation edge was found to have the profile matching with distribution of the volume fraction of the monoclinic phase from the edge of the indentation to the distance away from the edge (Figure 5.17 a-c). This clearly shows that the amount of the uplift around the indentation surface was directly connected with the amount of the phase transformation. This agrees with the findings from Gogotsi et al. (1995) that the

surface bloated the most on the edge of the indentation where there had the most transformation.

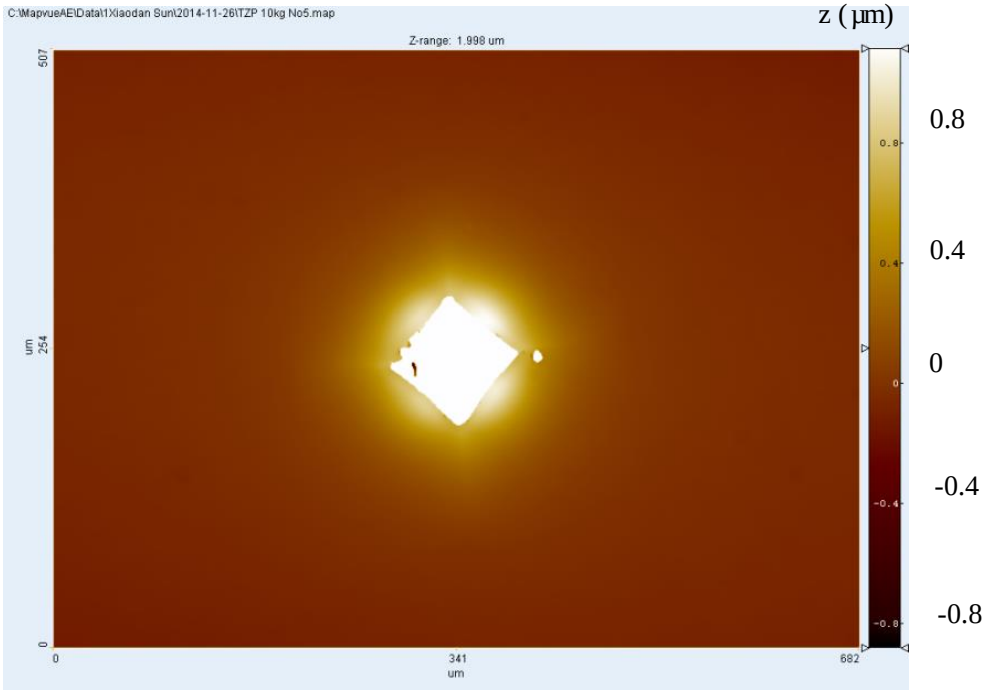


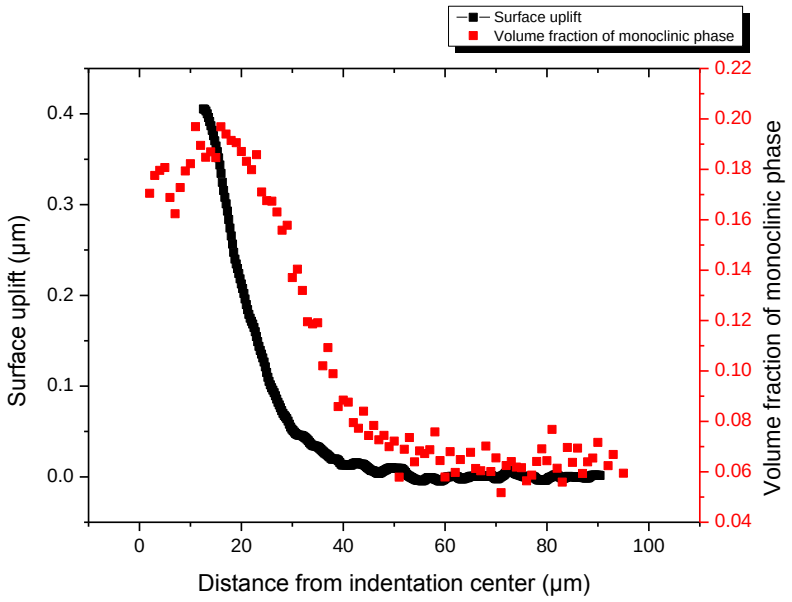
Figure 5.16 Surface profile of the 24.5 N TZP indentation by MicroXAM mapping.

To characterise the correlation between surface uplift and the volume fraction curve, the Pearson correlation factors of these two sets of data were determined in Origin software. Only the range of *x* (direction from indenter center) where both information of the surface uplift and the volume fraction of the monoclinic phase were collected was considered. As the surface uplift curve has more data points than the volume fraction curve and some indentation profiles have longer tails than others, to make

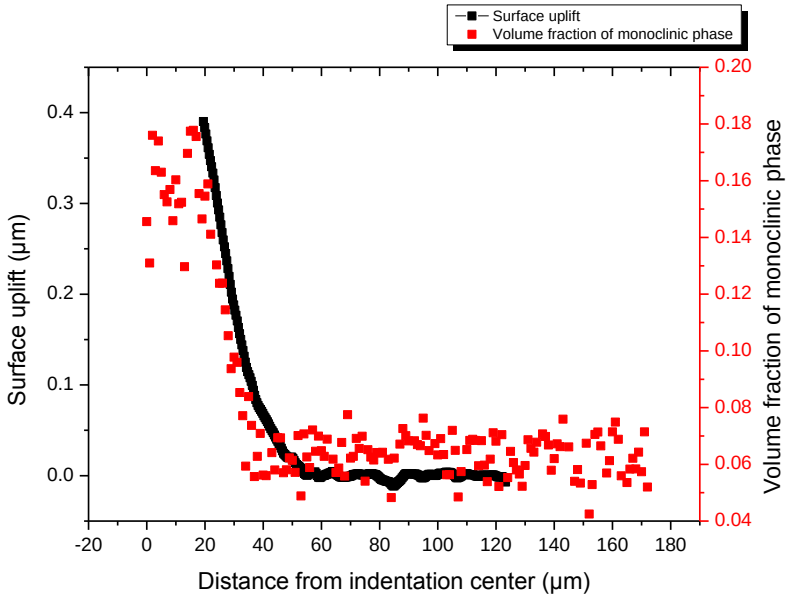
the Pearson correlation meaningful, only the surface uplift points corresponding to the same x as the volume fraction data points, and only the data between the indentation edge and 4*a* (twice the indentation diagonal length) from the indentation center were selected.

Pearson correlation factors of the surface uplift and the volume fraction of the monoclinic phase curves for the 9.8N, 24.5N and 49N TZP indentations are 0.855, 0.913 and 0.978, respectively. Evans (1996) suggests that correlation factors in the range 0.80-1.00 (64% to 100%) represent a “very strong” level of correlation. This strongly supports the observation above that the amount of uplift around the indentation surface was directly connected with the amount of the phase transformation. This dependence increases as the load increases. This is probably because compared with the perfectly smooth surface, any disturbances (like the grain boundaries, dirt, microcracks) may degrade the correlation. This effect is more significant when the indentation load is small and the surface profile is sensitive to these disturbances.

(a)


Surface uplift
Volume fraction of monoclinic phase
Surface uplift (μm)
Volume fraction of monoclinic phase
Distance from indentation center (μm)
0.0
0.1
0.2
0.3
0.4
0.04
0.06
0.08
0.10
0.12
0.14
0.16
0.18
0.20
0.22
0
20
40
60
80
100

(b)


Surface uplift
Volume fraction of monoclinic phase
Surface uplift (μm)
Volume fraction of monoclinic phase
Distance from indentation center (μm)
0.0
0.1
0.2
0.3
0.4
0.04
0.06
0.08
0.10
0.12
0.14
0.16
0.18
0.20
-20
0
20
40
60
80
100
120
140
160
180

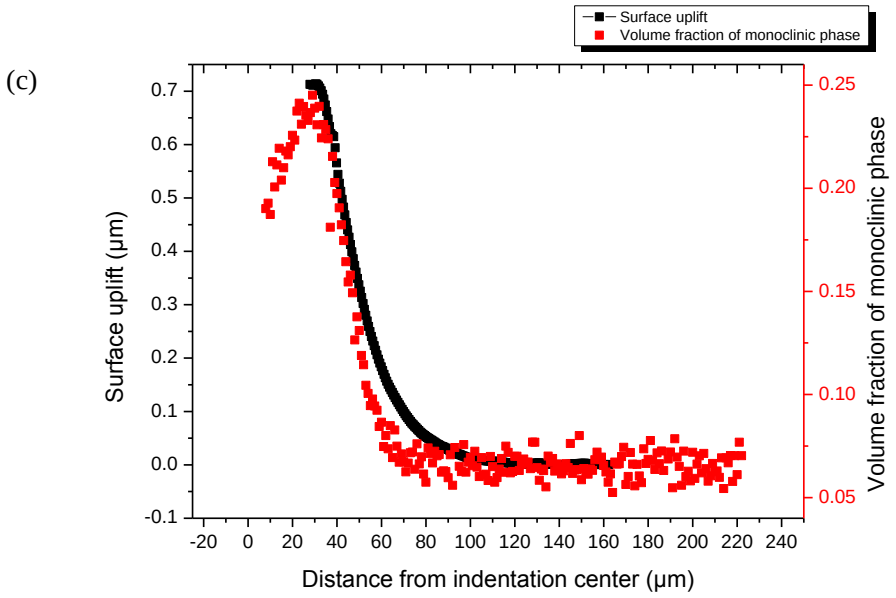


Figure 5.17 Surface profile and the volume fraction of monoclinic phase as a function of the distance from the indentation center on (a) 9.8, (b) 24.5 and (c) 49 N TZP indentations.

5.3 Conclusions

The main purpose of this chapter was to measure indentation parameters and the residual stresses for the SiC and TZP indentations and the findings will be used in Chapter 6 to test the residual stress model derived from alumina. Several key findings are listed below:

SiC:

- The indentation parameters of SiC indentations were measured and corrected using the method described in Section 4.3.3.

- The Raman spectra of SiC were characterised, and the 6H-SiC polytype was found to be the primary polytype. The 6H-SiC A_{1t} peak (789 cm^{-1}) was selected for the residual stress study due to its strong peak intensity and less overlapping with other peaks. The PS coefficient of this peak was found to be -4.88 ± 0.11 $GPa^{-1}cm^{-1}$.

- Lateral cracking was found beneath the SiC indentations. The depth of the lateral crack of the SiC indentation was found to be close to the half diagonal length. The lateral crack lengths of the SiC indentations determined from the surface profile are close to the radial crack length, and this is similar to the findings for alumina indentations.

- The residual stresses around the 9.8 N, 24.5 N and 49 N indentations on SiC were measured and more analyses will be made in Chapter 6 to test the new model.

TZP:

- The indentation parameters for TZP indentations were measured and corrected using the method described in Section 4.3.3. Lateral cracking was not found beneath the TZP indentations.

- The Raman spectra of TZP were characterised. In as annealed TZP, the tetragonal phase was in the majority and the monoclinic phase had the minor volume fraction.

- The residual stresses around the 9.8 N, 24.5 N and 49 N indentations in TZP were measured and more analyses will be made in Chapter 6 to test the new model

- The highest volume fraction of the monoclinic zirconia phase was found near the edge of the TZP indentation this was thought to be caused by the high concentration of the tensile and shear stresses.

- Around the TZP indention, the surface uplift was found to have the profile matching with the distribution of the volume fraction of the monoclinic phase.

References

ANDERSON, R. M. & BRAUN, L. M. 1990. Technique for the R‐Curve Determination of Y‐TZP Using Indentation‐Produced Flaws. Journal of the American Ceramic Society, 73, 3059-3062.

BEHRENS, G., DRANSMANN, G. W. & HEUER, A. H. 1993. On the Isothermal Martensitic Transformation in 3Y‐TZP. Journal of the American Ceramic Society, 76, 1025-1030.

BELNAP, D. J., TSAI, J.-F. & SHETTY, D. K. 1994. Direct measurement of crack shielding in ceramics by the application of Raman microprobe spectroscopy. Journal of materials research, 9, 3183-3193.

CASELLAS, D., ALCALA, J., LLANES, L. & ANGLADA, M. 2001. Fracture variability and R-curve behavior in yttria-stabilized zirconia ceramics. Journal of materials science, 36, 3011-3025.

CHANG, K. J. & COHEN, M. L. 1987. Ab initio pseudopotential study of structural and high-pressure properties of SiC. Physical Review B, 35, 8196.

DEBERNARDI, A., ULRICH, C., SYASSEN, K. & CARDONA, M. 1999. Raman linewidths of optical phonons in 3 C-S i C under pressure: First-principles calculations and experimental results. Physical Review B, 59, 6774.

DIGREGORIO, J., FURTAK, T. & PETROVIC, J. 1992. A technique for measuring residual stress in SiC whiskers within an alumina matrix through Raman spectroscopy. Journal of Applied Physics, 71, 3524-3531.

DIGREGORIO, J. F. & FURTAK, T. E. 1992. Analysis of Residual Stress in 6H‐SiC Particles within Al2O3/SiC Composites through Raman Spectroscopy. Journal of the American Ceramic Society, 75, 1854-1857.

EVANS, J. D. 1996. Straightforward statistics for the behavioral sciences, Brooks/Cole.

F NFSCHILLING, S., FETT, T., OBERACKER, R., HOFFMANN, M. J., SCHNEIDER, G. A., BECHER, P. F. & KRUZIC, J. J. 2011. Crack‐Tip Toughness from Vickers Crack‐Tip Opening Displacements for Materials with Strongly Rising R‐Curves. Journal of the American Ceramic Society, 94, 1884-1892.

FELDMAN, D., PARKER JR, J. H., CHOYKE, W. & PATRICK, L. 1968. Phonon Dispersion Curves by Raman Scattering in SiC, Polytypes 3 C, 4 H, 6 H, 1 5 R, and 2 1 R. Physical review, 173, 787.

GOGOTSI, G., DUB, S., LOMONOVA, E. & OZERSKY, B. 1995. Vickers and knoop indentation behaviour of cubic and partially stabilized zirconia crystals. Journal of the European Ceramic Society, 15, 405-413.

GOGOTSI, G. & LOMONOVA, E. 2000. A micro-Raman study of phase transformations of zirconia crystals upon introduction of a vickers indentor. Refractories and industrial ceramics, 41, 191-195.

GUO, S. 2008. Fluorescence Microscopy Investigation on Residual Stresses in Alumina-based Ceramics.

GUO, S. & TODD, R. I. 2011. Quantitative optical fluorescence microprobe measurements of stresses around indentations in Al2O3 and Al2O3/SiC nanocomposites: The influence of depth resolution and specimen translucency. Acta materialia, 59, 2637-2647.

HARADA, K., SHINYA, A., YOKOYAMA, D. & SHINYA, A. 2013. Effect of loading conditions on the fracture toughness of zirconia. Journal of prosthodontic research, 57, 82-87.

JONES, S., NORMAN, C. & SHAHANI, R. 1987. Crack-profile shapes formed under a Vickers indent pyramid. Journal of Materials Science Letters, 6, 721-723.

KALISZEWSKI, M. S., BEHRENS, G., HEUER, A. H., SHAW, M. C., MARSHALL, D. B., DRANSMANRI, G. W., STEINBRECH, R. W., PAJARES, A., GUIBERTEAU, F. & CUMBRERA, F. L. 1994. Indentation Studies on Y2O2 ‐ Stabilized ZrO2: I, Development of Indentation ‐ Induced Cracks. Journal of the American Ceramic Society, 77, 1185-1193.

KATAGIRI, G., ISHIDA, H., ISHITANI, A. & MASAKI, T. 1986. Direct determination by a Raman microprobe of the transformation zone size in Y 2 O 3 containing tetragonal ZrO 2 polycrystals. Advances in ceramics, 24, 537-544.

KOUROUKLIS, G. A. & LIAROKAPIS, E. 1991. Pressure and temperature dependence of the Raman spectra of zirconia and hafnia. Journal of the American Ceramic Society, 74, 520-523.

LANKFORD, J. & DAVIDSON, D. L. 1979. The crack-initiation threshold in ceramic materials subject to elastic/plastic indentation. Journal of materials science, 14, 1662-1668.

LAUGIER, M. 1987. New formula for indentation toughness in ceramics. Journal of Materials Science Letters, 6, 355-356.

LAUGIER, M. T. 1985. The elastic/plastic indentation of ceramics. Journal of Materials Science Letters, 4, 1539-1541.

LAWN, B. R., EVANS, A. & MARSHALL, D. 1980. Elastic/plastic indentation damage in ceramics: the median/radial crack system. Journal of the American Ceramic Society, 63, 574-581.

LI, Z., GHOSH, A., KOBAYASHI, A. S. & BRADT, R. C. 1989. Indentation fracture toughness of sintered silicon carbide in the Palmqvist crack regime. Journal of the American Ceramic Society, 72, 904-911.

LIANG, K., ORANGE, G. & FANTOZZI, G. 1990. Evaluation by indentation of fracture toughness of ceramic materials. Journal of materials science, 25, 207-214.

LIPKIN, D. M. & CLARKE, D. R. 1995. Sample ‐ probe interactions in spectroscopy: Sampling microscopic property gradients. Journal of Applied Physics, 77, 1855-1863.

MAGNANI, G., MINOCCARI, G. & PILOTTI, L. 2000. Flexural strength and toughness of liquid phase sintered silicon carbide. Ceramics International, 26, 495-500.

MU OZ TABARES, J. A. & ANGLADA, M. J. 2010. Quantitative Analysis of Monoclinic Phase in 3Y ‐ TZP by Raman Spectroscopy. Journal of the American Ceramic Society, 93, 1790-1795.

NAWA, M., YAMADA, K. & KURIZOE, N. 2013. Effect of the t–m transformation morphology and stress distribution around the crack path on the measured toughness of zirconia ceramics: A case study on Ce-TZP/alumina nanocomposite. Journal of the European Ceramic Society, 33, 521-529.

NEMLI, S. K., YILMAZ, H., AYDIN, C., BAL, B. T. & TIRAŞ, T. 2012. Effect of fatigue on fracture toughness and phase transformation of Y ‐ TZP ceramics by X ‐ ray diffraction and Raman spectroscopy. Journal of Biomedical Materials Research Part B: Applied Biomaterials, 100, 416-424.

PITTAYACHAWAN, P., MCDONALD, A., YOUNG, A. & KNOWLES, J. C. 2009. Flexural strength, fatigue life, and stress ‐ induced phase transformation study of Y ‐ TZP dental ceramic. Journal of Biomedical Materials Research Part B: Applied Biomaterials, 88, 366-377.

REECE, M., TETLOW, P. & GALIOTIS, C. 1992. Phase transformation around indentations in zirconia. Journal of Materials Science Letters, 11, 575-577.

SULLIVAN, J. & LAUZON, P. 1986. Shape profiles of cracks formed under a Vickers pyramid indenter.

Journal of Materials Science Letters, 5, 247-248.

WILLARDSON, R. K. & WEBER, E. R. 1998. SiC materials and devices, Academic Press.

YONEZU, A., XU, B. & CHEN, X. 2009. Indentation induced lateral crack in ceramics with surface hardening. Materials Science and Engineering: A, 507, 226-235.

Chapter 6 Indentation model

6.1 Introduction

In this chapter, a new model for the stress field of the Vickers indentation is presented. This model serves to predict the residual stress field around Vickers indentations on ceramics with the relaxation due to both radial and lateral cracking being considered. This residual stress model was then tested on Al_2O_3, SiC and TZP indentations. From the residual stress model, an expression for the stress intensity factor, *K*, is deduced. In this chapter, the model is explained first with its assumptions elaborated and then its stress field prediction and the deduced stress intensity factor, *K*, are derived. The calculations are then tested using results for Al_2O_3 and SiC indentations described in Chapters 4 and 5.

6.2 Indentation residual stress model

6.2.1 Introduction

From the observation of the indentation cracking process which is commonly accepted, it is clear that the resulting residual stress development allows for the propagation of radial and lateral cracking in the unloading phase. In order to understand and describe the process, some analytical models have been proposed

(Lawn et al., 1980; Yoffe, 1982; Chiang et al., 1982; Ahn et al., 1998). In their analyses, an elastic stress field from a the point load on a semi-infinite space has been combined with a plastic stress field associated with an expanding cavity. Their models are appropriate for the determination of the initiation of the cracks, e.g. Chiang et al.'s model is able to describe the maximum tensile stress in the vicinity of the plastic zone therefore locating where the lateral crack is going to be initiated. The crack forming process and even the location of the crack initiation were successfully predicted. There was, however, no further experimental verification of the distribution of the residual stresses, which determine the extent of the subsequent crack propagation.

In this study, the residual stress distributions measured along line scans from the indentation center on the surface around the Vickers indentations (Figure 4.22) have shown that Yoffe's model is not suitable for describing the residual stresses on the surface of ceramics. This is supposed to be due to the lack of consideration of the relaxation effect from the radial and lateral cracking, which was observed in this study (Figure 4.15 and 4.16). Hence, the modifying effect of the lateral cracking to the surface stress field is considered in the following model in order to provide better understanding of the indentation residual stress field and more importantly the fracture toughness measurements related to the stress field.

6.2.2 Model assumptions

Based on the results in alumina, the following assumptions can be made before proposing the model:

(1) Basic model

The model starts with the following basics: (a) hemispherical plastic zone, (b) radial/ median semi-circular crack system and (c) lateral cracks parallel to the surface at a depth equal to the radius of the plastic zone, which in principle reproduces the basic geometry of many previous works (for example, the model proposed by Marshall et al. (1982)). The alumina indentation investigated in this study has been proved to follow the cracking pattern described above.

(2) The length of the lateral crack is equal to the radial crack and just before crack arrest the two cracks propagate at the same rate.

This assumption is based on the results in Section 4.2.3.2, 4.2.4 and discussions in Section 4.3.5 and 4.3.6. In the Section 4.2.4, the lateral crack was found to propagate at the same speed as the radial crack. Although, this observation was obtained from the ruby, the single crystal alumina and the polycrystalline alumina are similar in terms of composition therefore the fundamental crack growth mechanism,

i.e. the reaction between the Al-O bonds and the environmental species is assumed to be the same for both. The polycrystalline alumina has the bridging effect but this should affect equally the growth of both the radial and the lateral crack. Therefore, the finding that the lateral crack propagates simultaneously with the radial crack on ruby would very likely to be the same case for the polycrystalline alumina.

(3) There is a well-defined interface between the plastic zone and the elastic region and the radius of the plastic zone is equal to half the indentation diagonal length.

This assumption is based on the discussion in Section 4.3.1.

(4) The stress field between the lateral crack and the surface has an approximately cylindrical symmetry and the radial cracking completely relaxes the hoop stress between the edge of the plastic zone and the radial crack tips.

Figure 6.1 is the FLM peak position map on the 9.8 N alumina indentation. The stress field has an almost circular symmetry and the hydrostatic stress is the same in the vicinity of the radial cracks (except close to the radial crack tips) as points at the same distance from the indentation center away from radial crack. A simple explanation for this is that the radial cracks have relaxed the surface hoop stress

completely. The hoop stress component must be zero on the crack faces and there is lack of hydrostatic stress variation away from the crack faces in the annulus at a certain distance from indentation center (Figure 6.1). This evidence suggests that the hoop stress is essentially zero everywhere in the annulus of material extending from the indentation to the radial crack tip. Outside the radial crack tip, this assumption is not valid as hoop stress cannot be relaxed by radial crack. Using the Chiang et al. (1982) model, the predicted tangential stress on the alumina would correspond to ~4 GPa. The cracking during indentation is therefore very likely to occur at such stresses and hence to relieve the tangential stress component, limiting the extent of yield outside the indentation. Although a constant hydrostatic stress could also be maintained in principle by equal and opposite variations of radial and tangential stress away from the cracks, the circular symmetry of the indentation plastic zone, which should be sensitive mainly to the radial stress at its interface with the surrounding material, supports the idea that the simpler solution of approximately zero hoop stress is substantially correct.

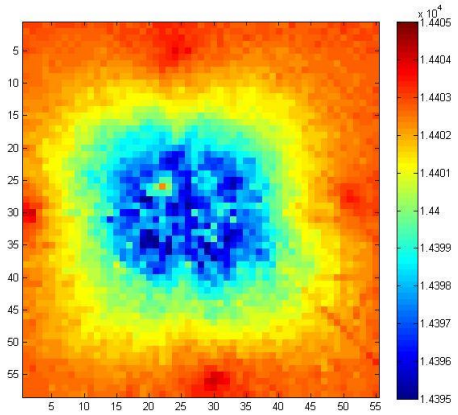


Figure 6.1 FLM peak position map on the surface of the 9.8N indentation on alumina.

6.2.3 Model for stresses around an indentation in the presence of radial and lateral cracking

6.2.3.1 Geometry of indentations and associated cracking

Adapting the assumptions above, the indentation is simplified into a model with cylindrical geometry (Figure 6.2). In this model, a disc of material lies above the lateral crack and extends as far as the lateral and radial cracks. The cylindrical hole has a volume equal to that of the actual indentation, ΔV:

$$\Delta V = \pi a_i^2 h \qquad \text{Equation 6.1}$$

Then a concentric cylinder represents the plastic zone and has a volume equal to that of the real plastic zone V. The radial misfit, δa_0, is relative to its surroundings

such that the volume of the misfit is equal to 2/3 of the indentation volume based on the assumption that the expansion of the plastic zone occurs equally in the three principal directions, with the expansion in the direction normal to the surface being absorbed in the lateral cracking. This is a simplified plastic zone compared to Chiang et al. (1982)'s hemi-sphere plastic zone model.

$$V = \pi a_0^2 h$$ Equation 6.2

$$\frac{2}{3}\Delta V = 2\pi a_o h\, \delta a_o$$ Equation 6.3

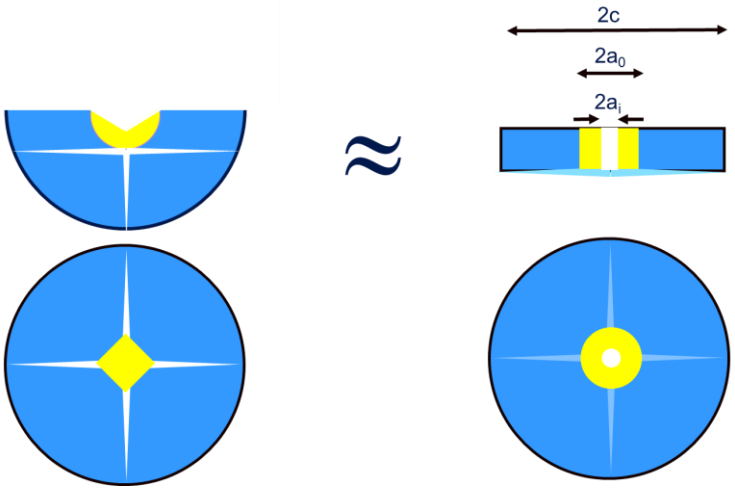


Figure 6.2 Sketch of the indentation model.

The stresses must be found in two cylindrical regions of the specimen. General solutions are first explained for each region and then matched to the boundary conditions to find upper and lower bound solutions. Because the width of the disc is larger than its thickness, plane stress is assumed and the cylindrical coordinates *r*, θ, *z* are used. The flexure of the model disc identified in Chapter 4 on alumina is not

included in the model. When the model disc is too thin, the residual stress can be relaxed by bending (Green, 1998, Yu and Hutchinson, 2002). Because the thickness of the model disc, *h*, (Chapter 4 Table 4.4) is as large as the indentation half diagonal length, the model disc is considered too thick to relieve stress significantly by bending in this manner.

6.2.3.2 The model plastic zone.

This is presented by a misfitting elastic hollow cylinder with internal radius a_i and outer radius a_o as shown in Figure 6.2. The radial stress is zero at the inner surface and is σ_{pz} at the outer surface. The radial displacement *u* is of the form indicated by the compatibility equations:

$$u = Ar + \frac{B}{r}$$

Equation 6.4

where *A* and *B* are constants. Combining the radial and tangential strains deduced from Equation 6.4, Hooke's law and the radial stresses at the inner and outer surface give:

$$A_{pz} = \frac{\sigma_{pz}(1-\nu)}{E\left(1-\frac{a_i^2}{a_o^2}\right)}$$

Equation 6.5

$$B_{pz} = \frac{\sigma_{pz} a_i^2 (1+\nu)}{E\left(1-\frac{a_i^2}{a_o^2}\right)}$$

Equation 6.6

where the subscript *pz* for A and B represents that they apply only in the plastic zone.

The surface plane principal stresses are:

$$\sigma_r = \frac{\sigma_{pz}\left(1-\frac{a_i^2}{r^2}\right)}{1-\frac{a_i^2}{a_o^2}}$$

Equation 6.7

$$\sigma_\theta = \frac{\sigma_{pz}\left(1+\frac{a_i^2}{r^2}\right)}{1-\frac{a_i^2}{a_o^2}}$$

Equation 6.8

6.2.3.3 The model elastic region between the plastic zone and the radial crack tips.

This region is represented as a hollow cylinder with inner and outer radii a_o and c respectively. The hoop (tangential) stress is assumed to be relaxed by the radial cracking (Assumption 4 above), $\sigma_\theta = 0$. In this case, equilibrium of forces in the radial direction requires that:

$$\sigma_r hr = D$$

Equation 6.9

where D is a constant with units of force. The radial strain ε_{ez} is given by:

$$\varepsilon_r = \frac{du}{dr} = \frac{\sigma_r}{E} = \frac{D}{Ehr}$$

Equation 6.10

$$\therefore u = \frac{D}{Eh}\ln r + g$$

Equation 6.11

where g is a constant of integration.

For the sake of determining the stresses in terms of the indentation parameters of interest, the plastic and elastic zones in the model disc must be connected to each other and to the rest of the specimen at the outer circumference of the model disc ($r = c$). Upper and lower bounds for the stresses are calculated from different assumptions regarding the constraining effect of the material outside the disc of the model. The solutions are obtained by requiring continuity in radial stress and radial displacement at the interfaces between the different parts of the model. Continuity in the tangential and axial strains is improved under these conditions. It is assumed that these discrepancies are accommodated by minor perturbations in the stresses within small distances from the interfaces. In the case of the tangential strains this can be accomplished due to the relaxation provided by the radial cracks. The assumption in the axial direction amounts to the plane stress criterion justified above.

In this model, the concentric cylinder is separated by the lateral crack from the material below. Therefore, the edge effect on the bottom of the cylinder is quite small and the residual stress below the cylinder should be close to zero. This approximation also assumes the constraint of the material under plastic zone is small as the point of attachment is close to the centre and the displacements involved are relatively small. This can be supported by the cross-sectional pictures shown in Figure 4.15 and 4.16.

6.2.3.4 Upper bound stress solution

For an upper bound to the indentation stress level, we assume that the material beyond and below the disc of the model is rigid, i.e. $u(r = c) = 0$. This is obviously an overestimate of the constraint by the surrounding material as in reality some elastic relaxation will occur. According to Equation 6.11, the radial displacement outside the plastic zone of the model disc is provided under this constraint by:

$$u = \frac{D}{Eh}\ln\frac{r}{c} \qquad a_o < r < c$$

Equation 6.12

Matching the displacements at the edge of the plastic zone, $r = a_o$ by using Equations 6.4-6.6 and 6.12:

$$\delta a_o + \frac{\sigma_{pz} a_o}{E}\left[\frac{(1-\nu)a_o^2 + (1+\nu)a_i^2}{a_o^2 - a_i^2}\right] = \frac{D}{Eh}\ln\frac{a_o}{c}$$

Equation 6.13

and from the continuity of σ_r at the same interface Equation (9):

$$D = h a_o \sigma_{pz}$$

Equation 6.14

Eliminating *D* between Equations 6.13 and 6.14 gives:

$$\sigma_{pz} = -\frac{E\delta a_o}{a_o} \cdot \frac{a_o^2 - a_i^2}{a_i^2(1+v) + a_0^2(1-v) + (a_o^2 - a_i^2)\ln\frac{c}{a_0}}$$

Equation 6.15

Equations 6.7, 6.8, 6.9, 6.14 and 6.15 can now be employed to find expressions for the principal stresses at the surface of the model disc:

In the plastic zone:

$$\sigma_r = -\frac{E\delta a_o}{a_o} \cdot \frac{a_o^2}{a_i^2(1+v) + a_0^2(1-v) + (a_o^2 - a_i^2)\ln\frac{c}{a_0}} \cdot \left(1 - \frac{a_i^2}{r^2}\right)$$

$a_i < r < a_o$ eq. 6.16

$$\sigma_\theta = -\frac{E\delta a_o}{a_o} \cdot \frac{a_o^2}{a_i^2(1+v) + a_0^2(1-v) + (a_o^2 - a_i^2)\ln\frac{c}{a_0}} \cdot \left(1 + \frac{a_i^2}{r^2}\right)$$

$a_i < r < a_o$ eq. 6.17

Between the plastic zone and the crack tips:

$$\sigma_r = -\frac{E\delta a_o}{r} \cdot \frac{a_o^2 - a_i^2}{a_i^2(1+v) + a_0^2(1-v) + (a_o^2 - a_i^2)\ln\frac{c}{a_0}}$$

$a_o < r < c$

Equation 6.18

$$\sigma_\theta = 0$$

$a_o < r < c$

Equation 6.19

The material is undeformed beyond the crack tips.

6.2.3.5 Lower bound stress solution

Regarding a lower bound to the indentation stress level, we assume that the material beyond the disc of the model is an uncracked annulus of material with the same thickness, h, as the model disc, inner radius c and outer radius extending to infinity. This has to be an underestimate of the constraint because in reality the material outside the model disc is continuous at depths beneath the surface beyond h. The radial displacement in this outer annulus has the form of Equation 6.4 but in this case the boundary condition that $\sigma_r \rightarrow 0$ as $r \rightarrow \infty$ requires that $A_{r>c} = 0$. The principal stresses for $r > c$ are therefore:

$$\sigma_r = -\sigma_\theta = -\frac{2\mu B_{r>c}}{r^2} \qquad r > c$$

Equation 6.20

with the subscript $r > c$ providing validity beyond the crack tips. The values of g, $B_{r>c}$, σ_{pz} and D for the lower bound solution can be found from the four simultaneous equations obtained by requiring continuity of radial displacement and radial stress at $r = a_0$ and $r = c$, as for the upper bound solution. Once these are known, the complete lower bound stress state can be obtained from Equations 6.7-6.9 and 6.20 as follows:

In the plastic zone:

$$\sigma_r = -\frac{E\delta a_o}{a_o} \cdot \frac{a_o^2}{2a_0^2 + \left(a_o^2 - a_i^2\right)\ln\frac{c}{a_0}} \cdot \left(1 - \frac{a_i^2}{r^2}\right)$$

$a_i < r < a_o$ Equation 6.21

$$\sigma_\theta = -\frac{E\delta a_o}{a_o}\cdot\frac{a_o^2}{2a_0^2+\left(a_o^2-a_i^2\right)\ln\frac{c}{a_0}}\cdot\left(1+\frac{a_i^2}{r^2}\right) \qquad a_i < r < a_o \qquad \text{Equation 6.22}$$

Between the plastic zone and the crack tips:

$$\sigma_r = -\frac{E\delta a_o}{r}\cdot\frac{a_o^2-a_i^2}{2a_0^2+\left(a_o^2-a_i^2\right)\ln\frac{c}{a_0}} \qquad a_o < r < c \qquad \text{Equation 6.23}$$

$$\sigma_\theta = 0 \qquad a_o < r < c \qquad \text{Equation 6.24}$$

Beyond the crack tips:

$$\sigma_r = -\sigma_\theta = -\frac{Ec\delta a_o}{r^2}\cdot\frac{a_o^2-a_i^2}{2a_0^2+\left(a_o^2-a_i^2\right)\ln\frac{c}{a_0}} \qquad c< r \qquad \text{Equation 6.25}$$

6.2.4 Relating the model to the experiments

The model is connected to the experiments by the radial crack length, *c*, and Equations 6.1-6.3, which relate the dimensions in the model appearing in the Equations 6.5 to 6.25 to the volume of the indentation, ΔV, and the volume of the plastic zone, *V*. The volume of a perfect Vickers indentation is provided by:

$$\Delta V = \frac{\sqrt{2}}{3}\left(\frac{d}{2}\right)^3 \cot\psi \qquad \text{Equation 6.26}$$

where *d* is the indentation diagonal length, ψ = 68° is half the dihedral angle of the pyramidal faces of the indenter.

The volume of the hemispherical plastic zone (taken to include the volume of the indentation) is:

$$V = \frac{2}{3}\pi r_p^3$$

Equation 6.27

where r_p is the radius of the plastic zone. According to the assumptions described in Section 6.2.2:

$$h = r_p = \alpha d/2 = \alpha a_V$$

Equation 6.27.0

Combining these relations with Equations 6.1 to 6.3 allows that model variables to be written in terms of the indentation semi-diagonal a_v as follows:

$$a_o = \sqrt{\frac{2}{3}}\alpha a_v$$

Equation 6.27.1

$$a_i = \frac{2^{1/4}}{\sqrt{3\alpha k}}\, a_v$$

Equation 6.27.2

$$\delta a_o = \frac{a_v}{3\sqrt{3}\alpha^2 k}$$

Equation 6.27.3

in which $k = \pi \tan\psi$.

This then allows the stress solutions 6.16-19 and 6.21-25 to be written as follows:

Upper bound solution:

$$\sigma_r = -E \cdot \frac{\sqrt{2}}{3\left\{2\alpha^3 k + \sqrt{2} + \left(2\alpha^3 k - \sqrt{2}\right)\left[\ln\left(\sqrt{\frac{3}{2}}\frac{c}{\alpha a_V}\right) - \nu\right]\right\}} \cdot \left(1 - \frac{\sqrt{2}}{3\alpha k}\frac{a_V^2}{r^2}\right)$$

$$\left(\frac{\sqrt{2}}{3\alpha k}\right)^{1/2} < \frac{r}{a_V} < \alpha\sqrt{\frac{2}{3}}$$

Equation 6.28

$$\sigma_\theta = -E \cdot \frac{\sqrt{2}}{3\left\{2\alpha^3 k + \sqrt{2} + \left(2\alpha^3 k - \sqrt{2}\right)\left[\ln\left(\sqrt{\frac{3}{2}}\frac{c}{\alpha a_V}\right) - \nu\right]\right\}} \cdot \left(1 + \frac{\sqrt{2}}{3\alpha k}\frac{a_V^2}{r^2}\right)$$

$$\left(\frac{\sqrt{2}}{3\alpha k}\right)^{1/2} < \frac{r}{a_V} < \alpha\sqrt{\frac{2}{3}}$$

Equation 6.29

Between the plastic zone and the crack tips:

$$\sigma_r = -E \cdot \frac{2\alpha^3 k - \sqrt{2}}{3\sqrt{3}\alpha^2 k\left\{2\alpha^3 k + \sqrt{2} + \left(2\alpha^3 k - \sqrt{2}\right)\left[\ln\left(\sqrt{\frac{3}{2}}\frac{c}{\alpha a_V}\right) - \nu\right]\right\}} \cdot \frac{a_v}{r}$$

$$\alpha\sqrt{\frac{2}{3}} < \frac{r}{a_V} < \frac{c}{a_V}$$

Equation 6.30

$$\sigma_\theta = 0 \qquad \alpha\sqrt{\frac{2}{3}} < \frac{r}{a_V} < \frac{c}{a_V}$$

Equation 6.31

$$\sigma_r = \sigma_\theta = 0 \qquad r > c$$

Equation 6.32

Lower bound solution:

In the plastic zone:

$$\sigma_r = -E \cdot \frac{\sqrt{2}}{3\left\{4\alpha^3 k + \left(2\alpha^3 k - \sqrt{2}\right)\ln\left(\sqrt{\frac{3}{2}}\frac{c}{\alpha a_V}\right)\right\}} \cdot \left(1 - \frac{\sqrt{2}}{3\alpha k}\frac{a_V^2}{r^2}\right)$$

$$\left(\frac{\sqrt{2}}{3\alpha k}\right)^{1/2} < \frac{r}{a_V} < \alpha\sqrt{\frac{2}{3}}$$

Equation 6.33

$$\sigma_\theta = -E \cdot \frac{\sqrt{2}}{3\left\{4\alpha^3 k + \left(2\alpha^3 k - \sqrt{2}\right)\ln\left(\sqrt{\frac{3}{2}}\frac{c}{\alpha a_V}\right)\right\}} \cdot \left(1 + \frac{\sqrt{2}}{3\alpha k}\frac{a_V^2}{r^2}\right)$$

$$\left(\frac{\sqrt{2}}{3\alpha k}\right)^{1/2} < \frac{r}{a_V} < \alpha\sqrt{\frac{2}{3}}$$

Equation 6.34

Between the plastic zone and the crack tips:

$$\sigma_r = -E \cdot \frac{2\alpha^3 k - \sqrt{2}}{3\sqrt{3}\alpha^2 k\left\{4\alpha^3 k + \left(2\alpha^3 k - \sqrt{2}\right)\ln\left(\sqrt{\frac{3}{2}}\frac{c}{\alpha a_V}\right)\right\}} \cdot \frac{a_v}{r}$$

$$\alpha\sqrt{\frac{2}{3}} < \frac{r}{a_V} < \frac{c}{a_V}$$

Equation 6.35

$$\sigma_\theta = 0 \qquad \alpha\sqrt{\frac{2}{3}} < \frac{r}{a_V} < \frac{c}{a_V}$$

Equation 6.36

Beyond the crack tips:

$$\sigma_r = -\sigma_\theta = -E \cdot \frac{2\alpha^3 k - \sqrt{2}}{3\sqrt{3}\alpha^2 k\left\{4\alpha^3 k + \left(2\alpha^3 k - \sqrt{2}\right)\ln\left(\sqrt{\frac{3}{2}}\frac{c}{a_V}\right)\right\}} \cdot \frac{ca_v}{r^2}$$

$c < r$ Equation 6.37

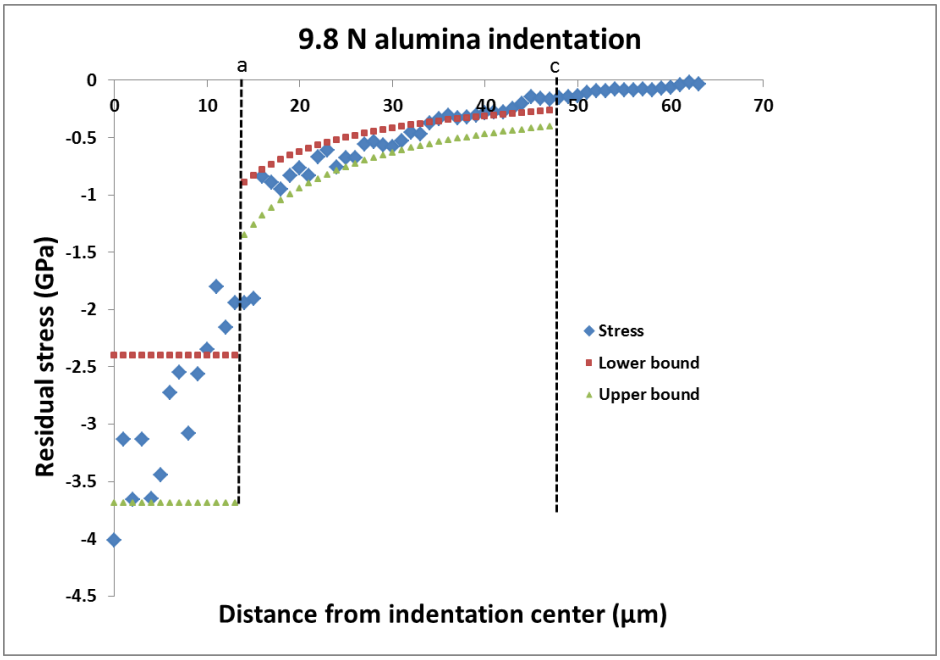
It is evident that for a given ratio of crack length to indentation half diagonal, c/a_V, the stresses at a given normalised distance r/a_V from the indentation centre are predicted to be independent of the size of the indentation and, therefore, of the indentation load.

6.3 Comparison with experiments and discussion

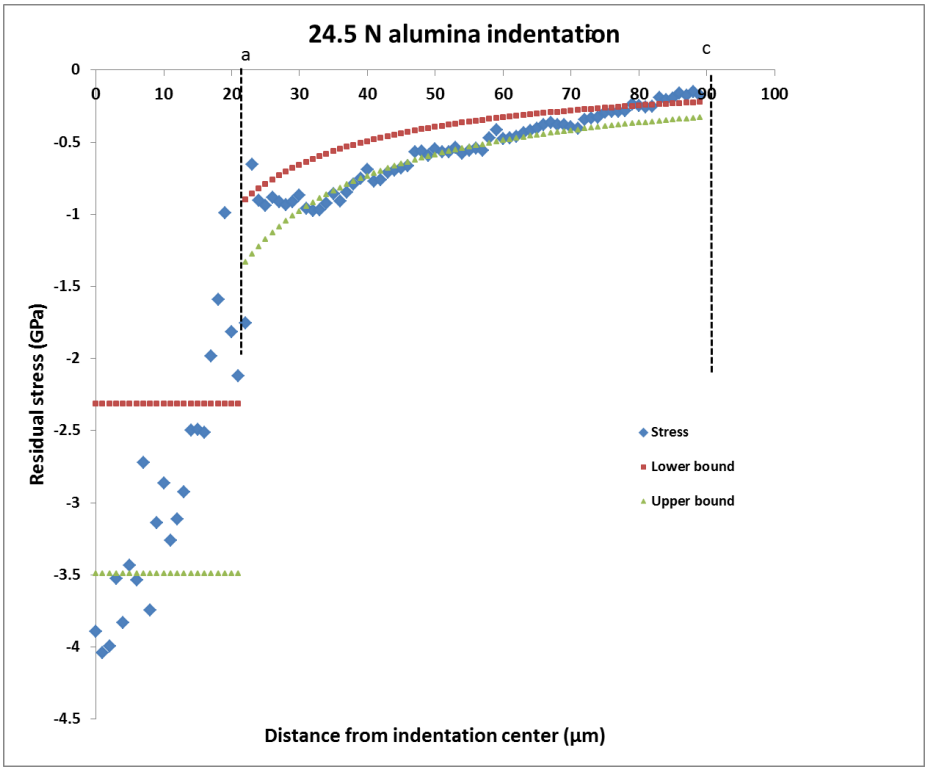
6.3.1 Al_2O_3

The residual stress distributions on the line scans made normal to the indentation edges on the 9.8 N, 24.5 N, and 49 N indentations on alumina were shown in the previous Section 4.2.3.1. To compare with the prediction of the model, the experimental values of a_V and c, $\alpha = 1$ (see model assumption 3), $E = 413$ GPa (T. Rodriguez Suarez, unpublished work) and $\nu = 0.23$ (Mott and Roland, 2009), were used.

(a)


9.8 N alumina indentation
a
c
0
-0.5
-1
-1.5
-2
-2.5
-3
-3.5
-4
-4.5
0
10
20
30
40
50
60
70
Residual stress (GPa)
Distance from indentation center (µm)
Stress
Lower bound
Upper bound

(b)


24.5 N alumina indentation
a
c
0
-0.5
-1
-1.5
-2
-2.5
-3
-3.5
-4
-4.5
0
10
20
30
40
50
60
70
80
90
100
Residual stress (GPa)
Distance from indentation center (µm)
Stress
Lower bound
Upper bound

(c)

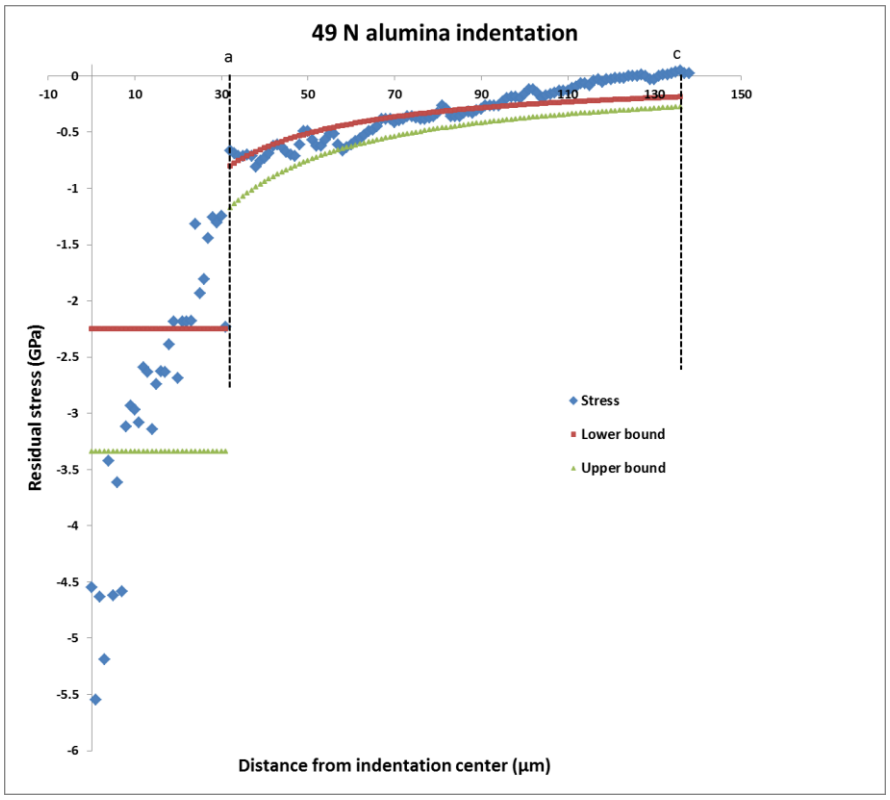
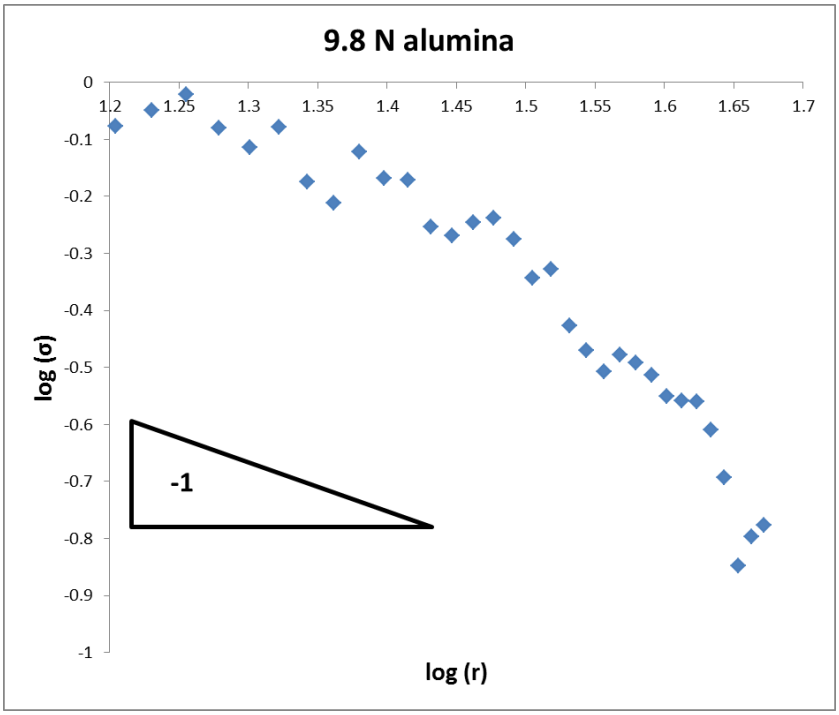


Figure 6.3 Comparison of the residual stress profiles of (a) 9.8 N, (b) 24.5 N, (c) 49 N alumina indentation line scans with the predictions of the model.

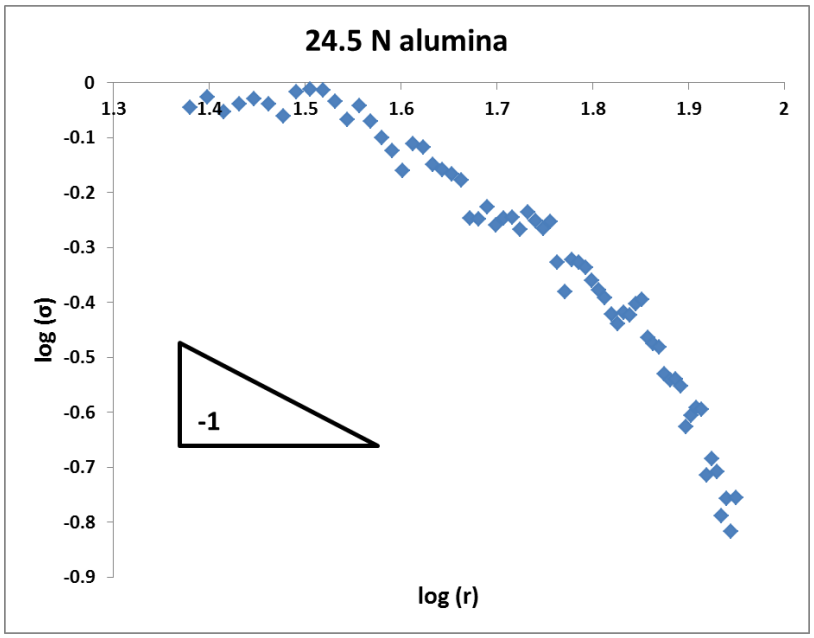
Figure 6.3 are the comparisons between the model's predictions and the experimental results of lines scans on alumina. The lengths of the indentation parameters *a,* and *c* were marked on the graphs. A relatively good agreement between the model's predictions and the experimental measurement can be found as most of the experimental data points lay between the upper and the lower bound predictions; whereas the points which lie outside these bounds are mostly close to the abrupt boundaries in the model at the outer edge of the assumed plastic zone ($r = a_o$) and at and beyond the outer extent of the radial cracks ($r \geq c$) where the both the

upper and lower bound models predict that $\Delta\nu$ falls to zero. In reality, a more gradual transition than is predicted is to be expected as these physical boundaries are geometrically less sharp in reality and the finite resolution of the FLM will also smooth out sharp changes in the peak shift.

(a)



(b)



(c)

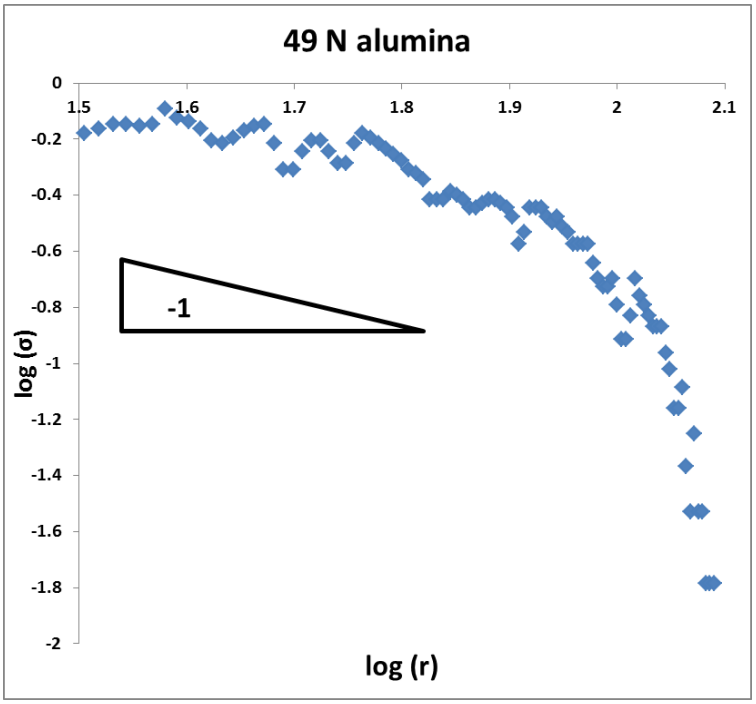


Figure 6.4 Residual stress as the function of r on the log-log plots ($a_o < r < c$) for (a) 9.8, (b) 24.5 and (c) 49 N TZP indentation line scans.

One distinctive feature of this model is its predicted $1/r$ dependence of the residual stresses in the region between the plastic zone and the tip of the radial crack ($a_o < r < c$). This differs from other models with no consideration of the cracking, such as the Yoffe model where the $1/r^3$ stress dependence is used. The present prediction is a direct consequence of the assumed separation of the disc of the material above the lateral cracks from the bulk below and of the relaxation of the hoop stresses. Figure 6.4 shows stress as a function of r on the log-log plot ($a_o < r < c$). The $1/r$ stress dependence is borne out in practice in the central part of each plot and the discrepancies at either end of this range have been explained above.

It should be pointed out that the cracks only grow to their full length after the removal of the indenter as post-indentation crack growth has been found in this study and is also supported by Anstis et al. (1981), who make the same assumption in this respect. It is seemingly impossible to measure the crack propagation and residual stress accurately during loading and unloading of the indenter. Therefore stress models such as the Boussinesq stress field (Lawn and Swain, 1975), which deals with the situation where the indenter is still loaded on a featureless surface, are not relevant (and would in any case be difficult to test). There are also some models, like Chiang et al. (1982)'s, Yoffe (1982)'s and Hirsch et al. (1985)'s, which consider the plastic zone as an inclusion and residual stresses are generated due to a size mismatch. However, the main drawback is that these models all ignore the relaxation of the cracking; therefore their models deviate significantly from the "real" situation after indentation of a brittle material, and hence are untestable. The new model proposed in this study considered the stress condition after the indentation (removal of the indenter) and the impact of cracking on the residual stress. Although the new model makes the assumptions on the shape of the plastic zone and the way the residual stresses relax due to cracking, it is more akin to the "real" situation and, more importantly, its residual stress prediction can be tested.

6.3.2 SiC

The SiC indentations also have a radial-median-lateral crack system, and the lateral crack lengths of the SiC determined by the simple plate method were found close to their radial crack lengths (Section 5.2.4). SiC also has an E/H ratio close to that of alumina and in Chiang et al. (1982)'s model it was predicted to have relative dimension factor β close to alumina, although their model seemed to overestimate the radius of the plastic zone. Hence SiC indentations are expected to follow assumptions (1), (3) and the first half of the assumption (2) made in Section 6.2.2. Therefore indentations on SiC are also good candidates to test the model. The residual stress profiles on the line scans of SiC indentations described in Chapter 5 were used here to compare with the predictions of the model (Figure 6.5). The upper and lower bounds were calculated using the indentation parameters determined in Chapter 5. The corresponding log-log plots for the region between the plastic zone and the tip of the radial crack are shown in Figure 6.6.

The model provide fairly good predictions of the residual stresses on the SiC indentations (a<r<c) as the model predicts the correct magnitude of the residual stress level and the trends of the residual stress profiles follow the curves of the model predictions. The residual stress deviates from the model prediction in the region near the indentation imprint of the 24.5 N and 49 N indentations. This may be

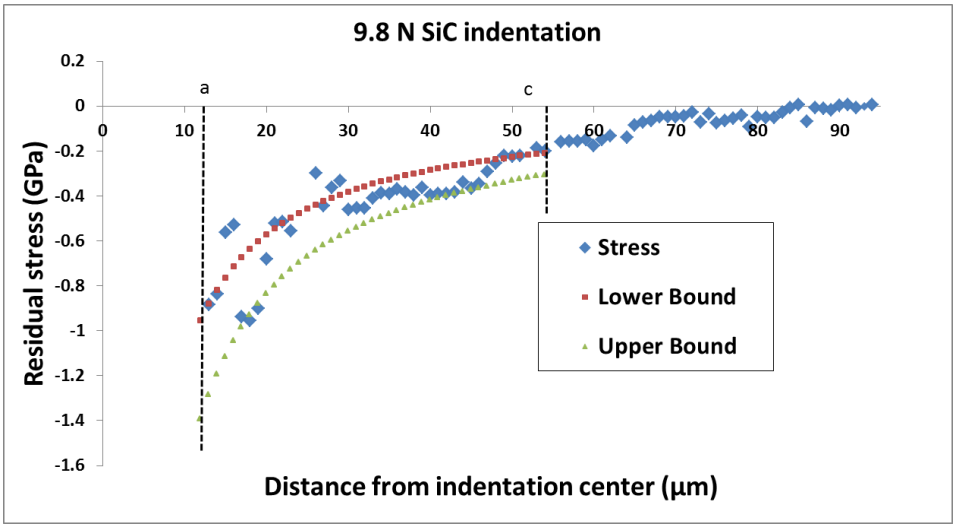
because in reality the tensile stress was not fully relaxed by the radial crack near the indentation edge and therefore the overall hydrostatic stress will be less compressive than predicted. In the classical model, for example, Chiang et al. (1982)'s model, the tangential tensile stress is predicted to be at its highest level close to the indentation edge for materials with low E/H ratio, therefore is expected to be difficult for it to be relaxed completely. This tangential stress is also proportional to the applied load, and this explains why more deviation was seen in the high load indentation. This phenomenon could also be found on the 24.5 N and 49 N alumina indentations (Figure 6.3). However, the deviation was much less than in the SiC. This is probably because the SiC is less transparent than alumina, therefore more of the highly compressive stress inside the indentation will be sampled near the indentation on alumina which to some extent counteracts the residual tensile stress, whereas the signal collected on SiC was more localised in the surface area near the indentation.

To characterise the correlations between the residual stress results and the model prediction, the Pearson correlation factors were determined by the method described in the Section 5.2.11. As the trend of the upper and lower bound predictions are almost the same, the Pearson correlation factor can be calculated using either the lower or the upper bound prediction. The Pearson correlation factors between residual stresses and the lower bound predictions are 0.858 for 9.8 N, 0.598 for 24.5 N, 0.514 for 49 N. According to Evans (1996)'s suggestion, 0.80-1.00 (64% to 100%)

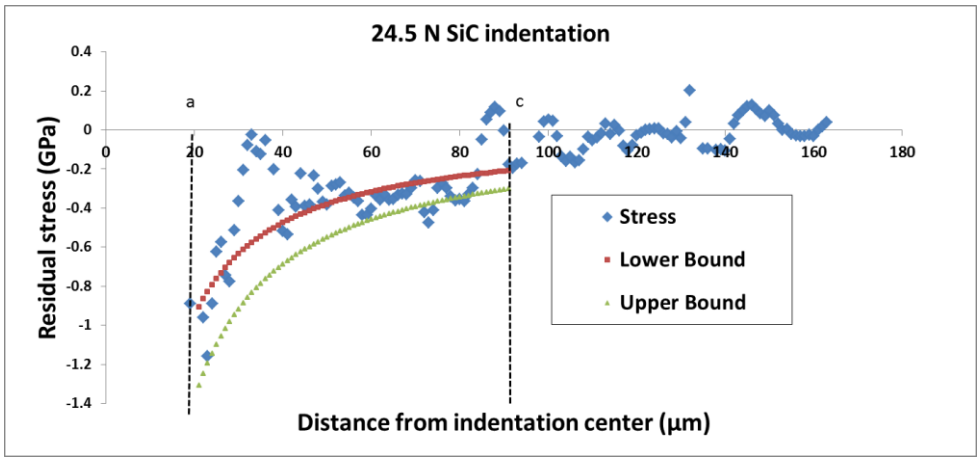
is a “very strong” level, 0.40-0.59 (16 to 36%) is “moderate” level. The 9.8 N stress profile apparently follows the prediction closely due to there being less scatter in stress data. The 24.5 N and 49 N indentations have smaller Pearson factors because in the region near the indentation imprint the residual stress deviates from the model prediction. Possible explanations for this have been given above.

There is significant scatter in the log-log plots (Figure 6.6) due to the scattering in the residual stress profiles. The possible reasons have been discussed in Section 5.2.6. From Figure 6.6, it is difficult to judge whether the data points follows the 1/r dependence. However, it can be seen from Figure 6.5 that the model provide fairly good residual stress predictions

(a)



(b)



(c)

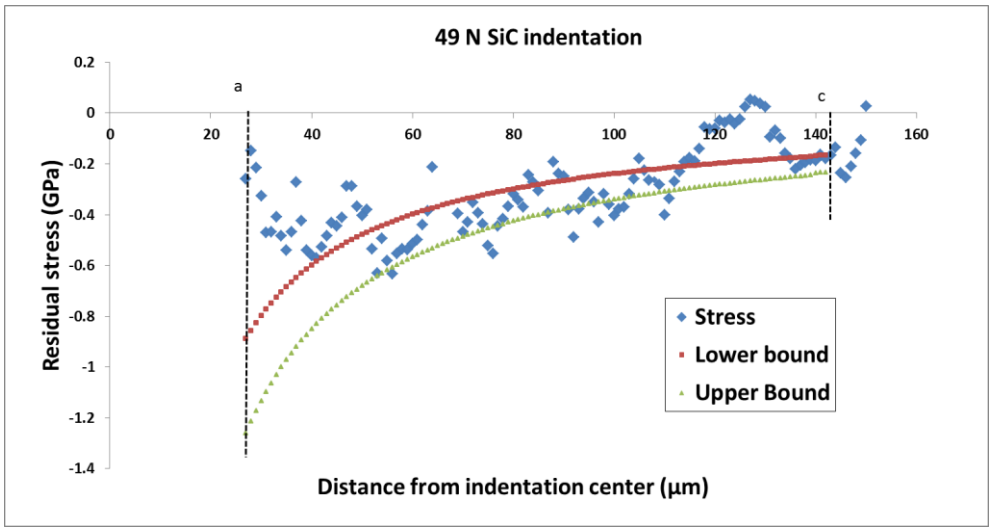
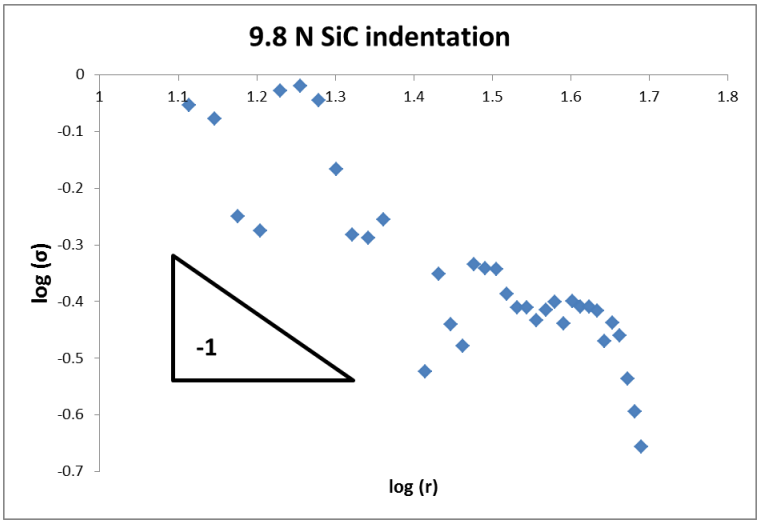
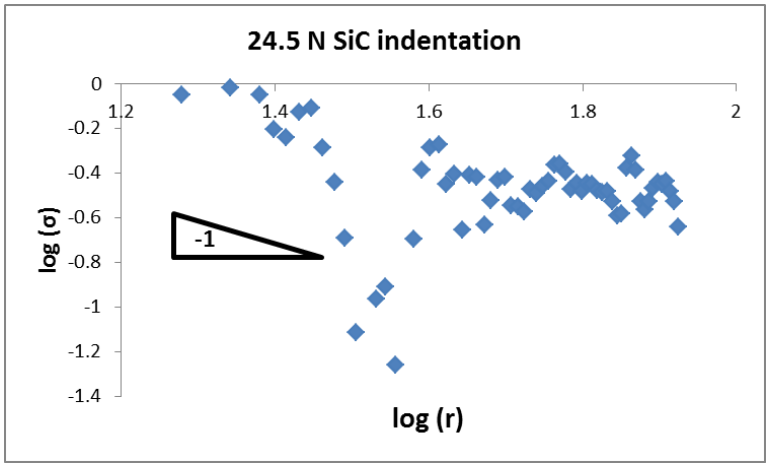


Figure 6.5 Comparison of the residual stress profiles of (a) 9.8 N, (b) 24.5 N and (c) 49 N SiC indentations with the prediction of the model.

(a)



(b)



(c)

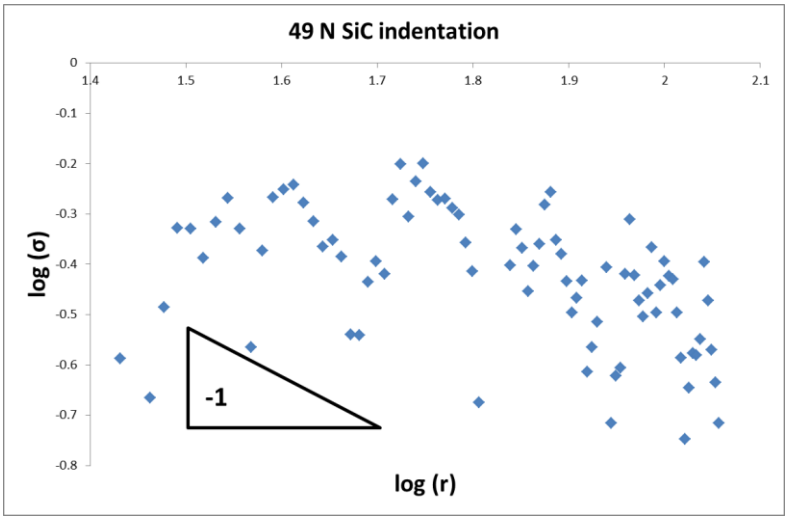


Figure 6.6 Residual stress as the function of *r* on the log-log plot for (a) 9.8, (b) 24.5 and (c) 49 N SiC indentation line scans

6.3.3 TZP

The TZP indentations with Palmqvist crack system and no lateral crack did not agree with the assumptions of the model. Nevertheless, the indentation stress field results were compared with the model to test the sensitivity of the residual stress to details of the crack pattern.

Like polycrystalline alumina and the SiC indentations, residual stress profiles (Figure 6.7) (compared with model prediction) and their corresponding log-log plots (Figure 6.8) of TZP indentations were made below. The lengths of the indentation parameters *a,* and *l* were marked on the graphs. As the Palmqvist crack did not normally exist on the 9.8 N TZP indentations, the model could not be used to compare the residual stress field of the 9.8 N indentation here. For the 24.5 N and 49 N indentations, the model's prediction was found larger than the residual stress inside the indentation (in a factor of 3~5). In the region outside the plastic zone of the 24.5 N indentation, the residual stress data only partially fit into the model's prediction and was more close to the lower bound. For the 49 N indentation, the predicted stresses were much more compressive than the actual results. This is probably because the dilatation associated with the transformation introduced large amount of tensile stresses and the these stresses cannot be relaxed effectively by

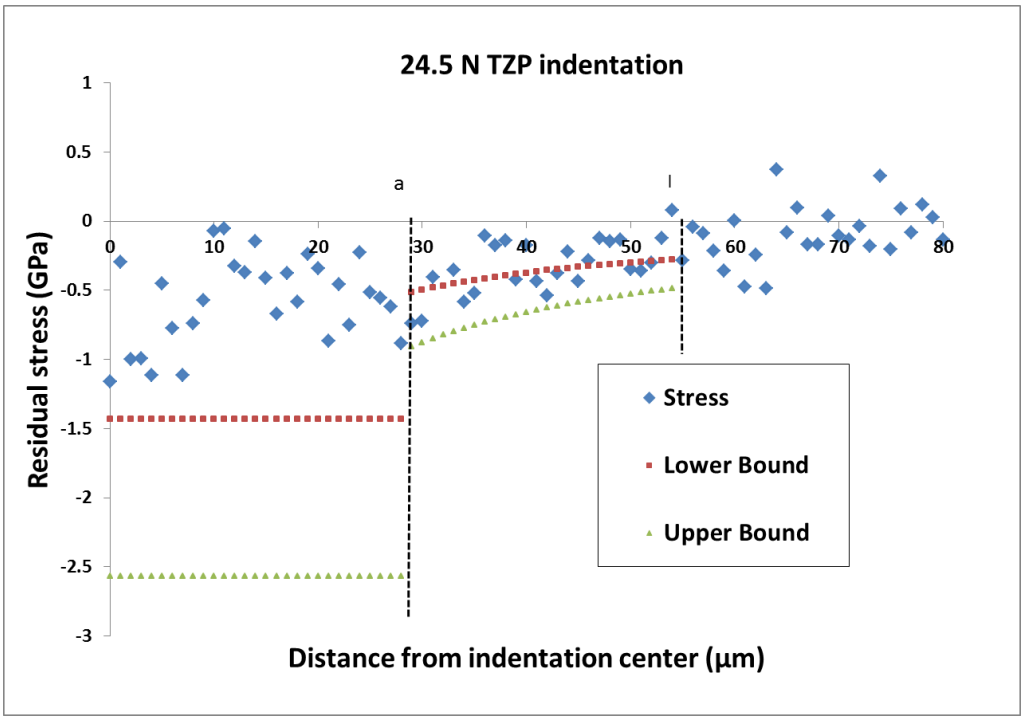
the Palmqvist crack than the radial-median-lateral crack system, therefore the overall hydrostatic stress is less compressive than the model prediction.

To characterise the correlations between the residual stress results and the model prediction outside the plastic zone, the Pearson correlation factors were determined by the method described in the Section 5.2.11. The Pearson correlation factors between residual stresses and the lower bound predictions are 0.632 for 24.5 N and 0.649 for 49 N. Evans (1996) suggested 0.60-0.79 (36% to 64%) is a “strong” level. This shows that the model successfully predicts the trend of the residual stress profile though it is clear that the magnitude of the prediction is too high, particularly for the higher indentation load

In the log-log plots, the 1/r dependence works well for most of the data points of 9.8 N indentation. For 24.5 N, the majority of the data was close to following the 1/r dependence (a dependence of $1/r^{-1.14}$ works best); and for 49 N, the dependence was hard to judge as there were only a few data points available within the region of $a < r < a+l$, but the overall trend seems to deviate from the 1/r relationship. For the indentation without cracking, like 9.8 N indentation, Yoffe’s model ($1/r^3$) should make a good prediction. However, the 9.8 N indentation residual stress field does not follow $1/r^3$ dependence. The residual stress profile of 49 N was found to be zero at a

distance (around 53 µm from indentation center) much shorter than the range of the Palmqvist crack tip (89 µm) this indicates the stress profile is not closely linked to the Palmqvist crack.

The disagreement of residual stress profile with the predictions from classical models and the present model is mainly due to the complexity of the phase transformation and the differences in crack pattern compared with the model. The results in Section 5.2.10 have clearly shown the phase transformation has the most impact on the residual stress around the indentation. The dilatation associated with the transformation introduces volume expansion which resembles the plastic zone and generates residual stress due to elastic constraint. This is complicated by the fact that this residual stress will further trigger more phase transformation and this process is autocatalytic and hence is difficult to understand quantitatively. Further studies have to be made on this to elaborate the link between the profiles of phase transformation and the residual stresses.



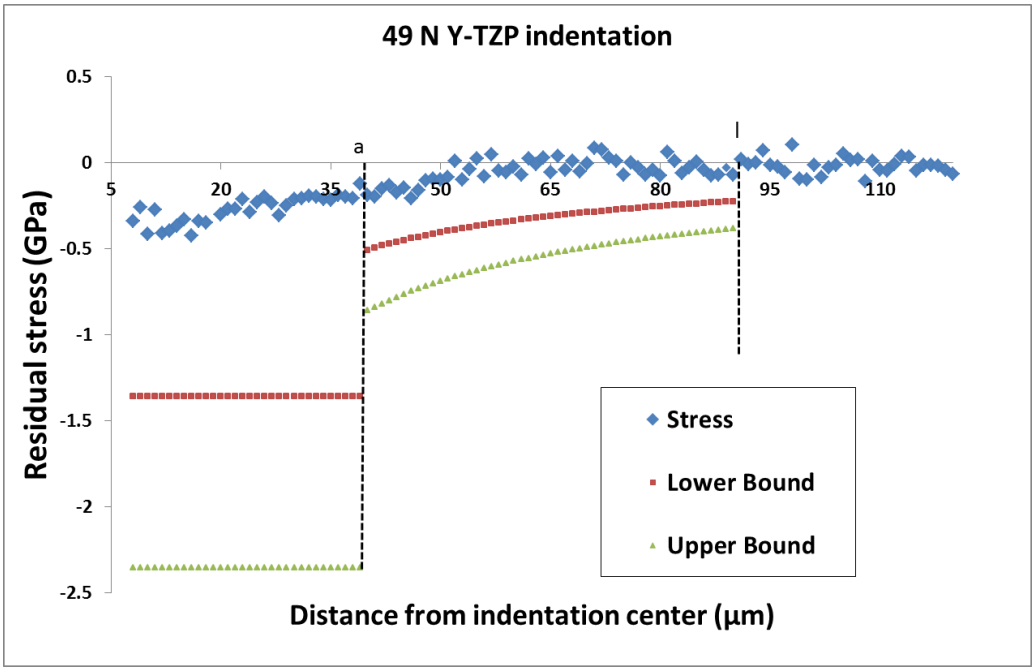
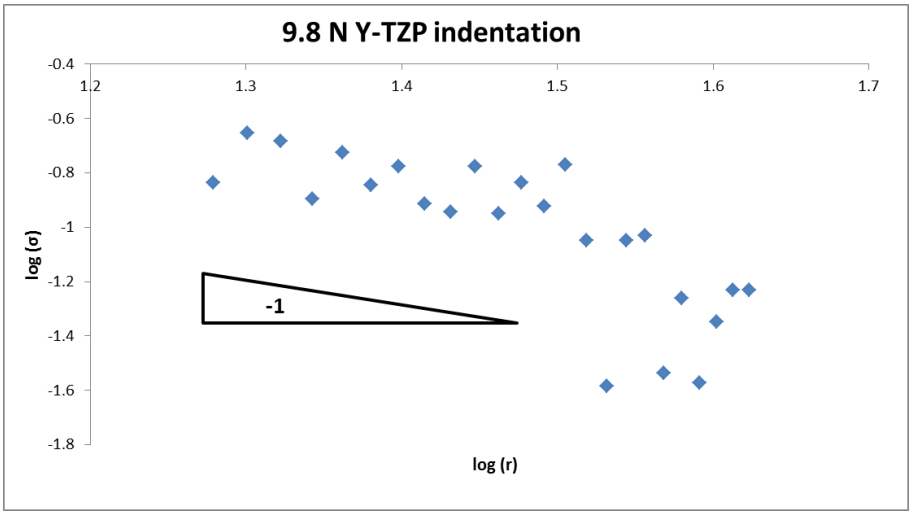
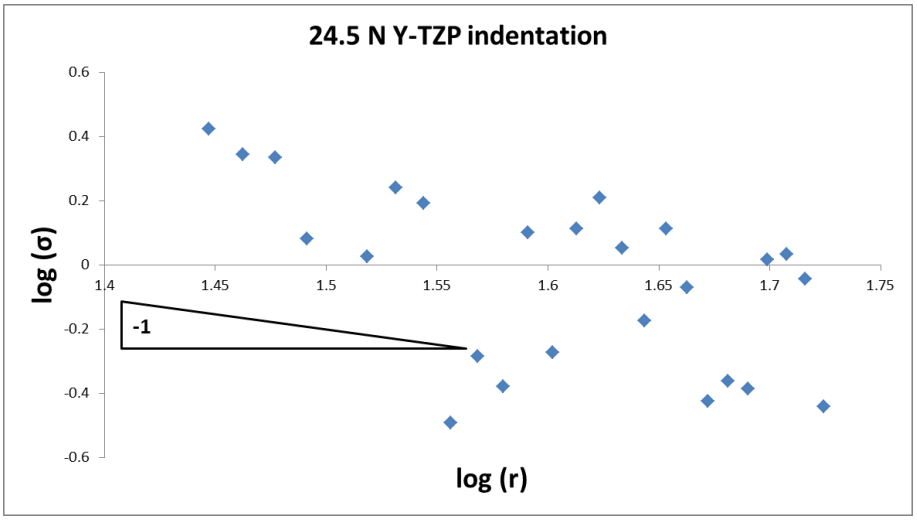


Figure 6.7 Comparison of the residual stress profiles of (a) 24.5 N and (b) 49 N TZP indentations with the predictions of the model. The mark “a” is the half diagonal length and “*l*” the Palmqvist crack length (from indentation corner).

(a)



(b)



(c)

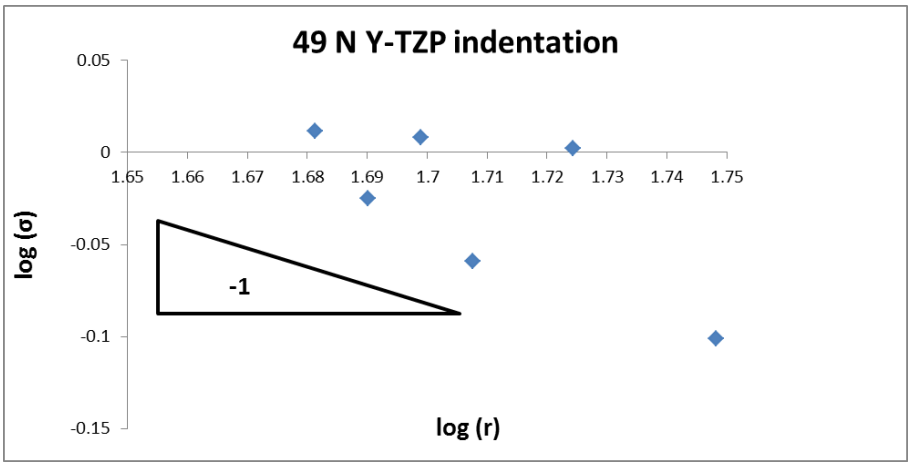


Figure 6.8 Residual stress as the function of *r* on the log-log plots for (a) 9.8, (b) 24.5 and (c) 49 N TZP indentation line scans.

The residual stress model presented in this Chapter has shown good agreement with the experimental data from polycrystalline alumina and SiC indentations and was poor on TZP. This indicates the model works well for the materials following the assumptions and not well for the material which does not. The previous models, like those of Yoffe (1982) and Chiang et al. (1982) are unable to be tested as both models ignore the modification to stresses caused by cracking and in reality the cracking associated with the indentation relaxes the residual stress field. The new residual stress field is based upon the radial-median-lateral crack system, and therefore is testable. This clearly shows the advantage of the new indentation residual stress model.

6.4 Derivation of mechanical energy release rate, *G*, and stress intensity factor, *K*, from the residual stress model

In this section, the residual stress model is used to calculate the total elastic strain energy of the system $U_{tot,}$ which is then used to derive the mechanical energy relase rate, *G*, as the cracks grow.

By integrating the strain energy density, *u*, over the strained volume in the model, with the assumption of plane stress and cylindrical symmetry, $U_{tot,}$ can be determined.

$$u = \frac{1}{2E}\left(\sigma_r^2 + \sigma_\theta^2 - 2\nu\sigma_r\sigma_\theta\right)$$ Equation 6.38.1

where σ_r and σ_θ are the radial and tangential stresses, E is Young's modulus and ν is Poisson's ratio.

Then, $U_{tot} = \int_{a_i}^{\infty} u(r) \cdot 2\pi r h \, dr$

where r is the radial distance and h is the thickness of the model disc and a_i is defined in Figure 6.2.

In terms of the upper bound in the model, there are two stressed regions, (1) $a_i < r < a_o$ and (2) $a_o < r < c$, where a_o was defined previously in Section 6.2.3.2 and c is the radial crack length.

$$U_{tot} = \int_{a_i}^{a_o} u_1 \cdot 2\pi r h \, dr + \int_{a_o}^{c} u_2 \cdot 2\pi r h \, dr$$ Equation 6.38.2

where u_1 and u_2 are the strain energy densities in regions 1 and 2. The principal stresses in each region have been described in Section 6.2.3.4 and 6.2.3.5 and by substituting these into the Equation 6.38.1 to find out the u_1 and u_2 and then using Equation 6.38.2, the U_{tot} can be obtained:

$$U_{tot} = \frac{\pi E h \delta a_o^2}{\ln\left(\frac{c}{a_o}\right) + f}$$ Equation 6.38.3

where for the upper bound solution,

$$f = f_{ub} = \frac{a_o^2 + a_i^2}{a_o^2 - a_i^2} - \nu$$

For the lower bound solution, the derivation of the U_{tot} is similar except that three regions, (1) $a_i < r < a_o$, (2) $a_o < r < c$ and (3) $r > c$, must be considered. The solution is:

$$U_{tot} = \frac{\pi E h \delta a_o^2}{\ln\left(\frac{c}{a_o}\right) + f}, \text{ but with } f = f_{lb} = \frac{2a_o^2}{a_o^2 - a_i^2}$$

U_{tot} is then used to calculate the mechanical energy release rate, G, considering the cracking geometry described in the model (Figure 6.2):

$$G = -\frac{dU_{tot}}{dA} = -\frac{\partial U_{tot}}{\partial c} \cdot \frac{1}{Nh + 2\pi c}$$

where N is the number of radial cracks (N = 4 for the classical Vickers geometry in the Figure 6.2). This assumes that the crack driving force is equal along all crack fronts (radial and lateral), being consistent with assumption (2).

Differentiation of the equation gives:

$$G = \frac{\pi E h \delta a_o^2}{c\left(\ln\left(\frac{c}{a_o}\right) + f\right)^2 (Nh + 2\pi c)} \qquad \text{Equation 6.38.4}$$

This equation can be written with the experimental parameters:

$$G = \frac{\pi E a_v^3}{27\alpha^3 k^2 c\left(\ln\sqrt{\frac{3}{2}}\frac{c}{\alpha a_v} + f\right)^2 \left(N\alpha a_v + 2\pi c\right)}$$

where, $f = f_{ub} = \frac{2\alpha^3 k + \sqrt{2}}{2\alpha^3 k - \sqrt{2}} - \nu$ for the upper bound solution;

and $f = f_{lb} = \frac{4\alpha^3 k}{2\alpha^3 k - \sqrt{2}}$ for the lower bound solution.

When α=1 and N=4 the upper and lower bound solutions for *G* are respectively:

$$G_{ub} = \frac{1.92\times10^{-3} E a_v^3}{c\left(6.28c + 4a_v\right)\left(\ln\left(\frac{c}{a_v}\right) + 1.40 - \nu\right)^2}$$

$$G_{lb} = \frac{1.92\times10^{-3} E a_v^3}{c\left(6.28c + 4a_v\right)\left(\ln\left(\frac{c}{a_v}\right) + 2.40\right)^2}$$

The approach above describes the mechanical energy release rate which drives the indentation cracks to advance. This also gives the estimation of the resistance of the materials to the advance of the crack on the assumption that the cracks are either growing at the same rate either rapidly on crack extension at all points on the crack fronts or slowly by the subcritical crack growth mechanism. For the former case, as seen from the Section 4.2.4 the radial crack grows at the same speed as the lateral crack, therefore all the cracks have the same *G*. The latter case indicates that once the cracks have grown stably to the full length, the crack arrest at close to the critical mechanical energy release rate, G_0.

The stress intensity factor *K* can be derived by

$$K = \sqrt{GE}$$ Equation 6.38.5

and

$$K = E\sqrt{\frac{\pi a_v^3}{27\alpha^3 k^2 c\left(\ln\sqrt{\frac{3}{2}}\frac{c}{\alpha a_v} + f\right)^2 \left(N\alpha a_v + 2\pi c\right)}}$$

The loading mode of the lateral cracks is less clear. According to the geometry shown in Figure 6.2, a strong Mode II component may be expected but this asymmetry may be counteracted by effects not explicitly accounted for here such as the flexure of the model disc outwards from the surface identified by Marshall et al. (1982). The tendency of the lateral cracks to remain parallel to the surface suggests that the actual loading is close to Mode I.

The calculation method for the indentation stress intensity factor derived above offers a new way of calculating the Vickers indentation fracture toughness (VIF) for ceramics. Although like all models, this is established on some assumptions and approximations, in the present case these have been tested to a greater extent than is possible with models using the stres state before cracking as a starting point. To calculate *K* at each indentation load, K_{ub} and K_{lb} are first calculated by the method described in the section above and then *K* is estimated as a first attempt by finding

the average of K_{ub} and K_{lb}. Based on the assumptions of the model, only alumina and SiC are discussed below as they have shown the radial-median and lateral crack system.

$$K = E\left(\sqrt{\frac{\pi a_v^3}{27\alpha^3 k^2 c\left(\ln\sqrt{\frac{3}{2}}\frac{c}{\alpha a_v} + \frac{2\alpha^3 k + \sqrt{2}}{2\alpha^3 k - \sqrt{2}} - \nu\right)^2 \left(N\alpha a_v + 2\pi c\right)}} + \sqrt{\frac{\pi a_v^3}{27\alpha^3 k^2 c\left(\ln\sqrt{\frac{3}{2}}\frac{c}{\alpha a_v} + \frac{4\alpha^3 k}{2\alpha^3 k - \sqrt{2}}\right)^2 \left(N\alpha a_v + 2\pi c\right)}}\right) / 2$$

Equation 6.39

6.5 Calculation of the stress intensity factor, *K* for polycrystalline alumina and silicon carbide indentations

6.5.1 Al_2O_3

In Chapter 4, the statement has been made that the crack length measured is the fully-developed crack length. Therefore, for alumina using the stabilised radial crack length, *c*, the stress intensity factor, *K*, calculated from the model will be the threshold K_{I0}.

The measurement of $K_{I0} = 2.5 \pm 0.2$ MPa$\sqrt{m}$ from De Aza et al. (2002)'s work is used here as a reference for the alumina. The grain size of the alumina used in the project is 2 μm which is very close to the grain size (1.7 μm) of the alumina used in De Aza et al. (2002)'s work. The fracture toughness of the alumina used in this study has been tested previously with the single V-notch beam method (SEVNB) in our

research group to be 3.7 MPa$\sqrt{m}$, which is slightly below the K_{IC} measured by De Aza et al. (2002) (~4.2 MPa$\sqrt{m}$) with the double torsion technique.

Table 6.1 Equations for calculating VIF based on the radial-median crack system.

Author	Equation
Anstis et al. (1981)	$K_{IC}= 0.016(E/H)^{0.5}(P/c^{3/2})$
Evans and Charles (1976a)	$K_{IC}= 0.0752\ P/c^{3/2}$
Lawn and Fuller (1975)	$K_{IC}= 0.0726\ P/c^{3/2}$

Table 6.2 K_{I0} of polycrystalline alumina calculated by the new equation and other mainstream equations (stress intensity factors are all in units of MPa$\sqrt{m}$).

	Load (N)	New model			Anstis			Evans and Charles			Lawn and Fuller		
alumina	9.8	2.18	±	0.17	1.93	±	0.17	2.18	±	0.20	2.11	±	0.19
	24.5	2.35	±	0.11	1.93	±	0.10	2.10	±	0.11	2.03	±	0.11
	49	2.35	±	0.10	2.00	±	0.10	2.30	±	0.11	2.22	±	0.11
	98	2.67	±	0.09	1.98	±	0.08	2.04	±	0.08	1.97	±	0.07
Average		2.39	±	0.11	1.96	±	0.11	2.15	±	0.13	2.08	±	0.12

The mainstream equations for calculating indentation fracture toughness of ceramics based on the radial-median crack system are shown in Table 6.1. All of these equations originated from the fundamental Griffith energy-balance concept (Griffith, 1920, Lawn and Fuller, 1975) therefore their equations should not only be applicable to determining the indentation fracture toughness, K_{IC}, from the crack length

immediate after indentation, but also be able to calculate the threshold stress intensity factor, K_{I0}, from the radial crack length when the growth arrested.

Table 6.2 gives the K_{I0} calculated by the new equation and other mainstream VIF equations for the radial-median crack system. The K_{I0} predicted by the new model (average value of 2.39±0.11 MPa$\sqrt{m}$) on alumina shows the best match to the reference (K_{I0} = 2.5±0.2 MPa$\sqrt{m}$). Considering the alumina material used by De Aza et al. (2002) is slightly tougher (larger K_{IC}) than the alumina investigated in this thesis, a slightly smaller K_{I0} we have obained is reasonable. Other equations were found to underestimate the K_{I0} of alumina and the new model shows a better prediction.

6.5.2 SiC

Table 6.3 K_{IC} of SiC calculated by the new equation and other mainstream equations (fracture toughness numbers all in unit of MPa$\sqrt{m}$).

	Load (N)	New model	Anstis	Evans and Charles	Lawn and Fuller
SiC	9.8	1.74 ± 0.13	1.48 ± 0.14	1.85 ± 0.17	1.79 ± 0.17
	24.5	2.21 ± 0.13	1.75 ± 0.12	2.03 ± 0.14	1.96 ± 0.14
	49	2.09 ± 0.12	1.72 ± 0.12	2.17 ± 0.16	2.09 ± 0.15
	98	2.63 ± 0.12	1.88 ± 0.10	2.06 ± 0.11	1.99 ± 0.11
Average		2.17 ± 0.13	1.71 ± 0.12	2.03 ± 0.14	1.96 ± 0.14

Sintered SiC exhibits negligible subcritical slow crack growth for temperatures below 1200℃ (Fett et al., 1997). Putting the indentation parameters of SiC obtained in Chapter 5 into the equations in Table 6.1, the indentation fracture toughness K_{IC} for

SiC was calculated and is shown in Table 6.3. The K_{IC} obtained by the SEVNB method in our research group was 2.55 ± 0.13 MPa$\sqrt{m}$. The K_{IC} calculated from the new equation is again closer to the K_{IC} from SEVNB. Other equations still underestimated the K_{IC}.

The underestimation of the equations from Anstis et al. (1981) Evans and Charles (1976a) Lawn and Fuller (1975) is probably because that they forcibly calibrate the equation to match with fracture toughness results from other standard methods. However, the radial crack lengths in their work were all measured by optical microscope and the work in this thesis has shown that the optical microscope will significantly underestimate the radial crack length. Therefore, when a higher radial crack length was put into their equation, the stress intensity factor results will be smaller than the actual value. For instance, even though the Anstis et al. (1981) equation was calibrated using Al_2O_3 and SiC amongst other materials, it still underestimates the K_{I0} of alumina and K_{IC} of SiC using the present crack length results. It is emphasised that the present equation contain no force fitted empirical variables.

In Section 4.2.5, the optical microscope was found to introduce underestimation of radial crack lengths. Table 6.4 shows the K_{I0} of polycrystalline alumina and K_{IC} of SiC

calculated with and without correction. The *K* calculated by using crack length from OM, K_{OM}， was found significantly higher than from corrected value, $K_{corrected}$ for all the equations. The overestimation of the K_{OM} (in the percentage of $K_{corrected}$) increases as load decreases and for 9.8 N, the differences are as high as 34% and 46% for alumina and SiC, respectively, which is quite significant. Therefore, the OM method for crack length measurement can produce significant errors and a precise measurement of the radial crack length is suggested for the VIF test. This will be further discussed in Section 6.10. Additional, it can be seen that on Al_2O_3 and SiC, the stress intensity factor *K* has the tendency to increase with the increase of the applied load and this will be further discussed in Section 6.8.

Table 6.4 The K_{I0} of polycrystalline alumina and K_{IC} of SiC calculated by the new equation and other mainstream equations using radial crack lengths with and without correction for the resolution of the optical microscope (fracture toughness numbers all in unit of MPa$\sqrt{m}$).

	Load (N)	New model			Anstis		Evans and Charles		Lawn and Fuller	
		OM	FLM	% of FLM	OM	FLM	OM	FLM	OM	FLM
alumina	9.8	2.93	2.18	34%	2.72	1.93	3.07	2.18	2.97	2.11
	24.5	2.95	2.35	26%	2.54	1.93	2.76	2.10	2.66	2.03
	49	2.76	2.35	17%	2.41	2.00	2.77	2.30	2.68	2.22
	98	3.05	2.67	14%	2.32	1.98	2.38	2.04	2.30	1.97
Average		2.92	2.39	22%	2.50	1.96	2.75	2.15	2.65	2.08
		OM	Corrected	%	OM	Corrected	OM	Corrected	OM	Corrected
SiC	9.8	2.54	1.74	46%	2.32	1.48	2.90	1.85	2.80	1.79
	24.5	2.83	2.21	28%	2.34	1.75	2.73	2.03	2.64	1.96
	49	2.49	2.09	19%	2.12	1.72	2.67	2.17	2.58	2.09
	98	2.95	2.63	12%	2.15	1.88	2.36	2.06	2.28	1.99
Average		2.70	2.17	25%	2.23	1.71	2.67	2.03	2.57	1.96

6.6 Testing the model with Si_3N_4 indentation results from Quinn and Bradt

To further test the new equation calculating K_{IC}, Quinn and Bradt (2007) original data on Si_3N_4 (another ceramic with radial-median crack system (Lube, 2001)) was reanalysed (Table 6.5). Quinn and Bradt (2007) indented the standard reference material (SRM) 2100 silicon nitride on two sides of the specimen. Quinn and Bradt (2007) did not test whether the indentation on this Si_3N_4 had lateral cracking or not, but from previous research (Lube, 2001), Si_3N_4, is very likely to have lateral cracking beneath indentations. This material has been claimed by Quinn et al. (2002) as the "world's first ceramic fracture toughness reference material" as almost identical results from SEPB, CNB and SCF methods can be found on this material. The new equation produces results (Table 6.4) with average value falling into the tolerance of the certified K_{IC} (with uncertainty of $\pm$ 0.11 MPa$\sqrt{m}$) on the 4mm$\times$25mm face but deviates from the reference on the 3 mm$\times$25 mm faces. A disagreement of the two sets results by VIF methods has been found also in the work of Quinn and Bradt. This is probably due to the scatter in the indentation parameters as the crack lengths often differ by 2%-11% in their work or possibly because the two faces are with different surface conditions. There is also uncertainty on the accuracy of their radial crack length measurement. Quinn and Bradt did not mention how the crack lengths were measured in their paper; however, according to their previous routine (Quinn and D QUINN, 1997, Quinn and Quinn, 2009), the crack lengths were most likely to have been measured by traditional optical microscopy. Therefore, the crack lengths

they obtained were likely to be underestimated and the indentation fracture toughness should accordingly be overestimated by the new equation. The new equation gives an average fracture toughness value of 4.75 MPa$\sqrt{m}$ from the results on two surfaces and is slightly larger than the certificated fracture toughness 4.57 MPa$\sqrt{m}$, this is reasonable considering the analysis above. On this point, the new equation provides the better results than the VIF equations shown in Table 6.6 and 6.7 (Anstis et al., 1981, Niihara et al., 1984, Miyoshi et al., 1985) used by Bradt and Quinn.

Table 6.5 Vickers indentation fracture resistance results for a standard reference material (SRM) 2100 silicon nitride test piece with indentations in a 3 mm×25 mm and 4mm×25mm faces with original data imported from Quinn and Bradt (2007).

Indentation load (N)	a(μm)	c(μm)	Certified K_{IC} (MPa√m)	New Model (MPa√m)
4 mm×25 mm face				
9.8	16.2	33.0	4.57	4.04
19.6	23.5	52.0	4.57	4.36
49.0	37.5	94.0	4.57	4.67
98.0	53.3	148.9	4.57	4.83
				Average=4.47±0.30
3 mm×25 mm face				
9.8	16.7	30.9	4.57	4.67
19.6	23.7	49.6	4.57	4.71
49.0	37.9	91.7	4.57	4.92
98.0	53.6	145.6	4.57	5.02
196.0	76.5	222.0	4.57	5.50
				Average=4.96±0.30

Table 6.6 VIF results on the 4mm×25mm face on Silicon Nitride test piece (Quinn and Bradt, 2007).

Indentation load (N)	Average diagonal half length a (μm)	Average crack half length c (μm)	SRM 2100† certified K_{Ic} (MPa·m$^{1/2}$)	Anstis‡ K_c (MPa·m$^{1/2}$)	Niihara§ K_c (MPa·m$^{1/2}$)	Miyoshi¶ K_c (MPa·m$^{1/2}$)
9.8	16.2±0.3	33.0±1.4	4.57	3.44±0.20	5.14±0.30	4.02±0.23
19.6	23.5±0.1	52.0±1.0	4.57	3.56±0.11	5.29±0.16	4.16±0.13
49	37.5±0.2	94.0±1.5	4.57	3.69±0.09	5.47±0.13	4.31±0.10
98	53.3±0.3	148.9±1.9	4.57	3.72±0.08	5.51±0.11	4.34±0.09

Table 6.7 VIF results on the 3 mm×25 mm face on Silicon Nitride test piece (Quinn and Bradt, 2007).

Indentation load (N)	Average diagonal half length a (μm)	Average crack half length c (μm)	SRM 2100† certified K_{Ic} (MPa·m$^{1/2}$)	Anstis‡ K_c (MPa·m$^{1/2}$)	Niihara§ K_c (MPa·m$^{1/2}$)	Miyoshi¶ K_c (MPa·m$^{1/2}$)
9.8	16.7±0.3	30.9±0.5	4.57	3.89±0.13	5.78±0.18	4.55±0.15
19.6	23.7±0.3	49.6±0.9	4.57	3.84±0.10	5.70±0.14	4.49±0.12
49	37.9±0.4	91.7±1.4	4.57	3.86±0.10	5.72±0.15	4.51±0.12
98	53.6±0.4	145.6±3.7	4.57	3.87±0.15	5.73±0.22	4.52±0.17
196	76.5±0.7	222.0±6.4	4.57	4.15±0.18	6.13±0.27	4.85±0.21

6.7 Possible adjustable parameters for the model

Although the model has shown its robustness from the predictions on *K*, there are three adjustable parameters which could be introduced to further strengthen the model. This helps understanding the assumptions in the model and variance in *K* with load found in Section 6.5.

6.7.1 Plastic zone dimension factor, α

The dimension factor, α, is the factor defined in $r_p = \alpha d/2 = \alpha a_{V,}$ where r_p is the radius of the plastic zone and $a_{V,}$ is the indentation half-diagonal length. The model assumes α =1 for the calculation of *K*. The value of *K* is very sensitive to α. A ±10% variance of the α (0.9-1.1) leads to ±11%-14% variance of *K* for alumina and SiC and a higher α corresponds to a lower *K* value. α =1 worked very well on alumina and this has been experimentally approved. The SiC used here has a smaller E/H ratio (15.5) compared with alumina (18.3). According to the analysis proposed by Chiang et al. (1982), the relative plastic zone radius of SiC should be smaller. This implies the α of SiC is likely to be less than 1. This may explain the reason why the results in Section 6.5.2 underestimated the fracture toughness of the SiC. Similarly, the Si_3N_4 used by Quinn and Bradt (2007) on the 4 mm×25 mm face has an E/H ratio of 18.8, which is very close to alumina and the fracture toughness predicted by the model is quite close to the reference. On the 3 mm×25 mm face the E/H ratio (19.5) is slightly larger than alumina (hence the α is likely to be larger than 1), therefore the results shows mild overestimation. From Chiang et al. (1982)'s analysis, the relative plastic zone radius hence the α used in this study is a parameter which relates to the material property. The actual value of the α of the SiC and Si_3N_4 certainly needs more experimental investigation.

6.7.2 Weighting factor, β

In the new model, the stress intensity factor, *K,* is calculated from the average of the upper and lower bound, K_{upper} and K_{lower}. More precisely, a weighting factor could be introduced to deal with the situations when the actual indentation cracking and residual stress are more close to the upper or the lower bound condition. *K* will then be expressed as:

$$K = \beta K_{upper} + (1-\beta)K_{lower}$$

The parameter, β ($0 \leq \beta \leq 1$), is the weighting factor. This factor may change with material property or the indentation load. For quantitative analysis, the β could be calculated from the residual stress data and for each data point, the weighting factor can be ascertained by:

$$\beta_0 = \frac{|\sigma - \sigma_{lb}|}{|\sigma - \sigma_{lb}| + |\sigma - \sigma_{ub}|}$$

where σ is the residual stress, σ_{lb} is the predicted residual stress by lower bound condition, and σ_{ub} is by upper bound condition. The β value will be the average of β_0 for all data points for each load. Table 6.8 compares the *K* value with and without the introduction of the weighing factor. On average, the adjusted *K* has a similar value as before and most β values are smaller than 0.5 indicating the residual stress seems to be a bit closer to the lower bound condition. For general use of the Equation 6.39, a β=0.5 will give a satisfactory result.

Table 6.8 Comparison of the K value with and without the adjustment of the weighing factor.

	Load (N)	Former K	Adjusted K	β
alumina	9.8	2.18	2.10	0.40
	24.5	2.35	2.44	0.61
	49	2.35	2.22	0.35
	Average	2.29±0.08	2.25±0.14	
SiC	9.8	1.96	1.70	0.44
	24.5	2.30	2.11	0.37
	49	2.17	2.05	0.44
	Average	2.14±0.14	1.95±0.18	

6.7.3 Crack depth dimension factor, γ

The model assumes the depth of the lateral crack is equal to the radius of the plastic zone and roughly the half-diagonal length ($h = r_p = \alpha d/2 = \alpha a_V$). However, it can be noticed from the results in Section 4.2.8 that the depth of the lateral crack is normally smaller than the indentation half-diagonal length. To consider this fact, a crack depth dimension factor, γ, is introduced and defined as $\gamma = h/r_p$. Assuming, α=1, $\gamma = h/a_V$. For alumina indentations, the measured values of γ are shown in Table 6.9.

Table 6.9 Crack depth dimension factor,γ, for different loads on alumina.

Indentation loads (N)	Lateral crack depth (μm)	Half-diagonal length (μm)	γ
9.8	12.4	13.8	0.90
24.5	21.6	22.7	0.95
49	26.1	30.3	0.86
98	43.1	48.1	0.90

The model also assume that the radial misfit, a_0, is relative to its surroundings such that the volume of the misfit is equal to 2/3 of the indentation volume based on the assumption that the expansion of the plastic zone occurs equally in the three principal directions, with the expansion in the direction normal to the surface being absorbed in the lateral cracking. This assumption simplified the misfit due to indentation volume as the plastic zone was initially treated as cylindrical. Here a more rigorous solution is made starting with the consideration of the plastic zone as a hemi-sphere:

The expansion of the plastic zone due to the indentation volume is described as:

$$2\pi r_p^2 \varepsilon = \Delta V \qquad \text{Equation 6.40}$$

where, ε is the radial misfit (Figure 6.9) of the entire plastic zone, r_p is the radius of the plastic zone, ΔV is the volume of the Vickers indentation.

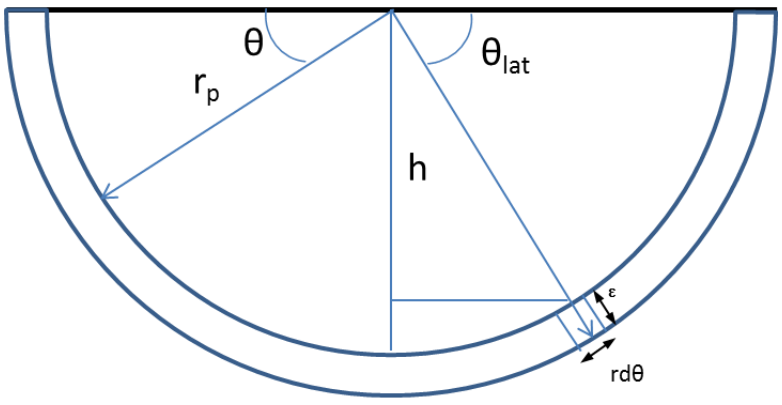


Figure 6.9 Sketch of the expansion of the plastic zone due to the volume of the indentation.

The total volume of the misfit can be also expressed as

$$\mathrm{V}_{total} = \int_0^{\pi/2} r_p d\theta \varepsilon \cdot 2\pi r_p \cos\theta$$

The average misfit component, $\delta a_0'$, parallel to the surface due to the expansion is

$$\delta a_0{}' = \frac{\int \varepsilon \cos\theta dV}{\mathrm{V}_{total}} = \frac{\varepsilon \int_0^{\pi/2} \cos^2\theta d\theta}{\int_0^{\pi/2} \cos\theta d\theta}$$

Only considering the volume expansion above the lateral crack, i.e. $0 \le \theta \le \theta_{lat}$, and $sin\theta_{lat} = h/r_p = \gamma$, the mean misfit δa_0 in this case is:

$$\delta a_0 = \frac{\varepsilon \int_0^{\theta_{lat}} \cos^2\theta d\theta}{\int_0^{\theta_{lat}} \cos\theta d\theta}$$

Combing with Equation 6.40 and Equation 6.26 to eliminate ε,

$$\delta a_0 = \frac{\sqrt{2}a_v}{6k\alpha^2} \cdot \frac{\frac{1}{2}sin^{-1}\gamma + \frac{1}{2}\gamma\sqrt{1-\gamma^2}}{\gamma} = \frac{a_v}{3\sqrt{3}k\alpha^2} \cdot \frac{\sqrt{6}}{2} \cdot \frac{\frac{1}{2}sin^{-1}\gamma + \frac{1}{2}\gamma\sqrt{1-\gamma^2}}{\gamma}$$

in which $k = \pi tan\psi$

The corresponding a_0 value can be determined from volume of the plastic zone above the lateral crack with a spherical cap being truncated:

$$\frac{2\pi \mathrm{r_p}^3}{3} - \frac{\pi\left(\mathrm{r_p} - h\right)^2}{3}\left(2\mathrm{r_p} + h\right) = \pi a_0^2 h$$

The new expression for Equations 6.27.2 will be $a_i = \frac{2^{\frac{1}{4}}}{\sqrt{3\alpha\gamma k}} a_v$

Taking δa_0, a_i, a_0 into Equations 6.38.3, 6.38.4 and 6.38.5 *G* and *K* (assuming $\alpha = 1$) were calculated for different values of γ.

Table 6.10 compared the *K* value with and without the adjustment of crack depth dimension factor, γ for alumina indentations. The adjusted *K* have slightly larger values than before and the adjusted *K* increases as γ decreases. *K* is insensitive to γ, however, for all loads, as γ decreases from 0.9 to 0.6 (by 33%), the increase in K is only around 6%. This indicates the previous assumptions made in Section 6.2.2 and 6.2.3.1 are generally acceptable.

Table 6.10 Comparison of the K value with and without the adjustment of crack depth dimension factor, γ.

Load (N)	Former K	Adjusted K	γ
9.8	2.18	2.29	0.90
24.5	2.35	2.42	0.95
49	2.35	2.47	0.86
98	2.67	2.79	0.90
Average	2.39±0.11	2.49±0.18	

6.8 The apparent R-curve effect

The new model gives good predictions both in residual stress field and the stress intensity factor, *K*. However, like many other VIF equations, the new equation for the stress intensity factor *K* has the tendency to increase with the increase of the applied load (Quinn and Bradt, 2007) and this has been seen with the Al_2O_3, SiC and Si_3N_4 results, although the actual R-curve effect is thought to be small in these materials. In

many cases, the VIF is contradictory to the results obtained by other standard macroscopic methods (Quinn and Bradt, 2007) on the R-curve effect. The increase of *K* with load in VIF test on material thought to have no real R-curve is referred as the apparent R-curve effect here. The root cause of this issue for the VIF technique is still unclear.

The author believes this is mainly because the interference of the microstructural features with the crack will differ with different loads, which is also mentioned by Anstis et al. (1981) in their work. For instance, the 9.8 N indentations on Al_2O_3, SiC and Si_3N_4 have shown smaller *K* compared with other loads and the crack lengths (around 10-40 μm) will be close to the scale of microstructure features, such as the grain size and defects, such as porosities. This is something that users of the VIF technique should be aware of. From the present results, the author suggests to use this model on high indentation loads in which the scale of crack is much larger than the microstructure features. This is discussed further in the next Section 6.10 in which the suggestions for the practical applications of the VIF technique are made.

For the present model, the variance of the dimension factor, α, with the load may also contribute to the apparent R-curve effect on VIF. The R-curve issue is likely to

be caused by the combination of the drivers mentioned above and further research is required to understand this in depth.

6.9 Advantages and disadvantages of the model

Advantages:

(1) The residual stress model and the derived stress intensity equation do not have the adjustable parameters which are very common in other equations relating to indentations. This is a big advantage as many other equations have parameters calibrated by empirically force fitting to match valid data from other methods. Therefore this makes the model versatile for use with other materials and more predictive.

(2) The residual stress field from the model can be verified experimentally.

(3) The new model takes into consideration lateral cracking, which has normally been overlooked in previous research.

(4) The model predicts the right level of residual stress and stress intensity factor and its predictions on alumina and SiC indentation are satisfactory.

Disadvantages

(1) There are rigorous requirements on the cracking pattern and cracking behaviours to make the assumptions valid. Some assumptions are difficult to test, like the length and the growth of the lateral crack.

(2) The residual stress model has abrupt boundaries and changes of residual stress level at the outer edge of the assumed plastic zone ($r = a_o$) and at the outer extent of the radial cracks ($r = c$). In reality, a smoother transition of residual stresses is expected to occur at both boundaries.

(3) Like many other VIF equations, an apparent R-curve effect was still found from the model predictions and the root cause of this effect is still unclear.

Most engineering ceramics have been shown to follow radial-median-lateral crack system under the range of indentation loads normally used. For example, polycrystalline Al_2O_3, Si_3N_4 (Lube, 2001), soda-lime silicate glass (Cook and Liniger, 1993), SiC and TiB_2 (Yonezu et al., 2009) have all been proved to have lateral crack beneath indentations. Therefore, this model will be potentially usable for many ceramics and provides a new route to deduce fracture toughness. For using this model, the author suggests the model assumptions should be tested carefully, the crack lengths should be accurately measured and high indentation loads are also suggested. This is further elaborated in the following section.

6.10 Suggestions for the future use of the Vickers indentation

It has been nearly 40 years since the Vickers indentation technique was introduced to study fracture toughness of ceramics by Evans and Charles (1976b). During the past 40 years, numerous researchers have made efforts trying to determine the fracture toughness of their ceramics using the VIF technique. When the their results using previous equations gave puzzling conclusions, they tended to come up a new equation to better describe their results. This has led to more than 30 equations being published for different types of ceramics. However, the methods of conducting the VIF measurement and especially of measuring indentation parameters have not been standardised. Because this technique is easy to perform, many researchers did not pay much attention to the method of doing VIF measurement. There is no doubt that the VIF technique is important to the ceramic fracture community and in many cases this technique cannot be replaced by other fracture toughness techniques. During the period in which the author was writing this thesis, many new papers have been published which use VIF as a standard fracture toughness method (Tiegel et al., 2015, Lima et al., 2015). Therefore, it is important to have standard guidance on applying this technique, like many other standard tests, so that the VIF results are valid and can be compared. From the research in this thesis, the following suggestions can be made for the use of the Vickers indentation as a way of measuring fracture toughness.

(1) The indentations should be well made and well chosen. Indentations with badly split cracks or asymmetrical cracks or spalling or gross chipping should be rejected. Only indentations with four primary cracks emanating straightforwardly from each corner should be accepted.

(2) For materials with no slow crack growth behaviour, the indentation fracture toughness, K_{Ic}, could be determined from direct measurement after indentation. The crack length (radial-median or Palmqvist) should be measured by a method which has a good resolution to identify the tip of the crack, such as FLM, Raman microscopy, and environmental SEM. The optical microscope is not ideal because (a) the resolution of the OM is not good enough to identify the crack tip; (b) the measurement by OM is normally dependent on the operator's own judgement; (c) the crack tip may not be seen depending on the reflectivity of the sample (Anstis et al., 1981). As seen from Section 6.5.2, the underestimation by OM may introduce a large error for K and this is more prominent with low indentation loads. For materials with slow crack growth behaviour, the crack length should be measured by an in situ camera capable of capturing the crack image within 1s after indentation if measured and the camera should have good resolution to view the crack tip. This seems to be unrealistic for most cases, so measuring the K_{Io} will probably more practical and meaningful. The use of unreactive substance (such as oil) have been suggested to prevent the crack growth, however as noticed by (Anstis et al., 1981) the crack

growth was still fast even when the specimen was indented in oil as it is difficult to be exclude water completely.

(3) For the radial crack length measured by OM, this thesis also offered a COD method for correcting the radial crack length described in Section 4.3.3 and later employed for SiC and TZP. Therefore, the resolution of the optical microscope should be predetermined before using OM method. However, recommendation (2) above is still advised for best accuracy.

(4) The crack pattern should be examined to identify the cracking system (Palmqvist or radial-median) and the presence or absence of the lateral crack. This is clearly important so as to ascertain the crack system and select the most appropriate equation.

(5) For polycrystalline ceramics, the VIF should not be applied when the coarseness of the microstructural features is comparable with the indentation size and the length of the indentation crack. In this case, the cracking pattern and the crack growth are more susceptible to interference from the local microstructure (Anstis et al., 1981).

6.11 Summary

- A new Vickers indentation residual stress model has been presented based on experimental findings from alumina indentations.

- The residual stress model has successfully predicted the stress fields around indentations in polycrystalline alumina and SiC but failed on TZP because the crack pattern did not conform to the assumptions of the model.

- From the residual stress model, a new formula for the indentation stress intensity factor, *K,* was derived, which provided good results for threshold stress intensity factor, K_{I0}, on alumina, and for fracture toughness, K_{IC}, with SiC, and Si_3N_4 (using indentation parameters from Quinn and Bradt (2007).

- Three adjustable parameters, a plastic zone dimension factor, α, a weighting factor, β and a crack depth dimension factor, γ, can be added to strengthen the existing model.

- For the future use of the VIF technique some suggestions were made for making the VIF results valid and comparable.

References

ANSTIS, G., CHANTIKUL, P., LAWN, B. R. & MARSHALL, D. 1981. A critical evaluation of indentation techniques for measuring fracture toughness: I, direct crack measurements. *Journal of the American Ceramic Society,* 64**,** 533-538.

CHIANG, S., MARSHALL, D. & EVANS, A. 1982. The response of solids to elastic/plastic indentation. I. Stresses and residual stresses. *Journal of Applied Physics,* 53**,** 298-311.

COOK, R. F. & LINIGER, E. G. 1993. Kinetics of indentation cracking in glass. *Journal of the American Ceramic Society,* 76**,** 1096-1105.

DE AZA, A., CHEVALIER, J., FANTOZZI, G., SCHEHL, M. & TORRECILLAS, R. 2002. Crack growth resistance of alumina, zirconia and zirconia toughened alumina ceramics for joint prostheses. *Biomaterials,* 23**,** 937-945.

EVANS, A. & CHARLES, E. 1976a. Fracture toughness determinations by indentation. *Journal of the American Ceramic Society,* 59**,** 371-372.

EVANS, A. G. & CHARLES, E. A. 1976b. Fracture toughness determinations by indentation. *Journal of the American Ceramic Society,* 59**,** 371-372.

EVANS, J. D. 1996. *Straightforward statistics for the behavioral sciences*, Brooks/Cole.

FETT, T., MUNZ, D., KELLER, K. & HIMSOLT, G. 1997. Subcritical crack growth in silicon carbide. *Journal of Materials Science Letters,* 16**,** 324-327.

GREEN, D. J. 1998. *An introduction to the mechanical properties of ceramics*, Cambridge University Press.

GRIFFITH, A. A. 1920. *Phil. Trans. Roy. Soc. Lond. ,* A221 163.

HIRSCH, P., PIROUZ, P., ROBERTS, S. & WARREN, P. 1985. Indentation plasticity and polarity of hardness on {111} faces of GaAs. *Philosophical Magazine B,* 52**,** 759-784.

LAWN, B. & SWAIN, M. 1975. Microfracture beneath point indentations in brittle solids. *Journal of Materials Science,* 10**,** 113-122.

LAWN, B. R. & FULLER, E. 1975. Equilibrium penny-like cracks in indentation fracture. *Journal of Materials Science,* 10**,** 2016-2024.

LIMA, E. S., ITABORAY, L., SANTOS, A., SANTOS, C. & CABRAL, R. Mechanical Properties Evaluation of Al2O3-YAG Ceramic Composites. Materials Science Forum, 2015. Trans Tech Publ, 239-243.

LUBE, T. 2001. Indentation crack profiles in silicon nitride. *Journal of the European Ceramic Society,* 21**,** 211-218.

MARSHALL, D., LAWN, B. & EVANS, A. 1982. Elastic/plastic indentation damage in ceramics: the lateral crack system. *Journal of the American Ceramic Society,* 65**,** 561-566.

MIYOSHI, T., SAGAWA, N. & SASSA, T. 1985. Study on fracture toughness evaluation for structural ceramics. *Trans. Jap. Soc. Mech. Eng,* 51**,** 2487-2489.

MOTT, P. & ROLAND, C. 2009. Limits to Poisson's ratio in isotropic materials. *Physical Review B,* 80**,** 132104.

NIIHARA, K., NAKAHIRA, A. & HIRAI, T. 1984. The effect of stoichiometry on mechanical properties of boron carbide. *Journal of the American Ceramic Society,* 67**,** C‐13-C‐14.

QUINN, G. D. & BRADT, R. C. 2007. On the Vickers indentation fracture toughness test. *Journal of the American Ceramic Society,* 90**,** 673-680.

QUINN, G. D., XU, K., GETTINGS, R. J., SALEM, J. A. & SWAB, J. J. 2002. Does anyone know the real fracture toughness? SRM 2100: the world's first ceramic fracture toughness reference material. *ASTM SPECIAL TECHNICAL PUBLICATION,* 1409**,** 76-92.

QUINN, J. & D QUINN, G. 1997. Indentation brittleness of ceramics: a fresh approach. *Journal of materials science,* 32**,** 4331-4346.

QUINN, J. B. & QUINN, G. D. Hardness and brittleness of ceramics. 20th Annual Conference on Composites, Advanced Ceramics, Materials, and Structures-A: Ceramic Engineering and Science Proceedings, Volume 17, 2009. John Wiley & Sons, 59.

TIEGEL, M., HOSSEINABADI, R., KUHN, S., HERRMANN, A. & R SSEL, C. 2015. Young′ s modulus, Vickers hardness and indentation fracture toughness of alumino silicate glasses. *Ceramics International,* 41**,** 7267-7275.

YOFFE, E. 1982. Elastic stress fields caused by indenting brittle materials. *Philosophical Magazine A,* 46**,** 617-628.

YONEZU, A., XU, B. & CHEN, X. 2009. Indentation induced lateral crack in ceramics with surface hardening. *Materials Science and Engineering: A,* 507**,** 226-235.

YU, H.-H. & HUTCHINSON, J. W. 2002. Influence of substrate compliance on buckling delamination of thin films. *International journal of fracture,* 113**,** 39-55.

Chapter 7 Conclusions and suggestions for the future

7.1 Conclusions

7.1.1 Vickers indentation study on alumina

(1) Plastic zone

- There is a well-defined interface between the plastic zone and the elastic region and the radius of the plastic zone is close to half the indentation diagonal length.

(2) Residual stress field.

- The residual stress field around the indentations has been measured by FLM scans.
- Yoffe's model predicted higher stresses than the residual stress results because Yoffe's model did not consider relaxation of the stress by the radial and lateral cracking.

(3) Indentation cracking system.

- The indentation parameters for 9.8-98 N alumina indentations were measured.

The half indentation diagonal lengths were measured by OM. The radial crack lengths were measured by FLM, OM and SEM. The OM and SEM methods were found to significantly underestimate the crack lengths. The FLM line scan has shown much better accuracy and is therefore recommended for measuring the indentation radial crack length of alumina based ceramics.

- Post indentation slow crack growth was found on the radial cracks of the 49 N alumina and ruby indentations. The threshold K_{I0} of the radial cracks of the indentations on polycrystalline alumina and the ruby were determined to be 2.2 MPa$\sqrt{m}$ and 2.4 MPa$\sqrt{m}$, respectively.

- The radial-median crack system was found in the 9.8-98 N alumina indentations.

- Lateral cracks were also found for all the indentations, and their depths were found to be close to the half diagonal lengths. Lateral cracks join the tips of the radial cracks and are close to, but not perfectly circular (they extend further along the radial cracks than between them). The lateral crack has a similar length to the radial crack.

- The lateral crack was observed to have a similar growth rate to the radial crack in ruby and growth of both terminated at nearly the same time.

7.1.2 Vickers indentation study SiC and 3Y-TZP

SiC:

- The indentation parameters of SiC indentations were measured and corrected using the method described in Section 4.3.3.
- The Raman spectra of SiC were characterised, and the 6H-SiC polytype was found to be the primary polytype. The 6H-SiC A1t peak (789 cm^{-1}) was selected for the residual stress study due to its strong peak intensity and less overlapping with other peaks. The PS coefficient of this peak was found to be -4.88 ± 0.11 $GPa^{-1}cm^{-1}$.
- Lateral cracking was found beneath the SiC indentations. The depth of the lateral crack of the SiC indentation was found to be close to the half diagonal length. The lateral crack lengths of the SiC indentations determined from the surface profile are close to the radial crack length, and this is similar to the findings for alumina indentations.
- The residual stresses around the 9.8 N, 24.5 N and 49 N indentations on SiC were measured and analysed by the new indentation model.

TZP:

- The indentation parameters for TZP indentations were measured and corrected

using the method described in Section 4.3.3. Lateral cracking was not found beneath the TZP indentations.

- The Raman spectra of TZP were characterised. In as annealed TZP, the tetragonal phase was in the majority and the monoclinic phase had the minor volume fraction.

- The residual stresses around the 9.8 N, 24.5 N and 49 N indentations in TZP were measured and analysed by the new indentation model

- The highest volume fraction of the monoclinic zirconia phase was found near the edge of the TZP indentation this was thought to be caused by the high concentration of the tensile and shear stresses.

- Around the TZP indention, the surface uplift was found to have the profile matching with the distribution of the volume fraction of the monoclinic phase.

7.1.3 Vickers indentation model

- A new Vickers indentation residual stress model has been presented based on experimental findings from alumina indentations.

- The residual stress model has successfully predicted the stress fields around indentations in polycrystalline alumina and SiC but failed on TZP because the crack pattern did not conform to the assumptions of the model.

- From the residual stress model, a new formula for the indentation stress intensity factor, *K,* was derived, which provided good results for threshold stress intensity factor, K_{I0}, on alumina, and for fracture toughness, K_{IC}, with SiC, and Si3N4 (using indentation parameters from Quinn and Bradt (2007).

- Three adjustable parameters, a plastic zone dimension factor, α, a weighting factor, β and a crack depth dimension factor, γ, can be added to strengthen the existing model.

- For the future use of the VIF technique some suggestions were made for making the VIF results valid and comparable.

7.2 Future work

7.2.1 Lateral crack characterization

The length and depth of the lateral cracks beneath Vickers indentations are difficult to ascertained. In this study, the length of the lateral crack was measured from the surface profiles around the indentations which is an indirect measurement method. For direct observation of the lateral cracks, some nondestructive techniques, such as Scanning Acoustic Microscopy and Scanning Electron Acoustic Microscopy (Cantrell et al., 1990), could be employed. The nondestructive techniques could eliminate the growth of the crack during polishing or sectioning and potentially monitor the

post-indentation crack growth, which would provide insightful information for the understanding of the lateral crack.

7.2.2 Testing the model on more ceramics

Although the model made good predictions on Al_2O_3 and SiC indentations, the model needs to be tested on other ceramics to prove it is generally applicable. This involves (1) testing the model assumptions for other ceramics with radial-median-lateral indentation crack systems and (2) testing the residual stress and *K* predictions on these ceramics for a broad range of indentation loads. A good start will probably be to expand the investigation of the standard reference material 2100 silicon nitride mentioned in Chapter 6 as the fracture toughness of this material has been well characterized by Quinn et al. (2002). Although Quinn and Bradt (2007) have tested the material using Vickers indentations, their crack length measurements are not accurate, and the cracking pattern and behaviour of this material are still uncertain.

7.2.3 The apparent R-curve effect

The apparent R-curve effect in Vickers indentation is a persistent issue for the VIF technique. This has also been seen in the new model proposed in this thesis. Chapter 6 has shown that the value of K depends very sensitively on α, the plastic

zone dimension factor. Therefore, it is worth checking more if the α varies with the indentation load on various ceramics. This can be done by viewing the cross-section of the indentation (Van der Zwaag et al., 1980). When the indentation load is small, the interaction of the crack with the local microstructural features may also affect the apparent R-curve effect on Vickers indentation. Therefore it is also worth checking the effect of this interaction and finding out above which load the effect could be ignored.

References

CANTRELL, J. H., QIAN, M., RAVICHANDRAN, M. & KNOWLES, K. 1990. Scanning electron acoustic microscopy of indentation‐induced cracks and residual stresses in ceramics. *Applied physics letters,* 57, 1870-1872.

QUINN, G. D. & BRADT, R. C. 2007. On the Vickers indentation fracture toughness test. *Journal of the American Ceramic Society,* 90, 673-680.

QUINN, G. D., XU, K., GETTINGS, R. J., SALEM, J. A. & SWAB, J. J. 2002. Does anyone know the real fracture toughness? SRM 2100: the world's first ceramic fracture toughness reference material. *ASTM SPECIAL TECHNICAL PUBLICATION,* 1409, 76-92.

VAN DER ZWAAG, S., HAGAN, J. & FIELD, J. 1980. Studies of contact damage in polycrystalline zinc sulphide. *Journal of materials science,* 15, 2965-2972.